Kinetic Models for the Pt/CeO_2 Catalysed Water-Gas Shift Reaction

By

Darryl Edward Brown

Dissertation submitted to the University of Cape Town
in partial fulfilment of the requirements
for the degree of

Master of Science in Engineering

HySA/Catalysis Centre of Competence
Catalysis Institute
Department of Chemical Engineering
University of Cape Town

September 2017

Synopsis

As the global population grows, so does the world's demand for energy. Consequently, there exists an increased interest in the development of fuel cells for power generation due to their low greenhouse gas emissions. For fuel cells to be a successful power source, a reliable hydrogen source is required. Ultimately, the goal is for hydrogen to be supplied from renewable energy technology however, this type of technology is currently not mature enough to meet the continuous demand of the world's energy systems. Producing hydrogen from fossil fuels can be seen as a temporary solution while further advances are made in developing renewable hydrogen infrastructure. A fuel processing train, therefore, remains an important alternative to producing hydrogen. A fuel processing train converts fossil fuels into hydrogen for use in fuel cells and eliminates the need for hydrogen storage as hydrogen is produced on demand.

Currently, the water-gas shift (WGS) reactor is one of the largest components in a fuel processing train and thus opportunity exists to reduce the size of this reactor. To design future WGS catalysts and an optimised fuel processor, the reaction kinetics taking place must be understood and quantified.

In this study, kinetic measurements were conducted at 2 bar(a) and across a temperature range of 270 – 300 °C using 16 parallel fixed bed reactors (high throughput experimentation) over a 0.5 wt% Pt/CeO_2 catalyst. The feed composition was varied over the ranges 2 – 12 mol% CO, 20 – 45 mol% H_2O, 4 – 15 mol% CO_2 and 25 – 55 mol% H_2. An online micro gas chromatograph (μGC) was used to analyse the dry gas composition. Fitting of experimental data to various kinetic models was accomplished with the gPROMS software package.

An initial evaluation of several Langmuir-Hinshelwood (LH) type mechanisms to two data sets obtained from literature was undertaken to evaluate the strengths and weaknesses of different kinetic expressions. The results of the initial evaluation indicate that a dual-site mechanism with an intermediate species results in the best fit for reducible supports, while a single site mechanism offers a better fit for non-reducible supports. For both kinetic models, the formation of the intermediate species is most likely to be the rate determining step.

A power-rate law empirical rate expression and a LH type rate expression were both found to predict the WGS outlet composition well within 10 % error at 2bar(a). The apparent activation energy of the reaction was determined to be 110 kJ/mol. This value was confirmed to be constant, throughout the range of conditions evaluated, by means of a classical Arrhenius analysis.

Simulations of increasing total system pressure, using both the empirical and "best fitting" LH model, indicate a significant pressure effect for the LH type equation, whereas the power-rate law empirical equation predicts a small, negative effect on the reaction rate with increaseing pressure. Consequently, further experiments were conducted to determine the true effect of

pressure. It was found that increasing system pressure increased the WGS reaction rate, which has also been reported by Twigg (1989:288). Only the LH type rate expression was able to predict this.

It is therefore recommended that either the power-rate law empirical rate expression or the LH type rate expression be used to predict the WGS outlet composition when operating below 2 bar(a). Furthermore, when predicting reaction rates outside of the window in which the rate equations were derived, it is recommended that the LH model be used as it is expected to give a better prediction as it is based on fundamental steps.

The proposed kinetic models are given by the rate equations below, where r is the rate of consumption of CO [mol·kg$_{cat}^{-1}$·s^{-1}], P_i is the partial pressure of component i [bar(a)] and β [-] is the ratio of partial pressures of products to reactants to the equilibrium constant, viz. $\frac{P_{CO_2} \cdot P_{H_2}}{P_{CO} \cdot P_{H_2O} \cdot Keq}$.

$$r_{PRL} = \left((2.3 \pm 0.4) \times 10^{-4}\right) \cdot e^{\left(\left(\frac{-(110 \pm 3) \times 10^3}{R}\right) \cdot \left(\frac{1}{T} - \frac{1}{513}\right)\right)} \cdot P_{CO}^{0.1 \pm 0.03} \cdot P_{H_2O}^{0.8 \pm 0.08} \cdot P_{CO_2}^{-0.3 \pm 0.07} \cdot P_{H_2}^{-0.7 \pm 0.08} \cdot (1 - \beta)$$

Power-Rate Law

$$r_{LH} = \frac{\left((1.4 \pm 0.4) \times 10^{-1}\right) \cdot e^{\left(\left(\frac{-110 \pm 3}{R}\right) \cdot \left(\frac{1}{T} - \frac{1}{513}\right)\right)} \cdot \left(P_{CO} \cdot P_{H_2O} - \frac{P_{CO_2} \cdot P_{H_2}}{K_{Eq}}\right)}{\left(1 + \left((5.8 \pm 1) \times 10^2\right) \cdot e^{\left(\left(\frac{90 \times 10^3}{R}\right) \cdot \left(\frac{1}{T} - \frac{1}{513}\right)\right)} \cdot P_{CO}\right) \cdot \left(\sqrt{P_{H_2}} + \left((5.1 \pm 2.5) \times 10^{-1}\right) \cdot e^{\left(\left(\frac{-(95 \pm 10) \times 10^3}{R}\right) \cdot \left(\frac{1}{T} - \frac{1}{513}\right)\right)} \cdot P_{H_2O}\right)}$$

LH Type Rate Expression

Acknowledgements

First and foremost, I would like to express my deepest gratitude to my supervisor, Professor Jack C.Q. Fletcher, for giving me the opportunity to conduct this study, for his continuous support throughout the process and for creating an environment in which I was allowed to develop my own ideas for this study. I am extremely privileged to have been able to conduct my research under his guidance.

I am also extremely grateful to Dr Jack V. Fletcher for his help, support, thesis corrections and all the time he made available for valuable discussions. I would also like to thank Mr Niels Luchters, Mr Stephen Roberts, Mr Yi Zhou and Mr Waldo Koorts for their help, support and valuable input.

Thanks must also go to Professor Patricia Kooyman for her assistance in obtaining TEM images and to Professor Klaus Moller and Professor Eric van Steen for their valuable input.

Furthermore, I would like to express my appreciation to the support and technical staff of the Centre for Catalysis Research. Without them, this project would not have been completed successfully.

I would also like to extend a general thanks to all the members of the Centre for Catalysis Research for the friendly and helpful work environment – our Monday donuts were enjoyed and will be missed.

I would like to acknowledge the Ada and Bertie Levenstein Bursary and HySA/Catalysis for their financial support.

Lastly, I would like to thank my friends and family for their continuous support and encouragement.

Declaration

I know the meaning of plagiarism and declare that all the work in the document, save for that which is properly acknowledged, is my own. This thesis/dissertation has been submitted to the Turnitin module (or equivalent similarity and originality checking software) and I confirm that my supervisor has seen my report and any concerns revealed by such have been resolved with my supervisor.

Signed by candidate

Darryl Edward Brown

Electronically signed

26 September 2017

Table of Contents

List of Figures

List of Tables

Nomenclature

Where a variable has more than one subscript, the variable is repeated with each subscript to clarify the meaning of the subscript.

Symbol	Description
%	Percentage
°C	Degree Celsius
°C/min	Degree Celsius per minute
µ	Micro
µm	Micrometre (1×10^{-6} m)
µGC	Micro gas chromatograph
∑	Sum of
ΔW	Differential segment of the catalyst mass (i.e. weight)
Ag	Silver (element)
Ag_2O	Silver(I) oxide
Ar	Argon
$Area_i$	Peak area of component i obtained from the µGC
atm	Atmosphere
BET	Brunauer-Emmett-Teller
BF-STEM	Bright-field scanning transmission electron microscopy
BJH	Barrett-Joyner-Halenda
CH_4	Methane
C_2H_6	Ethane
C_3H_8	Propane
Ce	Cerium (element)
CeO_2	Cerium(IV) oxide
cm	Centimetre
CO	Carbon monoxide

CO_2	Carbon dioxide
Ea	Activation energy (J/mol)
g	Gram
GC	Gas Chromatograph
gPROMS	General process modelling system
H_2	Hydrogen
H_2O	Water
HAADF	High-angle annular dark-field
HCl	Hydrochloric acid
He	Helium
HF	Hydrofluoric acid
HNO_3	Nitric acid
ICP-OES	Inductively Coupled Plasma – Optical Emission Spectrometry
k	Reaction rate constant
K	Adsorption constant
K_{eq}	Equilibrium constant
l	Litre
LH	Langmuir Hinshelwood
MARR	Mean Absolute Relative Residual
MFC	Mass flow controller
mg	Milligram
min	Minute
ml	Millilitre
ml(STP)	Millilitre at standard temperature and pressure
ml(STP)/min	Millilitre at standard temperature and pressure per minute
mm	Millimetre
mmHg	Millimetre of Mercury

nm	Nanometre (1 x 10^{-9} m)
MS5A	Molsieve 5A
n	Sample size (standard deviation formula)
$\dot{n}_i$	Molar flow rate of component I (mol/s)
N_2	Nitrogen
nm	Nanometer
P	Pressure (bar)
PBR	Packed-bed reactor
PIC	Pressure indicator controller
ppb	Parts per billion
PPQ	Pora Plot Q
Pt	Platinum (element)
R	Real gas constant (8.314 $J \cdot mol^{-1} \cdot K^{-1}$)
$r_i^{'}$	Reaction rate with respect to component i ($moles \cdot catalyst_{weight}^{-1} \cdot time^{-1}$)
$RFF_{i,a}$	The ‘a’ component of the RFF factor for component i (-)
$RFF_{i,b}$	The ‘b’ component of the RFF factor for component i (-)
Ri	Reactor i
SD	Standard deviation
STEM	Scanning transmission electron microscopy
STP	Standard temperature and pressure (0 °C and 1 atm)
TCD	Thermal conductivity detector
TEM	Transmission electron microscopy
TPR	Temperature programmed reduction
$\dot{V}_i$	Volumetric flow rate ($ml_{(n)}$/min)
W	Catalyst weight
WR	Weighted Residual
wt	Weight

wt%	Weight percentage
x	Represents a sample point (standard deviation formula)
$\bar{x}$	Sample mean
X_{CO}	Conversion of CO

1. Introduction

The technology and transportation networks that drive today's society are mainly powered by fossil fuels. Since the supply of fossil fuels is limited, an alternative energy source is being sought. Additionally, with many governments introducing policies around CO_2 emissions, the use of an alternative energy source is becoming more attractive. One of the biggest challenges currently facing the world is the development of a clean, efficient and reliable energy conversion process.

Hydrogen is a promising alternative energy source for generating electricity with high efficiency. As such, the hydrogen economy has received particular attention in recent years. The increased attention the hydrogen economy is receiving has led to an increased interest in in fuel cell research and development. Fuel cell development has mainly focussed on transportation, stationary and distributed power systems. Of particular interest to the African continent, fuel cells have the potential to supply electricity to remote, off-the-grid locations where the capital cost of extending the national electrical grids are too high.

For fuel cells to be a successful power source, a reliable hydrogen source is required. Even though hydrogen is one of the earth's most abundant elements, it is not freely found in nature in its diatomic form. As such, hydrogen needs to be produced for fuel cells. It is expected that hydrogen will one day be produced from renewable resources however, the renewable technology currently available is not economically or technically (due to low efficiencies) feasible. Producing hydrogen from fossil fuels can be seen as a temporary solution while further advances are made to overcome the technical and economic barriers of renewable hydrogen sources. A fuel processor is an attractive technology for converting fossil fuels, such as liquified petroleum gas (LPG), into hydrogen. Fuel processing brings the added advantage of the elimination of the need for hydrogen storage as hydrogen is produced on demand.

Currently, the water-gas shift (WGS) reactor is one of the largest components in a fuel processing train. Reducing the size of the WGS reactor is therefore an important issue if a compact, efficient and reliable fuel processor is to be designed. To design future WGS catalysts and an optimised fuel processing system using process simulation and optimisation, the reaction kinetics taking place must be understood and quantified. Intrinsic kinetics are preferred as they are scale independent.

In this study, a kinetic model for the WGS reaction is developed at conditions that are relevant to fuel processors. These conditions include simulation of a realistic reformate feed stream over a leading monometallic WGS catalyst.

2. Literature Review

2.1. The Hydrogen Economy and Fuel Cells

Since the industrial revolution, the technology and transportation networks that drive society have been powered by fossil fuels (Crabtree, Dresselhaus & Buchanan, 2004:39). Continuation of fossil fuel use as a source of power puts extensive strain on the environment. This has resulted in policies, such as the Paris Agreement (United Nations, 2015), being developed to reduce CO_2 emissions. The introduction of environmental legislation is seen as one of the first steps in changing the world's energy system.

One of the biggest challenges currently facing the world is the development of a clean, efficient and reliable energy conversion process. This new process should meet sustainability goals and be a suitable replacement for the current fossil fuel processes. While alternative sustainable energy sources to fossil fuels exist, the hydrogen economy (a large-scale hydrogen energy system) has received particular attention in recent years (Barreto, Makihira & Riahi, 2003:267). A hydrogen based energy system has the potential to be an efficient, clean and safe means of delivering energy services while complying with 'zero emissions' sustainability goals (Ogden, 1999:229).

The technical and economic barriers currently facing the development of hydrogen energy infrastructure and technology are too great to be overcome. This is especially true for renewable energy technologies, which are currently not mature enough to meet the continuous demand of the world's energy systems. As such, the development of renewable hydrogen infrastructure will be many times more expensive than developing a system using a liquid fuel. It has therefore been proposed that hydrogen energy systems are powered using hydrogen produced from fossil fuels (Ogden, 1999:229). Producing hydrogen from fossil fuels can be seen as a temporary solution while further advances are made in tackling the technical and economic barriers currently facing the development of renewable hydrogen infrastructure. The ultimate goal, however, should be to produce hydrogen from non-fossil fuel sources.

Hydrogen fuel cells are seen as a leading technology to replace current fossil fuel energy production processes. Fuel cells convert chemical energy into electrical energy using a fuel (hydrogen) and an oxidant (air) with high efficiencies and few environmental effects. Currently, the development of fuel cells is focussed for use in transportation systems as well as stationary and distributed power systems (Shekhawat, Spivey & Berry, 2011:vii). Since hydrogen is not present in its free form in nature, a reliable hydrogen source is required if fuel cells are to be successful. A fuel processor remains an important alternative to producing hydrogen. Hydrogen can be produced on demand using a fuel processor, thereby eliminating the need for hydrogen storage.

2.2. Fuel Processors

Fuel processing, which includes hydrogen production, purification and storage is a key technology for the implementation of fuel cells (Shekhawat, Spivey & Berry, 2011:vii). The purpose of a fuel processor is to convert a commonly available fuel into a hydrogen rich gas stream that can be used as the feedstock for fuel cells. Fuel processors for low temperature fuel cells typically consists of a fuel reformer, which produces a hydrogen rich stream, followed by two CO clean-up stages – a water-gas shift (WGS) reactor and either a selective methanation (SMET) reactor or preferential oxidation (PROX) reactor. For high temperature fuel cells, the fuel processor typically only contains two steps – a fuel reformer and a WGS reactor. A schematic representation of a three-stage fuel processor is given in Figure 2.1.

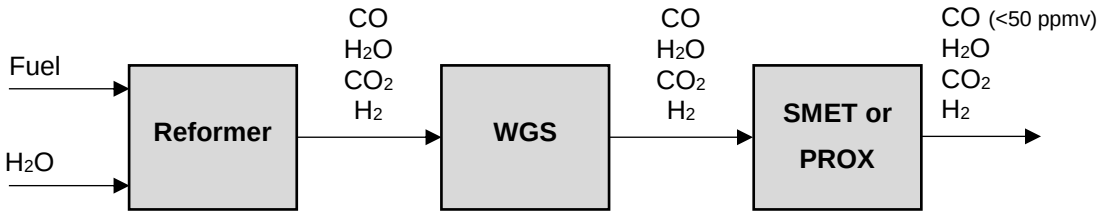

Figure 2.1: Three-stage fuel processing train

Steam reforming is the most widely used process for hydrogen production in fuel processors. Liquified petroleum gas (LPG, a mixture of propane and butane) is a preferred fuel over other suitable fuels due to its higher energy density (United States Department of Energy, 2014). During reforming of fossil fuels, a H_2 rich mixture is produced which contains a significant amount of CO (~10 %). This stream also contains a large amount of H_2O to meet the required relative humidity of the fuel cell feedstock as it is undesirable to have an extra unit operation to add or remove H_2O downstream. The high CO concentration in this stream is problematic as CO poisons the fuel cells' catalyst at concentrations above 50 ppmv (Faur Ghenciu, 2002:389). As such, CO clean-up stages are required to purify the H_2 rich mixture.

The first step in reducing the CO content in the reformate stream is the WGS reactor. This reactor requires low temperatures to achieve high equilibrium conversions (Shekhawat, Spivey & Berry, 2011:363) and in addition to reducing the CO concentration in the stream down to ~1 vol%, it brings the added advantage of producing additional H_2. Further CO clean-up is however required to reduce the CO concentration to levels that will not poison the fuel cell. This is usually achieved through a PROX reactor, in which CO reacts with O_2 to form CO_2, or through a SMET reactor, in which CO is converted to CH_4 (Shekhawat, Spivey & Berry, 2011:362;373-374;390).

Currently, the WGS reactor stage is one of the biggest components of a fuel processor (Alijani & Irankhah, 2013:209). As such, a key step in designing a compact fuel processor would be

reducing the size of the WGS reactor. To do this, the reaction kinetics taking place must be understood and quantified.

2.3. The Water-Gas Shift Reaction

2.3.1. Background of the water-gas shift reaction

The WGS reaction is a mildly exothermic reaction that involves the conversion of a mixture of carbon monoxide (CO) and water vapour (H_2O) into carbon dioxide (CO_2) and hydrogen (H_2) according to Equation 2.1.

$$CO + H_2O \rightleftarrows CO_2 + H_2 \qquad \Delta H = -41.1\ kJ/mol \qquad \text{Equation 2.1}$$

The technical importance of the WGS reaction was first recognised and applied in the Haber process for ammonia synthesis. The use of the WGS reaction allowed for easier removal of CO as CO_2 and brought the added advantage of a significantly increased yield of hydrogen (Twigg, 1989:284). In addition to ammonia synthesis, the WGS reaction forms an important part of the Fischer-Tropsch process and, more recently, has been used in fuel processors to reduce the CO content of the hydrogen feedstock for fuel cells (Shekhawat, Spivey & Berry, 2011:363). The advantage of using WGS in this context is that while the CO content of the feedstock is reduced, there is an increase in the yield of hydrogen which is to be fed into the fuel cell.

In general, the WGS reaction is classified as either being a high temperature shift (HTS) reaction (350 – 400 °C) or a low temperature shift (LTS) reaction (180 – 240 °C) (Faur Ghenciu, 2002:393). Under adiabatic operation, the conversion in a single-stage reactor is thermodynamically limited. To improve the CO conversion, a multiple-stage process is used in industry. First, the HTS reaction is run to capitalise on the rapid kinetics available at higher temperatures. This is then followed by the LTS reaction, which capitalises on the favourable equilibrium conversion at lower temperatures. It should be noted that the HTS catalyst is essentially inactive at LTS conditions and that the LTS catalyst is unstable at HTS conditions. Furthermore, rapid deactivation of the LTS catalyst is observed at HTS conditions (Shekhawat, Spivey & Berry, 2011:366).

2.3.2. Thermodynamics of the Water-Gas Shift Reaction

2.3.2.1. *Temperature*

Various factors need to be considered when choosing the reactor temperature, such as the maximum catalyst operating temperature, the endo/exo-thermic nature of the reactor and the position of the reaction equilibrium.

As shown in Equation 2.1, the WGS reaction is mildly exothermic and as such, the equilibrium constant (Equation 2.2) decreases with increasing temperature.

$$K_{eq}(T) = \frac{P_{H_2} \cdot P_{CO_2}}{P_{CO} \cdot P_{H_2O}}$$ Equation 2.2

Le Châtelier's principle states that for an exothermic reaction, a decrease in temperature favours the conversion of reactants. While a decrease in temperature is favourable in terms of conversion, it is unfavourable as it inhibits the reaction rate. As such, a compromise needs to be made between conversion and reaction rate when deciding on reaction temperature.

2.3.2.2. *Pressure*

According to Le Châtelier's principle, when pressure is applied to a system at equilibrium, the position of the equilibrium will move to reduce the pressure. That is, an increase in pressure will favour the reaction producing the least amount of moles and a decrease in pressure will favour the reaction producing the most amount of moles. For an equimolar reaction such as the WGS reaction, Le Châtelier's principle suggests that a change in pressure will have no effect on the equilibrium conversion of CO.

Twigg (1989:288) reports on literature that found the reaction rate to increase with pressure up until 5 bar, after which further increases in pressure had little effect on the reaction rate. This suggests that pressure could affect pore diffusion and reaction kinetics (Shekhawat, Spivey & Berry, 2011:364).

2.3.2.3. *Steam/Carbon Ratio*

An increase in the steam/carbon ratio favours the forward WGS reaction, resulting in a higher CO conversion (Shekhawat, Spivey & Berry, 2011:363-364). In practice, a steam/carbon ratio in the range 2.5 – 5 is usually used to improve the equilibrium conversion, decrease carbon deposition on the catalyst and prevent the formation of unwanted hydrocarbons which consumes valuable hydrogen (Twigg, 1989:338).

In the case of the WGS reaction in fuel processors, the steam/carbon ratio needs to be chosen to prevent any side reactions, such as methanation, CO disproportionation or catalyst decomposition from occurring (Faur Ghenciu, 2002:392). Also, it is preferable that the appropriate downstream fuel cell relative humidity can be achieved without the need for an additional unit operation for the addition or removal of H_2O.

2.3.3. Catalysts for the Water-Gas Shift Reaction

A considerable amount of work has been undertaken to study HTS catalysts over the years. These catalysts are widely used in industry due to their low cost, long lifespan (3 – 5 years) and resistance to poisoning (Shekhawat, Spivey & Berry, 2011:364). HTS catalysts are generally based on Fe_2O_3, with Cr_2O_3 and Al_2O_3 commonly used as promoters/stabilisers. Cr_2O_3 and Al_2O_3 help minimise sintering of Fe_2O_3, while Cr_2O_3 also increases the intrinsic activity of the iron oxide (Shekhawat, Spivey & Berry, 2011:364). The activity and stability of the HTS catalyst is dependent on the reaction conditions, with the stability being determined by the H_2O/H_2 ratio

and the CO_2/CO ratio (Shekhawat, Spivey & Berry, 2011:364). One of the major limitations of Fe-based HTS catalysts is that they are pyrophoric in their reduced (activated) state. As such, exposure to air can result in high, unsafe temperatures and dangerous conditions. Consequently, these catalysts must be 'gently' re-oxidized in dilute air before they can be removed from the reactor.

LTS catalysts are usually Cu-based, as these metals have good activity for the WGS reaction at low temperatures and show no methanation activity (Twigg, 1989:309). The most popular catalyst choice for the LTS reaction in industry today is $Cu/ZnO/Al_2O_3$. The activity of the $Cu/ZnO/Al_2O_3$ catalyst has been found to be dependent on the catalyst composition and preparation method (Shekhawat, Spivey & Berry, 2011:365). As for the HTS catalyst, the LTS catalyst is pyrophoric. The LTS catalyst is also sensitive at temperatures above ~280 °C, where rapid sintering occurs (Shekhawat, Spivey & Berry, 2011:366).

The current HTS and LTS catalysts are not feasible for use in fuel processors as the HTS catalyst is prone to coke formation while the kinetic limitations of the LTS catalyst will result in large reactor volumes (Smith, Loganathan & Shantha, 2010:5). In addition to this, these catalysts are also not suitable as they are pyrophoric, making catalyst removal from the reactor a lengthy process as the catalysts first need to be re-oxidized. Additionally, these catalysts require a lengthy pre-conditioning reduction process which is not desirable in fuel processors. Due to these limitations, new catalysts are being sought for the WGS reaction in fuel processors.

2.3.3.1. *Water-Gas Shift Catalysts in Fuel Processors*

Faur Ghenciu (2002:393) has outlined the requirements a catalyst must meet to be considered for use in the WGS reactor in fuel processors. These requirements include:

- High activity
- Stability under a typical reformate outlet to ensure a steady outlet CO concentration,
- Non-pyrophoric,
- Durability under steady-state and transient conditions,
- Stability to condensation and poisons from fuels and
- Not promote any side reactions that consume hydrogen under the required operating conditions.

In general, two trends are seen in the development of new WGS catalysts for use in fuel processors: non-precious metal catalysts and precious metal catalysts (Faur Ghenciu, 2002:393-394).

Non-precious metal catalysts would be preferred due to their lower cost compared to precious metal catalysts. These catalysts are reported on in literature to be active at temperatures >400 °C and to give reasonable CO conversion (>40 %) at low space velocities of <8000 h^{-1}

(Faur Ghenciu, 2002:393). If these catalysts are to be used in fuel processing applications, the low space velocity and high temperature required for reasonable CO conversions will result in further WGS reactors, containing more active catalyst and operating at a lower temperature, being needed to achieve the required CO concentration due to the equilibrium conversion limitations at higher temperatures.

Precious metal catalysts are reported to have good activity in the temperature range 250 – 350 °C (Alijani & Irankhah, 2013:210) and are therefore considered being more promising for the WGS reaction in fuel processors than non-precious metal catalysts. As such, more attention is being given to developing these catalysts and operating fuel processors at ~300 °C, where these catalysts are most active. The activity and stability of these catalysts in a fuel processing environment needs to be considered before deciding on the most suitable catalyst to use.

Activity of Precious Group Metal Catalysts

Precious group metal (PGM) catalysts that have been tested for use in fuel processors (at temperatures of ~300 °C) are reported to be bifunctional (Faur Ghenciu, 2002:394-395; Phatak et al., 2007:225,230; Kalamaras et al., 2009:128). That is, both the metal and support provide active sites for the reaction and as such, both influence the activity and stability of the catalyst. A discussion on the reaction mechanism will be provided in section 2.3.4 below.

Platinum (Pt) based catalysts are seen as the leading candidates for the WGS reaction in fuel processors due to the high activity seen with these catalysts compared to other PGM catalysts under a typical fuel processor reformate stream (Radhakrishnan et al., 2006:1892-1894; Shekhawat, Spivey & Berry, 2011:367). As such, Pt-based catalysts have been the most extensively studied (Azzam et al., 2008:129-140; Faur Ghenciu, 2002:389-399; Germani and Schuurman, 2006:1806-1813; Kalamaras et al., 2009:117-129; Phatak et al., 2007:224-234).

In addition to the metal, the support used has a significant impact on the activity of the catalyst (Alijani & Irankhah, 2013:210-213; Shekhawat, Spivey & Berry, 2011:367-368). A common trend observed in the literature reviewed and an important factor to note is that Pt-based catalysts appear to have significantly higher activities when supported on reducible oxides (e.g. TiO_2, CeO_2, ZnO_2) than on irreducible oxides (e.g. Al_2O_3, MgO). This suggests that the reducibility of the support influences the reaction mechanism and hence the activity of the catalyst.

A variety of different metal oxide supports, differing in their ability to be reduced, have been reported for Pt-based WGS catalysts (Azzam et al., 2007:163; Panagiotopoulou & Kondarides, 2006:49; Phatak et al., 2007:224; Ricote et al., 2006:35; Vignatti et al., 2011:297). Azzam et al. (2007:165) has shown that the activity of the following catalysts decreases in the order Pt/TiO_2 > Pt/CeO_2 > Pt/ZrO_2. Other studies (Panagiotopoulou & Kondarides, 2006:50; Ricote et al., 2006:46; Vignatti et al., 2011:300) have shown similar trends.

Work has been undertaken on using binary oxides as supports for Pt-based catalysts to increase the activity of the catalyst (Azzam et al., 2007:165; Ricote et al., 2006:46; Vignatti et al., 2011:300). The main oxides considered were $Ce_xZr_{1-x}O_2$, $Ti_xZr_{1-x}O_2$ and $Ti_xCe_{1-x}O_2$. The binary oxide supported catalysts however, did not show a measurable activity improvement over Pt/TiO_2, Pt/CeO_2 or Pt/ZrO_2.

Stability of Precious Group Metal Catalysts

While Pt catalysts supported on CeO_2 and TiO_2 have shown good activity for the WGS reaction stage of fuel processors, catalyst deactivation is of concern. Little work has been undertaken to study the long-term stability of these catalysts. Most studies consider the catalyst stability for <100 hours on stream, with a considerable amount of the work being undertaken for <24 hours on stream. One needs to question if the stability of the catalyst can be determined over such a short period of time, as the catalyst could still be going through its start-up cycle during this time. During start-up, surface modification is known to occur and as such, the catalyst surface/active sites could be changing.

Azzam et al. (2007:166) has commented on catalyst deactivation over a short time span of 20 hours. In the study, Pt/CeO_2 and Pt/TiO_2 showed similar signs of deactivation, with both catalysts losing approximately 40 % of their activity. The deactivation of Pt/CeO_2 was due to the formation of stable carbonate species on the ceria surface. This could be reversed through oxidative treatment, resulting in the recovery of the catalyst activity. The deactivation of Pt/TiO_2 was shown to be due to Pt sintering and as such, the activity of this catalyst could not be recovered.

Duarte de Farias et al. (2007:859), Liu et al. (2005:70-71) and Luengnaruemitchai, Osuwan & Gulari (2003:220) have all commented on the deactivation of Pt/CeO_2 over slightly longer timespans (50 – 70 hours on stream). All three studies showed a gradual decrease in the activity with time on stream. The deactivation mechanism in all three studies was due to stable carbonate formation on the support surface. Liu et al. (2005:74) showed that the catalyst could be regenerated by heating the catalyst to 450 °C in air and agrees with the findings by Azzam et al. (2007:166).

Liu et al. (2005:71) took their stability study a step further by simulating frequent start-up/shut-down cycles one might experience in fuel processors. Rapid catalyst deactivation was observed during start-up/shut-down cycles, suggesting that the formation of stable carbonates is more favoured at lower temperatures. The deactivation during start-up/shut-down cycles is another issue that will need to be addressed as fuel processors could include frequent start-ups and shut-downs depending on their application and power demand.

Based on their activity, Pt/TiO_2 and Pt/CeO_2 catalysts are currently seen to be the most promising for use in the WGS reaction stage of fuel processors. The stability of these catalysts must however be considered before they can be used in commercial applications

2.3.4. Mechanisms for the Water-Gas Shift Reaction

Currently, a lot of debate exists regarding the reaction mechanism for the WGS reaction, with different mechanisms reported in literature (Grabow et al., 2008:4608,4610; Kalamaras et al., 2011:298; Phatak et al., 2007:230; Rhodes et al., 1995:49-56). This is not surprising considering the large variety of catalysts (having different properties) available for the WGS reaction and the many different experimental conditions under study in the literature.

Broadly speaking, two mechanistic pathways have been proposed: (i) the associative mechanism and (ii) the regenerative (redox) mechanism.

2.3.4.1. *Associative Mechanism*

The associative mechanism as described by Shekhawat, Spivey & Berry (2011:367-368) proposes that the adsorbed species interact to form an adsorbed intermediate, which decomposes to form H_2 and CO_2. In this mechanism, the metal promotes the reduction of the support, forming active sites. The partially reduced support then adsorbs CO and H_2O, which interact to form a surface intermediate. This intermediate then decomposes to H_2 and CO_2. This mechanism may be described by the mechanistic steps given by Associative mechanism step 2.1 through Associative mechanism step 2.5 (Rhodes et al., 1995:49).

$CO + * \rightleftarrows CO^*$ Associative mechanism step 2.1

$H_2O + * \rightleftarrows H_2O^*$ Associative mechanism step 2.2

$CO^* + H_2O^* \rightleftarrows [intermediate^*] \rightleftarrows CO_2^* + H_2^*$ Associative mechanism step 2.3

$CO_2^* \rightleftarrows CO_2 + *$ Associative mechanism step 2.4

$H_2^* \rightleftarrows H_2 + *$ Associative mechanism step 2.5

* Indicates a vacant site

The true site location (support surface, metal-support interface, or metal surface) and chemical composition of the intermediate is still of debate (Kalamaras et al., 2011:299; Smith et al., 2010:7-8). Azzam et al. (2008:137), Grabow et al. (2008:4610), Jacobs et al. (2003:118), Kalamaras et al. (2011:295), Phatak et al. (2007:233) and Rhodes et al. (1995:49) suggest that a formate species is present during the reaction as an active intermediate. It is suggested that the formate (COOH) species is formed from adsorbed CO on the Pt and an adsorbed OH on a metal oxide support vacancy. The formate species then dissociates to give adsorbed CO_2 and adsorbed H. Grabow et al. (2008:4610), on the other hand, suggests a carboxyl intermediate.

2.3.4.2. *Regenerative (Redox) Mechanism*

Simply, the regenerative mechanism (commonly referred to as the redox mechanism) involves the breaking down of H_2O on the catalyst support to produce H_2 and subsequent oxidation of

the support surface. CO then reduces the support surface to form CO_2, returning the catalyst surface to its original state (Shekhawat, Spivey & Berry, 2011:367). This mechanism can be represented as follows:

$$H_2O + * \rightleftarrows H_2(g) + O^* \quad \text{Redox mechanism step 2.1}$$

$$CO + O^* \rightleftarrows CO_2\,(g) + * \quad \text{Redox mechanism step 2.2}$$

* Indicates a vacant site

Ovesen et al. (1992:446) has represented the mechanism using elementary steps as follows:

$$H_2O(g) + * \rightleftarrows H_2O^* \quad \text{Redox mechanism step 2.3}$$

$$H_2O^* + * \rightleftarrows OH^* + H^* \quad \text{Redox mechanism step 2.4}$$

$$2OH^* \rightleftarrows H_2O^* + O^* \quad \text{Redox mechanism step 2.5}$$

$$OH^* + * \rightleftarrows O^* + H^* \quad \text{Redox mechanism step 2.6}$$

$$2H^* \rightleftarrows H_2(g) + 2* \quad \text{Redox mechanism step 2.7}$$

$$CO(g) + * \rightleftarrows CO^* \quad \text{Redox mechanism step 2.8}$$

$$CO^* + O^* \rightleftarrows CO_2^* + * \quad \text{Redox mechanism step 2.9}$$

$$CO_2^* \rightleftarrows CO_2(g) + * \quad \text{Redox mechanism step 2.10}$$

* Indicates a vacant site

Redox mechanism step 2.3 through Redox mechanism step 2.7 represents the breaking down of H_2O. Redox mechanism step 2.8 through Redox mechanism step 2.10 represents CO oxidising the support to form CO_2. These elementary steps have therefore formed the basis of many kinetic modelling studies (Grabow et al., 2008:4608; Koryabkina et al., 2003:237; Phatak et al., 2007:230).

2.3.4.3. *Regenerative vs Associative Mechanism*

The notable difference between the regenerative and associative mechanism is that the regenerative mechanism does not account for the intermediate species that have been observed. Ovesen et al. (1996:173) has modified the regenerative mechanism outlined above to account for a formate intermediate through the addition of three elementary steps. Furthermore, Ovesen et al. (1996:173) suggests that formate coverage is negligible at atmospheric conditions, becoming significant at higher pressures. Grabow et al. (2008:4610) has also modified this mechanism to describe the carboxyl intermediate in their study. This was achieved through addition of four elementary steps.

Recently, there has been an increase in interest in determining the WGS reaction mechanism at temperatures applicable to fuel processors (250 - 350 °C). Ratnasamy & Wagner (2009:417) and Shekhawat, Spivey & Berry (2011:368) suggests that the reaction mechanism depends to

a large extent on the process conditions and nature of the catalysts. As such, no single mechanistic pathway can explain all experimental observations seen for the WGS reaction in fuel processors. Rather, different mechanisms can occur on the same catalyst under different reactant partial pressures and temperatures. Findings by Rhodes et al. (1995:56-57) seem to agree with this as it was noted that evidence exists to support both reaction mechanisms in the temperature range of interest. Fishtik & Datta (2002:229), on the other hand, claim that the associative mechanism best describes the reaction kinetics in this temperature range.

2.3.4.4. *Further Mechanistic Considerations*

Kalamaras et al. (2009:127) suggests that the WGS reaction mechanism follows a dual-site redox mechanism, where CO adsorbs on Pt and reacts with an O atom from the metal oxide support to form CO_2. This consequently forms a vacancy in the metal oxide support. The reduced metal oxide support is then re-oxidised by H_2O, forming OH on the metal oxide support and H adsorbed on Pt. The OH is dissociated into H adsorbed on Pt and O on the metal oxide support (filling the vacancy). H_2 is then formed on the Pt surface. Azzam et al. (2008:137) also proposes that this mechanism is the dominant pathway while Wang et al. (2006:433) have, via in situ DRIFTS, observed OH groups on the oxide support during the WGS reaction over a Cu/CeO_2 catalyst.

To further justify a bifunctional mechanism, Kalamaras et al. (2009:126) found the surface coverage of “H-containing” reaction intermediates to be larger than one. This suggests that these species exist on both the metal and metal oxide support. In situ DRIFTS results presented in their study suggests that vacancies in the metal oxide are present.

A study by Wang et al. (2006:428) over a Cu/CeO_2 catalyst showed oxygen vacancies in the metal oxide support to be one of the active sites for the WGS reaction with metallic copper another active site. Wang et al. (2006:431) proposes that oxygen vacancies are formed by CO reduction of Ce^{4+} to Ce^{3+}. The study by Wang et al. (2006:431) found the number of oxygen vacancies to increase with increasing temperature up to 300 °C. At higher temperatures, the amount of oxygen vacancies decreased. This is an important observation since the WGS stage of fuel processors is operated at ~300 °C. Based on the up to date literature, there is sufficient evidence to suggest that oxygen vacancies do indeed exist in the CeO_2 support under fuel processing conditions.

Debate exists on the suggested rate determining step. Jacobs et al. (2003:118) suggests that the rate determining step involves a vacancy in the metal oxide support. Kalamaras et al. (2011:295) suggests that an elementary reaction step involving the breaking or forming of a hydrogen chemical bond can be considered as the rate determining step. Both of these suggestions are very broad and cover a number of possible mechanistic steps. Azzam et al. (2008:137) suggested the surface oxidation of CO adsorbed on Pt with OH groups adsorbed on the metal oxide support forming adsorbed CO_2 and an adsorbed H to be the rate determining step (this can be seen as a step involving the formate intermediate). Grabow et al. (2008:4616)

proposed the decomposition of the formate intermediate into CO_2 and H to be the rate determining step. It should be noted that the rate determining step suggested by Grabow et al. (2008:4616) is supported by Azzam et al. (2008:137), Jacobs et al. (2003:118) and Kalamaras et al. (2011:295) if a bifunctional mechanism is considered.

If a bifunctional mechanism takes place over Pt/CeO_2 catalysts under fuel processor - WGS reaction conditions, the reaction most likely occurs along the Pt/support interface, as adsorbed molecules on Pt need to be in close vicinity of support O atoms in order to interact with them.

2.4. Rate Expressions

In heterogeneous catalysis, the catalytic reaction is thought to take place on an active site(s). For any given catalyst, the number of active sites is limited. Therefore, the rate of reaction is not only limited by the amount of reactants available for the reaction, but also by the amount of active sites available on which the reaction can take place. It is therefore important that rate expressions that describe the rate of expression for heterogeneously catalysed reactions take the limited number of active sites into account.

2.4.1. Types of Rate Expressions

Many types of rate expressions exist however, only three will be discussed here.

2.4.1.1. *Langmuir-Hinshelwood Rate Expressions*

Langmuir-Hinshelwood (LH) kinetics is the most commonly used reaction rate expression to explain the kinetics of heterogeneous catalytic processes (Kumar, Porkodi & Rocha, 2008:82). In this approach, the number of active sites is taken into account by assuming equilibrium between the species in the bulk gas and the adsorbed species.

When using this approach to derive a rate expression, the following assumptions are made (Scott Fogler, 2006:664-668):

- Adsorption of all species follows the langmuir-adsorption isotherm,
- All sites are energentically homogeneous,
- There is no interaction between adsorbed species and
- Adsorption and desorption follow a single mechanism.

Since LH rate expressions are based on a proposed reaction mechanism, they are usually applicable outside the conditions under which it is derived. The advantage of this type of rate expression is that it can give an indication of the prevailing reaction mechanism.

2.4.1.2. *Mars-van Krevelen Rate Expressions*

Mars-van Krevelen rate expressions are often used for heterogeneously catalysed oxidation reactions, which may be the underlying mechanism of the WGS reaction based on the mechanistic considerations discussed above. The following assumptions are made with this type of rate expression (Vannice, 2007:18-19):

- The oxidation step is first order with respect to the reactnt and the fraction of sites covered by oxygen,
- Certain lattice O atoms at the surface are involved in the oxidation step,
- Only lattice O atoms are assumed to exist on these sites (no reactanst or products) and

- The rate of surface reoxidation is proportional to $P_{O_2}^{n}$ and to the concentration of active sites free from oxygen.

Based on the mechanistic considerations presented in 2.3.4.4 above, the Mars-van Krevelen rate expression is not applicable. This is due to one of the assumptions of this mechanism, which assumes that only lattice O atoms are assumed to exist at the surface of the metal oxide support (no reactants or products). This is thought not to be true as products and reactants are thought to exist on these sites. Vannice (2007:22) further claims that LH type rate equations can fit rate data better, or at least as well as, the Mars-van Krevelen rate expression

2.4.1.3. *Empirical Rate Expressions*

The power-rate law is an empirical rate expression that can be used to determine the reaction orders of reactants and products by fitting the expression to experimental data. The power-rate law is given by Equation 2.3, where r is the reaction rate [units as defined under experimental conditions], k_0 is the reaction rate constant [units dependent on other variables], Ea is the activation energy of the reaction [J/mol], R is the gas constant [8.314 J·mol^{-1}·K^{-1}], T is the reaction temperature [K], P_i is the partial pressure of component i [pressure units], a, b, c and d are the reaction orders of CO, H_2O, CO_2 and H_2 respectively and β is the ratio of partial pressures of products to reactants to the equilibrium constant (K_{eq}), given by Equation 2.4.

$$r = k_0 \cdot \exp(-\frac{Ea}{R \cdot T}) \cdot P_{CO}^{a} \cdot P_{H_2O}^{b} \cdot P_{CO_2}^{c} \cdot P_{H_2}^{d} \cdot (1 - \beta) \qquad \text{Equation 2.3}$$

$$K_{Eq} = \frac{P_{CO_2} \cdot P_{H_2}}{P_{CO} \cdot P_{H_2O} \cdot K_{eq}} \qquad \text{Equation 2.4}$$

The disadvantage of this type of rate expression is that it does not take the number of available active sites or mechanism into account. Another weakness of this type of rate expression is that it is only applicable to the conditions under which it was derived.

An empirical rate expression can be used for reactor design if the proposed reactor operating conditions match the conditions under which the rate expression was determined.

2.4.2. Current Rate Expressions for the Water-Gas Shift Reaction

Many kinetic expressions, mainly derived from the mechanisms discussed in section 2.3.4, have been published for the WGS reaction as this reaction is used in many processes such as the manufacturing of ammonia, hydrocarbons and hydrogen. Many of the rate expressions that have been reported in literature were not derived from or fitted to data obtained over catalysts of interest to the WGS reaction in fuel processors (Smith et al., 2010:10-26). As such, these rate expressions will not be discussed here. Rather, this discussion will focus on rate expressions derived from experiments testing the WGS reaction in a fuel processing environment.

Very few studies have been conducted for the WGS reaction over Pt-based catalysts. In general, there are two types of rate expressions that are reported: empirical and non-empirical (LH type rate expressions).

2.4.2.1. *Empirical Rate Expressions*

With the current debate that exists in literature with regards to the reaction mechanism of the WGS reaction for fuel cell applications, many researchers note that the WGS reaction is not an elementary reaction, especially at high steam/carbon ratios. As such, many researchers are using empirical rate expressions to describe the WGS reaction for reactor design and optimisation, and as a way to attempt to start understanding the reaction mechanism.

Table 2.1 summarises the reaction order parameters found in literature for the power-rate law kinetic expression of various WGS catalysts and operating conditions. It should be noted that for some of the findings presented in Table 2.1, the reaction order with respect to CO_2 and H_2 is not always reported. In these works, the feed stream consisted of CO, H_2O and an inert and therefore does not represent a realistic reformate stream. A realistic reformate stream usually contains significant amounts of CO_2 and H_2 in addition to CO and H_2O, which will influence the reaction rate.

As seen in Table 2.1, rate expressions covering a wide range of experimental conditions have been studied for the WGS reaction in fuel cell applications. Most of the rate expressions have been derived for low temperature operation and at atmospheric pressure. The large number of rate expressions reported are as a result of the large variety of catalysts and the many different experimental conditions currently under study for the WGS reaction in fuel cell applications.

Table 2.1: Power-rate law kinetic parameters for various WGS catalysts and operating conditions (adapted from Smith et al. (2010:13-17))

Catalyst	Operating Conditions	Reaction Order				Reference
		a	b	c	d	
1%Pt/Al_2O_3	1 atm 225 – 285 °C	0.1	1.1	-0.07	-0.44	Phatak et al. (2007:230)
1%Pt/Al_2O_3	1 atm 285 – 345 °C	0.06	1	-0.09	-0.44	Phatak et al. (2007:230)
1.66%Pt/Al_2O_3	1 atm 285 °C	0.11	0.82	-0.06	-0.49	Phatak et al. (2007:230)
1.66%Pt/Al_2O_3	1 atm 300 °C	0.1	0.77	-0.08	-0.46	Phatak et al. (2007:230)
2%Pt/Al_2O_3	1 atm 270 °C	-0.21	0.75	-	-	Phatak et al. (2007:230)
0.9%Pt/Al_2O_3	1 atm 100 °C	0.02	0.55	-	-0.22	Phatak et al. (2007:230)
0.4%Pt/Al_2O_3	1 atm 544 °C	0.45	0.37	0	-0.73	Phatak et al. (2007:230)
Pt/Al_2O_3	270 °C	-0.21	0.75	-	-	Grenoble et al. (1981:94)
1%Pt/CeO_2	1 atm 200 °C	-0.03	0.44	-0.09	-0.38	Phatak et al. (2007:230)
1%Pt/CeO_2	1 atm 240 °C	0	1	-	-	Phatak et al. (2007:230)
1%Pt/CeO_2	1 atm 150 – 400 °C	0.14	0.66	-0.54	-0.08	Thinon et al. (2009:1942)
0.5%Pt/TiO_2	210 – 270 °C	0.5	1	0	-0.7	Kalamaras et al. (2009:121)
1%Pt/TiO_2	1 atm 150 – 400 °C	0.3	0.85	-0.67	0	Thinon et al. (2009:1942)
1.4%Pt-8.3% CeO_2/Al_2O_3	1 atm 260°C	0.13	0.49	-0.12	-0.45	Phatak et al. (2007:230)
2%Pt-1% Re/CeO_2-ZrO_2	1 atm 210 – 240 °C	-0.05	0.85	-0.05	-0.32	Phatak et al. (2007:230)

While a reaction mechanism cannot be directly obtained from the data in Table 2.1, we are able to get a better understanding of how each component affects the reaction and in some cases, the reaction mechanism. This is discussed below.

The reaction order with respect to CO varies across the literature values presented in Table 2.1, however, most studies report a reaction order close to zero. This suggests that the partial pressure of CO does not affect the reaction rate, or affects it to a small degree. Hilaire et al. (2001:273) has commented on this finding, suggesting that the metal surface is completely saturated with CO. CO would therefore not affect the reaction rate. Azzam et al. (2008:134) has made similar comments for their study over a Pt-Re/TiO_2 catalyst, however, they also found that the reaction order depends on the CO concentration in the feed stream. At high CO concentrations (4 – 12 vol%), the reaction order was found to be zero while at lower concentrations (1 – 3 vol%), the reaction order was found to be 0.4. Reaction orders of approximately 0.4 are also seen in Table 2.1. These results suggest that the concentration of CO in the feed stream has a great impact on the surface coverage of CO, which has a notable impact on the reaction rate.

The reaction order with respect to H_2O is found to be first order in most cases. This suggests that the reaction rate increases proportionally to the H_2O partial pressure. Kalamaras et al. (2009:125) has tried to explain this by suggesting that the rate limiting step is the oxidation of the support by H_2O. This is most likely to be the case if the reaction progresses along a redox mechanism. Interestingly, catalysts with a low platinum loading (<1 wt%) and catalysts supported on CeO_2 containing supports are seen to have a lower reaction order with respect to H_2O than the other catalysts reported in Table 2.1.

Other than two studies, the reaction order with respect to CO_2 is found to be approximately zero in all cases listed in Table 2.1. Phatak et al. (2007:229) commented on this observed reaction order, suggesting that there is a weak interaction between CO_2 and the metal. This would result in CO_2 easily desorbing from the metal (Kalamaras et al., 2009:126) and therefore not affecting the rate limiting step.

A negative reaction order is observed for H_2, indicating the presence of H_2 inhibits the forward WGS reaction. That is, an increase in the partial pressure of H_2 will increase its surface coverage, thereby reducing the number of free sites for CO which will inhibit the forward reaction. The results of Kalamaras et al. (2009:125) and Phatak et al. (2007:229) are consistent with this explanation.

2.4.2.2. *Non-Empirical Rate Expressions*

In addition to the empirical rate expressions that have been reported in literature, some attempts have been made to derive the rate expression from a possible reaction mechanism. One such rate expression has been derived by Germani & Schuurman (2006:1811). In their study, they propose a dual-site mechanism based on the associative mechanism. Experimental data was

collected over a 0.79 wt% Pt, 3.4 wt% Ce, 46.4 wt% Al platinum/ceria/alumina catalyst over the temperature range 200 – 400 °C.

In this mechanism platinum provides an adsorption site for CO and ceria an adsorption site for H_2O. The CO reacts with H_2O to yield a carboxyl species as an intermediate. This carboxyl species then reacts with a hydroxyl group and decomposes on a free platinum site forming CO_2 and H_2. In the mechanism proposed, a free platinum site appears in the rate determining step. The rate equation proposed is given by Equation 2.5, where r_{co} is the reaction rate with respect to CO [mol·kg_{cat}^{-1}·s^{-1}], k_{rds} is the rate constant of the rate determining step including the number of active sites [mol·$(bar^2)^{-1}$·kg_{cat}^{-1}·s^{-1}], K_i is the adsorption equilibrium constant for species i [bar^{-1}], P_i is the partial pressure of component i [bar] and β is as defined in Equation 2.4.

$$r_{CO} = \frac{k_{rds}K_{CO}K_{H_2O}P_{CO}P_{H_2O}(1-\beta)}{\left(1+K_{CO}P_{CO}+\sqrt{K_{H_2}P_{H_2}}\right)^2 \cdot \left(1+\sqrt{K_{H_2O}P_{H_2O}}+K_{CO_2}P_{CO_2}\right)} \qquad \text{Equation 2.5}$$

Germani & Schuurman (2006:1811) claim that this rate equation fits their data best. Thinon et al. (2009:1943) have also tested this rate expression (using data obtained in the temperature range 150 – 400 °C, over a 1.2 wt% Pt/CeO_2 and 1.1 wt% Pt/TiO_2 catalyst) and found it to model their experimental data well. They further conclude that the results based on this rate equation confirm a duel site mechanism, which adds to the discussion on the complexity of the WGS reaction.

Other rate equations based on LH type rate expressions have been derived. The following LH type rate expression has been derived based on the dual-site redox mechanism in which the rate determining step is the surface reaction of CO and H_2 (Sun et al., 2005:1259-1260). A proprietary precious metal catalyst was used. In Equation 2.6, r_{CO} is the reaction rate, k is the reaction rate constant, P_i is the partial pressure of component i, K_i is the adsorption equilibrium constant for component i and β is as defined in Equation 2.4. No units are reported by Sun et al. (2005:1260).

$$r_{CO} = \frac{kP_{CO}P_{H_2O}\cdot(1-\beta)}{(1+K_{CO}P_{CO})\left(1+K_{H_2}P_{H_2}\right)} \qquad \text{Equation 2.6}$$

Sun et al. (2005:1260-1263) has tested this rate expression and found it to give a better prediction of the WGS reaction than a power-rate law expression. In their work, they simplified their regression by assuming the reaction orders of CO_2 and H_2O to be zero and first order, respectively, even though they comment that the reaction order of CO_2 appears to be negative with increasing temperature. Since little information is given regarding the catalyst used in their study, due to it being a proprietary catalyst, it is difficult to comment on the validity of these assumptions. Rather, this limitation on the power-rate law needs to be considered and caution must be applied when drawing conclusions on which equation can predict the WGS reaction better.

The findings by Germani and Schuurman (2006:1811), Sun et al. (2005:1260), Thinon et al. (2009:1942) are of importance, as they all support the possibility of a dual-site mechanism.

3. Objectives and Key Questions

The aim of this study is to develop a kinetic model for the water-gas shift reaction at conditions relevant to fuel processors. These conditions include simulation of a realistic reformate feed stream resulting from propane steam reforming over an in-house prepared monometallic catalyst. Experiments will be designed to be free from mass transfer limitations resulting in data representative of intrinsic kinetics. Intrinsic kinetics are preferred as they are scale independent.

The objectives of this study are therefore to:

- Prepare a catalyst suitable for the water-gas shift reaction in fuel processors,
- Measure intrinsic water-gas shift reaction kinetics over the in-house prepared catalyst at conditions that would be relevant to fuel processing and
- Validate the intrinsic kinetics by means of appropriate reactor characterisation techniques.

The following key questions are posed:

- What influence does temperature have on the reaction kinetics and what is the activation energy?
- Will the reaction be insensitive to the total system pressure?
- How will varying process conditions (temperature, pressure, space velocity, feed composition) affect the water-gas shift reaction rate?
- Which reaction mechanisms describe the water-gas shift reaction over the prepared catalyst best and is there a clear statistical difference in the predictions between these mechanisms?
- Can the final model accurately predict the performance of the water-gas shift reaction under realistic fuel processing conditions?

4. Experimental Methodology and Model Development

4.1. Catalyst Synthesis

4.1.1. Wetness Impregnation

A 0.5 wt% platinum on cerium(IV) oxide (Pt/CeO_2) catalyst was prepared by wetness impregnation. Approximately 0.267 g chloroplatinic acid hydrate (37 – 40 wt% Pt) salt (Sigma-Aldrich, batch number: MKBX2395V) was dissolved in approximately 5 ml of deionised H_2O in a 5 ml volumetric flask. The metal solution was then added to 19.9 g of commercial cerium(IV) oxide powder (Sigma Aldrich, batch number: MKBN4671V) at room temperature. The mixture was stirred using a spatula. The resulting catalyst was subsequently dried in air as per steps 1 to 6 in Table 4.1 and then calcined as per steps 7 to 9. A slow heating rate was used to ensure the water was slowly evaporated.

Table 4.1: Catalyst drying and calcination procedure

Step #	Procedure
1	Heat from 40 °C to 60 °C at 1 °C/min
2	Hold at 60 °C for 5 hours
3	Heat from 60 °C to 90 °C at 1 °C/min
4	Hold at 90 °C for 5 hours
5	Heat from 90 °C to 120 °C at 1 °C/min
6	Hold at 120 °C for 5 hours
7	Heat from 120 °C to 350 °C at 1 °C/min
8	Hold at 350 °C for 5 hours
9	Cool from 350 °C to room temperature

4.2. Catalyst Characterisation

4.2.1. Inductively Coupled Plasma – Optical Emission Spectrometry

Inductively Coupled Plasma – Optical Emission Spectrometry (ICP-OES) was used to determine the chemical composition of the calcined catalyst. The catalyst sample (50 mg) was first digested in a mixture of 6 ml hydrochloric acid (HCl), 2 ml hydrofluoric acid (HF) and 2 ml nitric acid (HNO_3) and left overnight to allow the catalyst sample to dissolve. The solution was then placed in a MARS-5 microwave digester in which the temperature was ramped to 180 °C over 25 minutes and held at this temperature for 40 minutes. Once digested, the sample was diluted to concentrations within the calibration range of the ICP-OES instrument (200 ppb – 5 000 ppb). A Varian 730 ICP-OES instrument was then used to determine the Pt loading of the calcined catalyst.

4.2.2. Temperature Programmed Reduction

The reduction behaviour of the Pt/CeO_2 catalyst and CeO_2 support was studied by means of hydrogen temperature programmed reduction (TPR) in a Micromeritics AutoChem 2920. Typically, 200 mg of calcined catalyst or 30 mg of support was loaded into a quartz U-tube reactor. The sample was then heated to 950 °C at a linear programmed ramp rate of 10 °C/min in a 50 $ml_{(n)}$/min 5 % H_2 in Ar mixture. The hydrogen uptake due to metal oxide reduction was calculated from the resulting thermal conductivity detector (TCD) signal as a function of time. The TCD measures the difference in thermal conductivity between the pure 5 % H_2 in Ar mixture and the effluent gas. Before passing through the TCD, the reactor effluent passed through a cold trap to condense any volatiles and water. The cold trap is maintained at temperatures of approximately -80 °C by an isopropyl alcohol/liquid nitrogen slurry. The TCD was regularly calibrated using a known amount of Ag_2O, which allowed for the hydrogen consumption to be quantified.

4.2.3. Specific Surface Area and Pore Size Distribution

The specific surface area and pore volume of the Pt/CeO_2 catalyst and the CeO_2 support was determined by Brunauer-Emmett-Teller (BET) surface area analysis (Micromeritics Instrument Corporation, 2007:C8-C9) in a Micromeritics TriStar II 3020. Approximately 250 mg of calcined catalyst was loaded into a clean BET tube. First, the sample was degassed under vacuum at 130 °C overnight to remove any moisture and other adsorbates. The degassed sample was then weighed to determine the mass of the dry sample. N_2 adsorption isotherms were then measured at -196 °C with 10 seconds allowed for equilibration at each pressure. The specific surface areas were calculated using the BET method, assuming the adsorbed N_2 molecule has a cross sectional area of 0.162 nm^2. The pore volumes were calculated using the Barrett-Joyner-Halenda (BJH) method (Micromeritics Instrument Corporation, 2007:C13-C22).

4.2.4. CO Chemisorption

CO Chemisorption was performed on the reduced catalyst in a Micromeritics ASAP 2020 equipped with a Pfeiffer MVP015-2 vacuum pump to determine the available metallic surface area. A quartz U-tube reactor was loaded with approximately 200 mg of calcined catalyst. First, the sample was heated to 100 °C at a linear programmed rate of 10 °C/min in He to remove any adsorbed water. He was then replaced with H_2 and the sample was heated to 275 °C at a linear programmed rate of 2 °C/min to reduce the sample. The sample was held at 275 °C for 6 hours to ensure complete reduction. After reduction, the H_2 gas flow was stopped, the sample chamber was evacuated and the temperature reduced to 35 °C at a linear programmed rate of 5 °C/min. CO chemisorption was then performed by dosing the sample with CO at various pressures between 0.1 and 600 mmHg, with 20 seconds allowed for equilibration at each pressure. Repeat analysis was conducted to determine the amount of CO that was adsorbed reversibly and irreversibly. The irreversibly adsorbed CO gas should correspond to the CO adsorbed on the metal surface. Chemisorption stoichiometry of CO/Pt = 1 was assumed when determining the Pt dispersion on the CeO_2 support.

Rogemond et al. (1997:229) and Pantu & Gavalas (2002:255) suggest that traditional chemisorption techniques using H_2 and CO are not reliable as there is a possibility of both gases adsorbing on the ceria. This would lead to the overestimation of metal dispersion. To minimise this effect, CO chemisorption was conducted at a temperature near room temperature (in this case, the lowest temperature the apparatus would allow) as changes to the oxidation state of the support is minimal at this temperature (Perrichon et al., 2004:4). CO adsorption at higher temperatures can lead to the reduction of the support.

4.2.5. Transmission Electron Microscopy

Transmission electron microscopy (TEM) was used to determine the size distribution of the Pt nanoparticles and to comment on the dispersion of the Pt nanoparticles on the CeO_2 support.

Bright-field scanning transmission electron microscopy (BF-STEM) and high-angle annular dark-field (HAADF) TEM images were recorded using a JOEL JEM-ARM200F double Cs-corrected TEM equipped with a field emission gun, a scanning transmission electron microscopy (STEM) unit and a HAADF detector, operated at 200 kV.

The catalyst samples to be studied were dispersed in ethanol in an ultrasonic bath for five minutes. A plastic Pasteur pipette was used to deposit the suspension on a Quantifoil carbon film supported on copper TEM grids. The catalyst containing grid was left to dry for approximately ten minutes. Once dried, the grid was ready for viewing.

The freeware IMAGEJ was used to measure the Pt nanoparticle size distribution.

4.3. Catalytic Testing Apparatus

All experiments were conducted using the high throughput Flowrence reactor manufactured by Avantium Technologies (Avantium, n.d.). The Flowrence consists of three main sections: an upstream section, a reactor section and a downstream section. The upstream section is for mixing and distributing the liquid and gas feeds. The reactor section contains sixteen parallel fix bed reactors which allows experimentation to be conducted in high throughput mode. The downstream section contains backpressure regulators for each reactor and an online Gas Chromatograph (GC) for effluent gas analysis. A simplified flowsheet of the Flowrence is given in Figure 4.1.

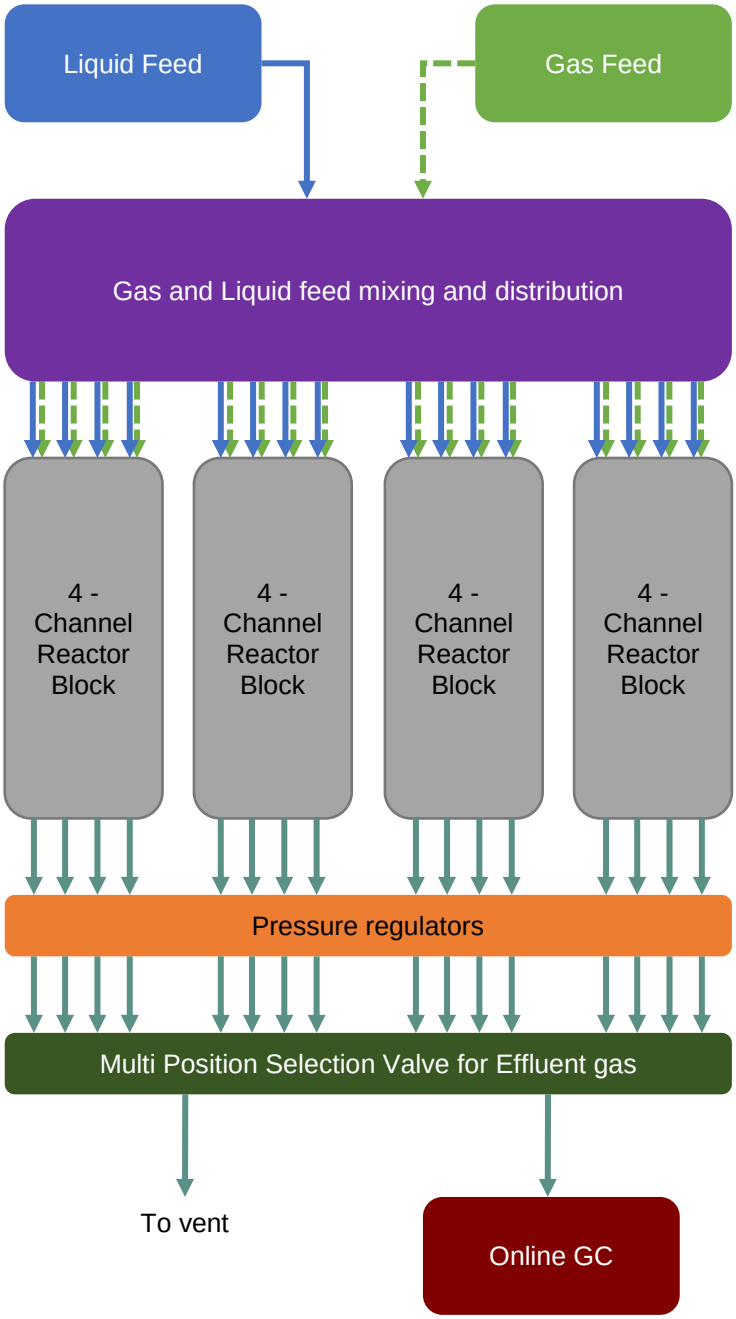

Figure 4.1: Simplified flowsheet of the Flowrence Reactor

4.3.1. Upstream Section

The upstream section consists of mass flow controllers (MFCs) for air, carbon dioxide (CO_2), carbon monoxide (CO), helium (He), hydrogen (H_2), methane (CH_4) and nitrogen (N_2) as well as a Jasco PU-2080 Plus HPLC pump for water. The dry gas, which is mixed through diffusion in the tubing, and the liquid feed each have their own flow distribution to the sixteen reactors and are combined as a wet stream at the top of the reactor tube before the catalyst bed.

Flow distribution is based on an equal pressure drop to all sixteen reactors. The equal pressure drop is created using a capillary, which offers a resistance. Each reactor contains two capillaries, one for the dry gas feed (ID 50 µm, 100 cm) and one for the liquid feed (ID 50 µm, 175 cm).

4.3.2. Reactor Section

The reactor section is divided into four independently heated reactor blocks, with each reactor block containing four quartz reactors (2 mm diameter) in a fixed-bed setup. The reactor system offers identical testing conditions across pressure, flow and feed composition to all four blocks. Details on catalyst loading can be found in section 4.5.2.

To prevent a pressure difference between the inside and outside of the reactor tubes, nitrogen diluent was flowed along the outside of the reactor tube. Since the Flowrence does not contain a feed bypass, one reactor was not loaded. This empty reactor is referred to as the blank reactor and was used to sample the feed.

4.3.3. Downstream Section

The backpressure regulators of all sixteen reactors are controlled through a single pressure indicator controller (PIC). This results in an equal pressure in all reactors. Once flow has passed through the backpressure regulators, it goes to a sixteen-port selection valve. The valve selects a single reactor at a time and flow from this reactor first goes through a water knock-out pot. The dry gas is then fed to the online GC for analysis. More information on the sampling procedure can be found in section 4.6.1.1. The flow from all other reactors passes through a separate water knock-out pot before being sent to the vent.

4.4. Operating Conditions for Catalytic Testing

The water-gas shift (WGS) performance of the catalyst under study was investigated across a range of operating conditions, most notably feed composition and temperature.

4.4.1. Gas Feed Compositions

An Aspen Plus V8 (AspenTech, 2016) simulation was conducted to determine a feasible WGS feed condition. The Peng Robinson Equation of State thermodynamic model was used to simulate the system. For simplification purposes, the feed stream was assumed to compose of only propane and not a propane/butane mixture (LPG). It was assumed that the propane reforming reactor operates at equilibrium. As such, a thermodynamic equilibrium reactor model was used to simulate the reactor. The product stream of the propane reformer represents the WGS feed stream. The Aspen Plus simulation model used to simulate the propane reforming reactor is depicted in Figure 4.2.

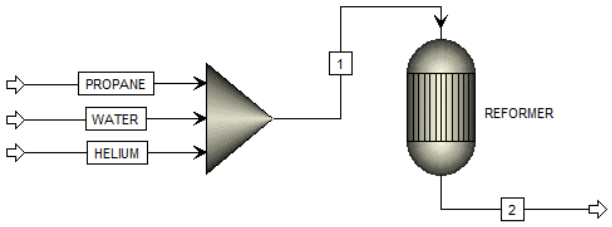

Figure 4.2: Aspen Plus simulation model

4.4.1.1. *Propane Reforming Reactions and Operating Conditions*

The following eight propane reforming reactions were considered in the simulation, as suggested by Häussinger, Lohmüller and Watson (2000:257) and Shekhawat, Spivey and Berry (2011:51).

$$C_3H_8 + 3H_2O \rightleftarrows 3CO + 7H_2 \quad \text{Equation 4.1}$$

$$C_3H_8 + 2H_2O \rightleftarrows CH_4 + 2CO + 4H_2 \quad \text{Equation 4.2}$$

$$C_3H_8 + H_2O \rightleftarrows C_2H_6 + CO + 2H_2 \quad \text{Equation 4.3}$$

$$C_2H_6 + 2H_2O \rightleftarrows 2CO + 5H_2 \quad \text{Equation 4.4}$$

$$C_3H_6 + H_2O \rightleftarrows CH_4 + CO + 2H_2 \quad \text{Equation 4.5}$$

$$CH_4 + H_2O \rightleftarrows CO + 3H_2 \quad \text{Equation 4.6}$$

$$CH_4 + 2H_2O \rightleftarrows CO_2 + H_2 \quad \text{Equation 4.7}$$

$$CO + H_2O \rightleftarrows CO_2 + H_2 \quad \text{Equation 4.8}$$

The system was simulated at 1 bar(a). Previous optimisation in-house has indicated that the reformer should be operated at 700 °C and with a steam-to-carbon ratio in the feed of 4. These conditions were applied to the simulation.

4.4.1.2. *Feed Conditions for Kinetic Experiments*

The results of the Aspen Plus propane (C_3H_8) reforming simulation are presented in Table 4.2. C_3H_8 and ethane (C_2H_6) are not considered further in this study as full conversion of these species is reached at the reaction conditions. Since the vol% of CH_4 was found to be close to zero (i.e. almost complete conversion), it also will not be considered further in this study either. Rather, CH_4 will be considered as inert material and the vol% of CH_4 will be combined with that of the inerts in the system.

Table 4.2: Results of the propane reforming Aspen Plus simulation

Component	**Composition (vol%)**
CO	6.3
H_2O	37
CO_2	8.6
H_2	43
C_3H_8	0
C_2H_6	0
CH_4	0.1
He (inert)	5

The experimental design was focussed on a one-at-a-time variation approach, which has been used in literature for kinetic studies (Amadeo & Laborde, 1995:951; Hilaire et al., 2001:274; Phatak et al., 2007:226). In this approach, the partial pressures of the inlet gases are varied one at a time while keeping the partial pressures of all other gases constant. The advantage of this type of approach is that the effect that changing the partial pressure of each component has on the reaction rate can be clearly seen.

To allow for the one-at-a-time variation approach to experimental design, a large amount of inert material needs to be present in the initial feed stream. When one of the partial pressures of the inlet gases is varied, the inert material's partial pressure can be varied as well to ensure the partial pressures of all other gases are held constant. To allow for a wide range in which the partial pressures of the reactant and product gases can be varied, a maximum of 30 vol% of inerts was used in the reactor feed stream for this study. The ratio of CO, H_2O, CO_2 and H_2, as seen in Table 4.2, was kept constant when altering the stream to include 30 vol% of inerts. The following gas feed composition was therefore used as the base reaction condition for the

experimental programme: 4.6 vol% CO, 27 vol% H_2O, 6.4 vol% CO_2, 32 vol% H_2 and 30 vol% inerts. This feed stream composition is referred to as the baseline from this point forward and forms the centre point for the experimental programme.

During the experimental programme, the baseline condition would be tested at pre-determined time intervals. This made it possible to monitor the catalyst deactivation during the experimental programme. If the catalyst deactivated, the experimental programme would be stopped and fresh calcined catalyst loaded.

The feed composition was varied over the following ranges during the experimental programme: 2 – 12 vol% CO, 20 – 45 vol% H_2O, 4 – 15 vol% CO_2 and 25 – 55 vol% H_2. He (used as the internal standard) and N_2 were used as inerts in the system and their partial pressures were varied to ensure the partial pressure of all gases not being varied were kept constant. In total, nine different feed conditions were tested – the baseline condition as well as a high and low concentration of each of the four WGS reactive gases. Details on all the feed compositions used for the experimental programme can be found in Appendix A.

Due to time constraints and the availability of the catalytic testing apparatus, the experimental programme was split into two sets of experiments. The first set of kinetic experiments comprised of testing the effects of feed conditions I through IV, while the second set of kinetic experiments comprised of testing the effects of feed conditions V through X (refer to Table A.1 in Appendix A for feed conditions).

4.4.1.3. *Feed Conditions for Pressure Experiments*

Pressure experiments were conducted with the baseline feed composition at a total volumetric flow rate of 272 $ml_{(n)}$/min.

4.4.2. Temperature

Catalytic testing was conducted in the temperature range between 270 °C and 325 °C.

4.4.3. Pressure

Reaction pressure was controlled by means of back pressure regulators. Usually, experiments were conducted at 2 bar(a). Experiments to investigate the effect of pressure on the WGS activity were conducted in the pressure range between 2 bar(a) and 8 bar(a).

4.4.4. Space Velocity

Gas hourly space velocity was manipulated to ensure that experiments are conducted away from equilibrium. Typically, catalytic testing was conducted at wet gas (i.e. gas containing water vapour) hourly space velocities between 7 000 hr^{-1} and 65 000 hr^{-1}. Details regarding the catalyst loadings for all experimental runs can be found in Appendix A.

4.5. Catalytic Testing Apparatus Operating Procedure

4.5.1. Sieving of Catalyst

Before the catalyst could be loaded into the reactors, a catalyst particle size had to be chosen to ensure all experiments were conducted free from any transport limitations. Using the calculations detailed in Appendix D and the results of previous experimental work conducted over the same catalyst as a guideline, it was determined that the catalyst should be sieved into the 100 – 150 µm size range. This would ensure the experiments were conducted free from any transport limitations.

Sieving of the catalyst into the 100 – 150 µm size range was done by first compressing the catalyst under 15 tonnes of pressure for 20 minutes using a Specac Atlas™ Power 25Ton Hydraulic Press. Once compressed, the catalyst was ground using a pestle and mortar. The ground catalyst was then sieved into the required size range. This process was repeated until sufficient catalyst in the right size range was obtained.

4.5.2. Catalyst Loading

The catalyst loading procedure was performed identically for all reactors and experiments so that the catalyst always sat within the isothermal zone of the reactor. The isothermal zone has previously been determined in-house (Luchters, 2016). The reactor loading was carried out from bottom-to-top.

The bottom of the reactor contains a quartz porous filter to ensure the contents of the reactor do not exit through the bottom. Silicon carbide (300 µm) was loaded first into the reactor until approximately 11 cm from the bottom, as this is where the isothermal zone begins. The packing was compacted gently by tapping the reactor. A layer of quartz wool (~ 3 mm) was then loaded and the catalyst packed on top of the quartz wool. The purpose of the quartz wool is to keep the catalyst separate from the silicon carbide. The packing was once again compacted gently by tapping the reactor. Another layer of quartz wool (~ 3 mm) was loaded on top of the catalyst bed, as this allows the catalyst to be easily recovered from the reactor if needed. Silicon carbide was then packed to fill up the reactor. The packing of the various materials within the reactor is shown in Figure 4.3.

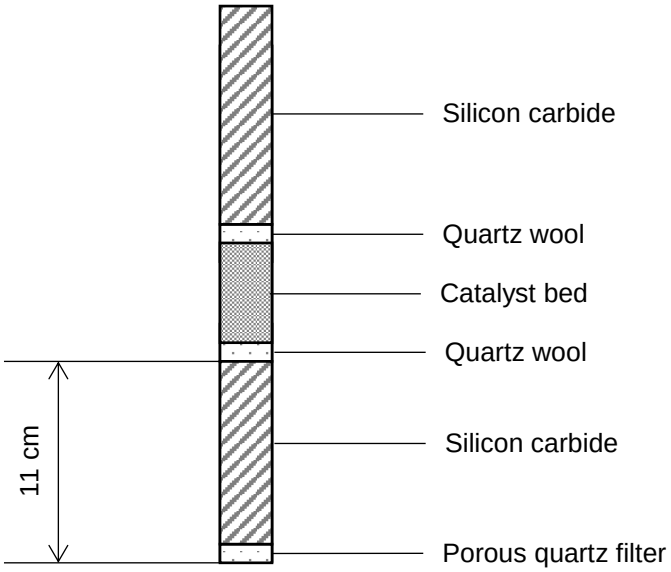

Figure 4.3: Packing of a typical reactor (not to scale)

Once packed, o-rings were placed on the top of the reactors. The reactors are then inserted into the heating blocks. The o-rings sit on an actively cooled plate and not on the heating block to prevent melting of the o-rings. An airtight seal is made by closing the lid of the reactor section onto the o-rings.

4.5.3. Catalytic Testing Apparatus Operation

4.5.3.1. *Catalyst Reduction*

The reduction procedure utilises H_2, He and N_2 and was performed consistently for all experiments. Firstly, a reaction mixture of composition 10 vol% H_2, 3 vol% He and 87 vol% N_2 was fed to all reactors at atmospheric pressure, room temperature and flow rate of 571 $ml_{(n)}$/min. Thereafter, the temperature of the reactor heating blocks was ramped at a linear heating rate of 2 °C/min to 275 °C and held at this temperature for six hours to complete the reduction procedure.

4.5.3.2. *Start-up Procedure*

The following start-up procedure was followed for all experiments:

1. The reduction procedure described in section 4.5.3.1 was followed.
2. After reduction, the temperature of the reactor heating blocks was ramped at a linear heating rate of 2 °C/min to their respective temperature setpoints under the reduction gas. Reactors were held at these temperatures for 10 minutes to allow the temperature to stabilise.
3. Directly thereafter, still under reduction atmosphere, the water pump setpoint was set as required for the first experiments and the pump was switched on. At the same time, the reactors were pressurised to their setpoints at a linear ramp rate of 0.8 bar(a)/min.

Reactors were held at these conditions for 15 minutes to allow the water flow rate and pressure to stabilise.

4. Thereafter, the gas composition was set as required for the first experiment and 2 hours wait time was allowed for the reactor system to stabilise before the first sample was taken.

4.5.3.3. *Online Operating Procedure*

Set procedures were followed when an operating condition was changed. After changing conditions, a 2 hour wait time was allowed for the system to re-stabilise before a sample was taken.

Temperature

When increasing or lowering the temperature of a reactor heating block during an experiment, the temperature was ramped at a linear rate of 2 °C/min.

Pressure

When increasing or decreasing pressure in the reactor system during an experiment, the pressure was ramped at a linear rate of 0.8 bar(a)/min.

Feed Composition/Space Velocity

When altering feed composition and space velocity during the experimental programme, all flow rates were adjusted simultaneously.

4.5.3.4. *Shut-down Procedure*

The following shut-down procedure was followed for all experiments conducted:

1. After completion of the experimental run, the flow of CO, H_2O, CO_2, H_2 and He was switched off.
2. The flow rate of N_2 was then set to 25 $ml_{(n)}$/min per reactor.
3. Thereafter, all reactor heating blocks were cooled to 30 °C at a linear ramp rate of 5 °C/min.
4. Once all reactor heating blocks had reached the required temperature, the heating blocks and gas flows were switched off.

4.6. Feed and Product Analysis

4.6.1. Gas Chromatographic Analysis

The composition of CO, CO_2, H_2, He and N_2 in the reactor effluent were analysed online using an Agilent Technologies 490 micro GC (µGC). The µGC contains four columns however, only two columns, a 20 m Molsieve 5A column (MS5A) and a 10 m Pora Plot Q column (PPQ), were required to analyse the components in this project. The PPQ column can detect H_2O however, the enormous tailing of the peak leads to inaccurate quantification. The amount of H_2O in the reactor effluent was therefore not analysed, but rather back calculated on a total molar basis.

4.6.1.1. *Sampling Procedure*

Online sampling was achieved by means of a sixteen-port selection valve. During general operation of the catalytic testing apparatus, the sixteen-port selection valve selects a reactor thus directing the gas product from that reactor to a water knock-out pot and then to the GC for analysis of the dry gas. A twenty-minute wait period was allowed after reactor selection for flushing of the tubing before the dry gas sample was injected into the GC

In all experiments, for each reaction condition, the reactors were sampled one by one (e.g. Reactor 1, 2, 3, …, 16). This was repeated three times to ensure three samples were taken at each reaction condition. After altering any of the reactor operating conditions, a two hour wait period was allowed for the system to re-stabilise before the sampling procedure began.

4.6.1.2. *Operating Conditions*

The Agilent 490 µGC used in this study contained four parallel injectors, columns and TCDs. An overview of the components detected on each column is presented in Table 4.3 and the µGC's operating conditions are presented in Table 4.4. Typical chromatograms are shown in Figure 4.4.

Table 4.3: Retention times of individual gaseous components in the micro gas chromatograph

Column	Species	Retention time (minutes)
MS5A	CO	2.75
MS5A	H_2	1.05
MS5A	He*	0.96
MS5A	N_2	1.6
PPQ	CO_2	0.51

*Used as the internal standard

Table 4.4: Micro gas chromatograph operating conditions

	20 m MS5A Column	**10 m PPQ Column**
Injector temperature (°C)	109	109
Column temperature (°C)	100	110
Carrier gas	Argon	-
Analysis time (minutes)	5	5
Injection time (ms)	75	75

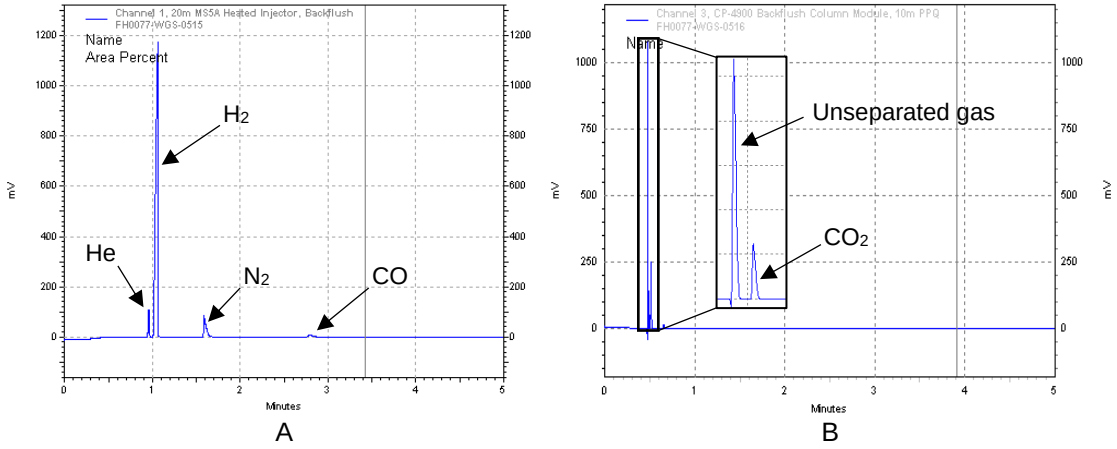

Figure 4.4: Typical chromatograms of the dry gas on a (A) MS5A column and (B) PPQ column

4.7. Data Analysis

4.7.1. Gas Chromatography Data

The peak areas obtained from the online µGC were related to the volumetric flow rate ($ml_{(n)}$/min) of the individual components using the relative response factors (RRF) and the known volumetric flow rate of the internal standard He (assumed to be non-reactive). This relationship is presented in Equation 4.9 where $\dot{V}_i$ is the volumetric flow rate of component i ($ml_{(n)}$/min), $Area_i$ is the peak area of component i obtained from the GC (-), $RFF_{i,a}$ is the 'a' component of the RFF factor for component i (-) and $RFF_{i,b}$ is the 'b' component of the RFF factor for component i (-). Determination of the RRFs can be found in Appendix E.

$$\dot{V}_i = \frac{\left(\frac{Area_i}{Area_{He}}\right) - RFF_{i,b}}{RFF_{i,a}} \times \dot{V}_{He} \qquad \text{Equation 4.9}$$

As indicated above, H_2O is not analysed by the online µGC. Given that the WGS reaction is an equimolar reaction, the amount of H_2O in the product stream can be back calculated on a total molar basis according to Equation 4.10, where $\dot{n}_i$ is the molar flow of component i (mol/s) and feed and product refer to the feed stream and product stream respectively.

$$\dot{n}_{H_2O} = \dot{n}_{total,feed} - \dot{n}_{CO,product} - \dot{n}_{CO_2,product} - \dot{n}_{H_2,product} - \dot{n}_{inerts,product} \qquad \text{Equation 4.10}$$

The conversion of CO (X_{CO}) in the WGS reaction was calculated according to Equation 4.11 where $\dot{F}_{CO}$ is the molar flow rate of CO (mol/s) and feed and product refer to the feed stream and product stream respectively.

$$X_{CO} = \frac{\dot{F}_{CO,feed} - \dot{F}_{CO,product}}{\dot{F}_{CO,feed}} \times 100\ \% \qquad \text{Equation 4.11}$$

When averaging out the conversion for a set of experiments, the standard deviation (SD) was calculated using Equation 4.12, where $\sum$ is the 'sum of', x is a sample point, $\bar{x}$ is the sample mean and n is the size of the sample.

$$SD = \sqrt{\frac{\sum x - \bar{x}}{n-1}} \qquad \text{Equation 4.12}$$

4.8. Model Development

The fixed-bed reactor used in this study was modelled as a packed-bed reactor (PBR). The following assumptions have been made when developing the reactor model and details regarding the testing of these assumptions can be found in Appendix D:

- Isothermal and isobaric operation of the reactor
- Absence of axial dispersion in the reactor (plug-flow behaviour only)
- Absence of radial gradients
- No catalyst deactivation

Development of the reactor model is closely followed from that described by Scott Fogler (2006:14-19). In a FBR, reactants are continually consumed as they flow down the length of the reactor. Consequently, the reaction rate varies down the length of the reactor. Consider a mole balance on species A in a differential segment of the catalyst mass (i.e. weight) ΔW. The differential catalyst mass, ΔW, is chosen sufficiently small such that there are no spatial variations in the reaction rate within this mass of catalyst. The mole balance is given by Equation 4.13, where Ḟ is the molar flow rate (moles/time), r_A' is the reaction rate (moles·$catalyst_{weight}^{-1}$·$time^{-1}$) and W is the catalyst weight (units: $catalyst_{weight}$).

(Molar flow rate of species A ***in*** at W (*moles/time*))	-	(Molar flow rate of species A ***out*** at (W + ΔW) (*moles/time*))	+	(Molar rate of ***generation*** of species A within ΔW (*moles/time*))	=	(Molar rate of ***accumulation*** of species A within ΔW (*moles/time*))
In	-	*Out*	+	*Generation*	=	*Accumulation*
$\dot{F}_{(A\|W)}$	-	$\dot{F}_{(A\|W+\Delta W)}$	+	$r_A'\Delta W$	=	0

Equation 4.13

Dividing by ΔW and rearranging gives Equation 4.14

$$\left[\frac{\dot{F}_{(A|W+\Delta W)} - \dot{F}_{(A|W)}}{\Delta W}\right] = r_A' \qquad \text{Equation 4.14}$$

The term in brackets should be recognised as the definition of a derivative. Taking the limit as ΔW approaches zero, the differential form of the steady state mole balance (Equation 4.15) on a PBR is obtained.

$$\frac{dF_A}{dW} = r_A' \qquad \text{Equation 4.15}$$

Equation 4.15 represents the reactor model used in this study. The formulation of the reaction rate equation describing r_A' is dealt with in Chapter 6.

4.9. Modelling of the Water-Gas Shift Reaction using gPROMS

In this study, a PBR model was used and was assumed to operate as an isothermal and isobaric plug flow reactor.

4.9.1. Model Validation

Validation of the gPROMS model was achieved through the validation of empirical equations reported in previous kinetic studies (Grabow et al., 2008; Kalamaras et al., 2009). The gPROMS model was used to re-fit the empirical equations to the data sets reported with the studies. If similar parameters are obtained, the empirical equations and gPROMS model can be validated.

The activation energy (Ea) found during parameter estimation could be validated by comparing it to the value found by means of a classical Arrhenius analysis.

4.9.2. Parameter Estimation

The fitting of experimental data to Equation 4.15 is accomplished with the gPROMS (general PROcess Modelling System) software package (Process Systems Enterprise Limited, 2017a). When solving a parameter estimation problem in gPROMS, the maximum likelihood objective function (Equation 4.16) is used (Process Systems Enterprise Limited., 2017b). The maximum likelihood objective function allows for simultaneous estimation of parameters in both the physical model and the variance model to maximise the probability that the mathematical model will predict the measured values obtained from experiments.

In Equation 4.16, Φ is the objective function, N is the total number of measurements taken for all experiments, θ is the set of model parameters to be estimated, NE is the number of experiments performed, NV_i is the number of variables measured in the i^{th} experiment, NM_{ij} is the number of measurements of the j^{th} variable in the i^{th} experiment, σ_{ijk}^2 is the variance of the k^{th} measurement of variable j in experiment i, $\tilde{z}_{ijk}$ is the k^{th} measured value of variable j in experiment i and z_{ijk} is the k^{th} (model-)predicted value of variable j in experiment i.

The maximum likelihood objective function assumes the difference between the experimental values and model prediction values ($\tilde{z}_{ijk} - z_{ijk}$) to be independent and normally distributed with zero mean and standard deviation σ_{ijk}.

$$\Phi = \frac{N}{2} \cdot \ln(2\pi) + \frac{1}{2} \cdot min_{\theta} \left\{ \sum_{i=1}^{NE} \sum_{j=1}^{NV_i} \sum_{k=1}^{NM_{ij}} \left[\ln\left(\sigma_{ijk}^2\right) + \frac{\left(\tilde{z}_{ijk} - z_{ijk}\right)^2}{\sigma_{ijk}^2} \right] \right\} \qquad \text{Equation 4.16}$$

Several variance models to describe the standard deviation for the measured experimental data are available in gPROMS. The constant variance model is used in this study. This variance model assumes a constant variance for the measurement error.

4.9.2.1. *Statistical Analysis*

Once the objective function has been satisfied, the weighted residual (WR) was compared to the chi-squared (X^2) value to determine the goodness of the fit. If the weighted residual was found to be less than the chi-squared value, the model was deemed to be a good fit based on the variance model set.

A 95 % t-value was calculated by gPROMS for all parameters estimated during the parameter estimation procedure. The 95 % t-value can be compared to the reference t-value to give an indication of the 'goodness' of the estimated parameter. If the 95 % t-value is smaller than the reference t-value, it is concluded that the data is not sufficient to estimate the parameter precisely. This implies that more data points are required to estimate the parameter with precision.

gPROMS also calculates the 95 % confidence interval for each parameter estimated. This interval represents the range of values in which there is a 95 % probability that the true value of the estimated parameter lies within it.

The correlation matrix for the estimated parameters is also reported by gPROMS. The correlation matrix provides useful information on the degree of dependence between the variables being estimated.

5. Results

5.1. Catalyst Characterisation

In this study, a 0.5 wt% Pt/CeO_2 catalyst was used. The characterisation results of this catalyst are presented below. The methodology followed for characterisation techniques is explained in Chapter 4.

5.1.1. Inductively Coupled Plasma – Optical Emission Spectrometry

Inductively Coupled Plasma – Optical Emission Spectrometry (ICP-OES) analysis was conducted to determine the metal loading of the catalyst. The metal loading was confirmed to be (0.50 ± 0.02) wt% by ICP-OES, which matches the target value of 0.5 wt%.

5.1.2. Transmission Electron Microscopy

Transmission electron microscopy (TEM) was used to determine the size distribution of the Pt nanoparticles and to comment on the dispersion of the Pt nanoparticles on the CeO_2 support. Samples were studied after calcination, after reduction and after experimentation. Due to their similar masses, the contrast between CeO_2 and Pt is low in TEM images. As such, high-angle annular dark-field (HAADF) imaging was used to identify Pt nanoparticles. The brighter spots seen on HAADF images correspond to particles/areas with a greater density. The TEM and HAADF images of the calcined and reduced catalyst are given in Figure 5.1 and Figure 5.2. Figure 5.3 shows the number-based TEM Pt nanoparticle size distribution.

Pt nanoparticles are seen in Figure 5.1 and Figure 5.2, although it is not always easy to distinguish these nanoparticles from the thicker regions of the CeO_2 support (such as in Figure 5.2 B.1). It is especially difficult to differentiate between what could be clusters of Pt on the CeO_2 support and areas that are simply thicker regions of the CeO_2 support.

In Figure 5.1, A.1 and B.1 shows well dispersed nanoparticles towards the outside of the CeO_2 support with very few nanoparticles observed towards the center of the CeO_2 support. Images A.2 and B.2 in Figure 5.1 show Pt nanoparticles following what appears to be a CeO_2 contour or nanopore, whiles images A.3 and B.3 give an overview of the catalyst being studied.

In Figure 5.2, A.1 and B.1 show Pt nanoparticles towards the outside of the CeO_2 support that are not well dispersed. There appears to be no nanoparticles toward the center of the CeO_2 support. In images A.2 and B.2 in Figure 5.2, Pt nanoparticles are observed that are not well dispersed on the CeO_2 support while images A.3 and B.3 show very few Pt nanoparticles.

In Figure 5.3, a reasonably narrow Pt size distribution is observed for the calcined catalyst and a bimodal distribution is observed for the reduced catalyst. A fraction of larger particles is observed after reduction, suggesting that sintering is occurring during reduction. It should be

noted that much fewer particles (209 vs. 81) were measured for the reduced catalyst than the calcined catalyst due to the number of particles that are visible in the images.

TEM and HAADF images of four used catalysts (refer to Appendix F) show no change in the Pt nanoparticle size during experimentation.

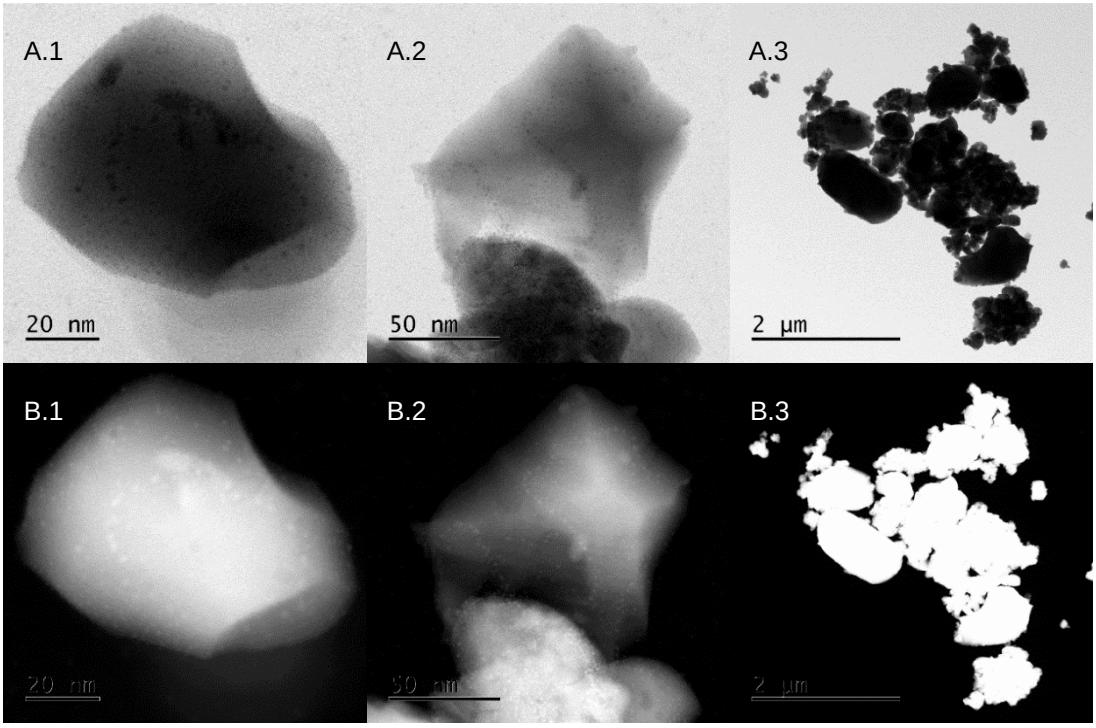

Figure 5.1: (A) TEM and (B) corresponding HAADF images of 0.5 wt% Pt/CeO_2 catalyst after calcination

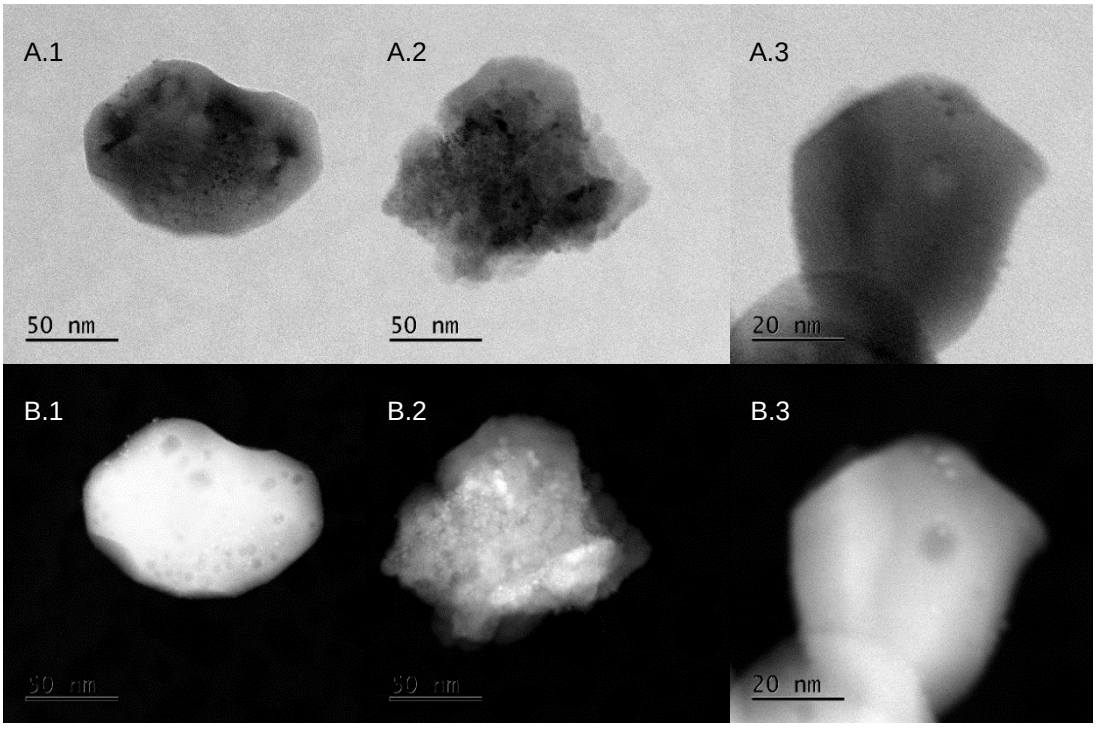

Figure 5.2: (A) TEM and (B) corresponding HAADF images of 0.5 wt% Pt/CeO_2 catalyst after reduction

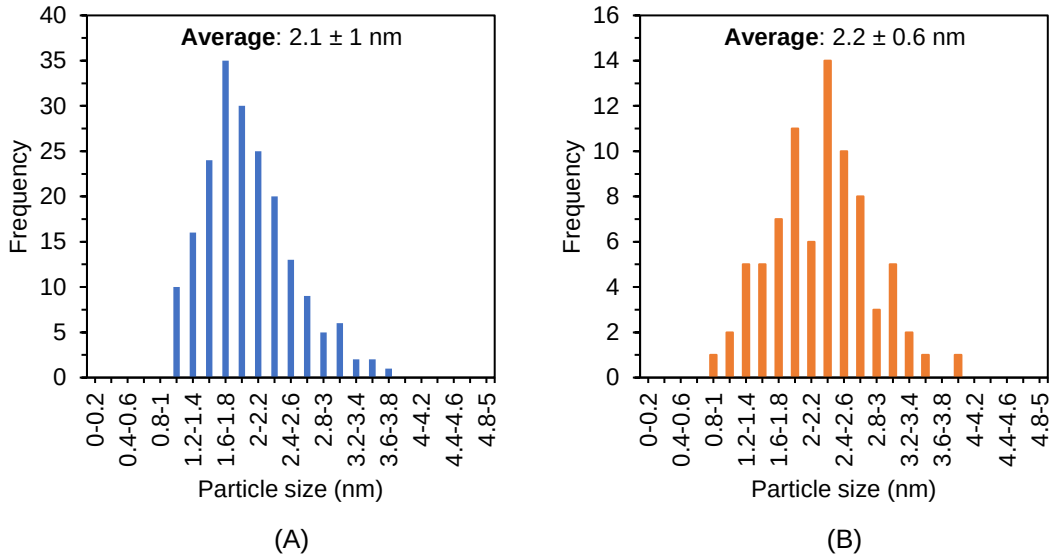

Figure 5.3: Pt particle size distribution of 0.5 wt% Pt/CeO_2 after (A) calcination and (B) reduction

5.1.3. Specific Surface Area and Pore Size Distribution

The specific surface area and pore volume of the calcined 0.5 wt% Pt/CeO_2 catalyst and CeO_2 support was determined by N_2 physisorption. No comparison of the surface areas can be made as they are below the precision rating of the instrument (10 m^2/g).

Table 5.1: N_2 physisorption analysis results

Property	Value	Units
BET surface area (Pt/CeO_2)	2.9 ± 0.2	m^2/g
BET surface area (CeO_2)	3.5 ± 0.1	m^2/g
Pore volume (Pt/CeO_2)	(17 ± 1) x 10^{-3}	cm^3/g
Pore volume (CeO_2)	(11 ± 1) x 10^{-3}	cm^3/g

5.1.4. CO Chemisorption

CO Chemisorption was performed on the reduced catalyst to determine the metallic surface area, dispersion of Pt on the CeO_2 support as well as the Pt nanoparticle size. The results obtained from CO chemisorption are presented in Table 5.2.

It is seen from Table 5.2 that the particle size determined by CO chemisorption is larger than that obtained from TEM (reported before in Figure 5.3). The difference in particle size could be due to the inaccurate CO/Pt chemisorption stoichiometry assumed. The stoichiometric factor

strongly depends on the arrangement of the surface atoms and is widely accepted to be one of the main limitations of gas chemisorption (Torrente-Murciano, 2016:2).

Table 5.2: CO chemisorption results

Property	**Value**	**Units**
Metallic surface area	0.3 ± 0.1	m^2/g
Dispersion	28 ± 4	%
Average Pt particle size from chemisorption	4.1 ± 0.6	nm

5.1.5. Temperature Programmed Reduction

Hydrogen temperature programmed reduction (TPR) was used as a means of studying the reduction behaviour of the CeO_2 support and the 0.5 wt% Pt/CeO_2 catalyst. Samples were heated from room temperature to 950 °C at a rate of 10°C/min in a 5 vol% H_2 in Ar stream. Hydrogen consumption is measured by means of a thermal conductivity detector (TCD). Figure 5.4 shows the TPR spectra of the CeO_2 support and of the 0.5 wt% Pt/CeO_2 catalyst.

The intensity of the peaks observed in the TPR spectra depends on the operating conditions (weight of sample, hydrogen flow rate) whereas the location of the peaks (the temperature corresponding to the local maximum) is an intrinsic factor of the sample under study (Giordano et al., 2000:274).

In the TPR spectra for CeO_2 (Figure 5.4), a single peak at 800°C is observed. This peak is assigned to the reduction of the Ce^{4+} species to Ce^{3+}, as shown in Equation 5.1. The peak temperature corresponds to that reported by Giordano et al. (2000:274) over a low surface area (3 m^2/g) CeO_2 sample.

$$2CeO_2 + H_2 \rightleftarrows 2CeO_{1.5} + H_2O \qquad \text{Equation 5.1}$$

The TPR spectra of the 0.5 wt% Pt/CeO_2 sample is characterised by four peaks, at 70 °C, 150 °C, 325 °C and 850 °C. The peak at 850 °C is attributed to the reduction of bulk Ce^{4+} species (Zhang et al., 2008:605). The intensity of this peak is much larger than that observed for the CeO_2 sample due to the larger sample mass used.

The peak around 325 °C is thought to be due to the reduction of the surface Ce^{4+} species (Jacobs et al., 2003:10400; Zhang et al., 2008:605). This peak is not observed in the TPR spectra for CeO_2 due to the small amount of sample used. This peak has, however, been observed in the TPR spectra of CeO_2 as recorded by Jacobs et al. (2003:10400) and Zhang et al. (2008:605).

The first two peaks (70 °C and 150 °C) possibly arise from the reduction of Pt metal. The hydrogen uptake for these two peaks is reported in Table 5.3. It is seen that the hydrogen uptake for the peak at 150 °C is comparable to that required for the reduction of PtO to Pt (Equation 5.2). It is therefore assumed that the reduction of PtO occurs at 150 °C. Zhang et al. (2008:605) found their Pt/CeO_2 catalyst prepared by impregnation reduced at a similar temperature (140 °C).

$$PtO + H_2 \rightleftarrows Pt + H_2O \qquad \text{Equation 5.2}$$

The first peak observed is thought to be due to impurities or moisture on the sample.

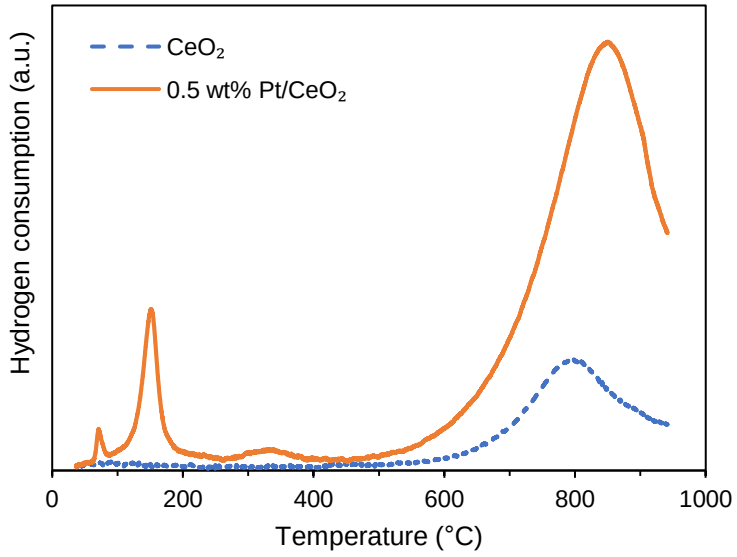

Figure 5.4: TPR spectra of the CeO_2 support (~30 mg) and 0.5 wt% Pt/CeO_2 catalyst (~200 mg) obtained by heating to 950 °C at a rate of 10 °C/min under 5 vol% H_2 in Ar (50 $ml_{(n)}$/min)

Table 5.3: TPR H_2 uptake for the two peaks corresponding to Pt reduction

Peak T (°C)	H_2 (µmol/g)	H_2 (µmol/g)* for $PtO_2 \rightarrow Pt^0$	H_2 (µmol/g)* for $PtO \rightarrow Pt^0$
70	0.8	20	10
150	9.7	–	–

*Theoretical H_2 uptake for the PtO_x reduction listed

5.1.6. Chlorine Concerns

Work by Pino et al. (2003:135-146) used a 1 wt% Pt/CeO_2 catalyst prepared by impregnation using chloroplatinic acid hydrate. In the work mentioned, it was found that the chloroplatinic acid hydrate had not completely dissociated after calcination at 800 °C for 2 hours. This is of concern, as chloroplatinic acid hydrate is used was used in the current study to synthesize the 0.5 wt% Pt/CeO_2 catalyst.

Due to the low Pt loading of the catalyst used in the current study, the amount of chlorine present (if any) is below the detection limits of the equipment available at the University of Cape Town. As such, the amount of chlorine present (if any) cannot be quantified on the catalyzed used in this study. The effect that chlorine may have on the WGS reaction is not considered in the scope of this study.

5.2. Kinetic Measurements

Appendix B contains the complete tabulated and processed experimental data set presented in this section.

5.2.1. Mass Balance

The mass balance was found to be accurate within 100 ± 2.2 % across all reactors.

5.2.2. Experimental Results

The results of the kinetic experiments conducted are presented in Figure 5.5 and Figure 5.6. All experiments were conducted free from mass and heat transport limitations and details concerning the calculations are presented in Appendix D. The feed conditions to all reactors are listed in Table A.1, Appendix A with details regarding catalyst loading in Table A.2 and Table A.3 of Appendix A. In the following figures, roman numerals denote different feed conditions. Additional figures showing time-on-stream performance per temperature setpoint can be found in Appendix C.

During the second set of kinetic experiments, the liquid feed distribution to reactor 2 (R2, orange circle) became blocked. This prevented the feed of H_2O to this reactor, resulting in no conversion being achieved from approximately 100 hours on stream. Due to the failure experienced by reactor 2 during the second set of experiments, all data from this reactor has been excluded from further kinetic modelling.

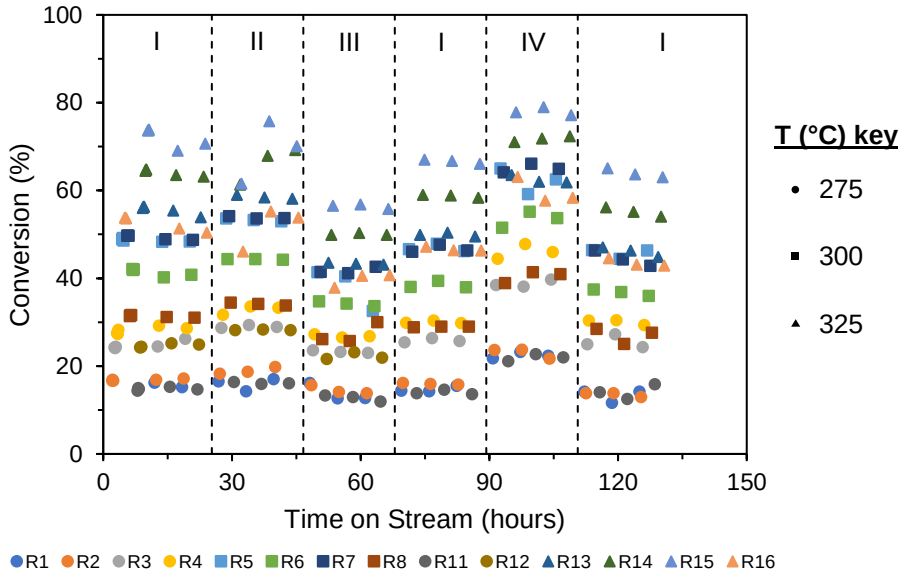

Figure 5.5: Time-on-stream performance under experimental conditions for the first set of kinetic experiments (refer to Chapter 5, section 5.4.1.2 for a description of the first set of kinetic experiments)

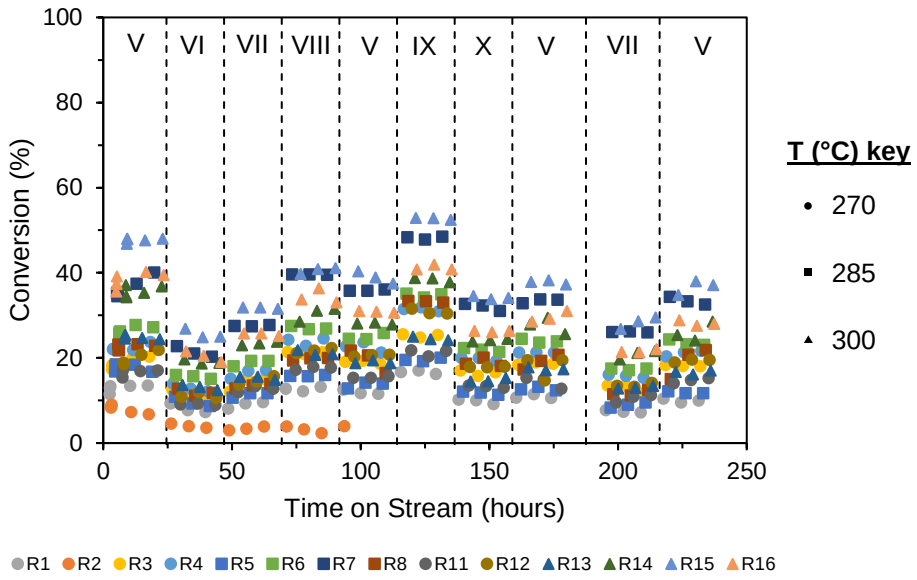

Figure 5.6: Time-on-stream performance under experimental conditions for the second set of kinetic experiments (refer to Chapter 5, section 5.4.1.2 for a description of the second set of kinetic experiments)

To ensure equilibrium conversion is not reached during the experiment, space velocity was varied in conjunction with the change in feed composition. The effect of changing feed composition on the reaction rate is presented in Table 5.4. Figures demonstrating the observed effects are given in Appendix C.

The trends presented in Table 5.4 are expected since an increase in reactant and decrease in product concentrations increases the reaction rate, while a decrease in reactant and increase in product concentrations decreases the reaction rate.

Table 5.4: Effect of changing reactant and product concentrations on the reaction rate (r_{CO})

Feed condition reference (Figure 5.5 & Figure 5.6)	**Description**	**Observed effect on reaction rate (r_{CO})[a]**
II	Low H_2 (25%)	Increase
III	High H_2 (54%)	Decrease
IV	Low CO (2%)	Decrease
VI	High CO (13%)	Increase
VII	Low H_2O (16%)	Decrease
VIII	High CO_2 (16%)	Decrease
IX	High H_2O (40%)	Increase
X	Low CO_2 (4%)	Increase

a Rate calculated assuming a linear concentration profile along the reactor

5.2.2.1. *Reproducibility of Results*

Figure 5.7 and Figure 5.8 show the time-on-stream performance for selected reactors. Each marker type represents a pair of reactors which are repeats of each other. For example, R1 and R11 of Figure 6.7, represented by circle markers, are repeats of each other.

Good reproducibility (within 10 % error) is observed in both sets of kinetic experiments (Figure 5.7 and Figure 5.8), with all repeat reactor pairs following the same trends. One important factor demonstrated by the good reproducibility is equal gas distribution to the reactors.

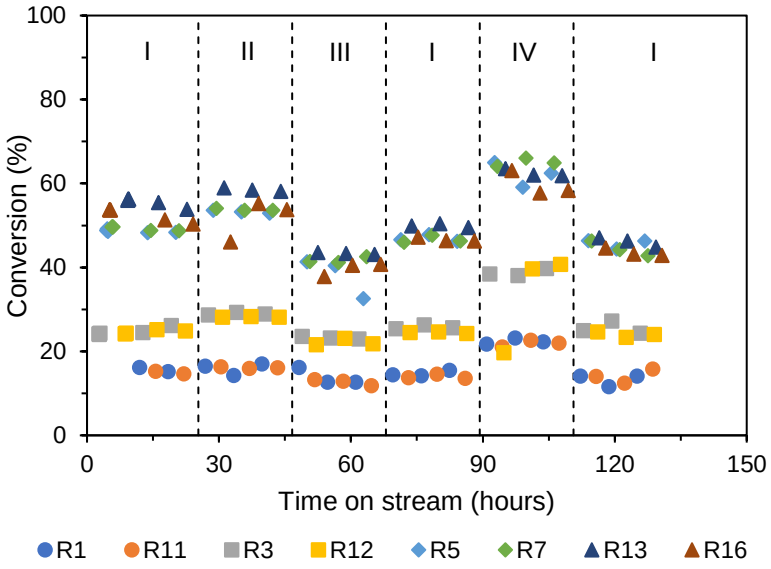

Figure 5.7: Reproducibility of the time-on-stream behaviour for the first set of kinetic experiments

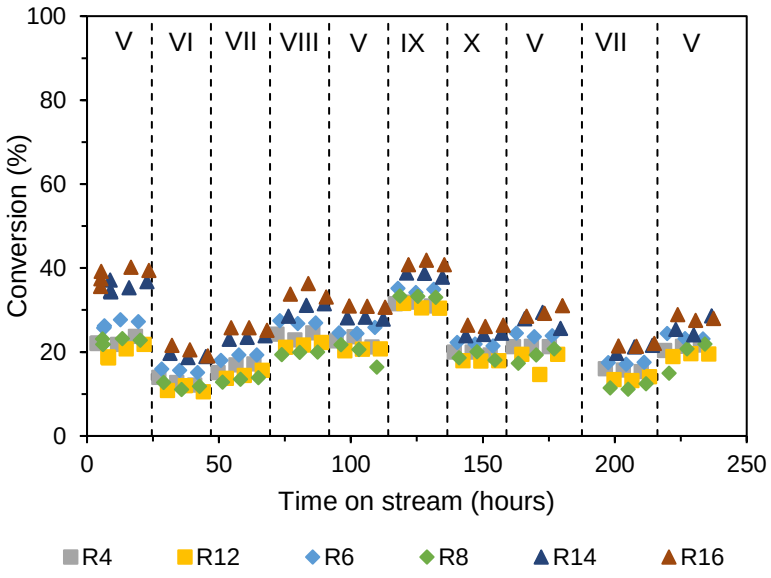

Figure 5.8: Reproducibility of the time-on-stream behaviour for the second set of kinetic experiments

5.2.3. Catalyst Deactivation

When measuring intrinsic catalyst kinetics, it is important to ensure the catalyst is not deactivating i.e. catalytic activity does not decrease. The change in activity over time on stream is monitored by comparing the initial and final conversions achieved at baseline conditions (refer to Chapter 5, section 5.4.1.2. for more details). The comparison between initial and final conversions achieved is presented in Table 5.5.

As mentioned previously, data from reactor 2 (R2) will not be considered for kinetic modelling due to the failure experienced with this reactor during the second set of kinetic experiments.

If the difference between the initial and final conversions crosses zero, it can be said that the conversions agree within experimental uncertainty. In this case, it is assumed that the change in catalytic activity is not significant and the data collected in the reactor can be used for kinetic modelling. Using this criterion, the data collected in R13, R14, R15 and R16 in both sets of kinetic experiments are eliminated and have not been used in the kinetic modelling.

The complete data set for kinetic modelling therefore consists of data collected from nine reactors over four temperatures. The grey shading in Table 5.5 indicates the reactors that have been eliminated from the data set.

Table 5.5: Initial and final conversion achieved in each reactor both sets of kinetic experiments

	Figure 5.5			Figure 5.6		
	Initial conversion (%)*	**Final conversion (%)***	**Difference (%)**	**Initial conversion (%)***	**Final conversion (%)***	**Difference (%)**
R1	16 ± 2	13 ± 2	3 ± 4	13 ± 2	10 ± 2	3 ± 4
R2	17 ± 2	13 ± 2	4 ± 4	8 ± 2	-2 ± 2	10 ±4
R3	25 ± 2	26 ± 3	-1 ± 5	19 ± 2	18 ± 2	1 ± 4
R4	28 ± 2	30 ± 2	-2 ± 4	22 ± 2	21 ± 2	1 ± 4
R5	49 ± 2	46 ± 2	3 ± 4	18 ± 3	12 ± 3	6 ± 6
R6	41 ± 2	37 ± 2	4 ± 4	27 ± 2	24 ± 2	3 ± 4
R7	49 ± 2	44 ± 3	5 ± 5	36 ± 3	33 ± 2	3 ± 5
R8	31 ± 2	27 ± 3	4 ± 5	23 ± 2	19 ± 4	4 ± 6
R11	15 ± 2	14 ± 3	1 ± 5	17 ± 2	15 ± 2	2 ± 4
R12	25 ± 2	24 ± 2	1 ± 4	20 ± 2	19 ± 2	1 ± 4
R13	56 ± 2	46 ± 2	10 ± 4	25 ± 2	17 ± 2	8 ± 4
R14	64 ± 2	55 ± 2	9 ± 4	36 ± 2	26 ± 3	10 ±5
R15	72 ± 3	64 ± 2	8 ± 5	48 ± 2	37 ± 3	11 ± 5
R16	52 ± 3	44 ± 2	8 ± 5	38 ± 3	28 ± 2	10 ± 5

*all at baseline condition

5.2.4. Equilibrium Considerations

An important consideration when conducting kinetic measurements is to ensure all data is collected sufficiently far from equilibrium. Conducting experiments away from equilibrium will ensure one measures the kinetic effects of changing feed conditions when conducting experiments over a fixed length catalyst bed.

To determine the “closeness” to equilibrium for the complete data set for kinetic modelling, one can compare the ratio of the partial pressures of the products to reactants $\left(\frac{P_{CO_2} \cdot P_{H_2}}{P_{CO} \cdot P_{H_2O}}\right)$ to the equilibrium constant (K_{eq}) at each temperature. This comparison is depicted in Figure 5.9. It

should be noted that only the experiments forming part of the ‘complete data set’ (see section 5.2.3) have been depicted in Figure 5.9.

In Figure 5.9, the experiments have been grouped by temperature. A ratio of 1 would indicate that the experiment was conducted at equilibrium. As seen in Figure 5.9, the largest ratio calculated is below 0.4 with most of the experiments being conducted under conditions such that the ratio is below 0.2. It can be said that the experiments were conducted away from equilibrium (Kalamaras et al., 2009:120; Ma et al., 2016:55).

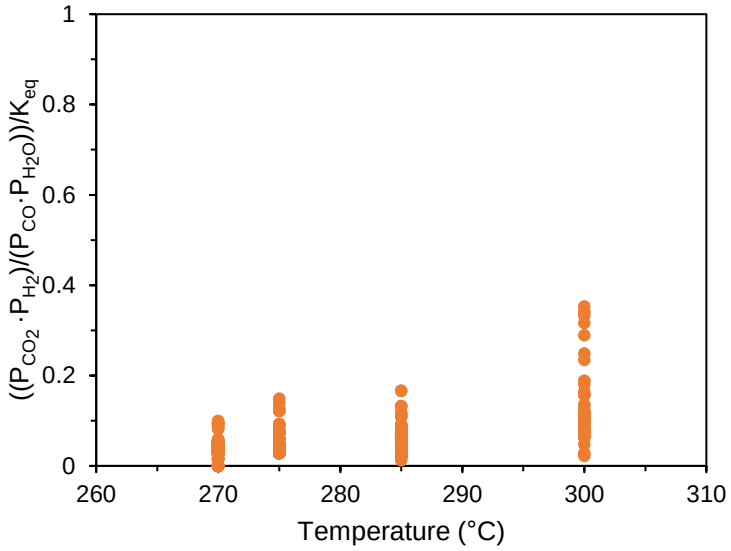

Figure 5.9: Comparison of the partial pressures of products to reactants to the equilibrium constant for both sets of kinetic experiments

6. Kinetic Model Fitting Results

6.1. Model Validation

In this study, the gPROMS software package was used to fit experimental data to different types of rate equations. A packed-bed reactor model was used to describe the reactor (see Chapter 4.8). To validate the gPROMS model used, the parameters of the power-rate law empirical equations reported by Grabow et al. (2008:4614) and Kalamaras et al. (2009:121) were re-estimated. This was achieved by fitting a power-rate law equation (Equation 2.3) to the data sets reported by Grabow et al. (2008:data set) and Kalamaras et al. (2009:data set). A comparison of the parameters estimated using the gPROMS model to those reported by Grabow et al. (2008:4614) and Kalamaras et al. (2009:121) are presented in Table 6.1 and Table 6.2 respectively.

In Equation 2.3, r is the reaction rate [units as defined under experimental conditions], k_0 is the reaction rate constant [units dependent on other variables], Ea is the activation energy of the reaction [kJ·mol^{-1}], R is the gas constant [8.314 J·mol^{-1}·K^{-1}], T is the reaction temperature [K], P_i is the partial pressure of component i [pressure units], a, b, c and d are the reaction orders of CO, H_2O, CO_2 and H_2 respectively and β is the ratio of partial pressures of products to reactants to the equilibrium constant (K_{eq}), as given in Equation 6.2.

$$r = k_0 \cdot e^{-\frac{Ea \times 1000}{R \cdot T}} \cdot P_{CO}^{a} \cdot P_{H_2O}^{b} \cdot P_{CO_2}^{c} \cdot P_{H_2}^{d} \cdot (1 - \beta) \qquad \text{Equation 6.1}$$

$$\beta = \frac{P_{CO_2} \cdot P_{H_2}}{P_{CO} \cdot P_{H_2O} \cdot K_{eq}} \qquad \text{Equation 6.2}$$

It is seen in Table 6.1 and Table 6.2 that the parameters estimated using gPROMS and the values reported by Grabow et al. (2008:4614) and Kalamaras et al. (2009:121) agree fairly well. In Table 6.1 and Table 6.2, there are 95 % t-values that are smaller than the reference t-value. These t-values are indicated by a *. This indicates that the data used for parameter estimation is not sufficient to estimate these parameters precisely. No correlation was found for the parameters estimated for both data sets. Furthermore, the weighted residual (WR) is greater than the Chi-squared (X^2) value for both estimations. This indicates that the estimated model fit is not a good fit. This, together with the 'failed' t-tests, could suggest that the data sets used for fitting in gPROMS are not sufficient to estimate a good, statistically relevant fit. It should be noted that these results were found based on the data sets that were available/accessible for model validation in gPROMS. These data sets might not represent the complete data sets used by Grabow et al. (2008:data set) and Kalamaras et al. (2009:data set). As such, while certain parameters were found to be statistically irrelevant in this fitting, no conclusions can be drawn on the statistical relevance of the parameters reported by Grabow et al. (2008:4614) and Kalamaras et al. (2009:121).

Table 6.1: Comparison of the gPROMS model fit to the fit reported by Grabow et al. (2008:4614)

Parameter	Reported by Grabow et al. (2008:4614)	Optimal estimate using gPROMS	Standard deviation	95 % t-value
Ea (kJ·mol^{-1})	6.8 x 10^{1}	6.6 x 10^{1}	2 x 10^{7}	1.7 x 10^{-6}*
a	-3.7 x 10^{-1}	-1.6 x 10^{-1}	0.5 x 10^{-1}	1.5 x 10^{0}*
b	7.0 x 10^{-1}	9.4 x 10^{-1}	0.6 x 10^{-1}	7.8 x 10^{0}
c	-0.3 x 10^{-1}	-1.2 x 10^{-1}	0.2 x 10^{-1}	3.7 x 10^{0}
d	-3.9 x 10^{-1}	-4.5 x 10^{-1}	0.2 x 10^{-1}	14 x 10^{0}
			95 % reference t-value	1.7 x 10^{0}
			WR/X^{2}	105/85

Table 6.2: Comparison of the gPROMS model fit to the fit reported by Kalamaras et al. (2009:121)

Parameter	Reported by Kalamaras et al. (2009:121)	Optimal estimate using gPROMS	Standard deviation	95 % t-value
Ea (kJ·mol^{-1})	4.5 x 10^{1}	5.8 x 10^{1}	1.6 x 10^{0}	18 x 10^{0}
a	0.5 x 10^{0}	4.3 x 10^{-1}	0.2 x 10^{-1}	9.3 x 10^{0}
b	1.0 x 10^{0}	9.6 x 10^{-1}	0.8 x 10^{-1}	6.2 x 10^{0}
c	0.0 x 10^{0}	0.1 x 10^{-1}	0.06 x 10^{-2}	1.1 x 10^{0}*
d	-0.7 x 10^{0}	-6.4 x 10^{-1}	0.2 x 10^{-1}	20 x 10^{0}
			95 % reference t-value	1.7 x 10^{0}
			WR/X^{2}	98/97

6.2. Evaluation of the Water-Gas Shift Reaction Kinetics (Paper Study)

An initial evaluation of water-gas shift (WGS) reaction kinetics was conducted by fitting various Langmuir-Hinshelwood (LH) type mechanisms to two data sets from literature. The results of this initial evaluation showed the strengths and weaknesses of different kinetic expressions and was thus used to determine the most likely mechanism to be occurring. The literature data sets used come from Grabow et al. (2008:data set) and Kalamaras et al. (2009:data set). The data set from Grabow et al. (2008:data set) was collected over a 3 wt% Pt/Al_2O_3 catalyst while the data set from Kalamaras et al. (2009:data set) was collected over a 0.5 wt% Pt/TiO_2 catalyst.

During the model fitting procedure, the activation energy (Ea) values reported by Grabow et al. (2008:4614) and Kalamaras et al. (2009:121) were fixed. The heats of adsorption for CO, H_2O, CO_2 and H_2 were also fixed. The values fixed for the heats of adsorption come from Thinon et al. (2009:1943) and are as follows: ΔH_{ads}^{CO} = -90 kJ·mol^{-1}, $\Delta H_{ads}^{H_2O}$ = -55 kJ·mol^{-1}, $\Delta H_{ads}^{CO_2}$ = -67 kJ·mol^{-1} and $\Delta H_{ads}^{H_2}$ = -110 kJ·mol^{-1}. These heats of adsorption values were estimated over a 1 wt% Pt/CeO_2 catalyst. By fixing these parameters, less parameters will have to be estimated during the model fitting process which simplifies the parameter estimation procedure.

The focus of this initial evaluation is on the goodness of fit obtained from different kinetic expressions. As such, this section will present the fits obtained for different models and not focus on the parameter values obtained. In most cases, no statistically relevant parameters could be estimated due to the small data sets used.

To discriminate between rival models, the mean absolute relative residual (MARR) value is used. The MARR value can be used as a measure of the goodness of fit and is calculated according to Equation 6.3, in which r_i is a reaction rate/flow rate datum point with n the size of the data set.

$$MARR\ (\%) = 100 \cdot \sum_{1}^{n} \left| \frac{r_i^{measured} - r_i^{predicted}}{r_i^{measured}} \right| \cdot \frac{1}{n} \qquad \text{Equation 6.3}$$

In the rate equations presented in this section, the rate constant, k, and adsorption constant, K, are expressed as in Equation 6.4 and Equation 6.5 respectively. In these equations, Ea is the activation energy [kJ·mol^{-1}], R is the gas constant [8.314 J·mol^{-1}·K^{-1}], T is the reaction temperature [K], ΔH_{ads} is the heat of adsorption [kJ·mol^{-1}] and k_0 and K_0 are both pre-exponential factors.

$$k = k_0 \cdot e^{-\frac{Ea \times 1000}{R \cdot T}} \qquad \text{Equation 6.4}$$

$$K = K_0 \cdot e^{-\frac{\Delta H_{ads} \times 1000}{R \cdot T}} \qquad \text{Equation 6.5}$$

The different mechanistic cases below have been derived based on the literature reviewed (refer to Chapter 2 section 2.3.4). In the figures below demonstrating the goodness of fit for each case presented in this section, the solid line represents the line y=x. For a perfect fitting model, all data points would lie on this line. The two dashed lines represent a 10 % error.

6.2.1. Case 1

Case 1 takes the form of a dual-site mechanism. In this case, CO adsorbs on site 1 (S1). The adsorbed CO then combines with an O atom on site 2 (S2) to form CO_2 on S1, which desorbs into the gas phase. H_2O then adsorbs on S2 and dissociates to an O atom on S2 and 2 H atoms on 2 S1 sites. The two H atoms then combined and finally desorb to give gaseous H_2. The mechanistic steps describing case 1 are presented in Case 1 Step 1 through Case 1 Step 6 below.

$$CO(g) + S1 \overset{K_1}{\rightleftarrows} CO - S1 \qquad \text{Case 1 Step 1}$$

$$CO - S1 + O - S2 \overset{K_2}{\rightleftarrows} CO_2 - S1 + S2 \qquad \text{Case 1 Step 2}$$

$$CO_2(g) + S1 \overset{K_3}{\rightleftarrows} CO_2 - S1 \qquad \text{Case 1 Step 3}$$

$$H_2O(g) + S2 \overset{K_4}{\rightleftarrows} H_2O - S2 \qquad \text{Case 1 Step 4}$$

$$H_2O - S2 + 2S1 \overset{K_5}{\rightleftarrows} O - S2 + 2H - S1 \qquad \text{Case 1 Step 5}$$

$$H_2(g) + 2S1 \overset{K_6}{\rightleftarrows} 2H - S1 \qquad \text{Case 1 Step 6}$$

Three different rate determining steps (RDS), based on what has been suggested in literature (see section 2.3.4.4), will be tested: step 2 (the formation of adsorbed CO_2), step 4 (adsorption of H_2O) and step 5 (dissociation of H_2O). The rate equations corresponding to the RDS listed are given below. As an example, the derivation of the rate equation when step 2 is assumed to be rate limiting is shown in Appendix G.

$$r_{case\ 1,RDS\ 2} = \frac{k \cdot \left(\frac{K_1 \cdot K_4 \cdot K_5}{K_6}\right) \cdot \left(\frac{P_{CO} \cdot P_{H_2O}}{P_{H_2}} - \frac{P_{CO_2}}{K_{Eq}}\right)}{\left(1 + K_1 \cdot P_{CO} + K_3 \cdot P_{CO_2} + \sqrt{K_6 \cdot P_{H_2}}\right) \cdot \left(1 + \frac{K_4 \cdot K_5}{K_6} \cdot \frac{P_{H_2O}}{P_{H_2}} + K_4 \cdot P_{H_2O}\right)} \qquad \text{Case 1 RDS 2}$$

$$r_{case\ 1,RDS\ 4} = \frac{k \cdot \left(P_{H_2O} - \frac{P_{CO_2} \cdot P_{H_2}}{P_{CO} \cdot K_{Eq}}\right)}{1 + \frac{K_3}{K_1 \cdot K_2} \cdot \frac{P_{CO_2}}{P_{CO}} + \frac{K_3 \cdot K_6}{K_1 \cdot K_2 \cdot K_5} \cdot \frac{P_{CO_2} \cdot P_{H_2}}{P_{CO}}} \qquad \text{Case 1 RDS 4}$$

$$r_{case\ 1,RDS\ 5} = \frac{k \cdot K_4 \cdot \left(P_{H_2O} - \frac{P_{CO_2} \cdot P_{H_2}}{P_{CO} \cdot K_{Eq}}\right)}{\left(1 + K_1 \cdot P_{CO} + K_3 \cdot P_{CO_2} + \sqrt{K_6 \cdot P_{H_2}}\right)^2 \cdot \left(1 + \frac{K_3}{K_1 \cdot K_2} \cdot \frac{P_{CO_2}}{P_{CO}} + K_4 \cdot P_{H_2O}\right)} \qquad \text{Case 1 RDS 5}$$

The fits of the three rate equations for case 1 to the literature data are presented in the following three figures. The MARR values for all fits are given in Table 6.1.

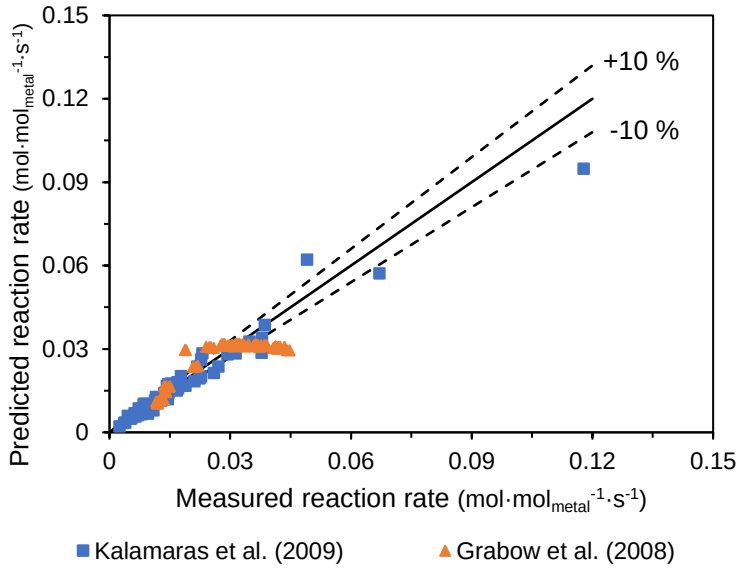

Figure 6.1: Comparison between experimentally measured reaction rates (Grabow et al.,2008; Kalamaras et al., 2009) and predicted reaction rates from Case 1 RDS 2

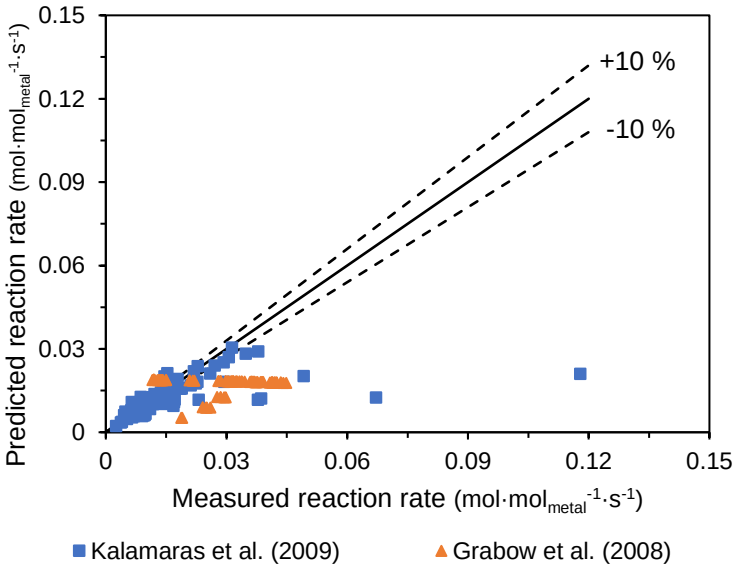

Figure 6.2: Comparison between experimentally measured reaction rates (Grabow et al.,2008; Kalamaras et al., 2009) and predicted reaction rates from Case 1 RDS 4

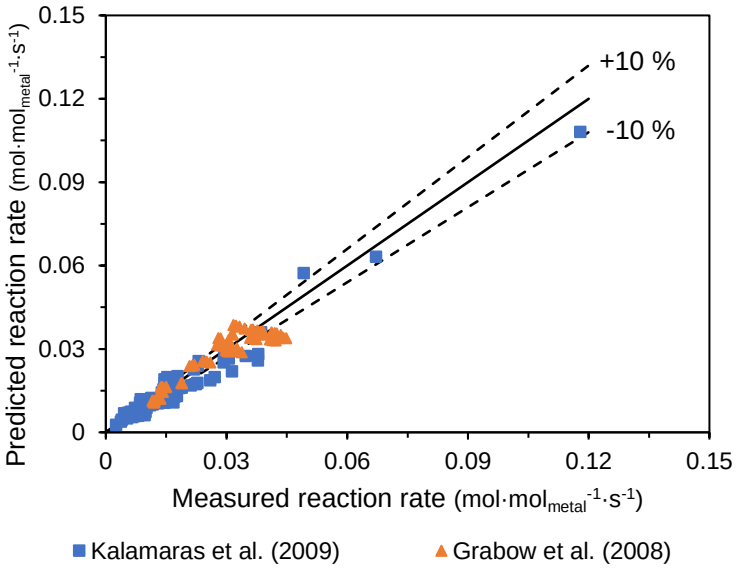

Figure 6.3: Comparison between experimentally measured reaction rates (Grabow et al.,2008; Kalamaras et al., 2009) and predicted reaction rates from Case 1 RDS 5

Table 6.3: Comparison of model predictions for Case 1

Rate Expression	MARR value for fit to Grabow et al. (2008) data set	MARR value for fit to Kalamaras et al. (2009) data set
Case 1 RDS 2	10	8.5
Case 1 RDS 4	34	18
Case 1 RDS 5	7	13

6.2.2. Case 2

Case 2 takes on the same mechanistic steps as case 1, except for only one active site being available. The mechanistic steps describing case 2 are presented in Case 2 Step 1 through Case 2 Step 6 below.

$$CO(g) + S1 \overset{K_1}{\rightleftarrows} CO - S1 \qquad \text{Case 2 Step 1}$$

$$CO - S1 + O - S1 \overset{K_2}{\rightleftarrows} CO_2 - S1 + S1 \qquad \text{Case 2 Step 2}$$

$$CO_2(g) + S1 \overset{K_3}{\rightleftarrows} CO_2 - S1 \qquad \text{Case 2 Step 3}$$

$$H_2O(g) + S1 \overset{K_4}{\rightleftarrows} H_2O - S1 \qquad \text{Case 2 Step 4}$$

$$H_2O - S1 + 2S1 \overset{K_5}{\rightleftarrows} O - S1 + 2H - S1 \qquad \text{Case 2 Step 5}$$

$$H_2(g) + 2S1 \overset{K_6}{\rightleftarrows} 2H - S1 \qquad \text{Case 2 Step 6}$$

As for Case 1, step 2 (the formation of adsorbed CO_2), step 4 (adsorption of H_2O) and step 5 (dissociation of H_2O) will be tested for as the rate determining step. The rate equations corresponding to the respective RDS listed are given below.

$$r_{case\ 2,RDS\ 2} = \frac{k \cdot \left(\frac{K_1 \cdot K_4 \cdot K_5}{K_6}\right) \cdot \left(\frac{P_{CO} \cdot P_{H_2O}}{P_{H_2}} - \frac{P_{CO_2}}{K_{Eq}}\right)}{\left(1 + K_1 \cdot P_{CO} + K_3 \cdot P_{CO_2} + K_4 \cdot P_{H_2O} + \frac{K_4 \cdot K_5}{K_6} \cdot \frac{P_{H_2O}}{P_{H_2}} + \sqrt{K_6 \cdot P_{H_2}}\right)^2} \quad \text{Case 2 RDS 2}$$

$$r_{case\ 2,RDS\ 4} = \frac{k \cdot \left(P_{H_2O} - \frac{P_{CO_2} \cdot P_{H_2}}{P_{CO} \cdot K_{Eq}}\right)}{1 + K_1 \cdot P_{CO} + K_3 \cdot P_{CO_2} + \frac{K_3}{K_1 \cdot K_2} \cdot \frac{P_{CO_2}}{P_{CO}} + \frac{K_3 \cdot K_6}{K_1 \cdot K_2 \cdot K_5} \cdot \frac{P_{CO_2} \cdot P_{H_2}}{P_{CO}} + \sqrt{K_6 \cdot P_{H_2}}} \quad \text{Case 2 RDS 4}$$

$$r_{case\ 2,RDS\ 5} = \frac{k \cdot K_4 \cdot \left(P_{H_2O} - \frac{P_{CO_2} \cdot P_{H_2}}{P_{CO} \cdot K_{Eq}}\right)}{\left(1 + K_1 \cdot P_{CO} + K_3 \cdot P_{CO_2} + K_4 \cdot P_{H_2O} + \frac{K_3}{K_1 \cdot K_2} \cdot \frac{P_{CO_2}}{P_{CO}} + \sqrt{K_6 \cdot P_{H_2}}\right)^3} \quad \text{Case 2 RDS 5}$$

The fits of the three rate equations for case 2 to the literature data are presented in the following three figures. The MARR values for all fits are given in Table 6.4.

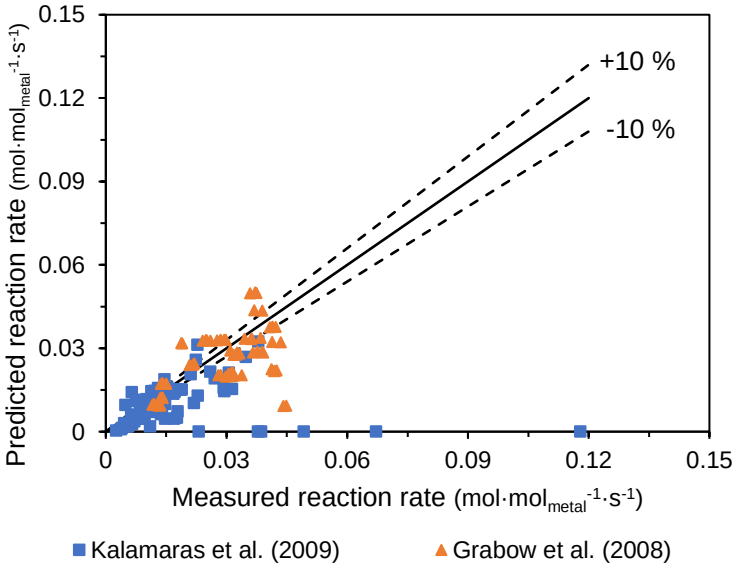

Figure 6.4: Comparison between experimentally measured reaction rates (Grabow et al.,2008; Kalamaras et al., 2009) and predicted reaction rates from Case 2 RDS 2

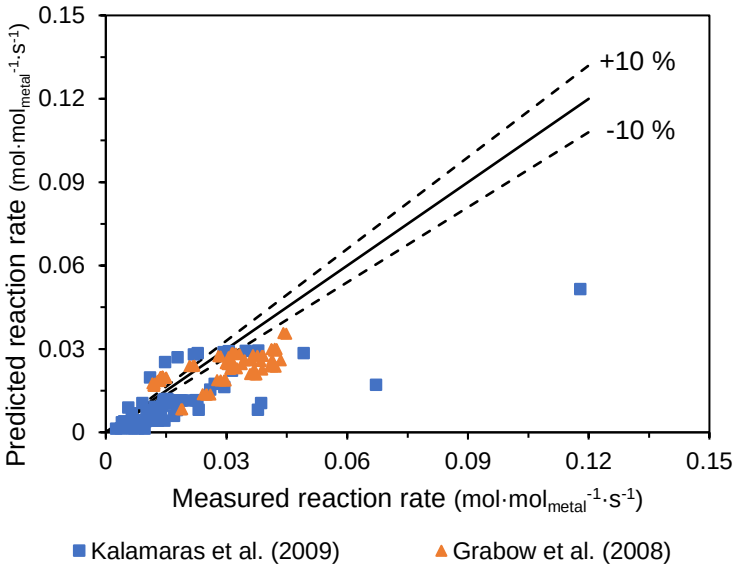

Figure 6.5: Comparison between experimentally measured reaction rates (Grabow et al.,2008; Kalamaras et al., 2009) and predicted reaction rates from Case 2 RDS 4

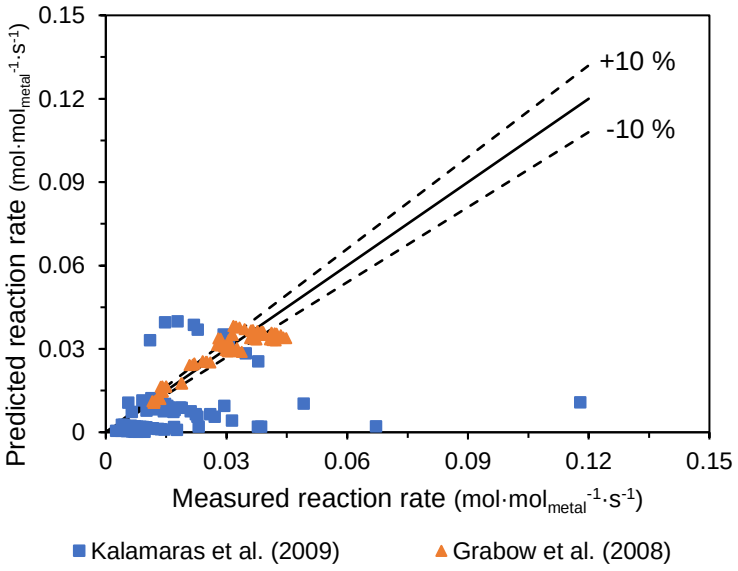

Figure 6.6: Comparison between experimentally measured reaction rates (Grabow et al.,2008; Kalamaras et al., 2009) and predicted reaction rates from Case 2 RDS 5

Table 6.4: Comparison of model predictions for Case 2

Rate Expression	MARR value for fit to Grabow et al. (2008) data set	MARR value for fit to Kalamaras et al. (2009) data set
Case 2 RDS 2	18	29
Case 2 RDS 4	23	37
Case 2 RDS 5	7	57

6.2.3. Case 3

Case 3 follows similar mechanistic steps to case 1, with the exception that CO_2 adsorbs on S2 instead of S1. The mechanistic steps describing case 3 are presented in Case 3 Step 1 through Case 3 Step 6 below.

$$CO(g) + S1 \overset{K_1}{\rightleftarrows} CO - S1 \qquad \text{Case 3 Step 1}$$

$$CO - S1 + O - S2 \overset{K_2}{\rightleftarrows} CO_2 - S2 + S1 \qquad \text{Case 3 Step 2}$$

$$CO_2(g) + S2 \overset{K_3}{\rightleftarrows} CO_2 - S2 \qquad \text{Case 3 Step 3}$$

$$H_2O(g) + S2 \overset{K_4}{\rightleftarrows} H_2O - S2 \qquad \text{Case 3 Step 4}$$

$$H_2O - S2 + 2S1 \overset{K_5}{\rightleftarrows} O - S2 + 2H - S1 \qquad \text{Case 3 Step 5}$$

$$H_2(g) + 2S1 \overset{K_6}{\rightleftarrows} 2H - S1 \qquad \text{Case 3 Step 6}$$

As for case 1 and case 2, step 2 (the formation of adsorbed CO_2), step 4 (adsorption of H_2O) and step 5 (dissociation of H_2O) will be tested for as the rate determining step. The rate equations corresponding to the respective RDS listed are given below.

$$r_{case\ 3,RDS\ 2} = \frac{k \cdot \left(\frac{K_1 \cdot K_4 \cdot K_5}{K_6}\right) \cdot \left(\frac{P_{CO} \cdot P_{H_2O}}{P_{H_2}} - \frac{P_{CO_2}}{K_{Eq}}\right)}{\left(1 + K_1 \cdot P_{CO} + \sqrt{K_6 \cdot P_{H_2}}\right) \cdot \left(1 + K_3 \cdot P_{CO_2} + \frac{K_4 \cdot K_5}{K_6} \cdot \frac{P_{H_2O}}{P_{H_2}} + K_4 \cdot P_{H_2O}\right)} \qquad \text{Case 3 RDS 2}$$

$$r_{case\ 3,RDS\ 4} = \frac{k \cdot \left(P_{H_2O} - \frac{P_{CO_2} \cdot P_{H_2}}{P_{CO} \cdot K_{Eq}}\right)}{1 + \frac{K_3}{K_1 \cdot K_2} \cdot \frac{P_{CO_2}}{P_{CO}} + \frac{K_3 \cdot K_6}{K_1 \cdot K_2 \cdot K_5} \cdot \frac{P_{CO_2} \cdot P_{H_2}}{P_{CO}} + K_3 \cdot P_{CO_2}} \qquad \text{Case 3 RDS 4}$$

$$r_{case\ 3,RDS\ 5} = \frac{k \cdot K_4 \cdot \left(P_{H_2O} - \frac{P_{CO_2} \cdot P_{H_2}}{P_{CO} \cdot K_{Eq}}\right)}{\left(1 + K_1 \cdot P_{CO} + \sqrt{K_6 \cdot P_{H_2}}\right) \cdot \left(1 + K_3 \cdot P_{CO_2} + \frac{K_3}{K_1 \cdot K_2} \cdot \frac{P_{CO_2}}{P_{CO}} + K_4 \cdot P_{H_2O}\right)} \qquad \text{Case 3 RDS 5}$$

The fits of the three rate equations for case 3 to the literature data are presented in the following three figures. The MARR values for all fits are given in Table 6.5.

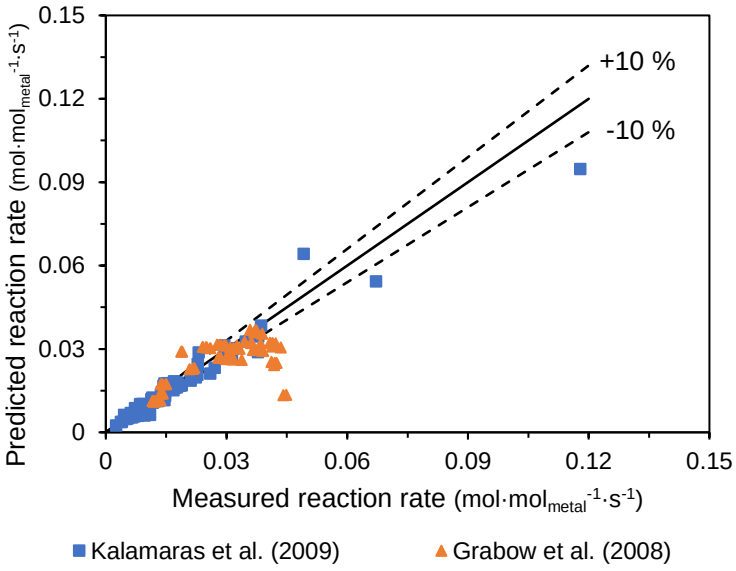

Figure 6.7: Comparison between experimentally measured reaction rates (Grabow et al.,2008; Kalamaras et al., 2009) and predicted reaction rates from Case 3 RDS 2

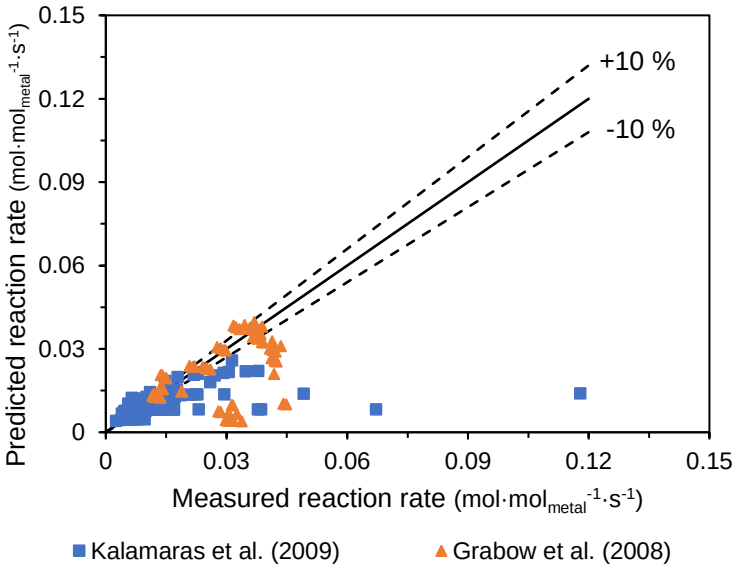

Figure 6.8: Comparison between experimentally measured reaction rates (Grabow et al.,2008; Kalamaras et al., 2009) and predicted reaction rates from Case 3 RDS 4 rate expression

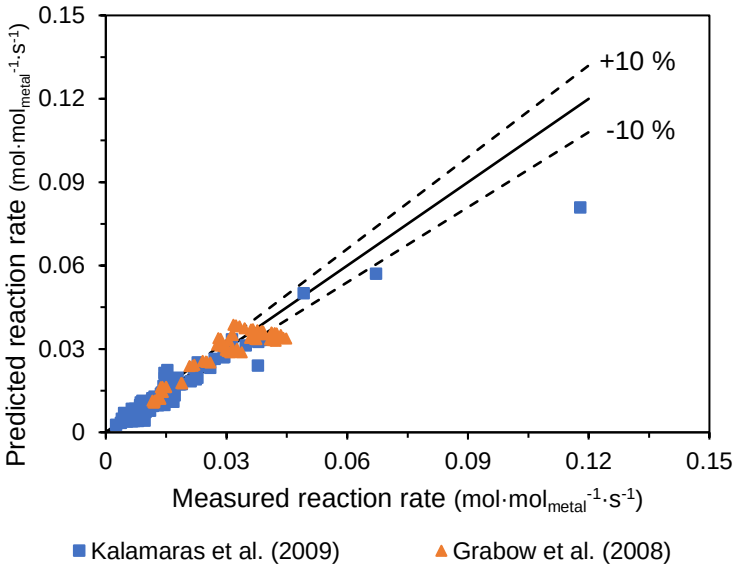

Figure 6.9: Comparison between experimentally measured reaction rates (Grabow et al.,2008; Kalamaras et al., 2009) and predicted reaction rates from Case 3 RDS 5

Table 6.5: Comparison of model predictions for Case 3

Rate Expression	**MARR value for fit to Grabow et al. (2008) data set**	**MARR value for fit to Kalamaras et al. (2009) data set**
Case 3 RDS 2	12	9
Case 3 RDS 4	20	24
Case 3 RDS 5	7	13

6.2.4. Case 4

Case 4 takes the form of a dual-site mechanism, in which H_2O adsorbs on S2. The adsorbed H_2O then dissociates into OH on S2 and H on S1. CO adsorbs on S1. The CO adsorbed on S1 and OH on S2 then combined to form a COOH intermediate on S2. The intermediate then decomposes into CO_2 on S2 and H on S1. Two H atoms form H_2 and desorb into the gaseous phase. CO_2 desorbs into the gaseous phase. The mechanistic steps describing case 4 are presented in Case 4 Step 1 through Case 4 Step 7 below.

$$H_2O(g) + S2 \overset{K_1}{\rightleftarrows} H_2O - S2 \qquad \text{Case 4 Step 1}$$

$$H_2O - S2 + S1 \overset{K_2}{\rightleftarrows} OH - S2 + H - S1 \qquad \text{Case 4 Step 2}$$

$$CO(g) + S1 \overset{K_3}{\rightleftarrows} CO - S1 \qquad \text{Case 4 Step 3}$$

$$CO - S1 + OH - S2 \overset{K_4}{\rightleftarrows} COOH - S2 + S1$$ Case 4 Step 4

$$COOH - S2 + S1 \overset{K_5}{\rightleftarrows} H - S1 + CO_2 - S2$$ Case 4 Step 5

$$H_2(g) + 2 - S1 \overset{K_6}{\rightleftarrows} 2H - S1$$ Case 4 Step 6

$$CO_2(g) + S2 \overset{K_7}{\rightleftarrows} CO_2 - S2$$ Case 4 Step 7

Three rate determining steps will be determined. These steps include step 2 (formation of OH on S2 and H on S1), step 4 (formation of COOH intermediate) and step 5 (decomposition of COOH intermediate). The rate equations corresponding to the RDS listed are given below.

$$r_{case\ 4,RDS\ 2} = \frac{k \cdot K_1 \cdot \left(P_{H_2O} - \frac{P_{CO_2} \cdot P_{H_2}}{P_{CO} \cdot K_{Eq}}\right)}{\left(1 + K_3 \cdot P_{CO} + \sqrt{K_6 \cdot P_{H_2}}\right) \cdot \left(1 + K_1 \cdot P_{H_2O} + K_7 \cdot P_{CO_2} + \frac{K_7 \cdot \sqrt{K_6}}{K_3 \cdot K_4 \cdot K_5} \cdot \frac{P_{CO_2} \cdot \sqrt{P_{H_2}}}{P_{CO}} + \frac{K_7 \cdot \sqrt{K_6}}{K_5} \cdot P_{CO_2} \cdot \sqrt{P_{H_2}}\right)}$$

Case 4 RDS 2

$$r_{case\ 4,RDS\ 4} = \frac{k \cdot K_1 \cdot K_2 \cdot K_3 \cdot \left(P_{CO} \cdot P_{H_2O} - \frac{P_{CO_2} \cdot P_{H_2}}{K_{Eq}}\right)}{\left(1 + K_3 \cdot P_{CO} + \sqrt{K_6 \cdot P_{H_2}}\right) \cdot \left(\sqrt{K_6 \cdot P_{H_2}} + K_1 \cdot \sqrt{K_6} \cdot P_{H_2O} \cdot \sqrt{P_{H_2}} + K_7 \cdot \sqrt{K_6} \cdot P_{CO_2} \cdot \sqrt{P_{H_2}} + K_1 \cdot K_2 \cdot P_{H_2O} + \frac{K_7 \cdot K_6}{K_5} \cdot P_{CO_2} \cdot P_{H_2}\right)}$$

Case 4 RDS 4

$$r_{case\ 4,RDS\ 5} = \frac{k \cdot K_1 \cdot K_2 \cdot K_3 \cdot K_4 \cdot \left(P_{CO} \cdot P_{H_2O} - \frac{P_{CO_2} \cdot P_{H_2}}{K_{Eq}}\right)}{\left(1 + K_3 \cdot P_{CO} + \sqrt{K_6 \cdot P_{H_2}}\right) \cdot \left(\sqrt{K_6 \cdot P_{H_2}} + K_1 \cdot \sqrt{K_6} \cdot P_{H_2O} \cdot \sqrt{P_{H_2}} + K_7 \cdot \sqrt{K_6} \cdot P_{CO_2} \cdot \sqrt{P_{H_2}} + K_1 \cdot K_2 \cdot P_{H_2O} + K_1 \cdot K_2 \cdot K_3 \cdot K_4 \cdot P_{CO} \cdot P_{H_2O}\right)}$$

Case 4 RDS 5

The fits of the three rate equations for case 4 to the literature data are presented in the following three figures. The MARR values for all fits are given in Table 6.6.

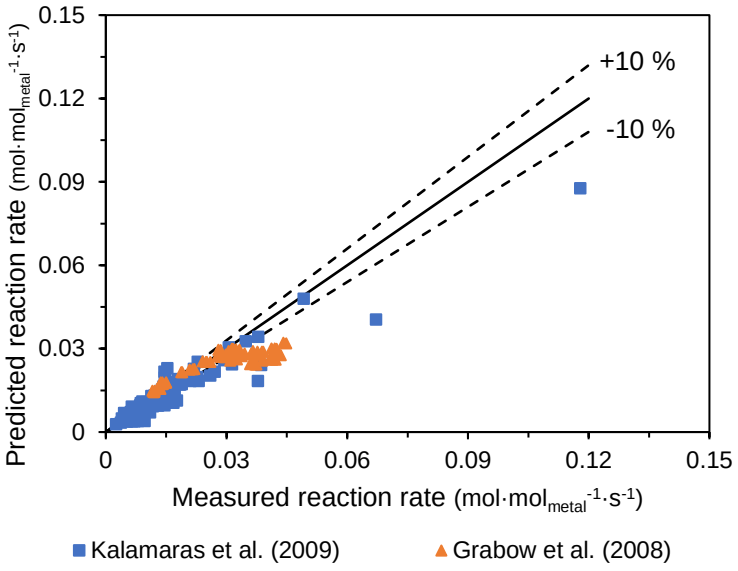

Figure 6.10: Comparison between experimentally measured reaction rates (Grabow et al.,2008; Kalamaras et al., 2009) and predicted reaction rates from Case 4 RDS 2

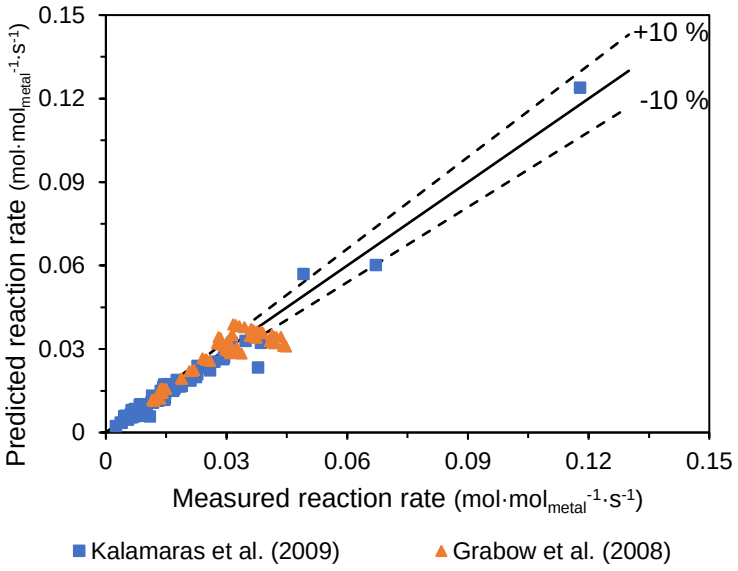

Figure 6.11: Comparison between experimentally measured reaction rates (Grabow et al.,2008; Kalamaras et al., 2009) and predicted reaction rates from Case 4 RDS 4

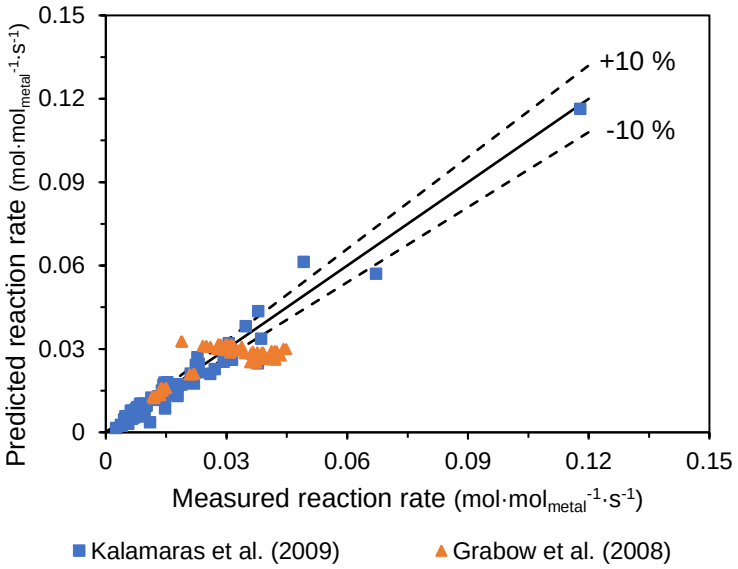

Figure 6.12: Comparison between experimentally measured reaction rates (Grabow et al.,2008; Kalamaras et al., 2009) and predicted reaction rates from Case 4 RDS 5

Table 6.6: Comparison of model predictions for Case 4

Rate Expression	MARR value for fit to Grabow et al. (2008) data set	MARR value for fit to Kalamaras et al. (2009) data set
Case 4 RDS 2	13	16
Case 4 RDS 4	7	9
Case 4 RDS 5	12	12

6.2.5. Initial Evaluation Findings

The findings of the initial evaluation of the kinetic models would suggest that the mechanism represented by case 4 is most likely to be occurring. For this mechanism, assuming mechanistic step 4 to be rate determining gave the best fitting rate equation.

6.3. Evaluation of Water-Gas Shift Reaction Kinetics from Experimental Measurements

In addition to the initial evaluation of the WGS kinetics, an evaluation was also performed using the experimental data collected during this study (refer to Chapter 5.2). The models used for this evaluation builds on the findings of the initial evaluation. The results of the evaluation of the kinetic models to the experimental data are presented in this section.

To discriminate between rival models, the WR and MARR values are reported. In the figures demonstrating the goodness of fit for each case presented in this section, the solid line represents the line y=x. For a perfect fitting model, all data points would lie on this line. The two dashed lines represent a 10 % error.

6.3.1. Power-Rate Law Empirical Equation

The power-rate law equation (Equation 2.3) was fitted to the experimental data. The results of the fitting are presented in Table 6.7 and the correlation matrix is given in Table 6.8. The fit of the power-rate law to the experimental data is presented in Figure 6.13.

It is seen in Table 6.7 that WR is less than the X^2 value. This indicates that the power-rate law can model the experimental data well. It is also seen that the 95 % t-values are all greater than the reference t-value. The correlation matrix presented in Table 6.8 shows no correlation between any of the estimated parameters.

Table 6.7: Results of fitting the power-rate law equation to the experimental data

Parameter	Optimal estimate	Standard deviation	95 % confidence interval	95 % t-value
k_0 ($\mu mol \cdot mg_{cat}^{-1} \cdot s^{-1}$)	2.3×10^{-4}	3.6×10^{-5}	7.0×10^{-5}	3.3×10^{0}
Ea ($kJ \cdot mol^{-1}$)	1.2×10^{2}	2.8×10^{0}	5.5×10^{0}	2.1×10^{1}
a	1.1×10^{-1}	2.7×10^{-2}	5.3×10^{-2}	2.0×10^{0}*
b	8.2×10^{-1}	7.7×10^{-2}	1.5×10^{-1}	5.5×10^{0}
c	-2.8×10^{-1}	6.9×10^{-2}	1.4×10^{-1}	2.0×10^{0}
d	-6.9×10^{-1}	8.1×10^{-2}	1.6×10^{-1}	4.3×10^{0}
			95 % reference t-value	1.6×10^{0}
			WR/X^2	140/1951
			MARR	2.0

Table 6.8: Correlation matrix for the fit of the power-rate law to the experimental data

Parameter	Parameter Number	1	2	3	4	5	6
a	**1**	1					
b	**2**	0.07	1				
c	**3**	-0.14	-0.09	1			
d	**4**	-0.08	-0.10	0.07	1		
Ea (kJ·mol^{-1})	**5**	0.34	0.18	-0.11	0.06	1	
k_0 (µmol·mg$_{cat}^{-1}$·s^{-1})	**6**	0.26	0.18	0.81	0.18	-0.23	1

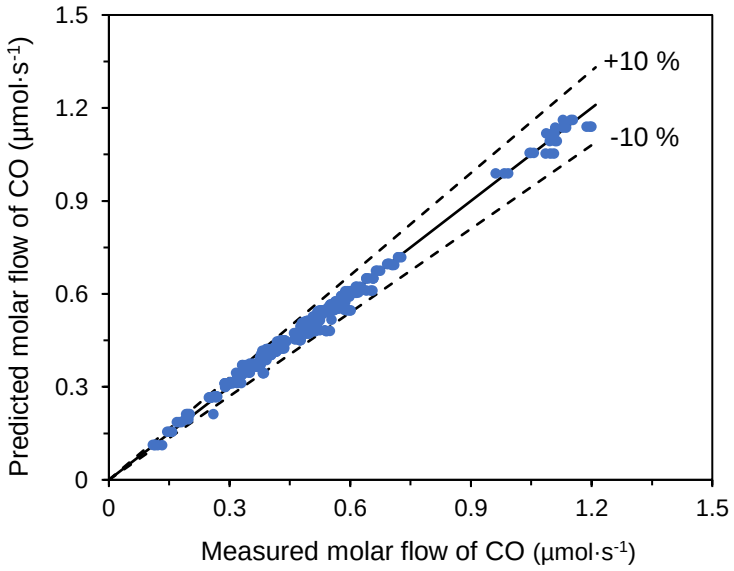

Figure 6.13: Comparison between experimentally measured CO molar flow rates (µmol·s^{-1}) and power-rate law predicted CO molar flow rates (µmol·s^{-1})

6.3.1.1. *Confirmation of Activation Energy*

To confirm the value of the activation energy found when fitting the power-rate law equation to the experimental data, the activation was calculated by a classical Arrhenius analysis. A plot of $ln(k)$, vs. $\frac{1}{T}$, where k is the reaction rate constant and T is temperature, will yield a plot with slope equal to $-\frac{Ea}{R}$ (Scott Fogler, 2006:95). This type of plot is referred to as an Arrhenius plot and is seen in Figure 6.14.

As seen in Figure 6.14, the slope of the plot is equal to -13 512 K. This corresponds to an activation energy of 110 kJ·mol^{-1}, which agrees with the value of 120 kJ·mol^{-1} found above.

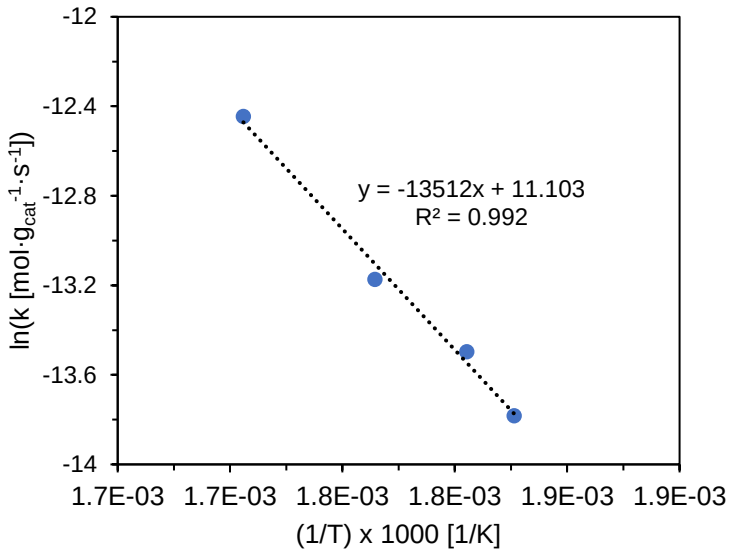

Figure 6.14: Arrhenius plot for calculating activation energy

6.3.2. Langmuir-Hinshelwood Type Rate Expressions

The fitting of LH type rate expressions builds on the findings of the initial evaluation (presented above). As such, the mechanistic steps given in case 4 will be considered as this mechanism was determined to be most likely occurring in the initial evaluation of the WGS reaction kinetics. Since the rate equation given from RDS 4 gave the best fit in case 4, this rate equation will be used as the starting point for this fitting.

In this section, the activation energy was fixed at 110 kJ·mol^{-1}, which is the value found by the classical Arrhenius analysis. As for the initial evaluation of kinetic models, the heats of adsorption for CO, H_2O, CO_2 and H_2 were fixed at the values mentioned before unless otherwise stated.

6.3.2.1. *Case 5*

Case 5 involves fitting the rate equation from case 4 RDS 4 to the experimental data. The results of the fitting are presented in Table 6.9 and the correlation matrix found is presented in Table 6.10. The parameters shaded in grey in Table 6.9 were fixed during the model fitting (i.e. they were not estimated). The correlation matrix only considers parameters that were estimated during the fitting. The fit of $r_{case4,\ RDS\ 4}$ to the experimental data is presented in Figure 6.15

As seen by the WR and X^2 value in Table 6.9, the model predicts the experimental data well. It is also seen that t-values for all parameters except k_3 are smaller than the reference t-value.

This indicates that the number and range of data points is not sufficient to estimate these parameters precisely.

The correlation matrix in Table 6.10 shows correlation between k_5 and $Ea_{step\ 5}$, and k_1 and k_2.

Table 6.9: Results of model fitting in case 5

Parameter	**Optimal estimate**	**Standard deviation**	**95 % confidence interval**	**95 % t-value**
k_0 (µmol·mg_{cat}^{-1}·s^{-1})	2.2 X 10^{-2}	8.2 X 10^{-2}	1.6 X 10^{-1}	1.4 X 10^{-1}
Ea (kJ·mol^{-1})	1.1 X 10^{2}			
K_1 (bar^{-1})	1.4 X 10^{-2}	3.1 X 10^{1}	6.1 X 10^{1}	2.4 X 10^{-4}
$\Delta H_{ads}^{H_2O}$ (kJ·mol^{-1})	-5.5 X 10^{1}			
K_2 (bar-1)	3.3 X 10^{-3}	7.2 X 10^{0}	1.4 X 10^{1}	2.4 X 10^{-4}
$Ea_{step\ 2}$ (kJ·mol^{-1})	2.7 X 10^{1}	1.8 X 10^{1}	3.5 X 10^{1}	7.7 X 10^{-1}
K_3 (bar^{-1})	3.5 X 10^{1}	8.7 X 10^{0}	1.7 X 10^{1}	2.1 X 10^{0}
ΔH_{ads}^{CO} (kJ·mol^{-1})	-9.0 X 10^{1}			
K_5 (bar^{-1})	1.4 X 10^{2}	1.2 X 10^{13}	2.4 X 10^{13}	6.1 X 10^{-12}
$Ea_{step\ 5}$ (kJ·mol^{-1})	6.4 X 10^{2}	6.7 X 10^{12}	1.3 X 10^{13}	4.9 X 10^{-11}
K_6 (bar^{-1})	1.0 X 10^{-9}	Optimal value at estimation bounds		
$\Delta H_{ads}^{H_2}$ (kJ·mol^{-1})	-1.1 X 10^{2}			
K_7 (bar^{-1})	1.0 X 10^{3}	Optimal value at estimation bounds		
$\Delta H_{ads}^{CO_2}$ (kJ·mol^{-1})	-6.7 X 10^{1}			
			95 % reference t-value	1.6 x 10^{0}
			WR/X^2	555/1951
			MARR	3.0

Values shaded in grey were fixed during the model fitting procedure

Table 6.10: Correlation matrix for model fitting in case 5

Parameter	Parameter Number	1	2	3	4	5	6	7
$Ea_{step\ 2}$ (kJ·mol^{-1})	**1**	1.00						
$Ea_{step\ 5}$ (kJ·mol^{-1})	**2**	0.56	1.00					
k_0 (µmol·mg$_{cat}^{-1}$·s^{-1})	**3**	-0.77	-0.15	1.00				
K_3 (bar^{-1})	**4**	-0.25	-0.18	-0.25	1.00			
K_1 (bar^{-1})	**5**	-0.76	-0.24	0.84	-0.01	1.00		
K_2 (bar-1)	**6**	0.76	0.24	-0.84	0.01	-1.00	1.00	
K_5 (bar^{-1})	**7**	-0.54	-1.00	0.14	0.18	0.23	-0.23	1.00

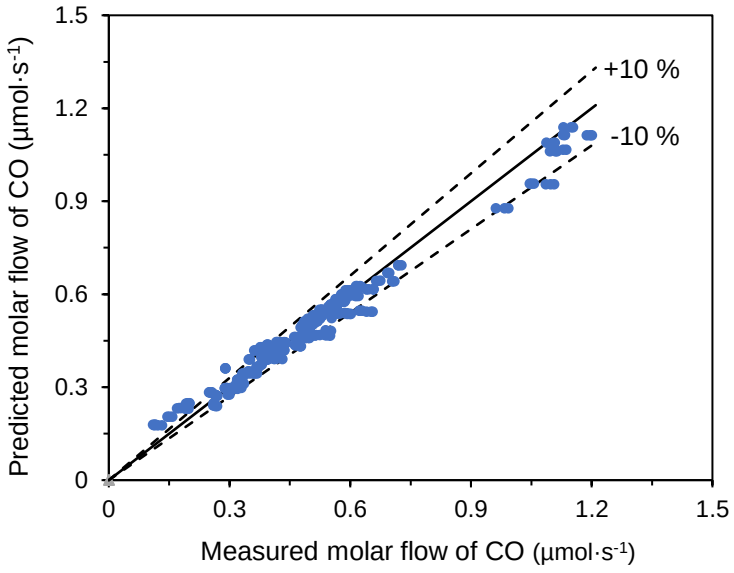

Figure 6.15: Comparison between experimentally measured CO molar flow rates (µmol·s^{-1}) and CO molar flow rates (µmol·s^{-1}) predicted from model fitting in case 5

6.3.2.2. *Case 6*

Case 6 is similar to case 5, with the exception that the heats of adsorption were also estimated during the fitting process. The results of the fitting are presented in Table 6.11. The resulting model fit to the experimental data is presented in Figure 6.16.

As seen in Table 6.11, no statistical analysis was performed. This is due to the solver being unable to derive any statistically relevant information from the experimental data for the

parameters to be estimated. The lack of information from the measured data could indicate that the parameters are highly correlated and/or the system is over-parameterised. Since no statistical analysis was performed, no correlation matrix is presented.

Table 6.11: Results of model fitting in case 6

Parameter	**Optimal estimate**	**Standard deviation**	**95 % confidence interval**	**95 % t-value**
k_0 (µmol·mg_{cat}^{-1}·s^{-1})	9.2 X 10^{-2}			
Ea (kJ·mol^{-1})	1.1 X 10^{2}			
K_1 (bar^{-1})	1.2 X 10^{-2}			
$\Delta H_{ads}^{H_2O}$ (kJ·mol^{-1})	-5.5 X 10^{1}			
K_2 (bar-1)	4.4 X 10^{0}			
$Ea_{step\ 2}$ (kJ·mol^{-1})	8.5 X 10^{1}			
K_3 (bar^{-1})	4.1 X 10^{1}	No statistical analysis due to lack of information from the measured data		
ΔH_{ads}^{CO} (kJ·mol^{-1})	-9.0 X 10^{1}			
K_5 (bar^{-1})	1.3 X 10^{0}			
$Ea_{step\ 5}$ (kJ·mol^{-1})	8.3 X 10^{2}			
K_6 (bar^{-1})	4.2 X 10^{2}			
$\Delta H_{ads}^{H_2}$ (kJ·mol^{-1})	-1.1 X 10^{2}			
K_7 (bar^{-1})	8.9 X 10^{2}			
$\Delta H_{ads}^{CO_2}$ (kJ·mol^{-1})	-6.7 X 10^{1}			
			95 % reference t-value	-
			WR/X^2	-
			MARR	2.9

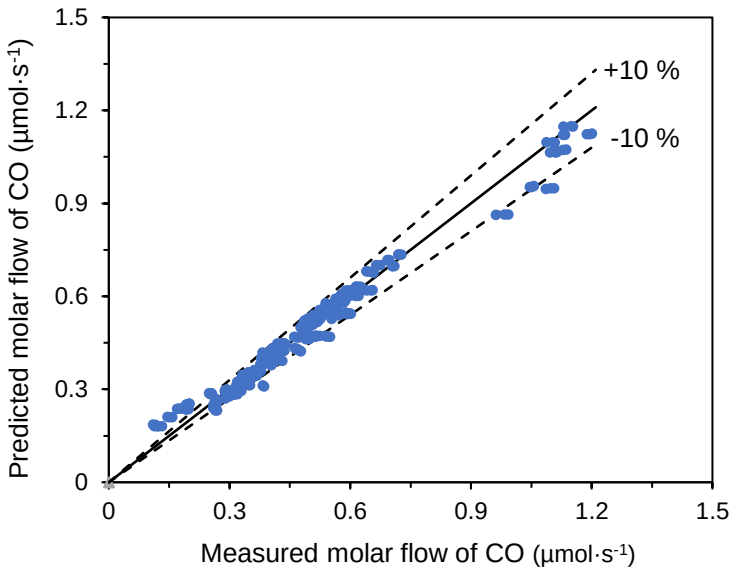

Figure 6.16: Comparison between experimentally measured CO molar flow rates (µmol·s^{-1}) and CO molar flow rates (µmol·s^{-1}) predicted from model fitting in case 6

6.3.2.3. *Case 7*

For case 7, the same mechanistic steps presented for case 4 apply. When deriving the rate equation, the assumption that the adsorption of H_2O, CO_2 and H_2 is negligible compared to the adsorption of CO, OH and COOH is made. Building on what was previously found, step 4 is still assumed to be the rate determining step. The rate equation corresponding to this rate determining step with the assumptions made is shown below.

$$r_{case\ 7} = \frac{k \cdot K_1 \cdot K_2 \cdot K_3 \cdot \left(P_{CO} \cdot P_{H_2O} - \frac{P_{CO_2} \cdot P_{H_2}}{K_{Eq}}\right)}{(1 + K_3 \cdot P_{CO}) \cdot \left(\sqrt{K_6 \cdot P_{H_2}} + K_1 \cdot K_2 \cdot P_{H_2O} + \frac{K_7 \cdot K_6}{K_5} \cdot P_{CO_2} \cdot P_{H_2}\right)} \qquad \text{Case 7}$$

The results of the fitting of $r_{case\ 7}$ to the experimental data is presented in Table 6.12. The resulting model fit to the experimental data is presented in Figure 6.17.

As for case 6, no statistical analysis was performed due to the lack of information from the experimental data.

Table 6.12: Results of model fitting for case 7

Parameter	Optimal estimate	Standard deviation	95 % confidence interval	95 % t-value
k_0 (µmol·mg_{cat}^{-1}·s^{-1})	9.2 X 10^{-2}			
Ea (kJ·mol^{-1})	1.1 X 10^{2}			
K_1 (bar^{-1})	1.2 X 10^{-2}			
$\Delta H_{ads}^{H_2O}$ (kJ·mol^{-1})	-5.5 X 10^{1}			
K_2 (bar-1)	4.4 X 10^{0}			
$Ea_{step\ 2}$ (kJ·mol^{-1})	8.5 X 10^{1}			
K_3 (bar^{-1})	4.1 X 10^{1}	No statistical analysis due to lack of information from the measured data		
ΔH_{ads}^{CO} (kJ·mol^{-1})	-9.0 X 10^{1}			
K_5 (bar^{-1})	1.3 X 10^{0}			
$Ea_{step\ 5}$ (kJ·mol^{-1})	8.3 X 10^{2}			
K_6 (bar^{-1})	4.2 X 10^{2}			
$\Delta H_{ads}^{H_2}$ (kJ·mol^{-1})	-1.1 X 10^{2}			
K_7 (bar^{-1})	8.9 X 10^{2}			
$\Delta H_{ads}^{CO_2}$ (kJ·mol^{-1})	-6.7 X 10^{1}			
			95 % reference t-value	-
			WR/X^2	-
			MARR	2.9

Values shaded in grey were fixed during the model fitting procedure

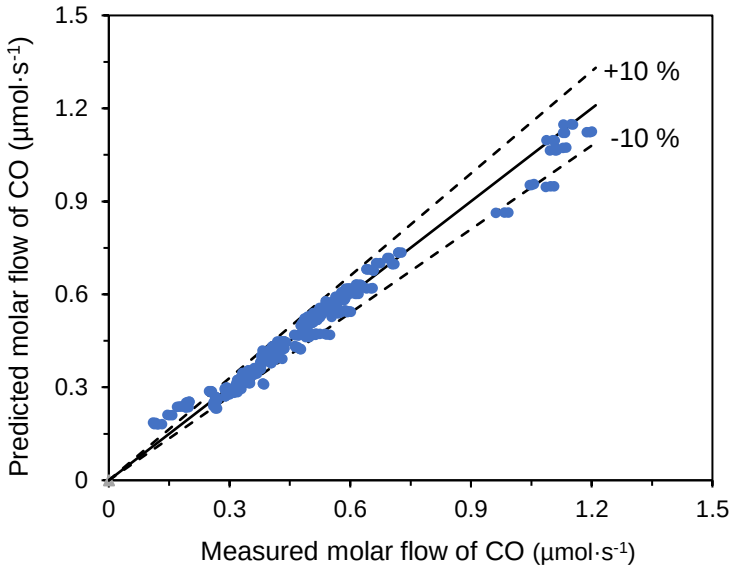

Figure 6.17: Comparison between experimentally measured CO molar flow rates (µmol·s^{-1}) and CO molar flow rates (µmol·s^{-1}) predicted from model fitting in case 7

6.3.2.4. *Case 8*

Case 8 further simplifies case 7 by assuming the adsorption of the COOH intermediate to be negligible. The rate equation incorporating this assumption is given below.

$$r_{case\ 8} = \frac{k \cdot K_1 \cdot K_2 \cdot K_3 \cdot \left(P_{CO} \cdot P_{H_2O} - \frac{P_{CO_2} \cdot P_{H_2}}{K_{Eq}}\right)}{(1 + K_3 \cdot P_{CO}) \cdot \left(\sqrt{K_6 \cdot P_{H_2}} + K_1 \cdot K_2 \cdot P_{H_2O}\right)} \qquad \text{Case 8}$$

The results of the fitting of $r_{case\ 8}$ to the experimental data is presented in Table 6.13. The resulting model fit to the experimental data is presented in Figure 6.18.

As for case 6 and 7, no statistical analysis was performed due to the lack of information from the experimental data.

Table 6.13: Results of model fitting in case 8

Parameter	Optimal estimate	Standard deviation	95 % confidence interval	95 % t-value
k_0 (µmol·mg_{cat}^{-1}·s^{-1})	2.1 X 10^{-3}			
Ea (kJ·mol^{-1})	1.1 X 10^{2}			
K_1 (bar^{-1})	6.8 X 10^{0}			
$\Delta H_{ads}^{H_2O}$ (kJ·mol^{-1})	-5.5 X 10^{1}			
K_2 (bar-1)	1.2 X 10^{-6}	No statistical analysis due to lack of information from the measured data		
$Ea_{step\ 2}$ (kJ·mol^{-1})	1.5 X 10^{1}			
K_3 (bar^{-1})	1.0 X 10^{3}			
ΔH_{ads}^{CO} (kJ·mol^{-1})	-9.0 X 10^{1}			
K_6 (bar^{-1})	2.2 X 10^{-9}			
$\Delta H_{ads}^{H_2}$ (kJ·mol^{-1})	-1.1 X 10^{2}			
			95 % reference t-value	-
			WR/X^2	-
			MARR	2.1

Values shaded in grey were fixed during the model fitting procedure

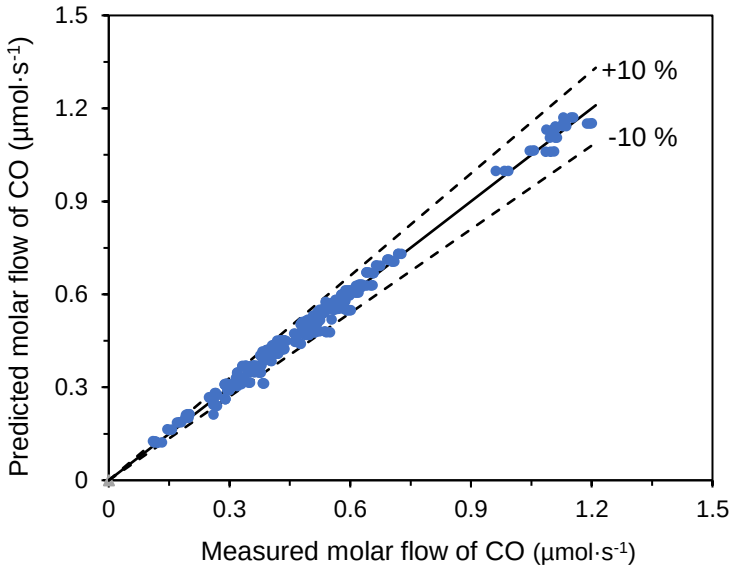

Figure 6.18: Comparison between experimentally measured CO molar flow rates (µmol·s^{-1}) and CO molar flow rates (µmol·s^{-1}) predicted from model fitting in case 8

6.3.2.5. *Case 9*

Case 9 further simplifies case 8 by grouping together constants where possible. The rate equation for case 9 is given below.

$$r_{case\ 9} = \frac{k' \cdot \left(P_{CO} \cdot P_{H_2O} - \frac{P_{CO_2} \cdot P_{H_2}}{K_{Eq}}\right)}{(1 + K_3 \cdot P_{CO}) \cdot \left(\sqrt{P_{H_2}} + K_1' \cdot P_{H_2O}\right)} \qquad \text{Case 9}$$

The results of the fitting of $r_{case\ 9}$ to the experimental data is presented in Table 6.14 and the correlation matrix found is presented in Table 6.15. The resulting model fit to the experimental data is presented in Figure 6.19.

As seen in Table 6.14, the model presented in case 9 is able to predict the experimental data well. It is also seen that the t-values for all parameters except k_1 is greater than the reference t-value. This indicates that there was not sufficient data to estimate k_1 precisely.

It is seen from the correlation matrix in Table 6.15 that no correlation was found between the estimated parameters.

Table 6.14: Results of model fitting in case 9

Parameter	Optimal estimate	Standard deviation	95 % confidence interval	95 % t-value
k_0' (µmol·mg_{cat}^{-1}·s^{-1})	1.4 X 10^{-1}	3.5 X 10^{-2}	6.9 X 10^{-2}	2.0 X 10^{0}
Ea (kJ·mol^{-1})	1.1 X 10^{2}			
K_1' (bar^{-1})	5.1 X 10^{-1}	2.5 X 10^{-1}	4.9 X 10^{-1}	1.0 X 10^{0}
Ea_1 (kJ·mol^{-1})	9.5 X 10^{1}	1.0 X 10^{1}	2.1 X 10^{1}	4.6 X 10^{0}
K_3 (bar^{-1})	5.8 X 10^{2}	1.0 X 10^{2}	2.0 X 10^{2}	2.9 X 10^{0}
ΔH_{ads}^{CO} (kJ·mol^{-1})	-9.0 X 10^{1}			
			95 % reference t-value	1.6 X 10^{0}
			WR/X^2	284/1951
			MARR	2.6

Values shaded in grey were fixed during the model fitting procedure

Table 6.15: Correlation matrix for model fitting in case 9

Parameter	Parameter Number	1	2	3	4
Ea_1 (kJ·mol^{-1})	**1**	1.00			
k_0' (µmol·mg_{cat}^{-1}·s^{-1})	**2**	-0.45	1.00		
K_3 (bar^{-1})	**3**	0.35	0.62	1.00	
K_1' (bar^{-1})	**4**	-0.94	0.69	-0.12	1.00

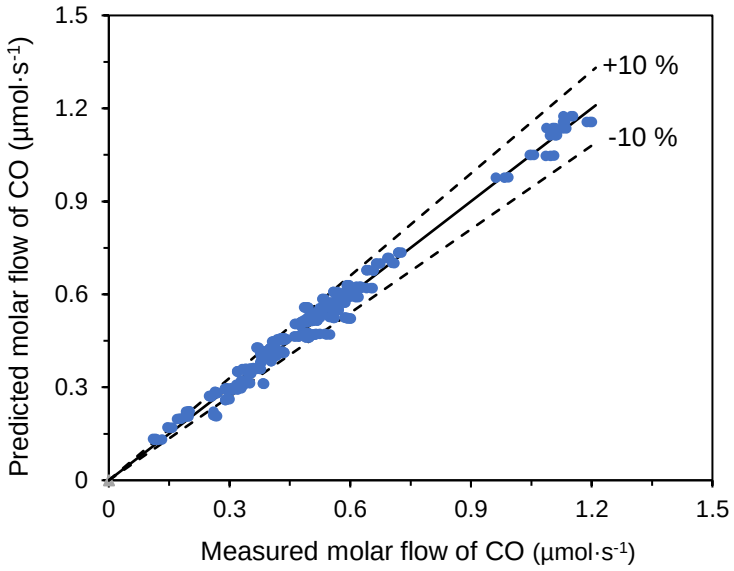

Figure 6.19: Comparison between experimentally measured CO molar flow rates (µmol·s^{-1}) and CO molar flow rates (µmol·s^{-1}) predicted from model fitting in case 9

6.4. Pressure Effects

Literature reported byTwigg (1989:288) suggests that the WGS reaction rate increases with increasing total system pressure up to approximately 5 bar. Simulations of the power law and “best fitting” LH model were performed and experiments were conduted at elevated pressures to test this effect (experimental results presented in Chapter 5.3).

6.4.1. Pressure Simulations

Simulations to test the influence of total system pressure on the reaction rate predicted by the power-rate law rate equation and the ‘best fitting’ LH type equation (given by $r_{case\ 9}$) were run using gPROMS. A feed stream of composition 4.6 % CO, 27 % H_2O, 6.4 % CO_2, 32 % H_2 and 30 % inert material was used for the simulations. The influence of pressure for the empirical and LH equations are depicted in Figure 6.20 and Figure 6.21 respectively.

Figure 6.20 indicates that the total system pressure has almost no effect on the predicted reaction rate while the trends observed in Figure 6.21 indicate a significant pressure effect for the LH type rate equation ($r_{case\ 9}$).

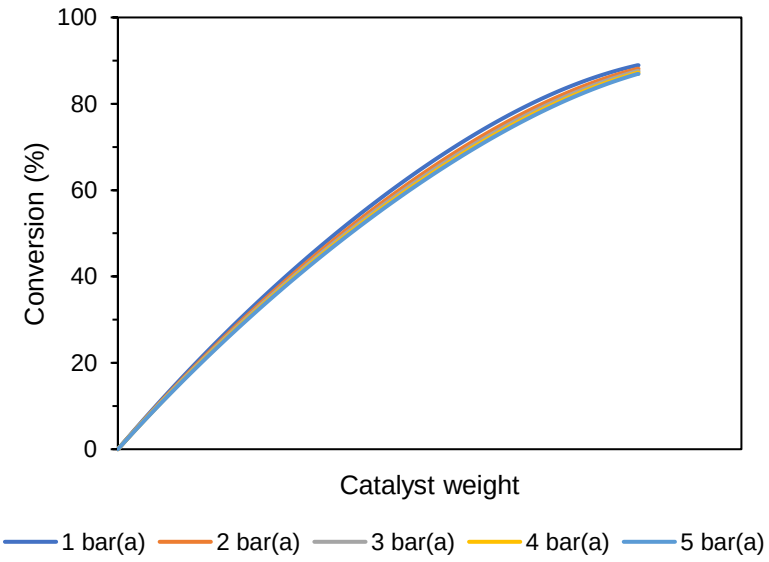

Figure 6.20: Influence of total system pressure on the prediction of the power-rate law rate equation

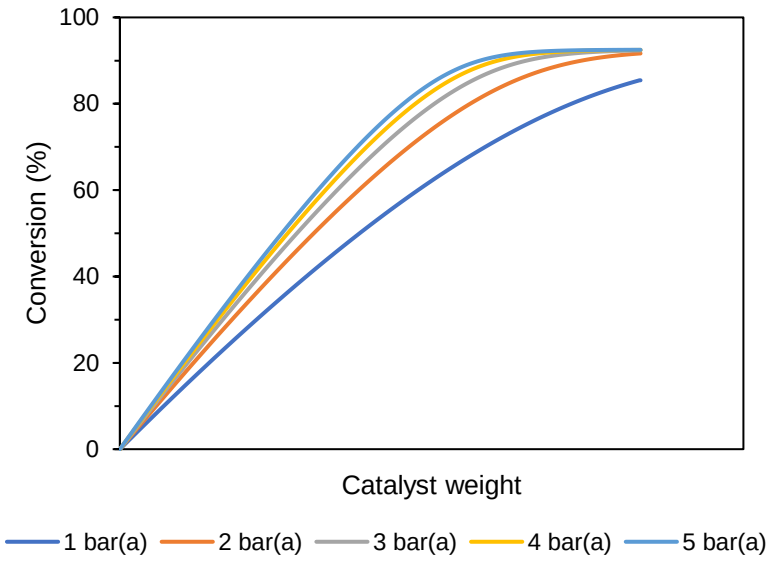

Figure 6.21: Influence of total system pressure on the prediction of $r_{case\ 9}$

6.4.2. Pressure Experiments

Appendix B contains the complete tabulated and processed experimental data set which is presented in this section.

To study the effect of total system pressure on the reaction rate, a set of experiments was conducted at different total pressures. For these experiments, a feed stream having a composition of 4.6 vol% CO, 27 vol% H_2O, 6.4 vol% CO_2, 32 vol% H_2, 2.3 vol% He and 27.7 vol% N_2 was fed to the reactors at a total flow rate of 17 $ml_{(n)}$/min per reactor. Details regarding the catalyst loadings can be found in Table A.4 of Appendix A. Figure 6.22 presents the time-on-stream performance when varying the total system pressure. The various pressures investigated are indicated on the figure. To monitor catalyst deactivation, a comparison between initial and final conversions achieved for the pressure experiments is presented in Table 6.16.

It is seen in Figure 6.22 and Table 6.16 that majority of the reactors deactivated significantly over the pressure experiment. This makes it difficult to comment on the effect of total pressure i.e. whether total pressure influences the reaction rate and to what degree if any. It would appear, however, that increasing total system pressure promotes catalyst deactivation.

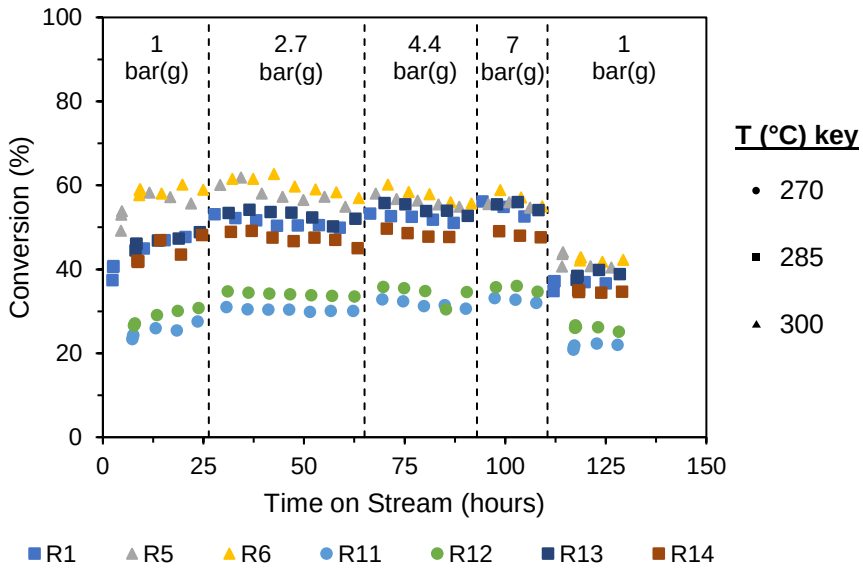

Figure 6.22: Time-on-stream performance when varying total system pressure

Table 6.16: Initial and final conversions achieved for the set of experiments in which total system pressure was varied

	Initial conversion (%)	Final conversion (%)	Difference (%)
R1	43 ± 4	37 ± 2	6 ± 6
R5	54 ± 3	42 ± 3	12 ± 5
R6	58 ± 2	42 ± 2	16 ± 4
R11	25 ± 2	22 ± 2	3 ± 4
R12	28 ± 2	26 ± 2	2 ± 4
R13	47 ± 2	39 ± 2	8 ± 4
R14	44 ± 3	35 ± 2	9 ± 5

7. Discussion

7.1. Catalyst Preparation and Characterisation

Wetness impregnation was successfully employed in the preparation of a 0.5 wt% Pt/CeO_2 catalyst. The synthesized catalyst was characterized in both the calcined and reduced state. Transmission electron microscopy (TEM) images show that Pt particles are not well dispersed on the CeO_2 support. CO chemisorption results support this, with a dispersion of 28 ± 4 % being reported when assuming a CO/Pt chemisorption stoichiometry of 1. Since the percentage of doubly bridged CO is very low (Perrichon et al., 2004:5), this is thought to be a reasonable assumption. The narrow Pt particle size distribution of 2.1 ± 1.1 nm was found after calcination and a bimodal Pt particle size distribution of 2.2 ± 0.6 nm was found after reduction. The presence of a fraction of large Pt particles in the size distribution after reduction suggests the Pt particles are sintering. No significant change was seen in the Pt particle size distribution of four used catalyst (refer to appendix E). This is of no surprise, as most literature reports on stable carbonate formation as the cause of catalyst deactivation (Azzam et al. 2007:166; Duarte de Farias et al., 2007:859; Liu et al., 2005:70-71 and Luengnaruemitchai, Osuwan & Gulari, 2003:220) and not sintering at conditions relevant to the WGS reaction in fuel processors. One would therefore not expect the Pt particles to sinter under the experimental conditions.

Temperature programmed reduction (TPR) provided valuable insight into the reducibility of the 0.5 wt% Pt/CeO_2 catalyst as well as the CeO_2 support. It was observed that PtO reduces fully at ~150 °C.

7.2. Model Fitting

The kinetic parameters of various models were determined using the gPROMS ModelBuilder software package. This software package has a dedicated parameter estimation entity that solves for the unknown parameters using the maximum likelihood objective function (Process Systems Enterprise Limited., 2017b). In order to determine the “best” kinetic model for prediction of the water-gas shift (WGS) reaction rate over the range of conditions measured, models were compared through comparison of the weighted residual (WR) values (for data sets of equal size), or by the mean absolute relative residual (MARR) (for data sets of differing size).

7.2.1. Model Validation

Before fitting experimental data to the various models, model validation was finalised to ensure the gPROMS model solved correctly. This was achieved through the validation of power-rate law equations reported in previous kinetic studies (Grabow et al., 2008; Kalamaras et al., 2009). The gPROMS model was used to re-fit the power-rate law equations to the data sets reported with the studies (Grabow et al., 2008:data set and Kalamaras et al., 2009:data set). Comparison of gPROMS model estimated parameters to the parameters reported by Grabow et al.

(2008:4614) and Kalamaras et al. (2009:121) (see Table 6.1 and Table 6.2) validated the gPROMS model as the parameters reported in the respective journal articles were successfully reproduced with the gPROMS models.

The statistical analysis performed in gPROMS shows that the data sets (Grabow et al., 2008:data set and Kalamaras et al., 2009:data set) used for model fitting were not sufficiently large enough to estimate all the parameters with statistical significance when a 10 % constant error was assumed. For the fitting to the data set by Grabow et al. (2008:data set), three out of the five parameters were determined to be statistically significant while for the fitting to the data set by Kalamaras et al. (2009:data set), four out of the five parameters were determined to be statistically significant. It should be noted that these results were found based on the data sets that were available/accessible and might not represent the complete data sets used by Grabow et al. (2008:data set) and Kalamaras et al. (2009:data set). As such, while certain parameters were found to be statistically irrelevant in this fitting, no conclusions can be drawn on the statistical relevance of the parameters reported by Grabow et al. (2008:4614) and Kalamaras et al. (2009:121).

7.2.2. Evaluation of the Water-Gas Shift Reaction Kinetics (Paper Study)

Literature indicates that Pt-based catalysts appear to have significantly higher activities when supported on reducible oxides (e.g. TiO_2, CeO_2, ZnO_2) vs. irreducible oxides (e.g. Al_2O_3, MgO) (Alijani & Irankhah, 2013:210-213; Shekhawat, Spivey & Berry, 2011:367-368). Since the 'reducibility' of the support material has a significant impact on the activity, it is thought that the support forms part of the reaction mechanism (possibly the O atom, with a more reducible support 'giving up' this O atom more easily, resulting in the higher activity seen). This would suggests that a dual-site mechanism is occuring for the WGS reaction, in which Pt provides one active site and the support provides another active site. Faur Ghenciu, (2002:394-395), Phatak et al., (2007:225,230) and Kalamaras et al., (2009:128) have all reported on PGM catalysts being bifuctional for the WGS reaction in fuel processors.

The first step of the initial evaluation was to determine if a single-site or dual-site derived reaction rate expression gives a better prediction of the data by Grabow et al. (2008:data set) and Kalamaras et al. (2009:data set). This is demonstrated by Case 1 (dual-site) and Case 2 (single-site), which are presented below as a reminder. Both of the mechanisms demonstrated in Case 1 and Case 2 are based on the redox mechanism, in which H_2O breaks down on the catalyst support to produce H_2 and subsequent oxidation of the support surface. CO then reduces the support surface to form CO_2, returning the catalyst surface to its original state.

$$CO(g) + S1 \overset{K_1}{\rightleftarrows} CO - S1$$ Case 1 Step 1

$$CO - S1 + O - S2 \overset{K_2}{\rightleftarrows} CO_2 - S1 + S2$$ Case 1 Step 2

$$CO_2(g) + S1 \overset{K_3}{\rightleftarrows} CO_2 - S1$$ Case 1 Step 3

$$H_2O(g) + S2 \overset{K_4}{\rightleftarrows} H_2O - S2$$ Case 1 Step 4

$$H_2O - S2 + 2S1 \overset{K_5}{\rightleftarrows} O - S2 + 2H - S1$$ Case 1 Step 5

$$H_2(g) + 2S1 \overset{K_6}{\rightleftarrows} 2H - S1$$ Case 1 Step 6

$$CO(g) + S1 \overset{K_1}{\rightleftarrows} CO - S1$$ Case 2 Step 1

$$CO - S1 + O - S1 \overset{K_2}{\rightleftarrows} CO_2 - S1 + S1$$ Case 2 Step 2

$$CO_2(g) + S1 \overset{K_3}{\rightleftarrows} CO_2 - S1$$ Case 2 Step 3

$$H_2O(g) + S1 \overset{K_4}{\rightleftarrows} H_2O - S1$$ Case 2 Step 4

$$H_2O - S1 + 2S1 \overset{K_5}{\rightleftarrows} O - S1 + 2H - S1$$ Case 2 Step 5

$$H_2(g) + 2S1 \overset{K_6}{\rightleftarrows} 2H - S1$$ Case 2 Step 6

Comparison of the findings from case 1 and case 2 shows a single-site derived rate expression predicts the data collected over the 3 wt% Pt/Al_2O_3 catalyst better while the dual-site derived rate expression predicts the data collected over the 0.5 wt% Pt/TiO_2 catalyst better. Since TiO_2 is more reducible than Al_2O_3, this is not a surprising result and confirms the assumption above that a dual-site mechanism is occurring over catalysts with reducible supports.

The catalyst of interest in this study (0.5 wt% Pt/CeO_2) is supported on CeO_2, which is classified as a reducible support. As such, a dual-site mechanism is likely occurring over this catalyst. Further mechanisms are therefore based on a dual-site mechanism due to the reducibility of the CeO_2 support.

Case 3 follows the same mechanistic steps to Case 1, with the exception that CO_2 adsorbs on S2 instead of S1. This is an interesting case to test, as the CO molecule and O atom that combine to form CO_2 come from different types of active sites (CO from S1 and O from S2). Comparison of the results from Case 1 and Case 3 will give insight into whether CO_2 forms on S1 or S2. When comparing the results of Case 1 to Case 3 it is seen that the rate expressions derived from Case 3 give a better prediction of the data sets than those derived from Case 1. This suggests that CO_2 forms on the active site that contains the O atom. Studies by Azzam et al. (2008:130), Kalamaras et al. (2009:127) and Kalamaras et al. (2011:298) suggests that CO_2 forms at the metal-support interface. This type of active site was not considered in this study. Azzam et al., (2008:135), Kalamaras et al. (2009:127), Kalamaras et al. (2011:296) and Pour

et al. (2010:364) all suggest that the adsorbed CO_2 desorbs from the surface quickly, forming gaseous CO_2.

Case 4 is based on a dual-site mechanism and considers OH groups that have been observed on the metal oxide support by Azzam et al. (2008:137), Kalamaras et al. (2009:127) and Wang et al. (2006:433). Furthermore, Case 4 considers the possibility of a COOH intermediate, which is suggested by Azzam et al. (2008:137), Grabow et al. (2008:4610), Jacobs et al. (2003:118), Kalamaras et al. (2011:295), Phatak et al. (2007:233) and Rhodes et al. (1995:49). As a reminder, the mechanistic steps for Case 4 are shown below.

$$H_2O(g) + S2 \overset{K_1}{\rightleftarrows} H_2O - S2 \qquad \text{Case 4 Step 1}$$

$$H_2O - S2 + S1 \overset{K_2}{\rightleftarrows} OH - S2 + H - S1 \qquad \text{Case 4 Step 2}$$

$$CO(g) + S1 \overset{K_3}{\rightleftarrows} CO - S1 \qquad \text{Case 4 Step 3}$$

$$CO - S1 + OH - S2 \overset{K_4}{\rightleftarrows} COOH - S2 + S1 \qquad \text{Case 4 Step 4}$$

$$COOH - S2 + S1 \overset{K_5}{\rightleftarrows} H - S1 + CO_2 - S2 \qquad \text{Case 4 Step 5}$$

$$H_2(g) + 2 - S1 \overset{K_6}{\rightleftarrows} 2H - S1 \qquad \text{Case 4 Step 6}$$

$$CO_2(g) + S2 \overset{K_7}{\rightleftarrows} CO_2 - S2 \qquad \text{Case 4 Step 7}$$

Comparing the model fitting results of Case 3 and Case 4 shows that the rate expressions from both cases give reasonably good fits, depending on the chosen rate determining step. Since the involvement of a COOH intermediate and OH group in the reaction mechanism is widely reported on in literature (see above), Case 4 is most likely a better representation of the reaction mechanism. Furthermore, the results from case 4 suggest that the formation of the COOH intermediate is the most likely rate determining step. This rate determining step has been previously suggested by Azzam et al. (2008:137). Since the COOH intermediate species forms from CO on S1 and OH on S2, an adsorbed CO molecule and an adsorbed OH molecule needs to be in close proximity to each other for them to interact. If the two adsorbed molecules are not in close proximity to each other, this mechanistic step cannot take place. This proximity 'issue' could further justify the formation of the COOH intermediate as the rate determining step.

Since case 4 accounts for the widely observed COOH intermediate and OH groups and gives better or equally as good predictions as the other cases presented in this section, is it thought that this mechanism is most likely to be occurring.

7.2.3. Evaluation of Water-Gas Shift Reaction Kinetics from Experimental Measurements

7.2.3.1. *Power-Rate Law Rate Expression*

To evaluate the WGS reaction kinetics in more detail over the 0.5 wt% Pt/CeO_2 catalyst prepared for this study, a set of kinetic experiments were conducted. Experiments were

conducted free of any transport limitations, deactivation and away from equilibrium (experiments were designed such that the effect that changing the partial pressure of each component has on the reaction rate can be clearly seen). Overall, nine different feed conditions were tested over a variety of space velocities and temperatures.

The trends observed from changing feed composition were as expected. An increase in reactant and decrease in product concentrations increased the reaction rate, while a decrease in reactant and increase in product concentrations decreased the reaction rate.

The orders of the WGS reaction with respect to the reactants and products for the 0.5 wt% Pt/CeO_2 catalyst were determined by fitting the experimental data to an empirical power-rate law rate expression. Reaction orders of 0.11 ± 0.03 for CO, 0.82 ± 0.08 for H_2O, -0.28 ± 0.07 for CO_2 and -0.69 ± 0.08 for H_2 were obtained. The activation energy was determined to be 120 ± 3 kJ/mol. No correlation was found between any of the parameters estimated. Figure 6.13 in Chapter 6 shows that the prediction of the power-rate law is in reasonable agreement with the experimental measurements. Furthermore, the weighted residual (WR) of 140 being less than the Chi-squared (X^2) value (1951) confirms that the power-rate law model fits the experimental data well, within 10 % error. It should be noted that the parameters found for the power-rate law are only applicable for the conditions under which it was derived.

While a reaction mechanism cannot be directly obtained from a power-rate law rate equation, we are able to get a better understanding of how each component affects the reaction. The reaction order found with respect to CO suggests that the partial pressure of CO affects the reaction rate to a small degree. This could suggest that the surface on which CO adsorbs is close to saturation. This has also been suggested by Hilaire et al. (2001:273) and Azzam et al. (2008:134).

The reaction order with respect to H_2O does not tell us any useful information besides that the reaction rate increases almost proportionally to the H_2O partial pressure.

The reaction order with respect to CO_2 was found to be a small, negative value. This suggests that the partial pressure of CO_2 affects the reaction rate to a small degree.

Lastly, a negative reaction order was found with respect to H_2. Increasing the partial pressure of H_2 will inhibit the forward reaction, as one would expect.

To confirm the value of the activation energy found when fitting the power-rate law equation to the experimental data, the activation energy was also determined by a classical Arrhenius analysis. Using a classical Arrhenius analysis, the activation energy was found to be constant throughout the range of conditions evaluated. The activation energy of 110 kJ/mol found by the Arrhenius plot agrees with the value determined using gPROMS when fitting the power-rate law equation to the experimental data. The agreement of these values is an important finding as it increases one's confidence in the gPROMS solver. Furthermore, the constant value found over the range of interest (represented by a straight line in Figure 7.14, Chapter 7) confirms

that the experiments were conducted free from any transport limitations. The activation energy found for WGS also agrees well with the 91 ± 5 kJ/mol found by Thinon et al. (2009:1942) over a 1 wt% Pt/CeO_2 catalyst and the 100 kJ/mol found by Panagiotopoulou & Kondarides (2006:51) over their CeO_2 supported materials.

Since the WGS reaction may not be an elementary reaction at high steam/carbon ratios, the power-rate law rate equation is used by many researchers to describe the WGS reaction for reactor design and optimization (see table 2.1 in Chapter 2). As such, all Langmuir-Hinshelwood (LH) type mechanisms tested will be compared to the power-rate law equation.

7.2.3.2. *Langmuir-Hinshelwood Type Rate Expressions*

In addition to the power-rate law equation, LH type rate equations were also fitted to the experimental data. To build on what was found in section 8.2.2 (evaluation of the water-gas shift reaction kinetics (paper study)), the starting point for the fitting to experimental data was the 'best fitting' rate equation found in section 8.2.2 (case 4, rate determining step (RDS) 4). The fitting of the rate equation from case 4 (see mechanistic steps above) RDS 4 to the experimental data is referred to as Case 5.

$$r_{case\ 4,RDS\ 4} = \frac{k \cdot K_1 \cdot K_2 \cdot K_3 \cdot \left(P_{CO} \cdot P_{H_2O} - \frac{P_{CO_2} \cdot P_{H_2}}{K_{Eq}}\right)}{\left(1 + K_3 \cdot P_{CO} + \sqrt{K_6 \cdot P_{H_2}}\right) \cdot \left(\sqrt{K_6 \cdot P_{H_2}} + K_1 \cdot \sqrt{K_6} \cdot P_{H_2O} \cdot \sqrt{P_{H_2}} + K_7 \cdot \sqrt{K_6} \cdot P_{CO_2} \cdot \sqrt{P_{H_2}} + K_1 \cdot K_2 \cdot P_{H_2O} + \frac{K_7 \cdot K_6}{K_5} \cdot P_{CO_2} \cdot P_{H_2}\right)}$$

Case 5

In the fitting of Case 5, the heats of adsorption of CO, H_2O, CO_2 and H_2, as well as the activation energy were fixed during the model fitting (i.e. they were not estimated). This was done to simplify the parameter estimation procedure, as it reduces the number of parameters that needed to be estimated. The WR (555) was found to be smaller than the X^2 value, indicating that the model predicts the experimental data well within 10 % error. The failed t-values and parameter correlation observed indicates that the data is not sufficient to estimate the parameters with statistical significance. Since the model gives several parameters without statistical validity, the model must be rejected. More experiments need to be conducted to estimate all parameters of this model with statistical significance.

Case 6 considers the same rate equation as for case 5, with the exception that the heats of adsorption were also estimated during the fitting process. This was done to see the effect that adding more parameters that could be varied would have on the fit obtained. During the fitting process for case 6, the solver was unable to derive any statistically relevant information from the experimental data for the parameters that needed to be estimated. As such, the model is rejected. The lack of information from the experimental data could mean one of two things: (1) the parameters to be estimated are highly correlated or (2) the system is over-parameterised. Comparing case 5 with case 6 (case 5 had fewer parameters to be estimated), one would believe that the system is over-parameterised in Case 6.

From the fitting of the power-rate law, it was said that the small negative order found with respect to CO_2 could be due to CO_2 easily desorbing into the gaseous phase, which would imply negligible adsorption. An assumption on negligible adsorption can be built into the rate equation. Pour et al. (2010:364) assumed that the adsorption of H_2O, CO_2 and H_2 is negligible compared to the adsorption of CO, OH and COOH when deriving their rate equation. Since these assumptions do not contradict any of our findings so far, they were applied when deriving the next rate equation from Case 4 RDS 4 (see mechanistic steps above). The resulting rate equation is shown below and the fitting of this rate equation to the experimental data is referred to as Case 7.

$$r_{case\ 7} = \frac{k \cdot K_1 \cdot K_2 \cdot K_3 \cdot \left(P_{CO} \cdot P_{H_2O} - \frac{P_{CO_2} \cdot P_{H_2}}{K_{Eq}}\right)}{(1 + K_3 \cdot P_{CO}) \cdot \left(\sqrt{K_6 \cdot P_{H_2}} + K_1 \cdot K_2 \cdot P_{H_2O} + \frac{K_7 \cdot K_6}{K_5} \cdot P_{CO_2} \cdot P_{H_2}\right)} \qquad \text{Case 7}$$

It is seen that the rate equation for Case 7 is simplified in terms of structure when compared to Case 5 however, the same number of parameters need to be estimated in both cases. As for Case 6, the solver was unable to pull any statistically relevant information from the experimental data for the parameters that needed to be estimated in Case 7. Comparing the MARR values for Case 5 (3.0) and Case 7 (2.9) shows that Case 7 does not improve the fit over Case 5. However, since no statistical analysis could be performed, little information is known about the parameters in Case 7 and as such, the rate equation in Case 7 does not provide one with much useful information. Case 7 must therefore be rejected.

Moving forward, a further assumption was made. Ovesen et al. (1996:173) has suggested that the COOH coverage is negligible at atmospheric conditions, the conditions under which the experiments were conducted in this study. It was therefore assumed that the adsorption of the COOH intermediate is negligible. In terms of the rate determining step, the formation of the COOH intermediate is still believed to be the rate determining step. This new assumption says that the COOH intermediate easily decomposes into CO_2 on S2 and H on S1. Consider the rate determining step (formation of COOH) and the COOH decomposition step shown below. Since a free S1 site is created when forming COOH, a readily available site exists for the COOH to decompose onto, which could result in COOH easily decomposing. The rate equation incorporating this additional assumption is shown below (Case 8).

$$CO - S1 + OH - S2 \overset{K_4}{\rightleftarrows} COOH - S2 + S1 \qquad \text{Case 4 Step 4}$$

$$COOH - S2 + S1 \overset{K_5}{\rightleftarrows} H - S1 + CO_2 - S2 \qquad \text{Case 4 Step 5}$$

$$r_{case\ 8} = \frac{k \cdot K_1 \cdot K_2 \cdot K_3 \cdot \left(P_{CO} \cdot P_{H_2O} - \frac{P_{CO_2} \cdot P_{H_2}}{K_{Eq}}\right)}{(1 + K_3 \cdot P_{CO}) \cdot \left(\sqrt{K_6 \cdot P_{H_2}} + K_1 \cdot K_2 \cdot P_{H_2O}\right)} \qquad \text{Case 8}$$

The additional assumption made when comparing Case 7 to Case 8 reduces the number of parameters that needs to be estimated from nine in Case 7 to six in Case 8. Again, the solver was unable to find a solution and no statistically relevant information about the estimated

parameters could be obtained. This is thought to be due to the parameters being highly correlated in Case 8. The smaller MARR value (2.1) for Case 8 compared to that for Case 5 (3.0) indicates a better fit is being obtained, which is thought to be due to the form of the simplified equation. The lack of statistical significance, however, results in the model being rejected.

The last case to be considered, Case 9, further simplifies Case 8 by grouping constants together where possible. This reduces the number of parameters to be estimated, which will simplify the parameter estimation procedure and hopefully result in a better fit than Case 8. By grouping constants, it must be noted that the rate equation derived (see below) is now a semi-empirical rate equation.

$$r_{case\ 9} = \frac{k \cdot \left(P_{CO} \cdot P_{H_2O} - \frac{P_{CO_2} \cdot P_{H_2}}{K_{Eq}}\right)}{(1 + K_3 \cdot P_{CO}) \cdot \left(\sqrt{P_{H_2}} + K_1 \cdot P_{H_2O}\right)} \qquad \text{Case 9}$$

The solver derived statistically relevant information for three out of the four estimated parameters (failed parameter -k^1) and indicated that the Case 9 rate equation can model the experimental data well (WR = 284, X^2 = 1951). The case can therefore be accepted. Since Case 5 and Case 9 were the only two cases in which statistical information was reported, these two cases will be compared to determine a 'best' case.

When comparing Case 5 to Case 9, it is seen that Case 9 provides little improvement over Case 5 (MARR of 2.6 vs MARR of 3.0). In Case 5, none of the parameters were determined with statistical validity whereas in Case 9, three out of the four parameters estimated were determined with statistical validity. Based on this, Case 9 is chosen as the 'best' case out of the LH type rate expressions. Caution must be applied with this model however, due to the one parameter without statistical significance.

Since the 'best' fitting case is a semi-empirical equation, it is difficult to comment on mechanistic aspects of the WGS reaction, However, in deriving the rate equation, it was assumed that the adsorption of H_2O, CO_2, H_2 and COOH is negligible and the formation of the COOH intermediate was assumed to be the rate determining step.

7.2.4. Comparison between Power-Rate Law and Case 9 rate expressions

To compare the fits obtained from the power-rate law rate expression and the rate expression given in Case 9, the WR's can be compared. The WR for the power-rate law rate expression (140) is smaller than that for the rate expression in Case 9 (284). This indicates that the power-rate law results in a better fitting model. When comparing MARR values (2.0 for the power-rate law rate expression and 2.6 for the rate expression given by Case 9), it is seen that the power-rate law rate expression results in only a slightly better fit. Both models appear to model the experimental data well at 2 bar(a).

7.3. Pressure Effects

Twigg (1989:288) has reported on literature that found the WGS reaction rate to increase with pressure up until approximately 5 bar. It is therefore important to study the effect that pressure has on the predictions given by the power-rate law rate equation and 'best' fitting LH type rate equation (given by Case 9) before deciding on the 'best' rate equation for the WGS reaction over a 0.5 wt% Pt/CeO_2 catalyst.

Simulations to test the influence of total system pressure on the reaction rate predicted by the power-rate law rate equation and the rate equation given in Case 9 were run using gPROMS (see Figure 7.1 for results). It is seen in Figure 7.1 that the LH type equation (Case 9) predicts the reaction rate to increase significantly with increasing pressure, whereas the power-rate law empirical equation predicts a small, negative effect on the reaction rate with increaseing pressure.

From a mechanistic point-of-view, increasing total system pressure will increase the amount of products and reactants adsorbed onto the surface. For the power-rate law empirical equation, the product containing terms have a bigger influence on the reaction rate than the reactant containing terms. This results in the negative effect on reaction rate observed when increasing total system pressure. When deriving the LH-type rate expression in case 9, it was assumed that the adsorption of H_2O, CO_2 and H_2 is negligible. Therefore, increasing total system pressure will result in more CO being adsorbed. More adsorbed CO will increase the probability that an adsorbed CO molecule is in close enough proximity of an adsorbed OH molecule, thus allowing the two molecules to interact. Since the interaction of these two molecules forms part of the rate determining step, more interactions will increase the reaction rate.

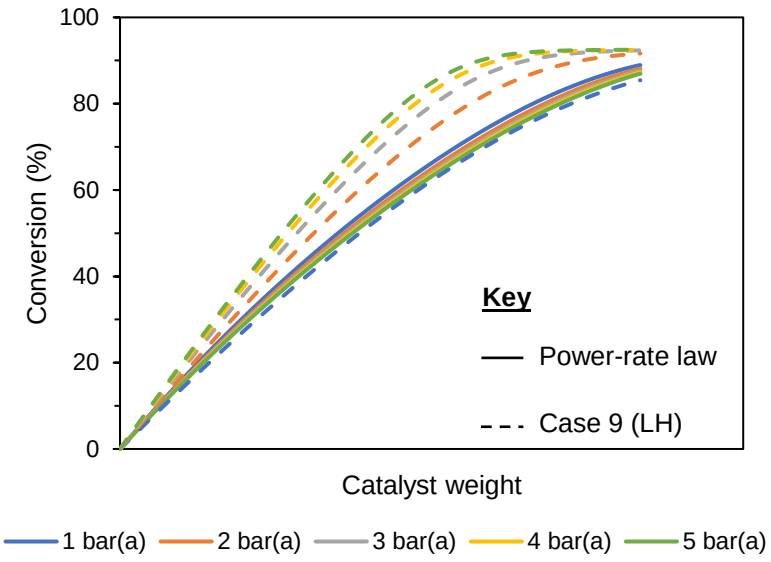

Figure 7.1: Influence of total system pressure on the predictions of the power-rate law equation and 'best' fitting Langmuir Hinshelwood type equation (given by case 9)

The opposing predictions for the influence of total system pressure seen from the two rate equations in Figure 7.1 is an interesting result and further experiments were conducted at elevated total pressure to validate the empirical power law vs. mechanistic LH rate model. For the experiments conducted at elevated pressure and following the validation of the kinetics models, it should be noted that the increase in total system pressure appeared to promote catalyst deactivation. In Figure 7.2, a comparison is made between the experimental data points obtained from the pressure experiments (represented by markers) and the model prediction given by the power-rate law rate equation (represented by a solid line) and in Figure 7.3, the same comparison is made with the model prediction given by the rate equation in case 9.

Considering that the catalyst deactivates over the experiment, the data points presented are lower than what they would have been if the catalyst had not deactivated (i.e. if the catalyst had not deactivated, conversion would have been higher). As such, it is difficult to draw conclusions on how well the models predict the data, as the models do not take catalyst deactivation into account. However, keeping in mind that the conversion would have been higher if the catalyst had not deactivated, it would appear as if pressure does influence the reaction rate.

It is seen in Figure 7.2 that the power-rate law empirical equation does not predict the reaction rate at higher pressure at all. In fact, this model predicts the opposite effect to what is observed experimentally (it predicts conversion to decrease with pressure, whereas it is observed that conversion increases with pressure). It is seen in Figure 7.3 that the LH-type rate expression predicts the experimental data better than the power rate law empirical equation. This is especially true for the data collected at 270 °C, where the LH-type rate expression gives a reasonably good prediction whereas the power-rate law does not predict the data well at all. When considering all the experimental data, a MARR value of 49 was found for the LH-type

rate expression and a MARR value of 61 was found for the power-rate law rate expression. This confirms that the LH-type rate expression predicts the experimental data better.

The LH-type rate expression giving a better prediction is a significant result and shows that this type of rate expression is an overall better model if one wants to operate outside of the operating window in which the rate expressions were derived.

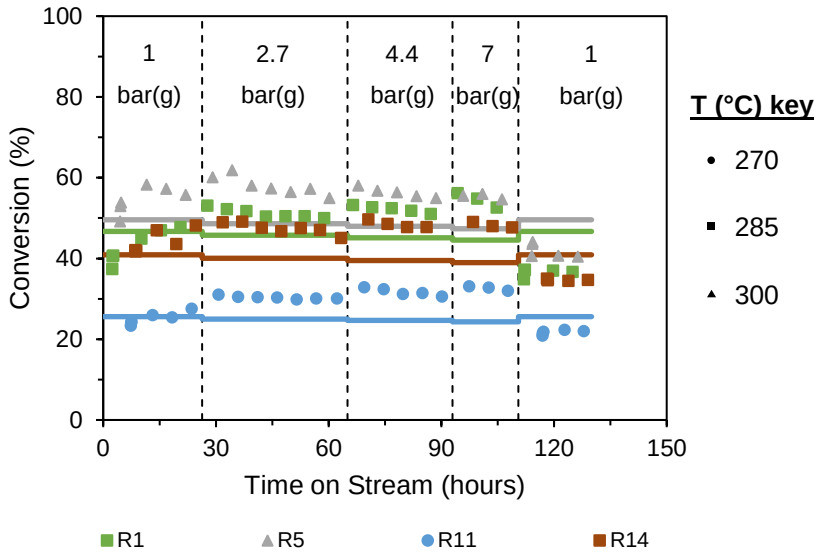

Figure 7.2: Comparison between the experimental data points obtained from the pressure experiments (represented by markers) and the model prediction given by the power-rate law rate equation (represented by solid line)

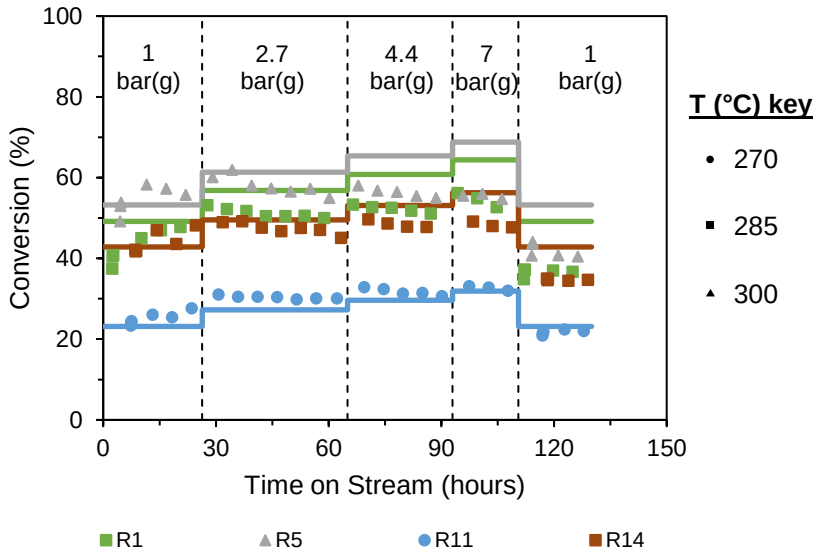

Figure 7.3: Comparison between the experimental data points obtained from the pressure experiments (represented by markers) and the model prediction given by the rate equation in case 9 (represented by solid line)

8. Conclusions and Recommendations

The main aim of this work was to develop a kinetic model that can predict the performance of the water-gas shift (WGS) reaction in fuel processors. Fuel processors produce the hydrogen feed for low temperature fuel cells. The main aim of the WGS reaction in the fuel processor is to reduce the CO concentration of the reformate stream to ~1 vol%.

An initial evaluation of the WGS reaction kinetics, using two data sets from literature (Grabow et al., 2008:data set; Kalamaras et al., 2009:data set) showed that a dual-site reaction mechanism favours catalysts supported on a support with a higher degree of reducibility and a single-site reaction mechanism favours catalysts supported on a support with a lower degree of reducibility. This finding supports previous claims (Alijani & Irankhah, 2013:210-213; Shekhawat, Spivey & Berry, 2011:367-368) that a dual-site mechanism is occuring for the WGS reaction over catalysts supported on supports with a higher degree of reducibility.

From a mechanistic point-of-view, the initial evaluation of the WGS reaction kinetics suggests that a dual-site mechanism with an intermediate species is occurring. H_2O adsorbs on site 2 (S2) and dissociates to H on site 1 (S1) and OH on S2. CO adsorbs on S1 and combines with OH on S2 to form a COOH intermediate on S2. The intermediate then decomposes to give CO_2 on S2 and H on S1. Two H atoms form H_2, which desorbs into the gaseous phase. CO_2 also desorbs into the gaseous phase. Of the three rate determining steps tested, the results suggest that the formation of the COOH intermediate is most likely to be the rate determining step, which has also been previously suggested by Azzam et al. (2008:137) as the rate determining step.

A 0.5 wt% Pt/CeO_2 catalyst was successfully produced by wetness impregnation and characterized in both the calcined and reduced state. Experiments were conducted to obtain kinetic information over the prepared catalyst. All experiments were conducted free from any transport limitations and deactivation. Using the experimental data obtained, the kinetic parameters of various Langmuir-Hinshelwood (LH) type reaction rate equations and a power-rate law rate equation were determined using the gPROMS ModelBuilder software.

After comparing various kinetic models, it was found that the power-rate law rate equation (Equation 8.1 below) resulted in a slightly better fit than the 'best' fitting Langmuir Hinshelwood (LH) type rate expression (Equation 8.2 below) ($MARR_{\text{power-rate law}}$ 2.0 vs $MARR_{LH}$ 2.6) at 2 bar(a). Since the fit is only 'slightly' better, it is concluded that both proposed kinetic models can provide a good prediction of the WGS outlet gas composition at 2 bar(a), for the conditions under study, within 10 % error. In the rate equations given below, r is the rate of consumption of CO [$mol \cdot kg_{cat}^{-1} \cdot s^{-1}$], P_i is the partial pressure of component i [bar(a)] and β [-] is the ratio of partial pressures of products to reactants to the equilibrium constant, viz. $\frac{P_{CO_2} \cdot P_{H_2}}{P_{CO} \cdot P_{H_2O} \cdot Keq}$

$$r_{CO} = \left((2.3 \pm 0.4) \times 10^{-4}\right) \cdot e^{\left(\left(\frac{-(110 \pm 3) \times 10^3}{R}\right) \cdot \left(\frac{1}{T} - \frac{1}{513}\right)\right)} \cdot P_{CO}^{0.1 \pm 0.03} \cdot P_{H_2O}^{0.8 \pm 0.08} \cdot P_{CO_2}^{-0.3 \pm 0.07} \cdot P_{H_2}^{-0.7 \pm 0.08} \cdot (1 - \beta)$$

Equation 8.1

$$r_{case\ 9} = \frac{\left((1.4 \pm 0.4) \times 10^{-1}\right) \cdot e^{\left(\left(\frac{-110 \pm 3}{R}\right) \cdot \left(\frac{1}{T} - \frac{1}{513}\right)\right)} \cdot \left(P_{CO} \cdot P_{H_2O} - \frac{P_{CO_2} \cdot P_{H_2}}{K_{Eq}}\right)}{\left(1 + \left((5.8 \pm 1) \times 10^2\right) \cdot e^{\left(\left(\frac{90 \times 10^3}{R}\right) \cdot \left(\frac{1}{T} - \frac{1}{513}\right)\right)} \cdot P_{CO}\right) \cdot \left(\sqrt{P_{H_2}} + \left((5.1 \pm 2.5) \times 10^{-1}\right) \cdot e^{\left(\left(\frac{-(95 \pm 10) \times 10^3}{R}\right) \cdot \left(\frac{1}{T} - \frac{1}{513}\right)\right)} \cdot P_{H_2O}\right)}$$

Equation 8.2

It is noted that the activation energy determined by a classical Arrhenius analysis (110 kJ/mol) agrees well with what has been reported in literature previously.

When studying the effect that total system pressure has on the WGS reaction rate, it was found that increasing pressure increased the WGS reaction rate. Only the LH type rate expression (Equation 8.2) was able to predict this. If operating at pressures higher than 2 bar(a), it is recommended that this rate equation be used to predict the outlet gas composition of the WGS reactor. Furthermore, when predicting reaction rates outside of the window in which the rate equations were derived, the LH model is expected to give a better prediction as it is based on fundamental steps.

The kinetic models presented above, together with the appropriate mass and energy balances, can be used for the design and optimisation of the WGS reactor in a fuel processor system.

For future work, it is recommended that an in-depth study be done on the influence of pressure on the WGS reaction. More understanding is needed on how pressure affects the activity of the WGS catalyst. It is also recommended that the experimental data set be expanded by testing more conditions. This will allow for better model fits to be obtained. Furthermore, it is recommended that the models presented in this study be fitted to data obtained over different WGS catalysts. For the LH model, if the same mechanism is occurring over different catalysts, the models presented in this study should be able to predict the performance of the WGS reaction over other catalysts as well. The reaction rate constants for the models will require re-fitting however, the form of the equations should remain the same.

9. References

Alijani, A. & Irankhah, A. 2013. Medium-Temperature Shift Catalysts for Hydrogen Purification in a Single-Stage Reactor. Chemical Engineering & Technology. 36:209-219. DOI: 10.1002/ceat.201200151.

Amadeo, N.E. & Laborde, M.A. 1995. Hydrogen Production from the Low-Temperature Water-Gas Shift Reaction: Kinetics and Simulation of the Industrial Reactor. International Journal of Hydrogen Energy. 20(12):949-956. DOI: 10.1016/0360-3199(94)00130-R.

AspenTech. 2016. *Aspen Plus*® [Computer software]. Version 8.

Avantium. n.d. Systems. Available: https://www.avantium.com/catalysis/systems/ [2017, August 18].

Azzam, K.G., Babich, I.V., Seshan, K. & Lefferts, L. 2007. A bifunctional catalyst for the single-stage water-gas shift reaction in fuel cell applications. Part 2. Roles of the support and promoter on catalyst activity and stability. Journal of Catalysis. 251:163-171. DOI: 10.1016/j.jcat.2007.07.011.

Azzam, K.G., Babich, I.V., Seshan, K. & Lefferts, L. 2008. Role of Re in Pt-Re/TiO_2 catalyst for water gas shift reaction: A mechanistic and kinetic study. Applied Catalysis B: Environmental. 80:129-140. DOI: 10.1016/j.apcatb.2007.11.015.

Barreto, L., Makihira, A. & Riahi, K. 2003. The hydrogen economy in the 21st century: a sustainable development scenario. International Journal of Hydrogen Energy. 28(3):267-284. DOI: 10.1016/S0360-3199(02)00074-5.

Crabtree, G.W., Dresselhaus, M.S. & Buchanan, M.V. 2004. The Hydrogen Economy. Physics Today. 57(12):39-44.

Duarte de Farias, A.M., Barandas, A.P.M.G., Perez, R.F. & Fraga, M.A. 2007. Water-gas shift reaction over magnesia-modified Pt/CeO_2 catalysts. Journal of Power Sources. 165:854-860. DOI: 10.1016/j.jpowsour.2006.12.054.

Eurokin. 2011. Eurokin spreadsheet on requirements for measurement of intrinsic kinetics in gas-solid fixed-bed reactors. Available: http://eurokin.org/wp-content/uploads/downloads/2012/08/EUROKIN_fixed-bed_html_guide.pdf [2017, July 16].

Faur Ghenciu, A. 2002. Review of fuel processing catalysts for hydrogen production in PEM fuel cell systems. Current Opinion in Solid State and Materials Science. 6:389-399. DOI: 10.1016/S1359-0286(02)00108-0.

Fishtik, I. & Datta, R. 2002. A UBI-QEP microkinetic model for the water-gas shift reaction on Cu(1 1 1). Surface Science. 512:229-254. DOI: 10.1016/S0039-6028(02)01689-8.

Germani, G. & Schuurman, Y. 2006. Water-Gas Shift Reaction Kinetics Over μ-Structured $Pt/CeO_2/Al_2O_3$ Catalysts. AIChE Journal. 52:1806-1813. DOI: 10.1002/aic.10764.

Giordano, F., Trovarelli, A., De Leitenburg, C. & Giona, M. 2000. A Model for the Temperature-Programmed Reduction of Low and High Surface Area Ceria. Journal of Catalysis. 193:273-282. DOI: 10.1006/jcat.2000.2900.

Grabow, L.C., Gokhale, A.A. Evans, S.T., Dumesic, J.A. & Mavrikakis, M. 2008. Mechanism of the Water Gas Shift Reaction on Pt: First Principles, Experiments, and Microkinetic Modeling [Article & Dataset]. The Journal of Physical Chemistry C. 112:4608-4617. DOI: 10.1021/jp7099702.

Grenoble, D.C., Estadt, M.M. & Ollis, D.F. 1981. The Chemistry and Catalysis of the Water Gas Shift ReactionL 1. The Kinetics over Supported Metal Catalysts. Journal of Catalysis. 67:90-102. DOI: 10.1016/0021-9517(81)90263-3.

Häussinger, P., Lohmüller, R. & Watson, A.M. 2000. Hydrogen, 2. Production. In *Ullmann's Encyclopedia of Industrial Chemistry*. 249-307. DOI: 10.1002/14356007.o13_o03.

Hilaire, S., Wang, X., Luo, T., Gorte, R.J. & Wagner, J. 2001. A comparative study of water-gas shift reaction over ceria supported metallic catalysts. Applied Catalysis A: General. 215:271-278. DOI: 10.1016/S0926-860X(01)00535-X.

Jacobs, G., Williams, L., Graham, U., Sparks, D. & Davis, B.H. 2003. Low-Temperature Water-Gas Shift: In-Situ DRIFTS-Reaction Study of a Pt/CeO_2 Catalyst for Fuel Cell Reformer Applications. Journal of Physical Chemistry B. 107:10398-10404. DOI:10.1021/jp0302055.

Kalamaras, C.M., Panagiotopoulou, P., Kondarides, D.I. & Efstathiou, A.M. 2009. Kinetic and mechanistic studies of the water-gas shift reaction on Pt/TiO2 catalyst [Article & Dataset]. Journal of Catalysis. 264:117-129. DOI: 10.1016/j.jcat.2009.03.002.

Kalamaras, C.M., Americanou, S. & Efstathiou, A.M. 2011. "Redox" vs "associative formate with -OH group regeneration" WGS reaction mechanism on Pt/CeO_2: Effect of platinum particle size. Journal of Catalysis. 279:287-300. DOI: 10.1016/j.jcat.2011.01.024.

Koryabkina, N.A., Phatak, A.A., Ruettinger, W.F., Farrauto, R.J. & Ribeiro, F.H. 2003. Determination of kinetic parameters for the water-gas shift reaction on copper catalysts under realistic conditions for fuel cell applications. Journal of Catalysis. 217:233-239. DOI: 10.1016/S0021-9517(03)00050-2.

Kumar, K.V., Porkodi, K. & Rocha, F. 2008. Langmuir-Hinshelwood kinetics – A theoretical study. Catalysis Communications. 9:82-84. DOI: 10.1016/j.catcom.2007.05.019.

Liu, X., Ruettinger, W., Xu, X. & Farrauto, R. 2005. Deactivation of Pt/CeO_2 water-gas shift catalysts due to shutdown/startup modes for fuel cell applications. Applied Catalysis B: Environmental. 56:69-75. DOI: 10.1016/j.apcatb.2004.04.026.

Luchters, N. 2016. High Throughput Experimentation: A Validation Study for use in Catalyst Development. MSc Thesis. University of Cape Town.

Luengnaruemitchai, A., Osuwan, S. & Gulari, E. 2003. Comparative studies of low-temperature water-gas shift reaction over Pt/CeO_2, Au/CeO_2 and Au/Fe_2O_3 catalysts. Catalysis Communications. 4:215-221. DOI: 10.1016/S1566-7367(03)00036-0.

Ma, W., Jacobs, G., Sparks, D.E., Klettlinger, J.L.S., Yen, C.H. & Davis, B.H. 2016. Fischer-Tropsch synthesis and water gas shift kinetics for a precipitated iron catalyst. 275:49-58. DOI: 10.1016/j.cattod.2016.01.006.

Micromeritics Instrument Corporation. 2007. TriStar 3000 Operator's Manual. Version 6.08. Norcross, Georgia. Available: http://www.micromeritics.com/repository/files/tristar_3000_operators_manual_v6.08.pdf [2017, August 18].

Ogden, J.M. 1999. Prospects for Building a Hydrogen Energy Infrastructure. Annual Review of Energy and the Environment. 24:227-279.

Ovesen, C.V., Clausen, B.S., Hammershøi, B.S., Steffensen, G., Askgaard, T., Chorkendorff, I., Nørskov, J.K., Rasmussen, P.B., Stoltze, P. & Taylor, P. 1996. A Microkinetic Analysis of the Water-Gas Shift Reaction under Industrial Conditions. Journal of Catalysis. 158:170-180. DOI: 10.1006/jcat.1996.0016.

Ovesen, C.V., Stoltze, P., Nørskov, J.K. & Campbell, C.T. 1992. A Kinetic Model of the Water Gas Shift Reaction. Journal of Catalysis. 134:445-468. DOI: 10.1016/0021-9517(92)90334-E.

Panagiotopoulou, P. & Kondarides, D.I. 2006. Effect of the nature of the support on the catalytic performance of noble metal catalysts for the water-gas shift reaction. Catalysis Today. 112:49-52. DOI: 10.1016/j.cattod.2005.11.026.

Pantu, P. & Gavalas, G.R. 2002. Methane partial oxidation on Pt/CeO_2 and Pt/Al_2O_3 catalysts. Applied Catalysis A: General. 223:253-260. DOI: 10.1016/S0926-860X(01)00761-X.

Perrichon, V., Retailleau, L., Bazin, P., Daturi, M. & Lavalley, J.C. 2004. Metal dispersion of CeO_2-ZrO_2 supported platinum catalysts measured by H_2 or CO chemisorption. Applied Catalysis A: General. 260:1-8. DOI: 10.1016/j.apcata.2003.09.031.

Phatak, A.A., Koryabkina, N., Rai, S., Ratts, J.L., Ruettinger, W., Farrauto, R.J., Blau, G.E., Delgass, W.N. & Ribeiro, F.H. 2007. Kinetics of the water-gas shift reaction on Pt catalysts supported on alumina and ceria. Catalysis Today. 123:224-234. DOI: 10.1016/j.cattod.2007.02.031.

Pino, L., Vita, A., Cordaro, M., Recupero, V. & Hegde, M.S. 2003. A comparative study of Pt/CeO_2 catalysts for catalytic partial oxidation of methane to syngas for application in fuel cell electric vehicles. Applied Catalysis A: General. 243:135-146. DOI: 10.1016/S0926-860X(02)00542-2.

Pour, A.N., Housaindokht, M.R., Tayyari, S.F. & Zarkesh, J. 2010. Kinetics of the water-gas shift reaction in Fischer-Tropsch synthesis over a nano-structured iron catalyst. Journal of Natural Gas Chemistry. 19:362-368. DOI: 10.1016/S1003-9953(09)60085-2.

Process Systems Enterprise Limited. 2017a. *gPROMS ModelBuilder* [Computer software]. Version 4.2.0. Hammersmith, London.

Process Systems Enterprise Limited. 2017b. gPROMS ModelBuilder Documentation. Hammersmith, London. Available as part of the *gPROMS ModelBuilder* computer software package.

Radhakrishnan, R., Willigan, R.R., Dardas, Z. & Vanderspurt, T.H. 2006. Water gas shift activity of noble metals supported on ceria-zirconia oxides. AIChE Journal. 52:1888-1894. DOI: 10.1002/aic.10785.

Ratnasamy, C. & Wagner, J.P. 2009. Water Gas Shift Catalysis. Catalysis Reviews. 51:325-440. DOI: 10.1080/01614940903048661.

Rhodes, C., Hutchings, G.J. & Ward, A.M. 1995. Water-gas shift reaction: finding the mechanistic boundary. Catalysis Today. 23:43-58.

Ricote, S., Jacobs, G., Milling, M., Ji, Y., Patterson, P.M. & Davis, B.H. 2006. Low temperature water-gas shift: Characterization and testing of binary mixed oxides of ceria and zirconia promoted with Pt. Applied Catalysis A: General. 303:35-47. DOI: 10.1016/j.apcata.2006.01.025.

Rogemond, E., Essayem, N., Frety, R., Perrichon, V., Primet, M. & Mathis, F. 1997. Characterization of Model Three-Way Catalysts I. Determination of the Accessible Metallic Area by Cyclohexane Aromatization Activity Measurements. Journal of Catalysis. 166:229-235. DOI: 10.1006/jcat.1997.1493.

Scott Fogler, H. 2006. *Elements of Chemical Reaction Engineering*. 4th edition. United States of America: Pearson Education, Inc.

Shekhawat, D., Spivey, J.J. & Berry, D.A. 2011. *Fuel Cells: Technologies for Fuel Processing*. Spain: Elsevier.

Smith, R.J.B., Loganathan, M. & Shantha, M.S. 2010. A Review of the Water Gas Shift Reaction Kinetics. International Journal of Chemical Reactor Engineering. 8:1-32. DOI: 10.2202/1542-6580.2238.

Sun, J., DesJardins, J., Buglass, J. & Liu, K. 2005. Nobel metal water gas shift catalysis: Kinetics study and reactor design. International Journal of Hydrogen Energy. 30:1259-1264. DOI: 10.1016/j.ijhydene.2005.02.013.

Thinon, O., Rachedi, K., Diehl, F., Avenier, P. & Schuurman, Y. 2009. Kinetics and Mechanism of the Water-Gas Shift Reaction Over Platinum Supported Catalysts. Topics in Catalysis. 52:1940-1945. DOI: 10.1007/s11244-009-9377-z.

Torrente-Murciano, L. 2016. The importance of particle-support interaction on particle size determination by gas chemisorption. Journal of Nanoparticle Research. 18:87. DOI: 10.1007/s11051-016-3385-2.

Twigg, M.V. 1989. Catalyst Handbook. 2nd edition. England: Wolfe Publishing Ltd.

United Nations. 2015. Paris Agreement. 12 December, Paris. Available: http://unfccc.int/paris_agreement/items/9485.php [2017, June 19].

United States Department of Energy. 2014. Alternative Fuels Data Center – Fuel Properties Comparison. Available: https://www.afdc.energy.gov/fuels/fuel_comparison_chart.pdf [2017, July 01].

Vannice, M.A. 2007. An analysis of the Mars-van Krevelen rate expression. Catalysis Today. 123:18-22. DOI: 10.1016/j.cattod.2007.02.002.

Vignatti, C.I., Avila, M.S., Apesteguía, C.R. & Garetto, T.F. 2011. Study of the water-gas shift reaction over Pt supported on CeO_2-ZrO_2 mixed oxides. Catalysis Today. 171:297-303. DOI: 10.1016/j.cattod.2010.12.041.

Wang, X., Rodriguez, J.A., Hanson, J.C., Gamarra, D., Martínez-Arias, A. & Fernández-García, M. 2006. In Situ Studies of the Active Sites for the Water Gas Shift Reaction over Cu-CeO2 Catalysts: Complex Interaction between Metallic Copper and Oxygen Vacancies of Ceria. Journal of Physical Chemistry B. 110:428-434. DOI: 10.1021/jp055467g.

Zhang, Y., Wang, Z., Zhou, J., Liu, J. & Cen, K. 2008. Effect of preparation method on platinum-ceria catalysts for hydrogen iodide decomposition in sulfur-iodine cycle. International Journal of Hydrogen Energy. 33:602-607. DOI: 10.1016/j.ijhydene.2007.10.041.

Appendix A: Summary of Catalyst Loadings and Experimental Operating Conditions

This appendix contains supporting information for chapter 5.

A.1. Feed Compositions

A.1.1. Kinetic Experiments

Table A.1 below lists the feed stream composition setpoints used for this study. It should be noted that baseline 1 represents the baseline condition used for the first set of kinetic experiments and baseline 2 represents the baseline condition used for the second set of kinetic experiments. Feeds I through IV were used for the first set of kinetic experiments, while feeds V through X were used for the second set of kinetic experiments. All kinetic experiments were conducted at 2 bar(a).

Table A.1: Experimental feed composition setpoints

Feed condition	Description	Composition (vol%)						Total flow (ml/min)*
		CO	H_2O	CO_2	H_2	He	N_2	
I	Baseline 1	4.6	27	6.4	32	26.5	3.5	264
II	Low H_2	4.6	27	6.4	25	26.5	10.5	264
III	High H_2	4.6	27	6.4	55	7	0	211
IV	Low CO	2	27	6.4	32	19.9	12.8	352
V	Baseline 2	4.6	27	6.4	32	1.9	28.1	320
VI	High CO	12	27	6.4	32	2.6	20	238
VII	Low H_2O	4.6	20	6.4	32	1.8	35.1	336
VIII	High CO_2	4.6	27	15	32	2.7	18.7	232
IX	High H_2O	4.6	45	6.4	32	1.8	10.2	352
X	Low CO_2	4.6	27	4	32	1.6	30.8	400

* Total flow to all 16 reactors. Flow per reactor is the total flow given divided by 16

A.2. Catalyst Loadings and Operating Conditions

A.2.1. Kinetic Experiments

Table A.2 and Table A.3 below presents the catalyst loadings as well as the temperature setpoints of the catalyst beds for both sets of kinetic experiments.

Table A.2: Reactor loadings and temperature setpoints for the first set of kinetic experiments (refer to Chapter 5, section 5.4.1.2 for a description of the first set of kinetic experiments)

Reactor #	Temperature setpoint (°C)	Catalyst weight (mg)	Catalyst bed length (mm)
1	275	50	6
2	275	74	10
3	275	100	13
4	275	126	17
5	300	75	10
6	300	56	7
7	300	75	10
8	300	40	5
9	275	Blank reactor to sample feed	
10	275	Not in use for this study	
11	275	51	7
12	275	100	13
13	325	36	4
14	325	45	6
15	325	55	7
16	325	35	4

Table A.3: Reactor loadings and temperature setpoints for the second set of kinetic experiments (refer to Chapter 5, section 5.4.1.2 for a description of the second set of kinetic experiments)

Reactor #	Temperature setpoint (°C)	Catalyst weight (mg)	Catalyst bed length (mm)
1	270	75	10
2	270	95	12
3	270	116	15
4	270	140	17
5	285	50	6
6	285	90	11
7	285	125	16
8	285	91	11
9	270	Blank reactor to sample feed	
10	270	Blank reactor to sample feed	
11	270	95	12
12	270	140	18
13	300	40	5
14	300	66	8
15	300	90	11
16	300	66	8

A.2.2. Pressure Experiments

Table A.4 below presents the catalyst loadings as well as the temperature setpoints of the catalyst beds for the pressure experiments.

Table A.4: Reactor loadings and temperature setpoints for the pressure experiments

Reactor #	Temperature setpoint (°C)	Catalyst weight (mg)	Catalyst bed length (mm)
1	285	140	17
2	285	Not in use for this study	
3	285	120	14
4	285	Not in use for this study	
5	300	79	10
6	300	79	9
7	300	Not in use for this study	
8	300	Not in use for this study	
9	270	Not in use for this study	
10	270	Not in use for this study	
11	270	140	17
12	270	140	16
13	285	140	16
14	285	120	13
15	285	Blank reactor to sample feed	
16	285	Not in use for this study	

Appendix B: Experimental Data

This appendix contains the processed experimental data presented in chapter 5.

Explanation of data in tables:

1. Every time the feed condition is changed, the table starts on a new page and the first entry in the table will indicate the new feed condition. Feed samples are represented by reactor 9 (unless otherwise stated) and the feed condition number is listed in the time on stream column. All feed streams are bolded in the tables.
2. All reactors are referenced to the feed sample taken before they are listed in the table and the conversion is calculated based on that feed sample.
3. ṅ represents molar flow rate.

B.1. Kinetic Measurements

Table B.1 and Table B.2 below contain all the processed experimental data for the kinetic experiments (Figure 5.5 and Figure 5.6 in Chapter 5). It is recommended that these tables are read together with the figures mentioned above as well as the list of feed conditions given in Table A.1 in Appendix A.

Table B.1: Processed experimental data for the first set of kinetic experiments

Time on stream (hours)	Reactor #	ṅ (µmol/s)						Conversion (%)	Mass balance (%)
		He	N_2	CO	H_2O	CO_2	H_2		
FEED I	**9**	**3.3**	**0.4**	**0.6**	**3.3**	**0.8**	**3.9**	**-**	**100**
2.1	2	3.3	0.4	0.5	3.2	0.9	4.0	17	99.5
2.2	2	3.3	0.4	0.5	3.2	0.8	4.0	17	99.5
2.3	2	3.3	0.4	0.5	3.2	0.9	4.0	17	99.6
2.7	3	3.3	0.4	0.4	3.2	0.9	4.1	24	99.5
2.8	3	3.3	0.4	0.4	3.2	0.9	4.1	24	99.4
2.9	3	3.3	0.4	0.4	3.2	0.9	4.1	24	99.4
3.3	4	3.3	0.4	0.4	3.2	0.9	4.1	27	99.6
3.4	4	3.3	0.4	0.4	3.2	0.9	4.1	27	99.4
3.5	4	3.3	0.4	0.4	3.2	0.9	4.1	28	99.4
4.5	5	3.3	0.4	0.3	3.1	1.0	4.2	49	99.3
4.6	5	3.3	0.4	0.3	3.1	1.0	4.2	49	99.2
4.7	5	3.3	0.4	0.3	3.1	1.0	4.2	49	99.3
5.1	16	3.3	0.4	0.3	3.1	1.0	4.2	54	99.3
5.2	16	3.3	0.4	0.3	3.1	1.0	4.2	54	99.4
5.3	16	3.3	0.4	0.3	3.1	1.0	4.2	54	99.4
5.7	7	3.3	0.4	0.3	3.1	1.0	4.2	50	99.3
5.8	7	3.3	0.4	0.3	3.0	1.0	4.2	50	99.2
5.9	7	3.3	0.4	0.3	3.1	1.0	4.2	50	99.2
6.3	8	3.3	0.4	0.4	3.1	0.9	4.1	31	99.4
6.4	8	3.3	0.4	0.4	3.1	0.9	4.1	32	99.4
6.5	8	3.3	0.4	0.4	3.1	0.9	4.1	32	99.5
6.8	6	3.3	0.4	0.3	3.1	1.0	4.2	42	99.2
7.0	6	3.3	0.4	0.3	3.1	1.0	4.2	42	99.1

Table B.1 continued

Time on stream (hours)	Reactor #	ṅ (µmol/s)						Conversion (%)	Mass balance (%)
		He	N_2	CO	H_2O	CO_2	H_2		
7.1	6	3.3	0.4	0.3	3.1	1.0	4.2	42	99.1
8.0	11	3.3	0.4	0.5	3.2	0.9	4.0	14	99.9
8.2	11	3.3	0.4	0.5	3.2	0.8	4.0	15	99.6
8.3	11	3.3	0.4	0.5	3.2	0.9	4.0	15	99.8
8.6	12	3.3	0.4	0.4	3.2	0.9	4.0	24	100
8.8	12	3.3	0.4	0.4	3.2	0.9	4.0	24	99.9
8.9	12	3.3	0.4	0.4	3.2	0.9	4.0	24	99.8
9.2	13	3.3	0.4	0.3	3.1	1.0	4.2	56	99.0
9.4	13	3.3	0.4	0.3	3.1	1.0	4.2	56	98.9
9.5	13	3.3	0.4	0.3	3.0	1.0	4.2	56	99.0
9.8	14	3.3	0.4	0.2	3.0	1.1	4.3	65	99.0
9.9	14	3.3	0.4	0.2	3.0	1.1	4.3	65	99.0
10.1	14	3.3	0.4	0.2	3.0	1.1	4.3	65	99.0
10.4	15	3.3	0.4	0.2	3.0	1.1	4.3	74	98.8
10.5	15	3.3	0.4	0.2	3.0	1.1	4.3	74	98.9
10.7	15	3.3	0.4	0.1	3.0	1.1	4.3	74	98.8
12.0	1	3.3	0.4	0.5	3.2	0.9	4.0	16	99.8
12.3	2	3.3	0.4	0.5	3.2	0.9	4.0	17	99.9
12.7	3	3.3	0.4	0.4	3.2	0.9	4.1	24	99.7
13.0	4	3.3	0.4	0.4	3.1	0.9	4.1	29	99.7
13.8	5	3.3	0.4	0.3	3.1	1.0	4.2	48	99.5
14.1	6	3.3	0.4	0.3	3.1	1.0	4.1	40	99.4
14.5	7	3.3	0.4	0.3	3.1	1.0	4.2	49	99.6
14.8	8	3.3	0.4	0.4	3.1	0.9	4.1	31	99.5

Table B.1 continued

Time on stream (hours)	Reactor #	ṅ (µmol/s)						Conversion (%)	Mass balance (%)
		He	N_2	CO	H_2O	CO_2	H_2		
15.5	11	3.3	0.4	0.5	3.2	0.9	4.0	15	99.8
15.9	12	3.3	0.4	0.4	3.2	0.9	4.1	25	99.8
16.3	13	3.3	0.4	0.3	3.0	1.0	4.2	55	99.2
17.0	14	3.3	0.4	0.2	3.0	1.1	4.3	63	99.3
17.3	15	3.3	0.4	0.2	3.0	1.1	4.3	69	99.1
17.7	16	3.3	0.4	0.3	3.0	1.0	4.2	51	99.3
18.4	1	3.3	0.4	0.5	3.2	0.9	4.0	15	99.8
18.8	2	3.3	0.4	0.5	3.2	0.9	4.0	17	99.7
19.1	3	3.3	0.4	0.4	3.2	0.9	4.1	26	99.7
19.5	4	3.3	0.4	0.4	3.2	0.9	4.1	29	99.5
20.2	5	3.3	0.4	0.3	3.1	1.0	4.2	48	99.4
20.6	6	3.3	0.4	0.3	3.1	1.0	4.2	41	99.4
20.9	7	3.3	0.4	0.3	3.1	1.0	4.2	49	99.6
21.3	8	3.3	0.4	0.4	3.1	0.9	4.1	31	99.5
22.0	11	3.3	0.4	0.5	3.2	0.9	4.0	15	100
22.3	12	3.3	0.4	0.4	3.2	0.9	4.1	25	100
22.7	13	3.3	0.4	0.3	3.0	1.0	4.2	54	99.4
23.4	14	3.3	0.4	0.2	3.0	1.1	4.3	63	99.2
23.8	15	3.3	0.4	0.2	3.0	1.1	4.3	71	98.9
24.1	16	3.3	0.4	0.3	3.0	1.0	4.2	50	99.3

Table B.1 continued

Time on stream (hours)	Reactor #	ṅ (µmol/s)						Conversion (%)	Mass balance (%)
		He	N_2	CO	H_2O	CO_2	H_2		
FEED II	**9**	**3.3**	**1.3**	**0.6**	**3.3**	**0.8**	**3.1**	**-**	**100**
26.9	1	3.3	1.3	0.5	3.2	0.9	3.1	16	99.8
27.2	2	3.3	1.3	0.5	3.2	0.9	3.2	18	99.8
27.6	3	3.3	1.3	0.4	3.2	0.9	3.2	29	99.7
27.9	4	3.3	1.3	0.4	3.2	0.9	3.2	32	99.7
28.7	5	3.3	1.3	0.3	3.1	1.0	3.3	54	99.2
29.0	6	3.3	1.3	0.3	3.1	1.0	3.3	44	99.2
29.4	7	3.3	1.3	0.3	3.1	1.0	3.3	54	99.3
29.7	8	3.3	1.3	0.4	3.1	0.9	3.2	34	99.6
30.4	11	3.3	1.3	0.5	3.2	0.9	3.1	16	99.9
30.8	12	3.3	1.3	0.4	3.2	0.9	3.2	28	99.8
31.2	13	3.3	1.3	0.2	3.0	1.1	3.4	59	99.2
31.9	14	3.3	1.3	0.2	3.0	1.1	3.4	61	99.1
32.2	15	3.3	1.3	0.2	3.0	1.1	3.4	62	99.1
32.6	16	3.3	1.3	0.3	3.1	1.0	3.3	46	99.4
33.3	1	3.3	1.3	0.5	3.2	0.9	3.1	14	99.9
33.7	2	3.3	1.3	0.5	3.2	0.9	3.2	19	99.8
34.0	3	3.3	1.3	0.4	3.2	0.9	3.2	29	99.7
34.4	4	3.3	1.3	0.4	3.1	0.9	3.2	34	99.6
35.1	5	3.3	1.3	0.3	3.1	1.0	3.3	53	99.4
35.4	6	3.3	1.3	0.3	3.1	1.0	3.3	44	99.4
35.8	7	3.3	1.3	0.3	3.0	1.1	3.3	54	99.5
36.2	8	3.3	1.3	0.4	3.1	1.0	3.2	34	99.6
36.9	11	3.3	1.3	0.5	3.2	0.9	3.1	16	99.9

Table B.1 continued

Time on stream (hours)	Reactor #	ṅ (µmol/s)						Conversion (%)	Mass balance (%)
		He	N_2	CO	H_2O	CO_2	H_2		
37.2	12	3.3	1.3	0.4	3.2	0.9	3.2	28	99.9
37.6	13	3.3	1.3	0.2	3.0	1.1	3.4	58	99.3
38.3	14	3.3	1.3	0.2	3.0	1.1	3.4	68	99.1
38.7	15	3.3	1.3	0.1	2.9	1.1	3.5	76	99.0
39.0	16	3.3	1.3	0.3	3.0	1.0	3.4	55	99.1
39.7	1	3.3	1.3	0.5	3.2	0.9	3.2	17	99.7
40.1	2	3.3	1.3	0.5	3.2	0.9	3.2	20	99.7
40.5	3	3.3	1.3	0.4	3.1	0.9	3.2	29	99.6
40.8	4	3.3	1.3	0.4	3.1	0.9	3.2	33	99.4
41.5	5	3.3	1.3	0.3	3.0	1.0	3.3	53	99.4
41.9	6	3.3	1.3	0.3	3.1	1.0	3.3	44	99.4
42.2	7	3.3	1.3	0.3	3.0	1.1	3.3	54	99.5
42.6	8	3.3	1.3	0.4	3.1	1.0	3.2	34	99.5
43.3	11	3.3	1.3	0.5	3.2	0.9	3.1	16	99.8
43.7	12	3.3	1.3	0.4	3.1	0.9	3.2	28	99.8
44.0	13	3.3	1.3	0.2	3.0	1.1	3.4	58	99.2
44.7	14	3.3	1.3	0.2	3.0	1.1	3.4	69	99.2
45.1	15	3.3	1.3	0.2	3.0	1.1	3.4	70	99.1
45.5	16	3.3	1.3	0.3	3.0	1.0	3.4	54	99.3

Table B.1 continued

Time on stream (hours)	Reactor #	ṅ (µmol/s)						Conversion (%)	Mass balance (%)
		He	N_2	CO	H_2O	CO_2	H_2		
FEED III	**9**	**0.7**	**0.0**	**0.5**	**2.8**	**0.7**	**5.3**	**-**	**100**
48.2	1	0.7	0.0	0.4	2.9	0.7	5.2	16	97.8
48.6	2	0.7	0.0	0.4	2.9	0.7	5.3	16	98.3
48.9	3	0.7	0.0	0.3	2.8	0.7	5.4	24	99.1
49.3	4	0.7	0.0	0.3	2.7	0.8	5.4	27	99.4
50.0	5	0.7	0.0	0.3	2.6	0.8	5.5	41	99.9
50.3	6	0.7	0.0	0.3	2.6	0.8	5.5	35	99.5
50.7	7	0.7	0.0	0.3	2.6	0.8	5.5	41	99.9
51.1	8	0.7	0.0	0.3	2.6	0.8	5.5	26	99.5
51.8	11	0.7	0.0	0.4	2.7	0.7	5.4	13	99.5
52.1	12	0.7	0.0	0.4	2.6	0.8	5.5	22	99.6
52.5	13	0.7	0.0	0.3	2.5	0.8	5.6	44	99.3
53.2	14	0.7	0.0	0.2	2.5	0.9	5.6	50	99.3
53.6	15	0.7	0.0	0.2	2.4	0.9	5.7	57	99.0
53.9	16	0.7	0.0	0.3	2.5	0.8	5.6	38	98.9
54.6	1	0.7	0.0	0.4	2.6	0.7	5.5	13	98.9
55.0	2	0.7	0.0	0.4	2.7	0.7	5.4	14	99.3
55.3	3	0.7	0.0	0.3	2.6	0.8	5.5	23	99.2
55.7	4	0.7	0.0	0.3	2.6	0.8	5.5	27	99.1
56.4	5	0.7	0.0	0.3	2.5	0.8	5.6	40	99.2
56.8	6	0.7	0.0	0.3	2.6	0.8	5.6	34	99.1
57.1	7	0.7	0.0	0.3	2.6	0.8	5.5	41	99.9
57.5	8	0.7	0.0	0.3	2.6	0.8	5.5	26	99.3
58.2	11	0.7	0.0	0.4	2.7	0.7	5.4	13	99.3

Table B.1 continued

Time on stream (hours)	Reactor #	ṅ (µmol/s)						Conversion (%)	Mass balance (%)
		He	N_2	CO	H_2O	CO_2	H_2		
58.6	12	0.7	0.0	0.3	2.6	0.8	5.5	23	99.4
58.9	13	0.7	0.0	0.3	2.5	0.8	5.6	43	98.8
59.6	14	0.7	0.0	0.2	2.5	0.9	5.6	50	98.8
60.0	15	0.7	0.0	0.2	2.4	0.9	5.7	57	99.0
60.3	16	0.7	0.0	0.3	2.5	0.8	5.6	41	99.0
61.1	1	0.7	0.0	0.4	2.7	0.7	5.4	13	99.4
61.4	2	0.7	0.0	0.4	2.7	0.7	5.4	14	99.5
61.8	3	0.7	0.0	0.3	2.6	0.7	5.5	23	99.0
62.1	4	0.7	0.0	0.3	2.6	0.8	5.5	27	99.2
62.8	5	0.7	0.0	0.3	2.6	0.8	5.6	33	99.0
63.2	6	0.7	0.0	0.3	2.6	0.8	5.5	34	98.9
63.6	7	0.7	0.0	0.3	2.5	0.9	5.6	43	99.7
63.9	8	0.7	0.0	0.3	2.6	0.8	5.5	30	99.3
64.6	11	0.7	0.0	0.4	2.7	0.7	5.4	12	99.5
65.0	12	0.7	0.0	0.4	2.6	0.8	5.5	22	100
65.4	13	0.7	0.0	0.3	2.5	0.8	5.6	43	99.3
66.1	14	0.7	0.0	0.2	2.5	0.9	5.6	50	99.2
66.4	15	0.7	0.0	0.2	2.5	0.9	5.7	56	99.1
66.8	16	0.7	0.0	0.3	2.6	0.8	5.6	41	99.5

Table B.1 continued

Time on stream (hours)	Reactor #	ṅ (µmol/s)						Conversion (%)	Mass balance (%)
		He	N_2	CO	H_2O	CO_2	H_2		
FEED I	**9**	**3.3**	**0.0**	**0.6**	**3.3**	**0.8**	**3.9**	**-**	**100**
69.5	1	3.3	0.0	0.5	3.2	0.9	4.0	14	99.2
69.9	2	3.3	0.0	0.5	3.2	0.9	4.0	16	99.4
70.2	3	3.3	0.0	0.4	3.2	0.9	4.1	25	99.3
70.6	4	3.3	0.0	0.4	3.2	0.9	4.1	30	99.3
71.3	5	3.3	0.0	0.3	3.1	1.0	4.2	47	99.2
71.7	6	3.3	0.0	0.4	3.1	1.0	4.1	38	99.3
72.0	7	3.3	0.0	0.3	3.1	1.0	4.2	46	99.6
72.4	8	3.3	0.0	0.4	3.2	0.9	4.1	29	99.4
73.1	11	3.3	0.0	0.5	3.2	0.9	4.0	14	99.9
73.5	12	3.3	0.0	0.4	3.2	0.9	4.0	24	99.7
73.8	13	3.3	0.0	0.3	3.1	1.0	4.2	50	99.2
74.5	14	3.3	0.0	0.2	3.1	1.1	4.2	59	99.2
74.9	15	3.3	0.0	0.2	3.0	1.1	4.3	67	99.2
75.2	16	3.3	0.0	0.3	3.1	1.0	4.2	47	99.4
76.0	1	3.3	0.0	0.5	3.3	0.9	4.0	14	99.8
76.3	2	3.3	0.0	0.5	3.3	0.9	4.0	16	99.9
76.7	3	3.3	0.0	0.4	3.2	0.9	4.0	26	99.5
77.0	4	3.3	0.0	0.4	3.2	0.9	4.0	30	99.9
77.7	5	3.3	0.0	0.3	3.1	1.0	4.2	48	99.0
78.1	6	3.3	0.0	0.4	3.1	1.0	4.1	39	99.2
78.5	7	3.3	0.0	0.3	3.1	1.0	4.2	48	99.4
78.8	8	3.3	0.0	0.4	3.2	0.9	4.1	29	99.4
79.5	11	3.3	0.0	0.5	3.3	0.9	4.0	15	100

Table B.1 continued

Time on stream (hours)	Reactor #	ṅ (µmol/s)						Conversion (%)	Mass balance (%)
		He	N_2	CO	H_2O	CO_2	H_2		
79.9	12	3.3	0.0	0.4	3.2	0.9	4.0	25	99.8
80.2	13	3.3	0.0	0.3	3.1	1.0	4.2	50	99.2
81.0	14	3.3	0.0	0.2	3.1	1.1	4.2	59	99.3
81.3	15	3.3	0.0	0.2	3.0	1.1	4.3	67	99.1
81.7	16	3.3	0.0	0.3	3.1	1.0	4.2	46	99.4
82.4	1	3.3	0.0	0.5	3.3	0.9	4.0	15	99.7
82.7	2	3.3	0.0	0.5	3.2	0.9	4.0	16	99.9
83.1	3	3.3	0.0	0.4	3.2	0.9	4.0	26	99.6
83.5	4	3.3	0.0	0.4	3.2	0.9	4.1	30	99.7
84.2	5	3.3	0.0	0.3	3.1	1.0	4.2	46	99.5
84.5	6	3.3	0.0	0.4	3.1	1.0	4.1	38	99.4
84.9	7	3.3	0.0	0.3	3.1	1.0	4.2	46	99.6
85.2	8	3.3	0.0	0.4	3.2	0.9	4.1	29	99.6
86.0	11	3.3	0.0	0.5	3.2	0.9	4.0	14	100
86.3	12	3.3	0.0	0.4	3.2	0.9	4.0	24	99.9
86.7	13	3.3	0.0	0.3	3.1	1.0	4.2	50	99.1
87.4	14	3.3	0.0	0.2	3.1	1.1	4.2	58	99.1
87.7	15	3.3	0.0	0.2	3.0	1.1	4.3	66	99.0
88.1	16	3.3	0.0	0.3	3.1	1.0	4.2	46	99.3

Table B.1 continued

Time on stream (hours)	Reactor #	ṅ (µmol/s)						Conversion (%)	Mass balance (%)
		He	N_2	CO	H_2O	CO_2	H_2		
FEED IV	**9**	**3.3**	**2.1**	**0.3**	**4.4**	**1.0**	**5.2**	**-**	**100**
90.8	1	3.3	2.1	0.3	4.3	1.1	5.3	22	100
91.2	2	3.3	2.1	0.2	4.3	1.1	5.3	24	100
91.6	3	3.3	2.1	0.2	4.3	1.1	5.4	38	99.8
91.9	4	3.3	2.1	0.2	4.3	1.2	5.4	44	99.8
92.6	5	3.3	2.1	0.1	4.2	1.2	5.5	65	99.6
93.0	6	3.3	2.1	0.2	4.3	1.2	5.4	52	100
93.3	7	3.3	2.1	0.1	4.2	1.2	5.4	64	99.7
93.7	8	3.3	2.1	0.2	4.3	1.2	5.4	39	99.8
94.4	11	3.3	2.1	0.3	4.3	1.1	5.3	21	99.8
94.8	12	3.3	2.1	0.3	4.2	1.2	5.4	20	99.9
95.1	13	3.3	2.1	0.1	4.2	1.2	5.5	64	99.5
95.9	14	3.3	2.1	0.1	4.2	1.2	5.5	71	99.6
96.2	15	3.3	2.1	0.1	4.2	1.3	5.5	78	99.5
96.6	16	3.3	2.1	0.1	4.2	1.2	5.4	63	99.6
97.3	1	3.3	2.1	0.2	4.3	1.1	5.3	23	99.9
97.6	2	3.3	2.1	0.2	4.3	1.1	5.3	24	99.8
98.0	3	3.3	2.1	0.2	4.3	1.1	5.4	38	99.7
98.4	4	3.3	2.1	0.2	4.2	1.2	5.4	48	99.5
99.1	5	3.3	2.1	0.1	4.2	1.2	5.4	59	99.8
99.4	6	3.3	2.1	0.1	4.3	1.2	5.4	55	99.7
99.8	7	3.3	2.1	0.1	4.2	1.2	5.4	66	99.7
100.1	8	3.3	2.1	0.2	4.3	1.2	5.4	41	99.7
100.9	11	3.3	2.1	0.3	4.3	1.1	5.3	23	99.8

Table B.1 continued

Time on stream (hours)	Reactor #	ṅ (µmol/s)						Conversion (%)	Mass balance (%)
		He	N_2	CO	H_2O	CO_2	H_2		
101.2	12	3.3	2.1	0.2	4.3	1.1	5.4	40	99.8
101.6	13	3.3	2.1	0.1	4.2	1.2	5.4	62	99.7
102.3	14	3.3	2.1	0.1	4.2	1.2	5.5	72	99.7
102.6	15	3.3	2.1	0.1	4.2	1.3	5.5	79	99.6
103.0	16	3.3	2.1	0.1	4.3	1.2	5.4	58	99.7
103.7	1	3.3	2.1	0.3	4.3	1.1	5.3	22	99.8
104.1	2	3.3	2.1	0.3	4.3	1.1	5.3	22	99.8
104.4	3	3.3	2.1	0.2	4.3	1.1	5.4	40	99.7
104.8	4	3.3	2.1	0.2	4.3	1.2	5.4	46	99.7
105.5	5	3.3	2.1	0.1	4.2	1.2	5.4	62	99.7
105.9	6	3.3	2.1	0.2	4.3	1.2	5.4	54	99.8
106.2	7	3.3	2.1	0.1	4.2	1.2	5.4	65	99.8
106.6	8	3.3	2.1	0.2	4.3	1.2	5.4	41	99.8
107.3	11	3.3	2.1	0.3	4.3	1.1	5.3	22	99.9
107.6	12	3.3	2.1	0.2	4.3	1.2	5.4	41	99.7
108.0	13	3.3	2.1	0.1	4.2	1.2	5.4	62	99.5
108.7	14	3.3	2.1	0.1	4.2	1.2	5.5	72	99.6
109.1	15	3.3	2.1	0.1	4.2	1.2	5.5	77	99.5
109.4	16	3.3	2.1	0.1	4.3	1.2	5.4	58	99.6

Table B.1 continued

Time on stream (hours)	Reactor #	ṅ (µmol/s)						Conversion (%)	Mass balance (%)
		He	N_2	CO	H_2O	CO_2	H_2		
FEED I	**9**	**3.3**	**0.4**	**0.6**	**3.3**	**0.8**	**3.9**	**-**	**100**
112.2	1	3.3	0.4	0.5	3.2	0.9	4.0	14	99.8
112.5	2	3.3	0.4	0.5	3.2	0.8	4.0	14	99.7
112.9	3	3.3	0.4	0.4	3.2	0.9	4.0	25	99.6
113.2	4	3.3	0.4	0.4	3.2	0.9	4.1	30	99.5
114.0	5	3.3	0.4	0.3	3.1	1.0	4.2	46	99.3
114.3	6	3.3	0.4	0.4	3.1	1.0	4.1	37	99.3
114.7	7	3.3	0.4	0.3	3.1	1.0	4.2	46	99.4
115.0	8	3.3	0.4	0.4	3.2	0.9	4.1	28	99.4
115.7	11	3.3	0.4	0.5	3.2	0.9	4.0	14	100
116.1	12	3.3	0.4	0.4	3.2	0.9	4.0	25	99.9
116.5	13	3.3	0.4	0.3	3.1	1.0	4.2	47	99.2
117.2	14	3.3	0.4	0.3	3.1	1.1	4.2	56	99.2
117.5	15	3.3	0.4	0.2	3.0	1.1	4.3	65	98.9
117.9	16	3.3	0.4	0.3	3.1	1.0	4.2	45	99.3
118.6	1	3.3	0.4	0.5	3.2	0.9	4.0	12	99.9
119.0	2	3.3	0.4	0.5	3.2	0.9	4.0	14	99.8
119.3	3	3.3	0.4	0.4	3.2	0.9	4.1	27	99.5
119.7	4	3.3	0.4	0.4	3.2	0.9	4.1	30	99.6
120.4	5	3.3	0.4	0.3	3.1	1.0	4.1	44	99.4
120.8	6	3.3	0.4	0.4	3.1	1.0	4.1	37	99.4
121.1	7	3.3	0.4	0.3	3.1	1.0	4.1	44	99.6
121.5	8	3.3	0.4	0.4	3.2	0.9	4.0	25	99.9
122.2	11	3.3	0.4	0.5	3.2	0.8	4.0	12	99.7

Table B.1 continued

Time on stream (hours)	Reactor #	ṅ (µmol/s)						Conversion (%)	Mass balance (%)
		He	N_2	CO	H_2O	CO_2	H_2		
122.5	12	3.3	0.4	0.4	3.2	0.9	4.0	23	99.9
122.9	13	3.3	0.4	0.3	3.1	1.0	4.2	46	99.3
123.6	14	3.3	0.4	0.3	3.0	1.0	4.2	55	98.9
124.0	15	3.3	0.4	0.2	3.0	1.1	4.3	64	98.5
124.3	16	3.3	0.4	0.3	3.1	1.0	4.1	43	99.5
125.0	1	3.3	0.4	0.5	3.2	0.8	4.0	14	99.5
125.4	2	3.3	0.4	0.5	3.2	0.9	4.0	13	100
125.8	3	3.3	0.4	0.4	3.2	0.9	4.0	24	99.8
126.1	4	3.3	0.4	0.4	3.2	0.9	4.1	29	99.6
126.8	5	3.3	0.4	0.3	3.1	1.0	4.2	46	99.4
127.2	6	3.3	0.4	0.4	3.1	0.9	4.1	36	99.3
127.5	7	3.3	0.4	0.3	3.1	1.0	4.1	43	99.7
127.9	8	3.3	0.4	0.4	3.2	0.9	4.1	28	99.4
128.6	11	3.3	0.4	0.5	3.2	0.9	4.0	16	99.7
129.0	12	3.3	0.4	0.4	3.2	0.9	4.0	24	99.8
129.3	13	3.3	0.4	0.3	3.1	1.0	4.2	45	99.3
130.0	14	3.3	0.4	0.3	3.1	1.0	4.2	54	99.4
130.4	15	3.3	0.4	0.2	3.0	1.1	4.3	63	99.2
130.8	16	3.3	0.4	0.3	3.1	1.0	4.1	43	99.3

Table B.2: Processed experimental data for the second set of kinetic experiments

Time on stream (hours)	Reactor #	ṅ (µmol/s)						Conversion (%)	Mass balance (%)
		He	N_2	CO	H_2O	CO_2	H_2		
FEED V	**9**	**0.3**	**4.2**	**0.6**	**3.9**	**1.0**	**5.2**	**-**	**100**
2.6	1	0.3	4.2	0.6	3.9	1.0	5.2	11	99.8
2.7	1	0.3	4.2	0.6	3.9	1.0	5.2	13	99.8
2.8	1	0.3	4.2	0.6	3.9	1.0	5.2	13	99.8
3.0	2	0.3	4.2	0.6	3.9	1.0	5.2	8	99.8
3.1	2	0.3	4.2	0.6	3.9	1.0	5.2	9	99.9
3.2	2	0.3	4.2	0.6	3.9	1.0	5.2	9	99.9
3.4	3	0.3	4.2	0.5	3.9	1.1	5.2	17	99.9
3.5	3	0.3	4.2	0.5	3.8	1.1	5.3	18	99.8
3.6	3	0.3	4.2	0.5	3.8	1.1	5.3	18	99.9
3.8	4	0.3	4.2	0.5	3.8	1.1	5.3	22	99.8
3.9	4	0.3	4.2	0.5	3.8	1.1	5.3	22	99.8
4.1	4	0.3	4.2	0.5	3.8	1.1	5.3	22	99.9
4.6	5	0.3	4.2	0.5	3.8	1.1	5.3	17	99.7
4.8	5	0.3	4.2	0.5	3.8	1.1	5.3	18	99.7
4.9	5	0.3	4.2	0.5	3.8	1.1	5.3	18	99.8
5.0	16	0.3	4.2	0.4	3.6	1.2	5.4	36	99.7
5.2	16	0.3	4.2	0.4	3.5	1.2	5.5	37	99.2
5.3	16	0.3	4.2	0.4	3.6	1.2	5.5	39	99.6
5.5	7	0.3	4.2	0.4	3.6	1.2	5.5	35	99.6
5.6	7	0.3	4.2	0.4	3.6	1.2	5.5	34	99.5
5.7	7	0.3	4.2	0.4	3.6	1.2	5.5	35	99.6
5.9	8	0.3	4.2	0.5	3.7	1.1	5.4	23	99.7
6.0	8	0.3	4.2	0.5	3.7	1.1	5.4	22	99.6

Table B.2 continued

Time on stream (hours)	Reactor #	ṅ (µmol/s)						Conversion (%)	Mass balance (%)
		He	N_2	CO	H_2O	CO_2	H_2		
6.1	8	0.3	4.2	0.5	3.7	1.1	5.4	22	99.6
6.3	6	0.3	4.2	0.5	3.6	1.1	5.4	26	99.6
6.4	6	0.3	4.2	0.5	3.6	1.1	5.4	26	99.4
6.5	6	0.3	4.2	0.5	3.7	1.1	5.4	26	99.6
7.5	11	0.3	4.2	0.5	3.8	1.1	5.3	15	99.9
7.6	11	0.3	4.2	0.5	3.7	1.1	5.3	17	99.8
7.7	11	0.3	4.2	0.5	3.8	1.1	5.3	18	99.8
7.9	12	0.3	4.2	0.5	3.8	1.1	5.3	19	100
8.0	12	0.3	4.2	0.5	3.8	1.1	5.3	19	99.9
8.2	12	0.3	4.2	0.5	3.7	1.1	5.3	19	99.9
8.3	13	0.3	4.2	0.5	3.7	1.1	5.4	25	99.8
8.4	13	0.3	4.2	0.5	3.7	1.1	5.4	25	99.7
8.6	13	0.3	4.2	0.5	3.7	1.1	5.4	25	99.7
8.7	14	0.3	4.2	0.4	3.6	1.2	5.4	37	99.7
8.9	14	0.3	4.2	0.4	3.6	1.2	5.4	35	99.7
9.0	14	0.3	4.2	0.4	3.6	1.2	5.4	34	99.7
9.1	15	0.3	4.2	0.3	3.5	1.3	5.5	47	99.6
9.3	15	0.3	4.2	0.3	3.5	1.3	5.6	48	99.5
9.4	15	0.3	4.2	0.3	3.5	1.3	5.6	48	99.5
10.5	1	0.3	4.2	0.6	3.7	1.1	5.3	13	99.7
10.9	2	0.3	4.2	0.6	3.8	1.0	5.2	7	99.9
11.2	3	0.3	4.2	0.5	3.7	1.1	5.4	20	99.7
11.6	4	0.3	4.2	0.5	3.6	1.1	5.4	22	99.5
12.3	5	0.3	4.2	0.5	3.7	1.1	5.3	18	99.8

Table B.2 continued

Time on stream (hours)	Reactor #	ṅ (µmol/s)						Conversion (%)	Mass balance (%)
		He	N_2	CO	H_2O	CO_2	H_2		
12.7	6	0.3	4.2	0.5	3.7	1.2	5.4	28	99.7
13.0	7	0.3	4.2	0.4	3.5	1.2	5.5	37	99.4
13.4	8	0.3	4.2	0.5	3.6	1.1	5.4	23	99.5
14.4	11	0.3	4.2	0.5	3.7	1.1	5.3	17	99.8
14.8	12	0.3	4.2	0.5	3.7	1.1	5.3	21	99.9
15.2	13	0.3	4.2	0.5	3.7	1.1	5.4	25	99.8
15.9	14	0.3	4.2	0.4	3.6	1.2	5.5	35	99.7
16.2	15	0.3	4.2	0.3	3.5	1.3	5.6	48	99.5
16.6	16	0.3	4.2	0.4	3.5	1.2	5.5	40	99.6
17.3	1	0.3	4.2	0.6	3.8	1.1	5.3	14	99.7
17.7	2	0.3	4.2	0.6	3.8	1.0	5.2	7	99.9
18.0	3	0.3	4.2	0.5	3.7	1.1	5.4	20	99.7
18.4	4	0.3	4.2	0.5	3.7	1.1	5.4	24	99.8
19.1	5	0.3	4.2	0.5	3.7	1.1	5.3	17	99.8
19.4	6	0.3	4.2	0.5	3.7	1.1	5.4	27	99.8
19.8	7	0.3	4.2	0.4	3.6	1.2	5.4	40	100
20.2	8	0.3	4.2	0.5	3.7	1.1	5.3	23	99.9
21.2	11	0.3	4.2	0.5	3.7	1.1	5.3	17	99.8
21.6	12	0.3	4.2	0.5	3.7	1.1	5.3	22	100
21.9	13	0.3	4.2	0.5	3.7	1.1	5.3	24	100
22.7	14	0.3	4.2	0.4	3.6	1.2	5.4	37	99.8
23.0	15	0.3	4.2	0.3	3.5	1.3	5.5	48	99.8
23.4	16	0.3	4.2	0.4	3.5	1.2	5.5	39	99.6

Table B.2 continued

Time on stream (hours)	Reactor #	ṅ (µmol/s)						Conversion (%)	Mass balance (%)
		He	N_2	CO	H_2O	CO_2	H_2		
FEED VI	**9.2**	**0.3**	**2.2**	**1.2**	**3.0**	**0.7**	**3.8**	**-**	**100**
26.1	1	0.3	2.2	1.1	2.9	0.8	3.9	9	99.6
26.5	2	0.3	2.2	1.2	2.9	0.8	3.8	5	99.9
26.8	3	0.3	2.2	1.1	2.8	0.9	4.0	13	99.6
27.2	4	0.3	2.2	1.1	2.8	0.9	4.0	14	99.6
27.9	5	0.3	2.2	1.1	2.9	0.8	3.9	11	99.8
28.3	6	0.3	2.2	1.0	2.8	0.9	4.0	16	99.6
28.6	7	0.3	2.2	1.0	2.7	1.0	4.1	23	99.8
29.0	8	0.3	2.2	1.1	2.8	0.9	4.0	13	99.5
30.0	11	0.3	2.2	1.1	2.8	0.9	4.0	9	99.7
30.4	12	0.3	2.2	1.1	2.8	0.9	4.0	11	99.9
30.8	13	0.3	2.2	1.1	2.8	0.9	4.0	14	99.6
31.5	14	0.3	2.2	1.0	2.7	1.0	4.1	20	99.6
31.8	15	0.3	2.2	0.9	2.6	1.1	4.2	27	99.4
32.2	16	0.3	2.2	1.0	2.7	1.0	4.1	22	99.5
32.9	1	0.3	2.2	1.1	2.9	0.8	3.9	8	99.9
33.3	2	0.3	2.2	1.2	2.9	0.8	3.8	4	100
33.6	3	0.3	2.2	1.1	2.8	0.9	4.0	11	99.7
34.0	4	0.3	2.2	1.1	2.8	0.9	4.0	13	99.8
34.7	5	0.3	2.2	1.1	2.9	0.8	3.9	9	99.9
35.0	6	0.3	2.2	1.0	2.8	0.9	4.0	16	99.6
35.4	7	0.3	2.2	1.0	2.7	1.0	4.1	21	99.8
35.8	8	0.3	2.2	1.1	2.7	0.9	4.0	11	99.5
36.8	11	0.3	2.2	1.1	2.8	0.8	3.9	9	99.8

Table B.2 continued

Time on stream (hours)	Reactor #	ṅ (µmol/s)						Conversion (%)	Mass balance (%)
		He	N_2	CO	H_2O	CO_2	H_2		
37.2	12	0.3	2.2	1.1	2.8	0.9	4.0	12	99.6
37.5	13	0.3	2.2	1.1	2.8	0.9	4.0	13	99.5
38.3	14	0.3	2.2	1.0	2.7	1.0	4.1	19	99.6
38.6	15	0.3	2.2	0.9	2.6	1.0	4.2	25	99.5
39.0	16	0.3	2.2	1.0	2.7	1.0	4.1	20	99.7
39.7	1	0.3	2.2	1.2	2.9	0.8	3.9	7	99.7
40.1	2	0.3	2.2	1.2	2.9	0.8	3.9	4	99.9
40.4	3	0.3	2.2	1.1	2.8	0.9	4.0	11	99.7
40.8	4	0.3	2.2	1.1	2.8	0.9	4.0	12	99.7
41.5	5	0.3	2.2	1.1	2.8	0.8	3.9	9	99.8
41.8	6	0.3	2.2	1.1	2.8	0.9	4.0	15	99.7
42.2	7	0.3	2.2	1.0	2.7	1.0	4.1	20	99.9
42.6	8	0.3	2.2	1.1	2.8	0.9	3.9	12	99.8
43.6	11	0.3	2.2	1.1	2.9	0.8	3.9	9	100
44.0	12	0.3	2.2	1.1	2.9	0.9	3.9	11	99.9
44.3	13	0.3	2.2	1.1	2.9	0.9	3.9	12	99.9
45.1	14	0.3	2.2	1.0	2.8	1.0	4.0	19	99.9
45.4	15	0.3	2.2	0.9	2.6	1.0	4.1	25	99.6
45.8	16	0.3	2.2	1.0	2.7	1.0	4.1	19	99.6

Table B.2 continued

Time on stream (hours)	Reactor #	ṅ (µmol/s)						Conversion (%)	Mass balance (%)
		He	N_2	CO	H_2O	CO_2	H_2		
FEED VII	**9.2**	**0.3**	**5.5**	**0.7**	**3.1**	**1.0**	**5.5**	**-**	**100**
48.5	1	0.3	5.5	0.6	3.1	1.1	5.5	8	99.8
48.9	2	0.3	5.5	0.7	3.1	1.1	5.5	3	100
49.2	3	0.3	5.5	0.6	3.0	1.1	5.5	12	100
49.6	4	0.3	5.5	0.6	3.0	1.1	5.6	15	100
50.3	5	0.3	5.5	0.6	3.0	1.1	5.5	11	100
50.7	6	0.3	5.5	0.6	3.0	1.1	5.6	18	100
51.0	7	0.3	5.5	0.5	2.9	1.2	5.7	27	99.9
51.4	8	0.3	5.5	0.6	3.0	1.1	5.6	13	99.8
52.4	11	0.3	5.5	0.6	3.0	1.1	5.6	12	99.7
52.8	12	0.3	5.5	0.6	3.0	1.1	5.6	14	99.8
53.2	13	0.3	5.5	0.6	2.9	1.1	5.6	16	99.6
53.9	14	0.3	5.5	0.5	2.9	1.2	5.7	23	99.7
54.2	15	0.3	5.5	0.5	2.8	1.2	5.7	32	99.7
54.6	16	0.3	5.5	0.5	2.9	1.2	5.7	26	99.8
55.3	1	0.3	5.5	0.6	3.0	1.1	5.6	9	99.8
55.7	2	0.3	5.5	0.7	3.1	1.1	5.5	3	100
56.0	3	0.3	5.5	0.6	3.0	1.1	5.6	15	99.8
56.4	4	0.3	5.5	0.6	3.0	1.1	5.6	17	99.8
57.1	5	0.3	5.5	0.6	3.0	1.1	5.6	12	99.9
57.4	6	0.3	5.5	0.5	2.9	1.2	5.7	19	99.7
57.8	7	0.3	5.5	0.5	2.9	1.2	5.7	27	99.8
58.2	8	0.3	5.5	0.6	3.0	1.1	5.6	14	99.7
59.2	11	0.3	5.5	0.6	3.0	1.1	5.6	13	99.9

Table B.2 continued

Time on stream (hours)	Reactor #	ṅ (µmol/s)						Conversion (%)	Mass balance (%)
		He	N_2	CO	H_2O	CO_2	H_2		
59.6	12	0.3	5.5	0.6	3.0	1.1	5.6	14	99.9
59.9	13	0.3	5.5	0.6	3.0	1.1	5.6	16	99.9
60.7	14	0.3	5.5	0.5	3.0	1.2	5.6	23	99.9
61.0	15	0.3	5.5	0.5	2.9	1.2	5.7	32	99.9
61.4	16	0.3	5.5	0.5	2.9	1.2	5.7	26	99.9
62.1	1	0.3	5.5	0.6	3.0	1.1	5.5	10	99.9
62.4	2	0.3	5.5	0.7	3.1	1.1	5.5	4	100
62.8	3	0.3	5.5	0.6	3.0	1.1	5.6	15	99.8
63.2	4	0.3	5.5	0.6	3.0	1.1	5.6	17	99.8
63.9	5	0.3	5.5	0.6	3.0	1.1	5.6	12	99.9
64.2	6	0.3	5.5	0.5	2.9	1.2	5.6	19	99.8
64.6	7	0.3	5.5	0.5	2.9	1.2	5.7	28	99.8
64.9	8	0.3	5.5	0.6	3.0	1.1	5.6	14	99.7
66.0	11	0.3	5.5	0.6	3.0	1.1	5.6	13	99.8
66.4	12	0.3	5.5	0.6	3.0	1.1	5.6	16	99.9
66.7	13	0.3	5.5	0.6	2.9	1.1	5.6	15	99.7
67.4	14	0.3	5.5	0.5	2.9	1.2	5.7	24	99.8
67.8	15	0.3	5.5	0.5	2.9	1.2	5.7	32	99.8
68.2	16	0.3	5.5	0.5	3.0	1.2	5.6	25	99.9

Table B.2 continued

Time on stream (hours)	Reactor #	ṅ (µmol/s)						Conversion (%)	Mass balance (%)
		He	N_2	CO	H_2O	CO_2	H_2		
FEED VIII	**9.2**	**0.3**	**2.0**	**0.5**	**3.1**	**1.7**	**3.7**	**-**	**100**
70.9	1	0.3	2.0	0.4	3.0	1.8	3.8	13	99.6
71.3	2	0.3	2.0	0.5	3.1	1.7	3.7	4	99.7
71.6	3	0.3	2.0	0.4	3.0	1.8	3.8	21	99.6
72.0	4	0.3	2.0	0.4	3.0	1.8	3.8	24	99.6
72.7	5	0.3	2.0	0.4	3.0	1.8	3.8	16	99.7
73.1	6	0.3	2.0	0.3	2.9	1.8	3.8	27	99.6
73.4	7	0.3	2.0	0.3	2.9	1.9	3.9	40	100
73.8	8	0.3	2.0	0.4	3.0	1.8	3.8	19	99.7
74.8	11	0.3	2.0	0.4	3.0	1.8	3.8	17	99.9
75.2	12	0.3	2.0	0.4	3.0	1.8	3.8	21	99.9
75.6	13	0.3	2.0	0.4	3.0	1.8	3.8	22	99.9
76.3	14	0.3	2.0	0.3	2.9	1.9	3.9	29	99.9
76.6	15	0.3	2.0	0.3	2.9	1.9	3.9	40	99.8
77.0	16	0.3	2.0	0.3	2.9	1.9	3.9	34	99.8
77.7	1	0.3	2.0	0.4	3.0	1.8	3.8	12	99.9
78.1	2	0.3	2.0	0.5	3.1	1.7	3.7	3	99.9
78.4	3	0.3	2.0	0.4	3.0	1.8	3.8	21	99.8
78.8	4	0.3	2.0	0.4	2.9	1.8	3.8	23	99.8
79.5	5	0.3	2.0	0.4	3.0	1.8	3.8	16	99.9
79.8	6	0.3	2.0	0.4	2.9	1.9	3.9	27	99.7
80.2	7	0.3	2.0	0.3	2.9	1.9	3.9	40	100
80.6	8	0.3	2.0	0.4	3.0	1.8	3.8	20	99.8
81.6	11	0.3	2.0	0.4	3.0	1.8	3.8	18	100

Table B.2 continued

Time on stream (hours)	Reactor #	ṅ (µmol/s)						Conversion (%)	Mass balance (%)
		He	N_2	CO	H_2O	CO_2	H_2		
82.0	12	0.3	2.0	0.4	3.0	1.8	3.8	22	99.9
82.3	13	0.3	2.0	0.4	3.0	1.8	3.8	21	99.6
83.1	14	0.3	2.0	0.3	2.9	1.9	3.8	31	99.8
83.4	15	0.3	2.0	0.3	2.9	1.9	3.9	41	99.6
83.8	16	0.3	2.0	0.3	2.9	1.9	3.9	36	99.7
84.5	1	0.3	2.0	0.4	3.0	1.8	3.7	13	99.9
84.8	2	0.3	2.0	0.5	3.1	1.7	3.7	2	100
85.2	3	0.3	2.0	0.4	3.0	1.8	3.8	21	99.8
85.6	4	0.3	2.0	0.4	3.0	1.8	3.8	25	99.9
86.3	5	0.3	2.0	0.4	3.0	1.8	3.8	16	99.9
86.6	6	0.3	2.0	0.4	2.9	1.9	3.8	27	99.8
87.0	7	0.3	2.0	0.3	2.9	1.9	3.9	40	100
87.3	8	0.3	2.0	0.4	3.0	1.8	3.8	20	99.8
88.4	11	0.3	2.0	0.4	3.0	1.8	3.8	18	100
88.8	12	0.3	2.0	0.4	3.0	1.8	3.8	22	99.9
89.1	13	0.3	2.0	0.4	3.0	1.8	3.8	21	99.9
89.8	14	0.3	2.0	0.3	2.9	1.9	3.9	32	99.5
90.2	15	0.3	2.0	0.3	2.9	1.9	3.9	41	99.7
90.6	16	0.3	2.0	0.3	2.9	1.9	3.9	33	99.7

Table B.2 continued

Time on stream (hours)	Reactor #	ṅ (µmol/s)						Conversion (%)	Mass balance (%)
		He	N_2	CO	H_2O	CO_2	H_2		
FEED V	**9.2**	**0.3**	**4.2**	**0.6**	**3.9**	**1.0**	**5.2**	**-**	**100**
93.3	1	0.3	4.2	0.5	3.9	1.1	5.2	13	99.9
93.7	2	0.3	4.2	0.6	4.0	1.0	5.2	4	99.7
94.0	3	0.3	4.2	0.5	3.8	1.1	5.3	19	100
94.4	4	0.3	4.2	0.5	3.8	1.1	5.3	23	100
95.1	5	0.3	4.2	0.6	3.8	1.1	5.3	13	100
95.4	6	0.3	4.2	0.5	3.8	1.1	5.3	25	99.8
95.8	7	0.3	4.2	0.4	3.7	1.2	5.4	36	100
96.2	8	0.3	4.2	0.5	3.8	1.1	5.3	22	99.9
97.2	11	0.3	4.2	0.5	3.8	1.1	5.3	15	99.9
97.6	12	0.3	4.2	0.5	3.8	1.1	5.3	20	100
97.9	13	0.3	4.2	0.5	3.8	1.1	5.3	19	99.8
98.7	14	0.3	4.2	0.5	3.7	1.2	5.4	28	99.7
99.0	15	0.3	4.2	0.4	3.6	1.3	5.5	40	99.6
99.4	16	0.3	4.2	0.4	3.7	1.2	5.4	31	99.8
100.1	1	0.3	4.2	0.6	3.8	1.1	5.3	12	99.8
100.5	2	0.3	4.2	0.7	3.9	1.0	5.2	-2	99.9
100.8	3	0.3	4.2	0.5	3.8	1.1	5.4	19	99.5
101.2	4	0.3	4.2	0.5	3.7	1.1	5.4	24	99.6
101.9	5	0.3	4.2	0.6	3.8	1.1	5.3	14	99.7
102.2	6	0.3	4.2	0.5	3.7	1.1	5.4	24	99.7
102.6	7	0.3	4.2	0.4	3.7	1.2	5.4	36	99.7
103.0	8	0.3	4.2	0.5	3.8	1.1	5.3	21	99.7
104.0	11	0.3	4.2	0.5	3.7	1.1	5.4	15	99.7

Table B.2 continued

Time on stream (hours)	Reactor #	ṅ (µmol/s)						Conversion (%)	Mass balance (%)
		He	N_2	CO	H_2O	CO_2	H_2		
104.4	12	0.3	4.2	0.5	3.8	1.1	5.3	21	100
104.7	13	0.3	4.2	0.5	3.8	1.1	5.3	19	100
105.5	14	0.3	4.2	0.5	3.7	1.2	5.4	28	99.8
105.8	15	0.3	4.2	0.4	3.7	1.2	5.4	39	99.8
106.2	16	0.3	4.2	0.4	3.7	1.2	5.4	31	99.8
106.9	1	0.3	4.2	0.6	3.8	1.1	5.3	12	99.8
107.2	2	0.3	4.2	0.7	3.9	1.0	5.2	-2	100
107.6	3	0.3	4.2	0.5	3.8	1.1	5.3	19	99.8
108.0	4	0.3	4.2	0.5	3.8	1.1	5.3	21	99.8
108.7	5	0.3	4.2	0.6	3.8	1.1	5.3	14	99.8
109.0	6	0.3	4.2	0.5	3.7	1.1	5.4	26	99.7
109.4	7	0.3	4.2	0.4	3.7	1.2	5.4	36	99.8
109.7	8	0.3	4.2	0.5	3.8	1.1	5.3	16	99.8
110.8	11	0.3	4.2	0.5	3.8	1.1	5.3	16	99.9
111.2	12	0.3	4.2	0.5	3.8	1.1	5.3	21	99.7
111.5	13	0.3	4.2	0.5	3.8	1.1	5.3	19	99.6
112.2	14	0.3	4.2	0.5	3.7	1.2	5.4	28	99.7
112.6	15	0.3	4.2	0.4	3.7	1.2	5.5	37	99.7
113.0	16	0.3	4.2	0.4	3.7	1.2	5.4	31	99.7

Table B.2 continued

Time on stream (hours)	Reactor #	ṅ (µmol/s)						Conversion (%)	Mass balance (%)
		He	N_2	CO	H_2O	CO_2	H_2		
FEED IX	**9.2**	**0.3**	**1.7**	**0.7**	**7.4**	**1.1**	**5.6**	**-**	**100**
115.7	1	0.3	1.7	0.5	7.3	1.2	5.7	17	99.9
116.1	2	0.3	1.7	0.7	7.5	1.1	5.6	0	99.9
116.4	3	0.3	1.7	0.5	7.2	1.3	5.8	25	99.9
116.8	4	0.3	1.7	0.5	7.2	1.3	5.8	31	99.9
117.5	5	0.3	1.7	0.6	7.3	1.2	5.8	19	99.9
117.8	6	0.3	1.7	0.5	7.2	1.3	5.9	35	99.6
118.2	7	0.3	1.7	0.4	7.1	1.4	6.0	48	99.9
118.6	8	0.3	1.7	0.5	7.2	1.3	5.9	33	99.7
119.6	11	0.3	1.7	0.6	7.3	1.2	5.8	22	99.9
120.0	12	0.3	1.7	0.5	7.2	1.3	5.9	32	99.9
120.3	13	0.3	1.7	0.5	7.3	1.3	5.8	25	99.8
121.1	14	0.3	1.7	0.4	7.2	1.4	5.9	39	99.9
121.4	15	0.3	1.7	0.3	7.0	1.5	6.0	53	99.8
121.8	16	0.3	1.7	0.4	7.1	1.4	5.9	41	99.8
122.5	1	0.3	1.7	0.6	7.3	1.2	5.8	17	99.7
122.8	2	0.3	1.7	0.7	7.4	1.1	5.6	-1	99.9
123.2	3	0.3	1.7	0.5	7.2	1.3	5.8	25	99.7
123.6	4	0.3	1.7	0.5	7.1	1.3	5.9	32	99.6
124.3	5	0.3	1.7	0.6	7.2	1.2	5.8	19	99.7
124.6	6	0.3	1.7	0.5	7.1	1.3	5.9	34	99.6
125.0	7	0.3	1.7	0.4	7.0	1.4	6.0	48	99.8
125.3	8	0.3	1.7	0.5	7.1	1.3	5.9	33	99.6
126.4	11	0.3	1.7	0.6	7.2	1.2	5.8	20	99.8

Table B.2 continued

Time on stream (hours)	Reactor #	ṅ (µmol/s)						Conversion (%)	Mass balance (%)
		He	N_2	CO	H_2O	CO_2	H_2		
126.8	12	0.3	1.7	0.5	7.2	1.3	5.9	30	99.8
127.1	13	0.3	1.7	0.5	7.2	1.3	5.8	24	99.8
127.8	14	0.3	1.7	0.4	7.1	1.4	5.9	39	99.7
128.2	15	0.3	1.7	0.3	7.0	1.5	6.1	53	99.6
128.6	16	0.3	1.7	0.4	7.1	1.4	6.0	42	99.6
129.3	1	0.3	1.7	0.6	7.3	1.2	5.8	16	99.8
129.6	2	0.3	1.7	0.7	7.4	1.1	5.6	-2	100
130.0	3	0.3	1.7	0.5	7.2	1.3	5.8	25	99.7
130.4	4	0.3	1.7	0.5	7.2	1.3	5.9	31	99.7
131.1	5	0.3	1.7	0.6	7.2	1.2	5.8	20	99.5
131.4	6	0.3	1.7	0.5	7.1	1.3	5.9	35	99.4
131.8	7	0.3	1.7	0.4	7.1	1.4	6.0	48	99.7
132.1	8	0.3	1.7	0.5	7.1	1.3	5.9	33	99.5
133.2	11	0.3	1.7	0.6	7.2	1.2	5.8	22	99.8
133.6	12	0.3	1.7	0.5	7.2	1.3	5.9	30	99.8
133.9	13	0.3	1.7	0.5	7.2	1.3	5.8	24	99.7
134.6	14	0.3	1.7	0.4	7.1	1.4	5.9	38	99.7
135.0	15	0.3	1.7	0.3	7.0	1.5	6.0	52	99.7
135.4	16	0.3	1.7	0.4	7.1	1.4	6.0	41	99.7

Table B.2 continued

Time on stream (hours)	Reactor #	ṅ (µmol/s)						Conversion (%)	Mass balance (%)
		He	N_2	CO	H_2O	CO_2	H_2		
FEED X	**9.2**	**0.3**	**5.7**	**0.8**	**4.8**	**0.8**	**6.5**	**-**	**100**
138.1	1	0.3	5.7	0.7	4.7	0.8	6.6	10	99.9
138.5	2	0.3	5.7	0.8	4.9	0.8	6.5	-1	99.9
138.8	3	0.3	5.7	0.7	4.7	0.9	6.6	17	100
139.2	4	0.3	5.7	0.6	4.7	0.9	6.7	20	99.9
139.9	5	0.3	5.7	0.7	4.7	0.9	6.6	12	99.8
140.2	6	0.3	5.7	0.6	4.6	0.9	6.7	22	99.8
140.6	7	0.3	5.7	0.5	4.5	1.0	6.8	33	99.7
141.0	8	0.3	5.7	0.7	4.7	0.9	6.7	19	99.9
142.0	11	0.3	5.7	0.7	4.7	0.9	6.6	13	100
142.4	12	0.3	5.7	0.7	4.7	0.9	6.6	18	100
142.7	13	0.3	5.7	0.7	4.7	0.9	6.7	14	99.8
143.5	14	0.3	5.7	0.6	4.6	1.0	6.8	24	99.7
143.8	15	0.3	5.7	0.5	4.5	1.0	6.9	35	99.5
144.2	16	0.3	5.7	0.6	4.6	1.0	6.8	26	99.6
144.9	1	0.3	5.7	0.7	4.7	0.8	6.6	10	99.9
145.3	2	0.3	5.7	0.8	4.9	0.7	6.5	-1	100
145.6	3	0.3	5.7	0.7	4.7	0.9	6.6	16	99.9
146.0	4	0.3	5.7	0.6	4.7	0.9	6.7	20	99.8
146.7	5	0.3	5.7	0.7	4.7	0.9	6.6	12	99.8
147.0	6	0.3	5.7	0.6	4.6	0.9	6.7	22	99.7
147.4	7	0.3	5.7	0.5	4.5	1.0	6.8	32	99.6
147.8	8	0.3	5.7	0.6	4.7	0.9	6.7	20	99.7
148.8	11	0.3	5.7	0.7	4.7	0.9	6.7	13	99.8

Table B.2 continued

Time on stream (hours)	Reactor #	ṅ (µmol/s)						Conversion (%)	Mass balance (%)
		He	N_2	CO	H_2O	CO_2	H_2		
149.2	12	0.3	5.7	0.7	4.7	0.9	6.7	18	99.7
149.5	13	0.3	5.7	0.7	4.7	0.9	6.7	15	99.8
150.3	14	0.3	5.7	0.6	4.6	0.9	6.8	24	99.6
150.6	15	0.3	5.7	0.5	4.5	1.0	6.9	34	99.6
151.0	16	0.3	5.7	0.6	4.6	1.0	6.8	26	99.6
151.7	1	0.3	5.7	0.7	4.7	0.8	6.6	9	99.8
152.0	2	0.3	5.7	0.8	4.9	0.7	6.5	-1	100
152.4	3	0.3	5.7	0.7	4.7	0.9	6.6	17	99.9
152.8	4	0.3	5.7	0.6	4.7	0.9	6.7	19	99.8
153.5	5	0.3	5.7	0.7	4.7	0.8	6.6	11	99.9
153.8	6	0.3	5.7	0.6	4.7	0.9	6.7	21	99.8
154.2	7	0.3	5.7	0.6	4.6	1.0	6.8	31	99.7
154.5	8	0.3	5.7	0.7	4.7	0.9	6.7	18	99.7
155.6	11	0.3	5.7	0.7	4.7	0.9	6.7	13	99.7
156.0	12	0.3	5.7	0.7	4.7	0.9	6.7	18	99.9
156.3	13	0.3	5.7	0.7	4.7	0.9	6.7	15	99.8
157.0	14	0.3	5.7	0.6	4.6	1.0	6.8	24	99.7
157.4	15	0.3	5.7	0.5	4.5	1.0	6.8	34	99.7
157.8	16	0.3	5.7	0.6	4.6	1.0	6.8	26	99.6

Table B.2 continued

Time on stream (hours)	Reactor #	ṅ (µmol/s)						Conversion (%)	Mass balance (%)
		He	N_2	CO	H_2O	CO_2	H_2		
FEED V	**9.2**	**0.3**	**4.2**	**0.6**	**3.9**	**1.0**	**5.2**	**-**	**100**
160.5	1	0.3	4.2	0.5	3.8	1.0	5.3	11	99.8
160.9	2	0.3	4.2	0.7	3.9	1.0	5.2	-3	99.9
161.2	3	0.3	4.2	0.5	3.8	1.1	5.3	18	99.8
161.6	4	0.3	4.2	0.5	3.7	1.1	5.3	21	99.8
162.3	5	0.3	4.2	0.6	3.8	1.1	5.3	13	99.9
162.6	6	0.3	4.2	0.5	3.7	1.1	5.4	24	99.7
163.0	7	0.3	4.2	0.4	3.7	1.2	5.4	33	99.8
163.4	8	0.3	4.2	0.5	3.8	1.1	5.3	17	99.8
164.4	11	0.3	4.2	0.5	3.8	1.1	5.3	15	100
164.8	12	0.3	4.2	0.5	3.8	1.1	5.3	19	100
165.1	13	0.3	4.2	0.5	3.8	1.1	5.3	18	99.9
165.9	14	0.3	4.2	0.5	3.7	1.1	5.4	28	99.8
166.2	15	0.3	4.2	0.4	3.7	1.2	5.4	38	99.8
166.6	16	0.3	4.2	0.5	3.7	1.2	5.4	29	99.8
167.3	1	0.3	4.2	0.6	3.9	1.0	5.2	11	100
167.6	2	0.3	4.2	0.7	4.0	1.0	5.1	-2	99.8
168.0	3	0.3	4.2	0.5	3.8	1.1	5.3	19	100
168.4	4	0.3	4.2	0.5	3.8	1.1	5.3	21	99.8
169.1	5	0.3	4.2	0.6	3.9	1.1	5.2	13	99.9
169.4	6	0.3	4.2	0.5	3.8	1.1	5.3	24	99.8
169.8	7	0.3	4.2	0.4	3.7	1.2	5.4	34	99.9
170.1	8	0.3	4.2	0.5	3.8	1.1	5.3	19	99.9
171.2	11	0.3	4.2	0.6	3.8	1.1	5.3	15	99.9

Table B.2 continued

Time on stream (hours)	Reactor #	ṅ (µmol/s)						Conversion (%)	Mass balance (%)
		He	N_2	CO	H_2O	CO_2	H_2		
171.6	12	0.3	4.2	0.6	3.8	1.1	5.3	15	100
171.9	13	0.3	4.2	0.5	3.8	1.1	5.3	17	99.8
172.6	14	0.3	4.2	0.5	3.7	1.2	5.4	29	99.7
173.0	15	0.3	4.2	0.4	3.6	1.2	5.5	38	99.7
173.4	16	0.3	4.2	0.5	3.7	1.2	5.4	29	99.8
174.1	1	0.3	4.2	0.6	3.8	1.0	5.3	11	99.9
174.4	2	0.3	4.2	0.7	3.9	1.0	5.2	-2	99.9
174.8	3	0.3	4.2	0.5	3.8	1.1	5.3	19	99.9
175.2	4	0.3	4.2	0.5	3.7	1.1	5.4	21	99.8
175.9	5	0.3	4.2	0.6	3.8	1.1	5.3	12	100
176.2	6	0.3	4.2	0.5	3.7	1.1	5.4	24	99.8
176.6	7	0.3	4.2	0.4	3.7	1.2	5.4	34	99.9
176.9	8	0.3	4.2	0.5	3.7	1.1	5.4	21	99.7
178.0	11	0.3	4.2	0.6	3.8	1.1	5.3	13	100
178.4	12	0.3	4.2	0.5	3.8	1.1	5.3	19	99.6
178.7	13	0.3	4.2	0.5	3.8	1.1	5.3	17	99.7
179.4	14	0.3	4.2	0.5	3.7	1.1	5.4	26	99.8
179.8	15	0.3	4.2	0.4	3.6	1.2	5.5	37	99.7
180.2	16	0.3	4.2	0.4	3.7	1.2	5.4	31	99.8

Table B.2 continued

Time on stream (hours)	Reactor #	ṅ (µmol/s)						Conversion (%)	Mass balance (%)
		He	N_2	CO	H_2O	CO_2	H_2		
FEED VII	**9.2**	**0.3**	**5.5**	**0.7**	**3.1**	**1.0**	**5.5**	**-**	**100**
195.3	1	0.3	5.5	0.6	3.0	1.1	5.5	8	99.8
195.7	2	0.3	5.5	0.7	3.1	1.0	5.4	-2	99.9
196.0	3	0.3	5.5	0.6	3.0	1.1	5.6	14	99.8
196.4	4	0.3	5.5	0.6	2.9	1.1	5.6	16	99.8
197.1	5	0.3	5.5	0.6	3.0	1.1	5.5	8	99.8
197.5	6	0.3	5.5	0.6	2.9	1.1	5.6	17	99.8
197.8	7	0.3	5.5	0.5	2.9	1.2	5.7	26	99.8
198.2	8	0.3	5.5	0.6	3.0	1.1	5.6	11	99.9
199.3	11	0.3	5.5	0.6	3.0	1.1	5.5	10	99.9
199.6	12	0.3	5.5	0.6	3.0	1.1	5.6	13	100
200.0	13	0.3	5.5	0.6	3.0	1.1	5.6	13	99.9
200.7	14	0.3	5.5	0.5	2.9	1.2	5.6	20	99.8
201.0	15	0.3	5.5	0.5	2.8	1.2	5.7	27	99.7
201.4	16	0.3	5.5	0.5	2.9	1.2	5.6	21	99.8
202.1	1	0.3	5.5	0.6	3.0	1.1	5.5	7	99.9
202.5	2	0.3	5.5	0.7	3.1	1.0	5.5	-2	100
202.8	3	0.3	5.5	0.6	3.0	1.1	5.6	14	99.9
203.2	4	0.3	5.5	0.6	2.9	1.1	5.6	16	99.8
203.9	5	0.3	5.5	0.6	3.0	1.1	5.5	9	99.9
204.3	6	0.3	5.5	0.6	2.9	1.1	5.6	17	99.6
204.6	7	0.3	5.5	0.5	2.8	1.2	5.7	26	99.7
205.0	8	0.3	5.5	0.6	2.9	1.1	5.6	11	99.7
206.0	11	0.3	5.5	0.6	3.0	1.1	5.6	11	99.9

Table B.2 continued

Time on stream (hours)	Reactor #	ṅ (µmol/s)						Conversion (%)	Mass balance (%)
		He	N_2	CO	H_2O	CO_2	H_2		
206.4	12	0.3	5.5	0.6	3.0	1.1	5.6	13	99.9
206.8	13	0.3	5.5	0.6	3.0	1.1	5.6	13	99.9
207.5	14	0.3	5.5	0.5	2.9	1.2	5.6	21	99.8
207.8	15	0.3	5.5	0.5	2.8	1.2	5.7	29	99.8
208.2	16	0.3	5.5	0.5	2.9	1.2	5.6	21	99.9
208.9	1	0.3	5.5	0.6	3.0	1.1	5.5	7	99.9
209.3	2	0.3	5.5	0.7	3.1	1.0	5.4	-1	100
209.6	3	0.3	5.5	0.6	3.0	1.1	5.6	12	99.9
210.0	4	0.3	5.5	0.6	2.9	1.1	5.6	15	99.9
210.7	5	0.3	5.5	0.6	3.0	1.1	5.5	9	100
211.0	6	0.3	5.5	0.6	2.9	1.1	5.6	18	99.9
211.4	7	0.3	5.5	0.5	2.9	1.2	5.6	26	99.9
211.8	8	0.3	5.5	0.6	3.0	1.1	5.6	12	99.9
212.8	11	0.3	5.5	0.6	3.0	1.1	5.5	11	100
213.2	12	0.3	5.5	0.6	3.0	1.1	5.5	14	100
213.5	13	0.3	5.5	0.6	3.0	1.1	5.5	13	99.9
214.3	14	0.3	5.5	0.5	3.0	1.2	5.6	22	99.9
214.6	15	0.3	5.5	0.5	2.9	1.2	5.6	30	100
215.0	16	0.3	5.5	0.5	2.9	1.2	5.6	22	100

Table B.2 continued

Time on stream (hours)	Reactor #	ṅ (µmol/s)						Conversion (%)	Mass balance (%)
		He	N_2	CO	H_2O	CO_2	H_2		
FEED V	**9.2**	**0.3**	**4.2**	**0.6**	**3.9**	**1.0**	**5.2**	**-**	**100**
217.7	1	0.3	4.2	0.5	3.9	1.0	5.2	10	99.8
218.1	2	0.3	4.2	0.7	4.0	1.0	5.1	-1	99.9
218.4	3	0.3	4.2	0.5	3.8	1.1	5.3	18	99.9
218.8	4	0.3	4.2	0.5	3.8	1.1	5.3	20	99.9
219.5	5	0.3	4.2	0.6	3.7	1.1	5.3	12	99.5
219.9	6	0.3	4.2	0.5	3.6	1.2	5.4	24	99.4
220.2	7	0.3	4.2	0.4	3.7	1.2	5.4	34	99.7
220.6	8	0.3	4.2	0.6	3.8	1.1	5.3	15	99.7
221.6	11	0.3	4.2	0.6	3.8	1.1	5.3	14	99.8
222.0	12	0.3	4.2	0.5	3.8	1.1	5.3	19	99.8
222.4	13	0.3	4.2	0.5	3.8	1.1	5.3	17	99.7
223.1	14	0.3	4.2	0.5	3.7	1.1	5.4	25	99.8
223.4	15	0.3	4.2	0.4	3.7	1.2	5.4	35	99.8
223.8	16	0.3	4.2	0.5	3.7	1.2	5.4	29	99.8
224.5	1	0.3	4.2	0.6	3.9	1.0	5.2	9	99.9
224.9	2	0.3	4.2	0.7	3.9	1.0	5.2	-2	100
225.2	3	0.3	4.2	0.5	3.8	1.1	5.3	18	99.8
225.6	4	0.3	4.2	0.5	3.8	1.1	5.3	21	99.8
226.3	5	0.3	4.2	0.6	3.8	1.1	5.3	12	99.9
226.7	6	0.3	4.2	0.5	3.8	1.1	5.3	23	99.8
227.0	7	0.3	4.2	0.4	3.7	1.2	5.4	33	99.8
227.4	8	0.3	4.2	0.5	3.8	1.1	5.3	21	99.7
228.4	11	0.3	4.2	0.6	3.8	1.1	5.3	15	100

Table B.2 continued

Time on stream (hours)	Reactor #	ṅ (µmol/s)						Conversion (%)	Mass balance (%)
		He	N_2	CO	H_2O	CO_2	H_2		
228.8	12	0.3	4.2	0.5	3.8	1.1	5.3	20	100
229.2	13	0.3	4.2	0.5	3.8	1.1	5.3	16	99.8
229.9	14	0.3	4.2	0.5	3.7	1.1	5.3	24	99.9
230.2	15	0.3	4.2	0.4	3.7	1.2	5.4	38	99.8
230.6	16	0.3	4.2	0.5	3.7	1.2	5.4	28	99.8
231.3	1	0.3	4.2	0.6	3.8	1.0	5.3	10	99.8
231.7	2	0.3	4.2	0.7	3.9	1.0	5.1	-2	99.9
232.0	3	0.3	4.2	0.5	3.8	1.1	5.3	18	99.9
232.4	4	0.3	4.2	0.5	3.8	1.1	5.3	22	99.9
233.1	5	0.3	4.2	0.6	3.8	1.1	5.3	12	99.9
233.4	6	0.3	4.2	0.5	3.8	1.1	5.3	23	99.8
233.8	7	0.3	4.2	0.4	3.7	1.2	5.4	33	99.9
234.2	8	0.3	4.2	0.5	3.8	1.1	5.4	22	99.6
235.2	11	0.3	4.2	0.5	3.9	1.1	5.2	15	100
235.6	12	0.3	4.2	0.5	3.8	1.1	5.3	20	99.9
235.9	13	0.3	4.2	0.5	3.9	1.1	5.3	17	99.9
236.7	14	0.3	4.2	0.5	3.7	1.2	5.4	29	99.9
237.0	15	0.3	4.2	0.4	3.7	1.2	5.4	37	99.8
237.4	16	0.3	4.2	0.5	3.7	1.2	5.4	28	99.9

B.2. Pressure Experiments

Table B.3 below lists the processed experimental data for the pressure experiments (Figure 6.22 Chapter 6). Unlike the tables presented before, every time the total system pressure changes the table will start on a new page and the first entry in the table will indicate the new total system pressure. Feed samples are represented by reactor 15 and details regarding feed composition can be found in Chapter 6 section 4.2.

Table B.3: Processed experimental data for the pressure experiments

Time on stream (hours)	Reactor #	ṅ (µmol/s)						Conversion (%)	Mass balance (%)
		He	N_2	CO	H_2O	CO_2	H_2		
P = 1 bar(g)	**15**	**0.3**	**3.5**	**0.5**	**3.4**	**0.8**	**4.3**	**-**	**100.0**
2.4	1	0.3	3.5	0.3	3.3	1.0	4.5	37	99.8
2.5	1	0.3	3.5	0.3	3.3	1.0	4.5	41	99.8
2.7	1	0.3	3.5	0.3	3.2	1.0	4.6	41	99.7
3.2	3	0.3	3.5	0.4	3.4	0.9	4.4	16	99.9
3.4	3	0.3	3.5	0.4	3.3	0.9	4.5	22	99.8
3.5	3	0.3	3.5	0.4	3.3	0.9	4.4	18	99.8
4.5	5	0.3	3.5	0.3	3.1	1.1	4.6	49	99.6
4.6	5	0.3	3.5	0.2	3.1	1.1	4.7	53	99.4
4.7	5	0.3	3.5	0.2	3.1	1.1	4.7	54	99.5
7.3	11	0.3	3.5	0.4	3.3	1.0	4.5	23	99.9
7.5	11	0.3	3.5	0.4	3.3	1.0	4.5	24	99.8
7.6	11	0.3	3.5	0.4	3.3	1.0	4.5	24	99.7
7.7	12	0.3	3.5	0.4	3.3	1.0	4.5	27	99.9
7.9	12	0.3	3.5	0.4	3.3	1.0	4.5	27	99.8
8.0	12	0.3	3.5	0.4	3.2	1.0	4.5	27	99.8
8.2	13	0.3	3.5	0.3	3.2	1.1	4.6	44	99.6
8.3	13	0.3	3.5	0.3	3.1	1.1	4.6	46	99.5
8.4	13	0.3	3.5	0.3	3.1	1.1	4.6	46	99.5
8.6	14	0.3	3.5	0.3	3.2	1.1	4.6	42	99.7

Table B.3 continued

Time on stream (hours)	Reactor #	ṅ (µmol/s)						Conversion (%)	Mass balance (%)
		He	N_2	CO	H_2O	CO_2	H_2		
8.7	14	0.3	3.5	0.3	3.2	1.1	4.6	42	99.6
8.8	14	0.3	3.5	0.3	3.2	1.1	4.6	42	99.6
9.0	6	0.3	3.5	0.2	3.1	1.1	4.7	58	99.4
9.1	6	0.3	3.5	0.2	3.1	1.2	4.7	59	99.5
9.2	6	0.3	3.5	0.2	3.1	1.2	4.7	59	99.4
10.2	1	0.3	3.5	0.3	3.2	1.1	4.6	45	99.6
10.7	3	0.3	3.5	0.4	3.3	0.9	4.5	20	99.6
11.5	5	0.3	3.5	0.2	3.1	1.1	4.7	58	99.6
13.2	11	0.3	3.5	0.4	3.3	1.0	4.5	26	99.9
13.4	12	0.3	3.5	0.4	3.3	1.0	4.5	29	100.0
13.7	13	0.3	3.5	0.3	3.2	1.1	4.6	47	99.8
14.3	14	0.3	3.5	0.3	3.1	1.1	4.6	47	99.8
14.5	6	0.3	3.5	0.2	3.1	1.1	4.7	58	99.5
15.4	1	0.3	3.5	0.3	3.2	1.1	4.6	47	99.7
15.9	3	0.3	3.5	0.4	3.3	0.9	4.5	21	99.6
16.7	5	0.3	3.5	0.2	3.1	1.1	4.7	57	99.6
18.4	11	0.3	3.5	0.4	3.3	1.0	4.5	25	99.9
18.6	12	0.3	3.5	0.4	3.3	1.0	4.5	30	100.0
18.9	13	0.3	3.5	0.3	3.1	1.1	4.6	47	99.6
19.4	14	0.3	3.5	0.3	3.2	1.1	4.6	43	99.7
19.7	6	0.3	3.5	0.2	3.1	1.2	4.7	60	99.5
20.5	1	0.3	3.5	0.3	3.1	1.1	4.7	48	99.5
21.1	3	0.3	3.5	0.4	3.2	1.0	4.5	20	99.8
21.9	5	0.3	3.5	0.2	3.1	1.2	4.7	56	99.7

Table B.3 continued

Time on stream (hours)	Reactor #	ṅ (µmol/s)						Conversion (%)	Mass balance (%)
		He	N_2	CO	H_2O	CO_2	H_2		
23.5	11	0.3	3.5	0.4	3.2	1.0	4.6	28	99.5
23.8	12	0.3	3.5	0.4	3.2	1.0	4.6	31	99.9
24.1	13	0.3	3.5	0.3	3.1	1.1	4.7	49	99.6
24.6	14	0.3	3.5	0.3	3.1	1.1	4.6	48	99.8
24.9	6	0.3	3.5	0.2	3.0	1.2	4.7	59	99.6

Table B.3 continued

Time on stream (hours)	Reactor #	ṅ (µmol/s)						Conversion (%)	Mass balance (%)
		He	N_2	CO	H_2O	CO_2	H_2		
P=2.7bar(g)	**15**	**0.3**	**3.5**	**0.5**	**3.5**	**0.9**	**4.3**	**-**	**100.0**
27.8	1	0.3	3.5	0.3	3.2	1.1	4.7	53	99.5
28.3	3	0.3	3.5	0.4	3.4	1.0	4.5	24	99.7
29.1	5	0.3	3.5	0.2	3.2	1.2	4.7	60	99.5
30.8	11	0.3	3.5	0.4	3.3	1.0	4.5	31	99.8
31.0	12	0.3	3.5	0.3	3.3	1.1	4.6	35	99.8
31.3	13	0.3	3.5	0.2	3.2	1.1	4.7	53	99.5
31.8	14	0.3	3.5	0.3	3.2	1.1	4.6	49	99.7
32.1	6	0.3	3.5	0.2	3.1	1.2	4.7	62	99.4
32.9	1	0.3	3.5	0.3	3.2	1.1	4.7	52	99.5
33.5	3	0.3	3.5	0.4	3.4	1.0	4.5	23	99.6
34.3	5	0.3	3.5	0.2	3.1	1.2	4.7	62	99.5
35.9	11	0.3	3.5	0.4	3.3	1.0	4.5	30	99.8
36.2	12	0.3	3.5	0.4	3.3	1.1	4.6	34	99.8
36.5	13	0.3	3.5	0.2	3.2	1.2	4.7	54	99.5
37.0	14	0.3	3.5	0.3	3.2	1.1	4.6	49	99.7
37.3	6	0.3	3.5	0.2	3.1	1.2	4.7	62	99.4
38.1	1	0.3	3.5	0.3	3.2	1.1	4.7	52	99.5
38.7	3	0.3	3.5	0.4	3.4	1.0	4.5	23	99.8
39.5	5	0.3	3.5	0.2	3.2	1.2	4.7	58	99.6
41.1	11	0.3	3.5	0.4	3.4	1.0	4.5	30	99.8
41.4	12	0.3	3.5	0.4	3.3	1.0	4.5	34	99.9
41.7	13	0.3	3.5	0.2	3.2	1.1	4.7	54	99.6
42.2	14	0.3	3.5	0.3	3.2	1.1	4.6	48	99.6

Table B.3 continued

Time on stream (hours)	Reactor #	ṅ (µmol/s)						Conversion (%)	Mass balance (%)
		He	N_2	CO	H_2O	CO_2	H_2		
42.5	6	0.3	3.5	0.2	3.1	1.2	4.7	63	99.3
43.3	1	0.3	3.5	0.3	3.2	1.1	4.7	50	99.5
43.9	3	0.3	3.5	0.4	3.4	1.0	4.5	22	99.7
44.7	5	0.3	3.5	0.2	3.1	1.2	4.7	57	99.4
46.3	11	0.3	3.5	0.4	3.3	1.0	4.5	30	99.8
46.6	12	0.3	4.0	0.4	2.8	1.1	4.6	34	97.9
46.9	13	0.3	3.5	0.2	3.2	1.1	4.7	53	99.3
47.4	14	0.3	3.5	0.3	3.2	1.1	4.7	47	99.4
47.7	6	0.3	3.5	0.2	3.1	1.2	4.7	60	99.3
48.5	1	0.3	3.5	0.3	3.2	1.1	4.7	50	99.6
49.0	3	0.3	3.5	0.4	3.4	1.0	4.5	22	99.8
49.9	5	0.3	3.5	0.2	3.2	1.2	4.7	56	99.6
51.5	11	0.3	3.5	0.4	3.3	1.0	4.5	30	99.7
51.8	12	0.3	3.5	0.4	3.3	1.1	4.6	34	99.8
52.0	13	0.3	3.5	0.3	3.2	1.1	4.7	52	99.4
52.6	14	0.3	3.5	0.3	3.2	1.1	4.6	47	99.7
52.9	6	0.3	3.5	0.2	3.1	1.2	4.7	59	99.5
53.7	1	0.3	3.5	0.3	3.2	1.1	4.7	50	99.5
54.2	3	0.3	3.5	0.4	3.4	1.0	4.5	22	99.8
55.0	5	0.3	3.5	0.2	3.2	1.2	4.7	57	99.6
56.7	11	0.3	3.5	0.4	3.4	1.0	4.5	30	99.7
56.9	12	0.3	3.5	0.4	3.3	1.1	4.6	34	99.8
57.2	13	0.3	3.5	0.3	3.2	1.1	4.7	50	99.7
57.8	14	0.3	3.5	0.3	3.2	1.1	4.6	47	99.7

Table B.3 continued

Time on stream (hours)	Reactor #	ṅ (µmol/s)						Conversion (%)	Mass balance (%)
		He	N_2	CO	H_2O	CO_2	H_2		
58.0	6	0.3	3.5	0.2	3.1	1.2	4.7	58	99.5
58.9	1	0.3	3.5	0.3	3.2	1.1	4.7	50	99.6
59.4	3	0.3	3.5	0.4	3.4	1.0	4.5	22	99.9
60.2	5	0.3	3.5	0.2	3.2	1.2	4.7	55	99.8
62.2	11	0.3	3.5	0.4	3.5	1.0	4.4	30	99.9
62.5	12	0.3	3.5	0.4	3.4	1.0	4.5	34	99.8
62.8	13	0.3	3.5	0.3	3.4	1.1	4.5	52	99.9
63.3	14	0.3	3.5	0.3	3.4	1.1	4.5	45	99.9
63.6	6	0.3	3.5	0.2	3.2	1.2	4.7	57	99.5

Table B.3 continued

Time on stream (hours)	Reactor #	ṅ (µmol/s)						Conversion (%)	Mass balance (%)
		He	N_2	CO	H_2O	CO_2	H_2		
P=4.4bar(g)	**15**	**0.3**	**3.5**	**0.5**	**3.5**	**0.9**	**4.3**	**-**	**100.0**
66.5	1	0.3	3.5	0.3	3.2	1.1	4.6	53	99.6
67.0	3	0.3	3.5	0.4	3.4	1.0	4.5	24	99.8
67.8	5	0.3	3.5	0.2	3.2	1.2	4.7	58	99.6
69.5	11	0.3	3.5	0.4	3.3	1.0	4.6	33	99.7
69.7	12	0.3	3.5	0.3	3.3	1.1	4.6	36	99.7
70.0	13	0.3	3.5	0.2	3.2	1.2	4.7	56	99.4
70.6	14	0.3	3.5	0.3	3.2	1.1	4.7	50	99.6
70.8	6	0.3	3.5	0.2	3.1	1.2	4.7	60	99.4
71.6	1	0.3	3.5	0.3	3.2	1.1	4.7	53	99.6
72.2	3	0.3	3.5	0.4	3.4	1.0	4.5	22	99.8
73.0	5	0.3	3.5	0.2	3.1	1.2	4.7	57	99.5
74.6	11	0.3	3.5	0.4	3.3	1.0	4.6	32	99.8
74.9	12	0.3	3.5	0.3	3.3	1.1	4.6	35	99.9
75.2	13	0.3	3.5	0.2	3.1	1.2	4.7	55	99.6
75.7	14	0.3	3.5	0.3	3.2	1.1	4.7	49	99.7
76.0	6	0.3	3.5	0.2	3.1	1.2	4.7	58	99.5
76.8	1	0.3	3.5	0.3	3.2	1.1	4.7	52	99.7
77.4	3	0.3	3.5	0.4	3.4	1.0	4.5	22	99.9
78.2	5	0.3	3.5	0.2	3.1	1.2	4.7	56	99.5
79.8	11	0.3	3.5	0.4	3.3	1.0	4.6	31	99.9
80.1	12	0.3	3.5	0.3	3.3	1.1	4.6	35	99.9
80.4	13	0.3	3.5	0.2	3.2	1.2	4.7	54	99.7
80.9	14	0.3	3.5	0.3	3.2	1.1	4.6	48	99.8

Table B.3 continued

Time on stream (hours)	Reactor #	ṅ (µmol/s)						Conversion (%)	Mass balance (%)
		He	N_2	CO	H_2O	CO_2	H_2		
81.2	6	0.3	3.5	0.2	3.1	1.2	4.7	58	99.6
82.0	1	0.3	3.5	0.3	3.2	1.1	4.6	52	99.8
82.6	3	0.3	3.5	0.4	3.4	1.0	4.5	22	100.0
83.4	5	0.3	3.5	0.2	3.2	1.2	4.7	55	99.7
85.0	11	0.3	3.5	0.4	3.3	1.0	4.5	31	100.0
85.3	12	0.3	3.5	0.4	3.3	1.1	4.6	30	100.0
85.6	13	0.3	3.5	0.2	3.2	1.1	4.7	54	99.7
86.1	14	0.3	3.5	0.3	3.2	1.1	4.6	48	99.8
86.4	6	0.3	3.5	0.2	3.2	1.2	4.7	56	99.6
87.2	1	0.3	3.5	0.3	3.2	1.1	4.6	51	99.8
87.7	3	0.3	3.5	0.4	3.4	1.0	4.5	22	99.9
88.6	5	0.3	3.5	0.2	3.2	1.1	4.7	55	99.6
90.2	11	0.3	3.5	0.4	3.4	1.0	4.5	31	99.9
90.5	12	0.3	3.5	0.4	3.3	1.0	4.5	35	99.8
90.7	13	0.3	3.5	0.3	3.2	1.1	4.7	53	99.4
91.3	14	0.3	3.5	0.4	3.0	1.1	4.8	32	99.1
91.6	6	0.3	3.5	0.2	3.2	1.1	4.7	56	99.5

Table B.3 continued

Time on stream (hours)	Reactor #	ṅ (µmol/s)						Conversion (%)	Mass balance (%)
		He	N_2	CO	H_2O	CO_2	H_2		
P = 7 bar(g)	**15**	**0.3**	**3.5**	**0.5**	**3.5**	**0.9**	**4.3**	**-**	**100.0**
94.4	1	0.3	3.5	0.2	3.2	1.1	4.7	56	99.6
95.0	3	0.3	3.5	0.4	3.4	1.0	4.4	19	99.9
95.8	5	0.3	3.5	0.2	3.1	1.1	4.7	55	99.6
97.4	11	0.3	3.5	0.4	3.3	1.0	4.5	33	99.7
97.7	12	0.3	3.5	0.3	3.3	1.1	4.5	36	99.8
98.0	13	0.3	3.5	0.2	3.1	1.2	4.7	55	99.6
98.5	14	0.3	3.5	0.3	3.2	1.1	4.6	49	99.7
98.8	6	0.3	3.5	0.2	3.1	1.2	4.7	59	99.5
99.6	1	0.3	3.5	0.2	3.1	1.1	4.7	55	99.3
100.1	3	0.3	3.5	0.4	3.3	1.0	4.5	22	99.6
101.0	5	0.3	3.5	0.2	3.2	1.1	4.7	56	99.7
102.6	11	0.3	3.5	0.4	3.3	1.0	4.5	33	99.8
102.9	12	0.3	3.5	0.3	3.3	1.1	4.5	36	99.9
103.1	13	0.3	3.5	0.2	3.1	1.2	4.7	56	99.5
103.7	14	0.3	3.5	0.3	3.2	1.1	4.6	48	99.7
104.0	6	0.3	3.5	0.2	3.1	1.2	4.7	57	99.6
104.8	1	0.3	3.5	0.3	3.2	1.1	4.7	53	99.6
105.3	3	0.3	3.5	0.4	3.3	1.0	4.5	21	99.7
106.1	5	0.3	3.5	0.2	3.1	1.1	4.7	55	99.6
107.8	11	0.3	3.5	0.4	3.3	1.0	4.6	32	99.7
108.0	12	0.3	3.5	0.4	3.3	1.0	4.5	35	99.8
108.3	13	0.3	3.5	0.2	3.1	1.1	4.7	54	99.4
108.9	14	0.3	3.5	0.3	3.2	1.1	4.6	48	99.6

Table B.3 continued

Time on stream (hours)	Reactor #	ṅ (µmol/s)						Conversion (%)	Mass balance (%)
		He	N_2	CO	H_2O	CO_2	H_2		
109.1	6	0.3	3.5	0.2	3.2	1.1	4.7	55	99.6

Table B.3 continued

Time on stream (hours)	Reactor #	ṅ (µmol/s)						Conversion (%)	Mass balance (%)
		He	N_2	CO	H_2O	CO_2	H_2		
P = 1 bar(g)	**15**	**0.3**	**3.5**	**0.5**	**3.5**	**0.9**	**4.3**	**-**	**100.0**
112.0	1	0.3	3.5	0.4	3.3	1.0	4.5	35	100.0
112.1	1	0.3	3.5	0.3	3.3	1.1	4.6	37	99.8
112.3	1	0.3	3.5	0.3	3.3	1.1	4.6	37	99.6
112.8	3	0.3	3.5	0.5	3.4	0.9	4.4	14	99.8
113.0	3	0.3	3.5	0.5	3.4	0.9	4.4	15	99.7
113.1	3	0.3	3.5	0.5	3.4	0.9	4.4	15	99.7
114.1	5	0.3	3.5	0.3	3.3	1.1	4.6	41	99.9
114.2	5	0.3	3.5	0.3	3.3	1.1	4.6	44	99.8
114.3	5	0.3	3.5	0.3	3.3	1.1	4.6	44	99.7
116.9	11	0.3	3.5	0.4	3.4	1.0	4.5	21	99.8
117.1	11	0.3	3.5	0.4	3.4	1.0	4.5	21	99.8
117.2	11	0.3	3.5	0.4	3.4	1.0	4.5	22	99.7
117.4	12	0.3	3.5	0.4	3.3	1.0	4.5	26	99.8
117.5	12	0.3	3.5	0.4	3.3	1.0	4.5	27	99.7
117.6	12	0.3	3.5	0.4	3.3	1.0	4.5	26	99.7
117.8	13	0.3	3.5	0.3	3.3	1.1	4.6	37	99.5
117.9	13	0.3	3.5	0.3	3.2	1.1	4.6	38	99.5
118.0	13	0.3	3.5	0.3	3.2	1.1	4.6	38	99.5
118.2	14	0.3	3.5	0.4	3.3	1.0	4.6	35	99.6
118.3	14	0.3	3.5	0.4	3.3	1.0	4.6	35	99.6
118.4	14	0.3	3.5	0.4	3.3	1.0	4.6	35	99.6
118.6	6	0.3	3.5	0.3	3.2	1.1	4.6	42	99.4
118.7	6	0.3	3.5	0.3	3.2	1.1	4.6	43	99.4

Table B.3 continued

Time on stream (hours)	Reactor #	ṅ (µmol/s)						Conversion (%)	Mass balance (%)
		He	N_2	CO	H_2O	CO_2	H_2		
118.8	6	0.3	3.5	0.3	3.2	1.1	4.6	43	99.4
119.8	1	0.3	3.5	0.3	3.3	1.1	4.6	37	99.7
120.3	3	0.3	3.5	0.5	3.4	0.9	4.4	15	99.8
121.1	5	0.3	3.5	0.3	3.2	1.1	4.6	41	99.7
122.8	11	0.3	3.5	0.4	3.4	1.0	4.5	22	100.0
123.1	12	0.3	3.5	0.4	3.3	1.0	4.5	26	99.9
123.3	13	0.3	3.5	0.3	3.3	1.1	4.6	40	99.8
123.9	14	0.3	3.5	0.4	3.3	1.0	4.5	34	99.9
124.1	6	0.3	3.5	0.3	3.2	1.1	4.6	42	99.7
125.0	1	0.3	3.5	0.3	3.3	1.1	4.6	37	99.8
125.5	3	0.3	3.5	0.5	3.4	0.9	4.4	15	99.9
126.3	5	0.3	3.5	0.3	3.3	1.1	4.6	40	99.8
128.0	11	0.3	3.5	0.4	3.4	1.0	4.5	22	99.9
128.2	12	0.3	3.5	0.4	3.3	1.0	4.5	25	99.9
128.5	13	0.3	3.5	0.3	3.3	1.1	4.6	39	99.7
129.1	14	0.3	3.5	0.4	3.3	1.0	4.5	35	99.8
129.3	6	0.3	3.5	0.3	3.2	1.1	4.6	42	99.6

Appendix C: Supporting Experimental Information

This appendix contains supporting information for Chapter 5.

C.1. Experimental Results

The figures presented below show the time-on-stream performance for both sets of kinetic experiments. The figures are grouped per temperature setpoint and aim to give a clearer view of the experimental data. The feed conditions are represented by roman numerals in the figures that follow. Details on the feed conditions can be found in Table A.1 in Appendix A.

C.1.1. First Set of Kinetic Experiments

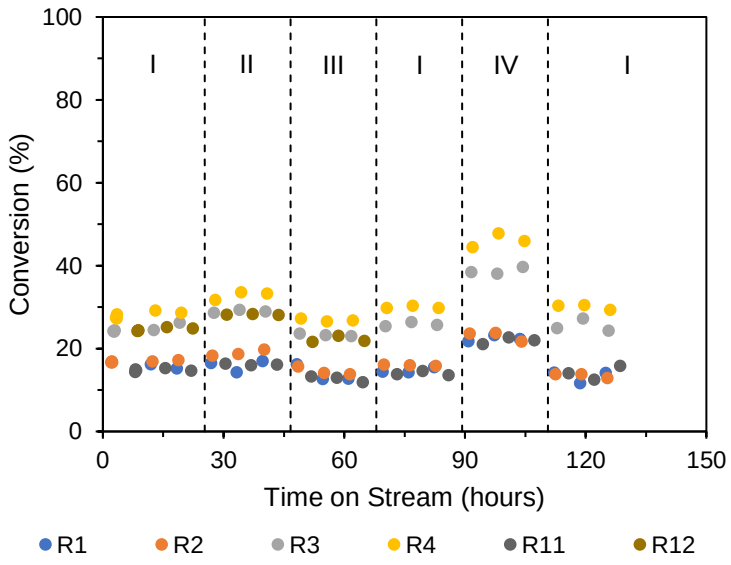

Figure C.1: Time-on-stream performance under experimental conditions for the first set of kinetic experiments at 275 °C

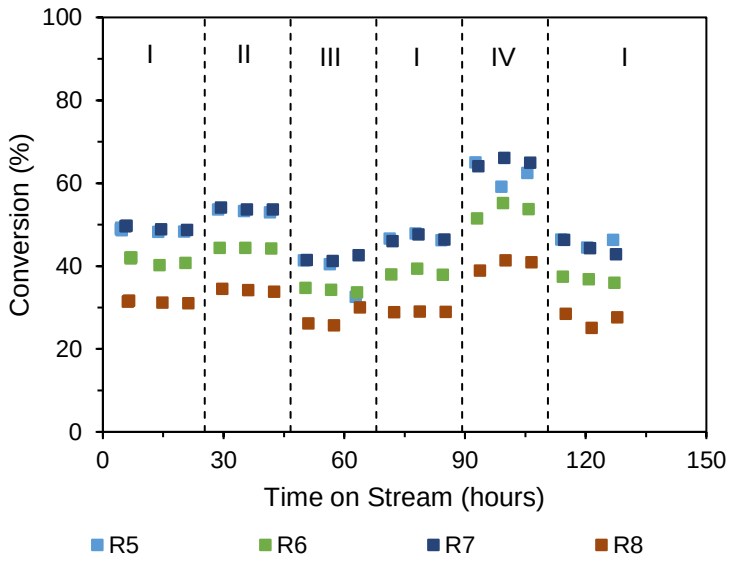

Figure C.2: Time-on-stream performance under experimental conditions for the first set of kinetic experiments at 300 °C

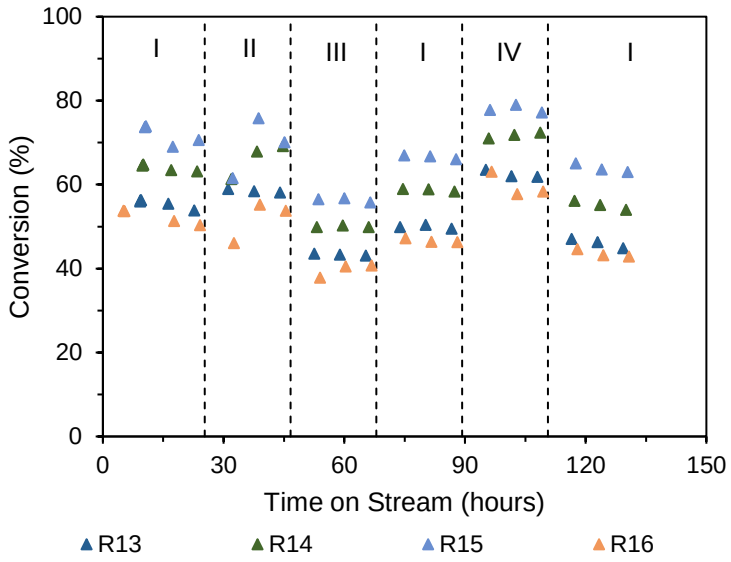

Figure C.3: Time-on-stream performance under experimental conditions for the first set of kinetic experiments at 325 °C

C.1.2. Second Set of Kinetic Experiments

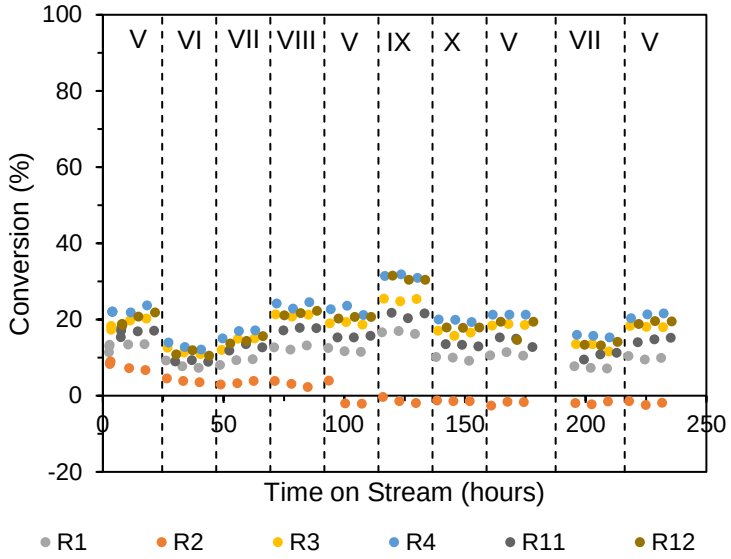

Figure C.4: Time-on-stream performance under experimental conditions for the second set of kinetic experiments at 270 °C

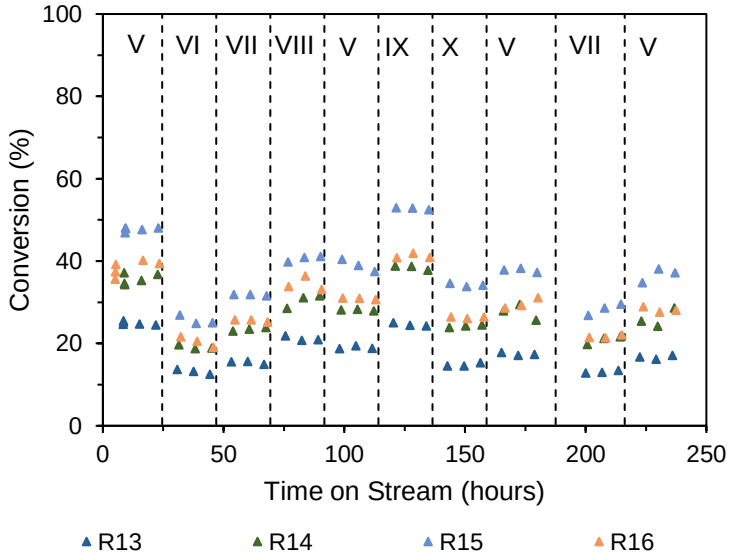

Figure C.5: Time-on-stream performance under experimental conditions for the second set of kinetic experiments at 285 °C

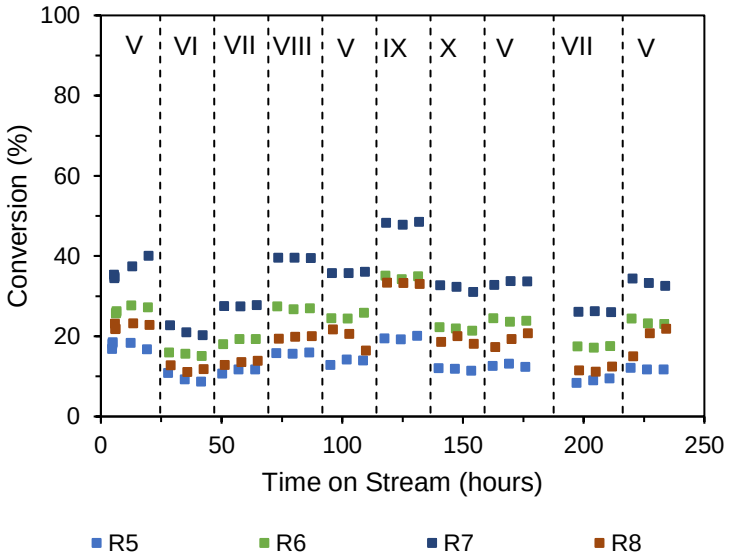

Figure C.6: Time-on-stream performance under experimental conditions for the second set of kinetic experiments at 300 °C

C.2. Trends Observed

The figures presented below aim to better depict the effect that changing feed conditions has on the reaction rate. It is recommended that the figures presented are read together with Table A.1 in Appendix A, which contains the feed conditions. The feed conditions are represented by roman numerals in the figures that follow.

Since space velocity was changed during experiments, the time-on-stream data that has been presented before does not always clearly show the effect. To show the effect of changing feed conditions has on the reaction rate, an average reaction rate has been calculated over the catalyst bed. This was done by assuming a linear concentration profile over the catalyst bed. The average reaction rate can then be calculated as follows:

$$r_{rate,average} = \frac{\dot{F}_{CO,in} - \dot{F}_{CO,out}}{w} \qquad \text{Equation C.1}$$

Where:

$r_{rate,average}$ is the average reaction rate over the catalyst bed

$\dot{F}_{CO,in}$ is the molar flow rate of CO into the reactor

$\dot{F}_{CO,out}$ is the molar flow rate of CO out of the reactor

w is the catalyst weight

A summary of the observed effects is presented in Table 5.4 of Chapter 5.

C.2.1. First Set of Kinetic Experiments

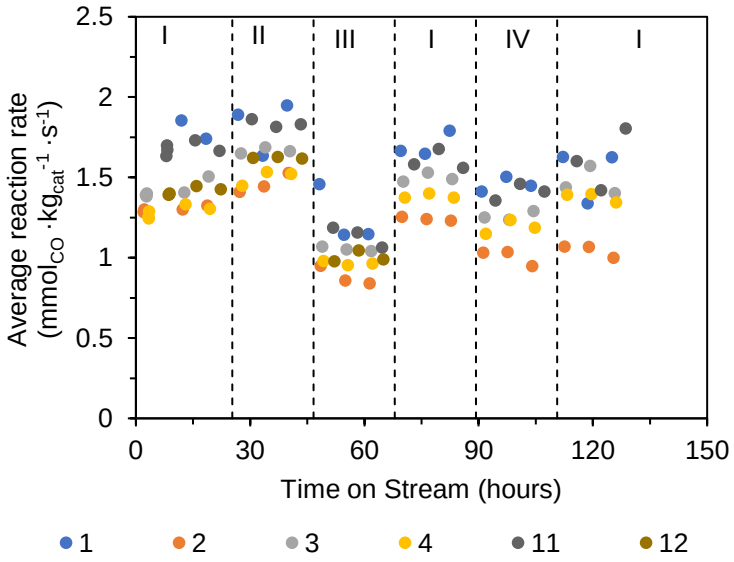

Figure C.7: Calculated average reaction rate for the first set of kinetic experiments at 275 °C

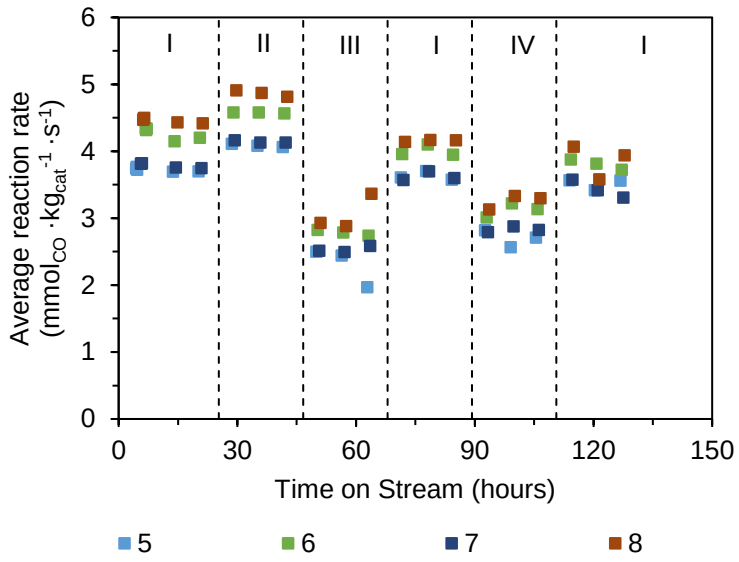

Figure C.8: Calculated average reaction rate for the first set of kinetic experiments at 300 °C

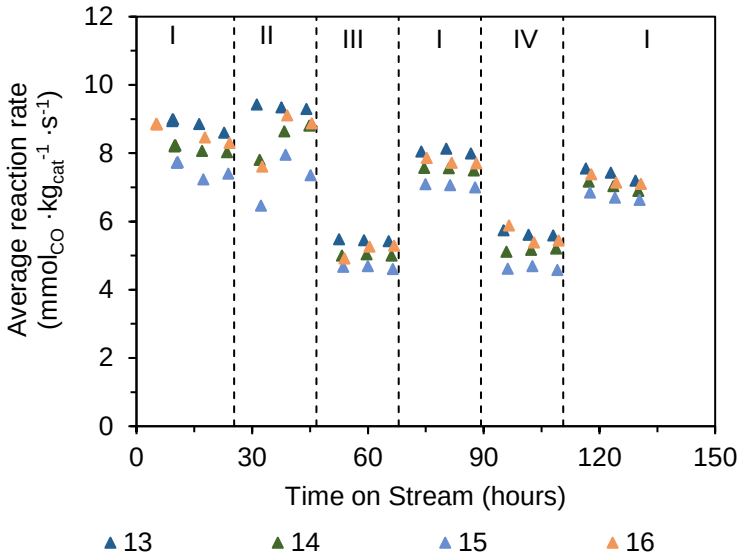

Figure C.9: Calculated average reaction rate for the first set of kinetic experiments at 325 °C

C.2.2. Second Set of Kinetic Experiments

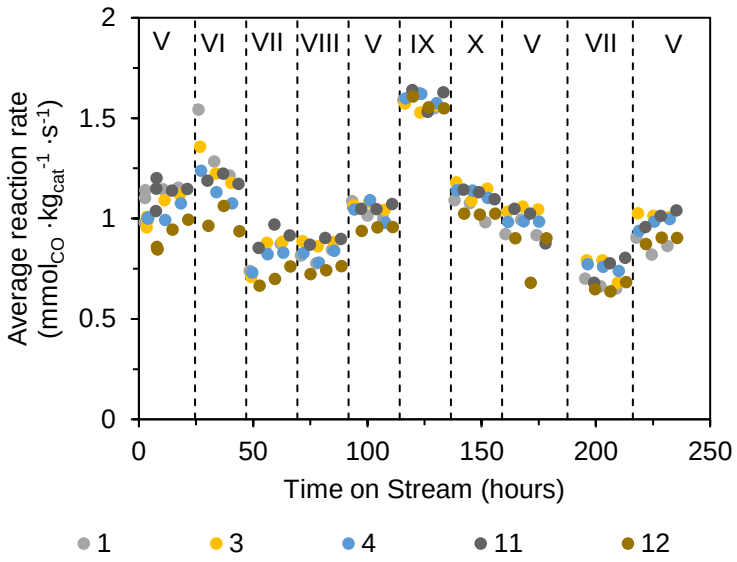

Figure C.10: Calculated average reaction rate for the second set of kinetic experiments at 270 °C

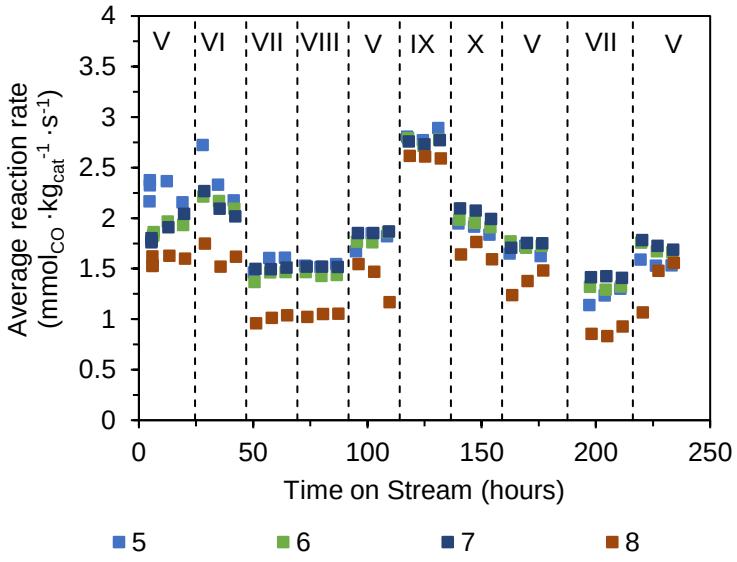

Figure C.11: Calculated average reaction rate for the second set of kinetic experiments at 285 °C

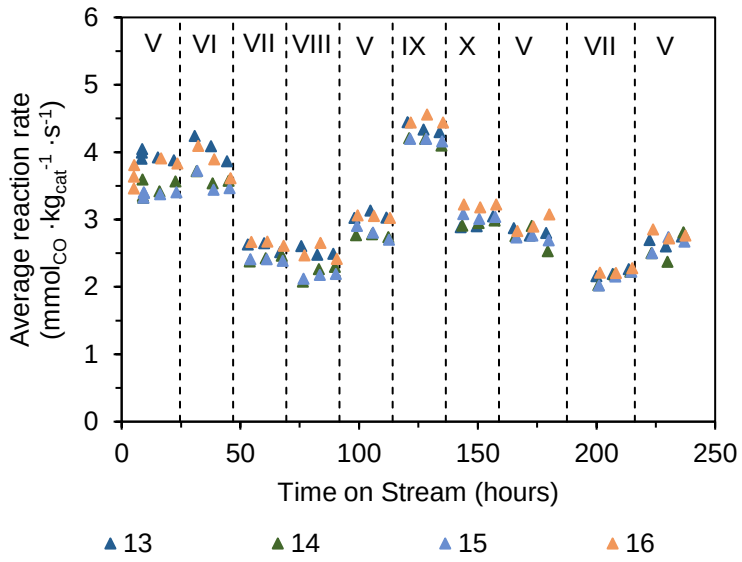

Figure C.12: Calculated average reaction rate for the second set of kinetic experiments at 300 °C

Appendix D: Testing for Transport Limitations and Assumptions

This appendix outlines the calculations to test for mass and heat transport limitations as well as the calculations to justify the assumptions made in developing the reactor model (See Chapter 4, section 8). The calculations follow very closely from the Eurokin fixed bed guide (Eurokin, 2011) and this appendix is referenced to this guide.

D.1. Relative Pressure Drop over Catalyst Bed

The pressure drop over the catalyst bed can be estimated from the Ergun equation (Equation D.1). In Equation D.1, ΔP is the pressure drop over the catalyst bed [Pa], h_{bed} is the height of the catalyst bed [m], ρ_g is the gas density [kg/m^3], u_0 is the superficial gas velocity [m/s], d_{pe} is the diameter of sphere of equivalent specific surface area, calculated as six times the ratio of the particle volume and the external surface area [m], ϵ_b is the bed porosity [m_{void}^3/m_{bed}^3] and Re is the Reynolds number [-].

$$\frac{\Delta P}{h_{bed}} = \frac{\rho_g u_o^2}{d_{pe}} \cdot \frac{(1-\epsilon_b)}{\epsilon_b^3} \cdot (1.75 + 150 \cdot \frac{(1-\epsilon_b)}{Re}) \qquad \text{Equation D.1}$$

The Reynolds number is calculated according to Equation D.2, where Re is the Reynolds number [-], d_{pe} is the diameter of sphere of equivalent specific surface area, calculated as six times the ratio of the particle volume and the external surface area [m], ρ_g is the gas density [kg/m^3], u_0 superficial gas velocity [m/s] and μ_G is the gas viscosity [kg/ms].

$$Re = \frac{d_{pe} \cdot \rho_g \cdot u_0}{\mu_G} \qquad \text{Equation D.2}$$

To ensure the relative pressure drop is acceptable, the following criterion needs to be met. ΔP is the pressure drop over the catalyst bed [Pa], P_{tot} is the total feed pressure [Pa] and n is the reaction order [-].

$$\Delta P < \frac{0.2 \cdot P_{tot}}{n} \qquad \text{Equation D.3}$$

D.2. Axial Dispersion

In order to neglect axial dispersion, thus allowing the assumption of plug-flow behaviour only, the criterion in Equation D.4 must be met. In Equation D.4, h_{bed} is the height of the catalyst bed [m], d_p is the particle diameter [m], Bo is the Bodenstein number [-], n is the reaction order [-] and X_A is the conversion of reactant A [-].

$$\frac{\mathrm{h_{bed}}}{d_p} > \frac{8}{Bo} \cdot n \cdot \ln\left(\frac{1}{1 - X_A}\right)$$ Equation D.4

The Bodenstein number is calculated by Equation D.5, in which ϵ_b is the bed porosity [m_{void}^3/m_{bed}^3], $D_{A,m}$ is the molecular diffusivity of A in the gas mixture [m^2/s], τ_b is the bed tortuosity [-], d_p is the particle diameter [m] and u_0 is the superficial gas velocity [m/s].

$$\frac{1}{Bo} = \frac{\epsilon_b \cdot D_{A,m}}{\tau_b \cdot d_p \cdot u_0} + 0.5$$ Equation D.5

The bed tortuosity can be calculated by Equation D.6, in which ϵ_b is the bed porosity [m_{void}^3/m_{bed}^3].

$$\tau_b = \frac{1}{\sqrt{\epsilon_b}}$$ Equation D.6

D.3. Radial Dispersion

To ensure the absence of radial concentration gradients, the criterion given by Equation D.7 must be met. In Equation D.7, d_t is the catalyst bed diameter [m] and d_p is the particle diameter [m].

$$\frac{d_t}{d_p} > 8$$ Equation D.7

D.4. External Mass Transfer Limitation

The extent of external mass transfer limitation is expressed by the Carberry number, given in Equation D.8. The criterion is that the resistance due to external mass transfer should be less than 5 % of the resistance due to the chemical reaction. In Equation D.8, Ca is the Carberry number [-], $R_{v,A}^{obs}$ is the observed volumetric reaction rate per unit of catalyst pellet volume [$mol/m_{catpellet}^3 s$], k_G is the external mass transfer coefficient [-], a_v is the specific external surface area of a single catalyst particle [m^2/m_{pellet}^3] (for a spherical particle, this is equal to $\frac{6}{d_p}$), $C_{A,b}$ is the bulk concentration of reactant A [mol/m_{gas}^3], $C_{A,s}$ is the concentration of reactant A at the external pellet surface [mol/m_{gas}^3] and n is the reaction order [-].

$$Ca = \frac{R_{v,A}^{obs}}{k_g \cdot a_v \cdot C_{A,b}} = \frac{C_{A,b} - C_{A,s}}{C_{A,b}} < \frac{0.05}{n} \quad (n > 0)$$ Equation D.8

The external mass transfer coefficient, k_g can be calculated by the following correlation. Sh is the Sherwood number, Re is the Reynolds number [-] (defined above in section D.1), and Sc is Schmidt number [-]. It should be noted that this correlation is only available in the range 0.1 < Re < 100.

$$Sh = 2 + 1.1 \cdot Re^{0.6} \cdot Sc^{\frac{1}{3}}$$ Equation D.9

The Sherwood number is calculated by Equation D.10, in which k_G is the external mass transfer coefficient [-], d_p is the particle diameter [m] and $D_{A,m}$ is the molecular diffusivity of A in the gas mixture [m^2/s].

$$Sh = \frac{k_G \cdot d_p}{D_{A,m}}$$ Equation D.10

The Schmidt number is calculated by Equation D.11, in which μ_G is the gas viscosity [kg/ms], ρ_g is the gas density [kg/m^3] and and $D_{A,m}$ is the molecular diffusivity of A in the gas mixture [m^2/s].

$$Sc = \frac{\mu_G}{\rho_g \cdot D_{A,m}}$$ Equation D.11

D.5. Internal Diffusion Limitation

The extent of internal diffusion limitation is expressed using the Weisz-Prater criterion, given by Equation D.12. The criterion states that the deviation caused by internal diffusion limitations should be smaller than 5 %. In Equation D.12, Φ is the Weisz modulus [-], $R_{v,A}^{obs}$ is the observed volumetric reaction rate per unit of catalyst pellet volume [mol/m$_{catpellet}$^{3}s], d_p is the particle diameter [m], $D_{A,eff}$ is the effective diffusivity inside the catalyst particles [m^2/s] and $C_{A,s}$ is the concentration of reactant A at the external catalyst particle surface [mol$_A$/m^3].

$$\Phi = \left(\frac{n+1}{2}\right) \cdot \left(\frac{R_{v,A}^{obs} \cdot \left(\frac{d_p}{6}\right)^2}{D_{A,eff} \cdot C_{A,s}} \right) < 0.08$$ Equation D.12

The Weisz modulus can be expressed as the ratio between the observed rate and the 'diffusion' rate according to Equation D.13, in which Φ is the Weisz modulus [-], η is the effectiveness factor and ϕ is the Thiele modulus.

$$\Phi = \eta \cdot \phi$$ Equation D.13

The Thiele modulus is given by Equation D.14, in which d_p is the particle diameter [m], $R_{v,A}$ is the actual reaction rate per unit of catalyst pellet volume [mol/m$_{catpellet}$^{3}s], $D_{A,eff}$ is the effective diffusivity inside the catalyst particles [m^2/s] and $C_{A,s}$ is the concentration of reactant A at the external catalyst particle surface [mol$_A$/m^3].

$$\phi = \frac{\mathrm{d_p}}{6} \cdot \sqrt{\left(\frac{n+1}{2}\right) \cdot \frac{R_{v,A}}{D_{A,eff} \cdot C_{A,s}}}$$ Equation D.14

If Φ is known, η and ϕ can be calculated by using a solver.

D.6. External Heat Transfer Limitation

The criterion for external heat transfer limitation is expressed in Equation D.15. In Equation D.15, ΔT_{film} is the temperature difference over the film surrounding the catalyst particles [K], $R_{v,A}^{obs}$ is the observed volumetric reaction rate per unit of catalyst pellet volume [mol/$m_{catpellet}^3$s], $\Delta_r H$ is the reaction enthalpy [J/mol], d_p is the particle diameter [m], α_p is the particle heat transfer coefficient [W/mK], R is the gas constant [8.314 J/(mol K)], T_G is the bulk gas temperature [K] and E_a is the apparent activation energy of the reaction [J/mol].

$$\Delta T_{film} = \frac{R_{v,A}^{obs} \cdot |\Delta_r H| \cdot d_p}{6 \cdot \alpha_p} < \frac{0.05 \cdot R \cdot T_G^2}{E_a} \qquad \text{Equation D.15}$$

The correlation represented in Equation D.16 can be used to estimate α_p and is valid in the range 0.1 < Re < 100. In Equation D.16, Nu is the Nusselt number [-], Re is the Reynolds number [-] and Pr is the Prandtl number [-].

$$Nu = 2 + 1.1 \cdot Re^{0.6} \cdot Pr^{\frac{1}{3}} \qquad \text{Equation D.16}$$

The Nusselt number is defined according to Equation D.17, in which α_p is the particle heat transfer coefficient [W/mK], d_p is the particle diameter [m] and λ_G is the thermal conductivity of the gas mixture [W/m K].

$$Nu = \frac{\alpha_p \cdot d_p}{\lambda_G} \qquad \text{Equation D.17}$$

The Prandtl number is defined according to Equation D.18, in which $C_{p,G}$ is the gas heat capacity [J/kg K], μ_G is the gas viscosity [kg/ms] and λ_G is the thermal conductivity of the gas mixture [W/m K].

$$\mathrm{Pr} = \frac{C_{p,G} \cdot \mu_G}{\lambda_G} \qquad \text{Equation D.18}$$

D.7. Radial Heat Transfer Limitation

The criterion expressed in Equation D.19 is valid for radial heat transport limitation in the catalyst bed. This criterion is valid when the reactor wall temperature is measured instead of the temperature at the centerline of the catalyst bed. In Equation D.19, ΔT_{rad} is the temperature difference between the bed near the wall and the average in the bed [K], Bi_w is the Biot number [-], $R_{v,A}^{obs}$ is the observed volumetric reaction rate per unit of catalyst pellet volume [mol/$m_{catpellet}^3$s], $\Delta_r H$ is the reaction enthalpy [J/mol], ϵ_b is the bed porosity [m_{void}^3/m_{bed}^3], b is the volume of inert material as a fraction of the total volume occupied by the solids [$m_{inert}^3/m_{inert+cat}^3$], d_t is the catalyst bed diameter [m], λ_{er} is the effective radial thermal conductivity in the bed [W/mK], R is the gas constant [8.314 J/(mol K)], T is the measured temperature of the catalyst bed [K] and E_a is the apparent activation energy of the reaction [J/mol].

$$\Delta T_{rad} = (1 + \frac{8}{Bi_w})] \cdot \frac{R_{v,A}^{obs} \cdot |\Delta_r H| \cdot (1 - \epsilon_b) \cdot (1 - b) \cdot d_t^2}{32 \cdot \lambda_{er}} < \frac{0.05 \cdot R \cdot T^2}{Ea}$$ Equation D.19

The Biot number at the internal reactor wall is defined as in Equation D.20. In Equation D.20, α_w is the heat transfer coefficient at the internal reactor wall [W/m²K], d_t is the catalyst bed diameter [m] and λ_{er} is the effective radial thermal conductivity in the bed [W/mK].

$$Bi_w = \frac{\alpha_w \cdot d_t}{\lambda_{er}}$$ Equation D.20

The following correlations for the effective radial heat conductivity (λ_{er}) and the heat transfer coefficient at the internal reactor wall (α_w) are valid for Re >40. The effective radial heat conductivity (λ_{er}) is estimated using Equation D.21, in which λ_{er} is the effective radial thermal conductivity in the bed [W/mK], λ_G is the effective thermal conductivity of the bulk gas [W/m K], $\lambda_{b,0}$ is the static contribution effective radial thermal conductivity [W/m K] and λ_{conv} is the convective contribution to the radial thermal conductivity [W/m K].

$$\frac{\lambda_{er}}{\lambda_G} = \frac{\lambda_{b,0}}{\lambda_G} + \frac{\lambda_{conv}}{\lambda_{\mathrm{G}}}$$ Equation D.21

To aid in calculating the correlation in Equation D.21, Equation D.22 and Equation D.24 can be used. In Equation D.22, Re is the Reynolds number [-; defined before], Pr is the Prandtl number [-; defined before] and Pe_{rif} is the Péclet number [-].

$$\frac{\lambda_{conv}}{\lambda_{\mathrm{G}}} = \frac{Re \cdot \mathrm{Pr}}{Pe_{rif}}$$ Equation D.22

Pe_{rif} is defined as in Equation D.23, in which d_t is the catalyst bed diameter [m] and d_p is the particle diameter [m].

$$Pe_{rif} = 8.65 \cdot \left[1 + 19.4 \cdot \left(\frac{d_p}{d_t}\right)^2\right]$$ Equation D.23

In Equation D.24, ϵ_b is the bed porosity [m_{void}^3/m_{bed}^3], λ_G is the effective thermal conductivity of the bulk gas [W/m K] and λ_p is the average thermal conductivity of the particles in the catalyst bed [W/m K].

$$\frac{\lambda_{b,0}}{\lambda_G} = \epsilon_b + \frac{1 - \epsilon_b}{0.220 \cdot \epsilon_b^2 + \frac{2}{3} \cdot \left(\frac{\lambda_G}{\lambda_p}\right)}$$ Equation D.24

The heat transfer coefficient at the wall, α_w, is estimated using Equation D.25. In Equation D.25, α_w^0 is the static contribution heat transfer coefficient gas-wall [W/m² K] and $\alpha_{w,conv}$ is the convective contribution heat transfer coefficient gas-wall [W/m² K].

$$\alpha_w = \alpha_w^0 + \alpha_{w,conv}$$ Equation D.25

α_w^0 is calculated by Equation D.26. In Equation D.26, λ_G is the effective thermal conductivity of the bulk gas [W/m K], d_p is the particle diameter [m], ϵ_b is the bed porosity [m_{void}^3/m_{bed}^3], d_t is the catalyst bed diameter [m] and λ_p is the average thermal conductivity of the particles in the catalyst bed [W/m K].

$$\frac{\alpha_w^0 \cdot d_p}{\lambda_G} = 2 \cdot \epsilon_b + \frac{1 - \epsilon_b}{0.0024 \cdot \left(\frac{d_t}{d_p}\right)^{1.58} + \frac{1}{3} \cdot \left(\frac{\lambda_G}{\lambda_p}\right)} \qquad \text{Equation D.26}$$

If Rep < 1200, $\alpha_{w,conv}$ is calculated according to Equation D.27. If Rep ≥ 1200, $\alpha_{w,conv}$ is calculated according to Equation D.28. In Equation D.27 and Equation D.28, λ_G is the effective thermal conductivity of the bulk gas [W/m K], d_p is the particle diameter [m], Re is the Reynolds number [-] and Pr is the Prandtl number [-].

$$\alpha_{w,conv} = 0.0835 \cdot \frac{\lambda_G}{d_p} \cdot Re_p^{0.91} \cdot \left(\frac{Pr}{Pr_{air,80\,°C}}\right)^{\frac{1}{3}} \qquad \text{Equation D.27}$$

$$\alpha_{w,conv} = 1.23 \cdot \frac{\lambda_G}{d_p} \cdot Re_p^{0.53} \cdot \left(\frac{Pr}{Pr_{air,80\,°C}}\right)^{\frac{1}{3}} \qquad \text{Equation D.28}$$

To emphasize, the correlations for λ_{er} and α_w presented above are only valid when Re > 40.

D.8. Intraparticle Heat Transport Limitation

The criterion presented in Equation D.29 is valid concerning intraparticle heat transport limitation. In Equation D.29, ΔT_{int} is the temperature difference between the edge and the average in particles [K], $R_{v,A}^{obs}$ is the observed volumetric reaction rate per unit of catalyst pellet volume [$mol/m_{catpellet}^3 s$], $\Delta_r H$ is the reaction enthalpy [J/mol], d_p is the particle diameter [m], λ_p is the average thermal conductivity of the catalyst particle [W/m K], R is the gas constant [8.314 J/(mol K)], T is the measured temperature of the catalyst bed [K] and E_a is the apparent activation energy of the reaction [J/mol].

$$\Delta T_{int} = \frac{R_{v,A}^{obs} \cdot |\Delta_r H| \cdot d_p^2}{60 \cdot \lambda_p} < \frac{0.05 \cdot R \cdot T^2}{E_a} \qquad \text{Equation D.29}$$

The average thermal conductivity of the catalyst particle (λ_p) can be calculated by Equation D.30, in which b is the volume of inert material as a fraction of the total volume occupied by the solids [$m_{inert}^3/m_{inert+cat}^3$], λ_{cat} is the conductivity of the catalyst pellets [W/m K] and λ_{dil} is the conductivity of the dilution pellets [W/m K].

$$\frac{1}{\lambda_p} = \frac{1 - b}{\lambda_{cat}} + \frac{b}{\lambda_{dil}} \qquad \text{Equation D.30}$$

D.9. Adiabatic Temperature Rise

The adiabatic temperature rise is a parameter of general interest and is easily calculated using Equation D.31. In Equation D.31, ΔT_{ad} is the adiabatic temperature rise [K], $\Delta_r H$ is the reaction enthalpy [J/mol], y_A is the molar fraction of reactant A in the feed [-], X_A is the conversion of reactant A [-] and $C_{p,G}$ is the heat capacity of the gas mixture [J/mol K].

$$\Delta T_{ad} = \frac{|\Delta_r H| \cdot y_A \cdot X_A}{C_{p,G}} \qquad \text{Equation D.31}$$

D.10. Axial Temperature Gradient

If the reactor wall can be assumed isothermal over the length of the catalyst bed, the effect of the axial temperature gradient in the bed is smaller than that for the radial temperature profile. As such, a criterion for the axial temperature profile in a fixed bed is normally not necessary.

D.11. Bulk Diffusivity

D.11.1. Binary molecular diffusivity in gases (bulk diffusivity)

The binary molecular diffusivity of gas A in gas B, D_{AB}, can be estimated by the semi-empirical correlation given in Equation D.32. In Equation D.32, D_{AB} is the diffusivity of A in B [m^2/s], T is the measured temperature of the catalyst bed [K], m_i is the molecular mass of component i [kg/mol], P_{tot} is the total system pressure [kPa] and ν is the diffusion volume of component i [m^3/mol]. The diffusion volume for the components of interest in this project is presented in Table.

$$D_{AB} = \frac{\left(3.2 \times 10^{-11} \cdot T^{1.75} \cdot \sqrt{\frac{1}{m_A} + \frac{1}{m_B}}\right)}{P_{tot} \cdot \left\{(\sum \nu)_A^{\frac{1}{3}} + (\sum \nu)_B^{\frac{1}{3}}\right\}^2} \qquad \text{Equation D.32}$$

Table D.1: Diffusion volumes used in the estimation of the molecular diffusivity

Component	Diffusion volume [10^{-6} m^3/mol]
CO	18.9
H_2O	12.7
CO_2	26.9
H_2	7.07
N_2	17.9
He	2.88

D.11.2. Bulk diffusivity in gas mixtures

The bulk diffusivity of a component in a gas mixture containing more than two molecules (D_{Am}) can be estimated from the individual binary diffusivities (D_{Ai}) according to the Wilke-equation shown in Equation D.33. In Equation D.33, X_A is the conversion of component A, N_c is the total number of components and x_i is the molar fraction of component i.

$$D_{Am} = (1 - X_A) \cdot \left(\sum_{i=1(i \neq A)}^{N_c} \frac{x_i}{D_{Ai}} \right)^{-1} \qquad \text{Equation D.33}$$

Equation D.33 is only valid in diluted mixtures in a stagnant medium. In most cases, the Stefan-Maxwell equation (Equation D.36) is more accurate to use. Equation D.36 considers the effect of the diffusion of the other components. The following three equations are used to calculate the effective diffusivity. In these equations, D_{Am}^0 is the reduced molecular diffusivity of A [m^2/s], N_c is the total number of components, x_i is the molar fraction of component i, ν_i is the diffusion volume of component i [m^3/mol], D_{Ai} is the individual binary diffusivities [m^2/s], f_A is the 'so-called' film factor [-] and $x_{A,i}$ is the molar fraction of component i at the gas-solid interface [-].

$$D_{Am}^0 = \frac{1 - x_A \cdot \sum_{i=1}^{N_c} \frac{\nu_i}{\nu_A}}{\sum_{i=1(i \neq A)}^{N_c} \left\{ \frac{1}{D_{Ai}} \cdot \left(x_i - x_A \cdot \frac{\nu_i}{\nu_A} \right) \right\}} \qquad \text{Equation D.34}$$

$$f_A = \frac{\left(x_{A,i} - x_A \right) \cdot \sum_{i=1}^{N_c} \left(\frac{\nu_i}{\nu_A} \right)}{\ln \left\{ \frac{1 - x_A \cdot \sum_{i=1}^{N_c} \left(\frac{\nu_i}{\nu_A} \right)}{1 - x_{A,i} \cdot \sum_{i=1}^{N_c} \left(\frac{\nu_i}{\nu_A} \right)} \right\}} \qquad \text{Equation D.35}$$

$$D_{Am} = D_{Am}^0 / f_A \qquad \text{Equation D.36}$$

For equimolar counter diffusion, the film factor f_A reduces to one.

D.12. Effective Diffusivity

The effective diffusivity in the catalyst particles pores, $D_{A,eff}$, is lower than the bulk diffusivity due to restrictions caused by the solid material of the catalyst particles. With gases and when the catalyst has narrow pores (which applies to most catalysts), the limitation due to Knudsen diffusion needs to be considered as well. Knudsen diffusion is when the transport of gas molecules is limited by molecule-wall collisions and not by molecule-molecule collisions as in bulk diffusion.

The effective diffusivity in the catalyst particles pores can be calculated by the following equation, in which ϵ_p is the catalyst porosity [-], τ_p is the catalyst pore tortuosity [-], $D_{A,m}$ is the bulk diffusivity of component A in the gas mixture [m^2/s] and $D_{A,k}$ is the Knudsen diffusivity of A [m^2/s].

$$D_{A,eff} = \frac{\frac{\epsilon_p}{\tau_p}}{\frac{1}{D_{A,m}} + \frac{1}{D_{A,k}}} \qquad \text{Equation D.37}$$

The Knudsen diffusivity of A can be calculated using Equation D.38, in which $\bar{r}$ is the average pore radius [m], R is the gas constant [8.314 J/(mol K)], T is the measured temperature [K] and m_A is the molecular mass of A [kg/mol].

$$D_{A,k} = \frac{2}{3} \cdot \bar{r} \cdot \sqrt{\frac{8 \cdot R \cdot T}{\pi \cdot m_A}} \qquad \text{Equation D.38}$$

The average pore radius can be calculated using Equation D.39. In Equation D.39, ϵ_p is the catalyst porosity [-], ρ_p is the catalyst particle density [kg/m$_{pellet}^3$] and S is the specific internal surface area [m^2/kg-cat].

$$\bar{r} = \frac{2 \cdot \epsilon_p}{\rho_p \cdot S} \qquad \text{Equation D.39}$$

Appendix E: Determination of Gas Chromatography Relative Response Factors

He was used as the internal standard for the experimental programme and forms the basis on which the concentrations of other species in the reactor are quantified. The relative response factors (RFFs) determined take the form of a straight-line equation, as shown in Equation E.1. In Equation E.1, $\dot{V}_i$ is the volumetric flow rate of component i ($ml_{(n)}$/min), $Area_i$ is the peak area of component i obtained from the GC (-), $RFF_{i,a}$ is the 'a' component of the RFF factor for component i (-) and $RFF_{i,b}$ is the 'b' component of the RFF factor for component i (-).

$$\frac{Area_i}{Area_{He}} = RFF_{i,a} \cdot \frac{\dot{V}_i}{\dot{V}_{He}} + RFF_{i,b} \qquad \text{Equation E.1}$$

The RFFs for each component was determined by sampling a known gas composition using the gas chromatograph (GC). This was repeated for a variety of gas compositions. A plot of $\frac{Area_i}{Area_{He}}$ vs. $\frac{\dot{V}_i}{\dot{V}_{He}}$ would then allow for $RFF_{i,a}$ and $RFF_{i,b}$ to be determined. The figures below show how the $RFF_{i,a}$ and $RFF_{i,b}$ factors were determined for the gases used in this study. A RFF for N_2 was not determined, as N_2 was assumed to be non-reactive in the system. The amount of N_2 in the feed stream is the amount of N_2 in the product stream because of this assumption.

In the case of CO (Figure E.1), RFFs were determined on both the COX and MS5A column. Since the MS5A column gave a better relationship, as judged by the R^2 value, this column was used to quantify the amount of CO in this study.

As seen in Figure E.2 and Figure E.3, the responses for CO_2 and H_2 changes significantly depending on the $\dot{V}_{CO_2}/\dot{V}_{He}$ and $\dot{V}_{H_2}/\dot{V}_{He}$ ratios respectively. As such, separate RFFs have been determined for high and low volumetric flow ratios.

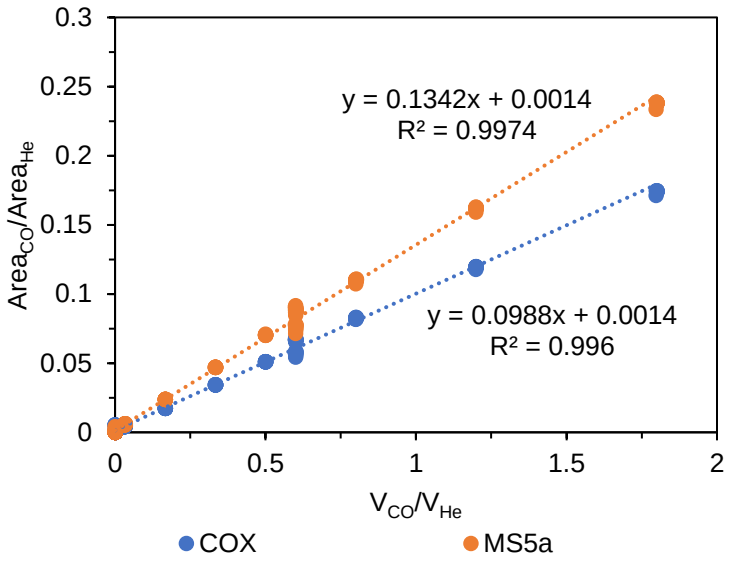

Figure E.1: Determination of the relative response factor for CO

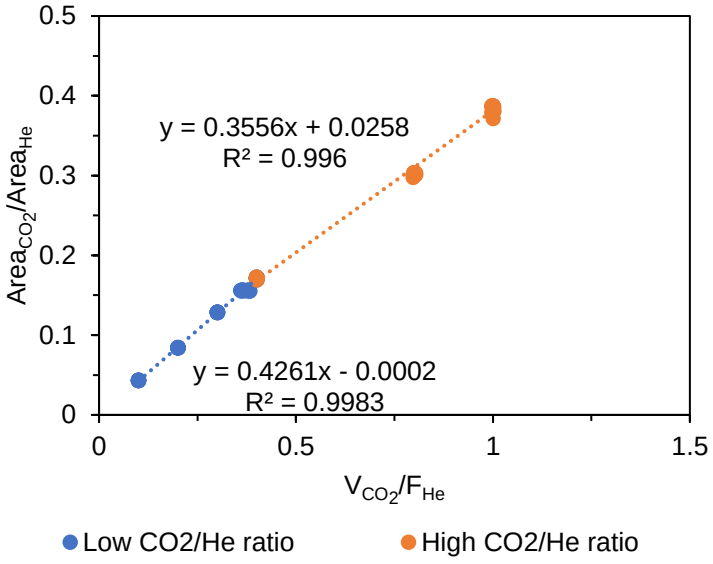

Figure E.2: Determination of the relative response factor for CO_2

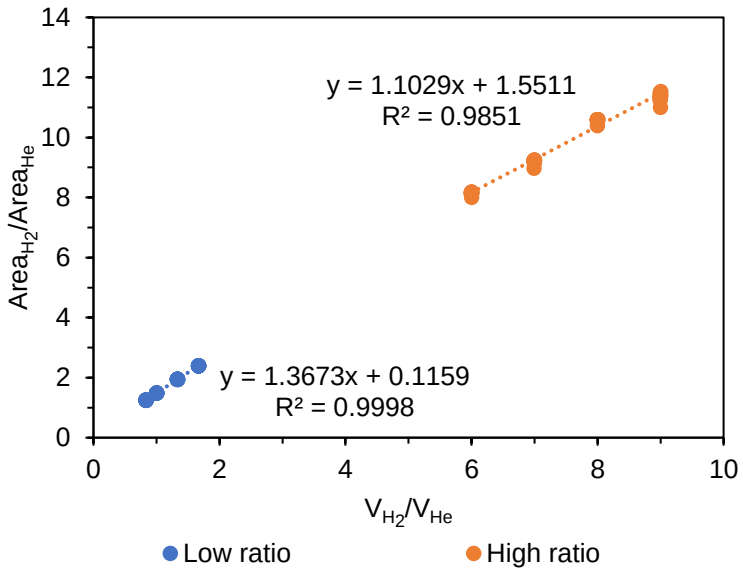

Figure E.3: Determination of the relative response factor for H_2

Appendix F: Transmission Electron Microscopy Images of Used Catalyst

Transmission Electron Microscopy (TEM) images of four used catalysts were taken to monitor any change in Pt particle size. Please refer to Chapter 5, section 2.2 for the experimental results. The following used catalysts were chosen to be studied by TEM for Pt particle size:

- First set of kinetic experiments, reactor 15,
- Second set of kinetic experiments, reactor 4,
- Second set of kinetic experiments, reactor 7 and
- Second set of kinetic experiments, reactor 15

The catalysts chosen showed the most significant deactivation at their respective temperatures. Details regarding the first and second sets of experiments can be found in Appendix A.

F.1. First Set of Kinetic Experiments, Reactor 15

The TEM and high-angle annular dark-field (HAADF) images of the used catalyst from reactor 15 (first set of kinetic experiments) are shown in Figure F.1. Figure F.2 shows the number-based TEM Pt nanoparticle size distribution.

A reasonably narrow size distribution is presented in Figure F.2. An average Pt particle size of 2.0 ± 0.5 nm has been determined from the TEM and HAADF images.

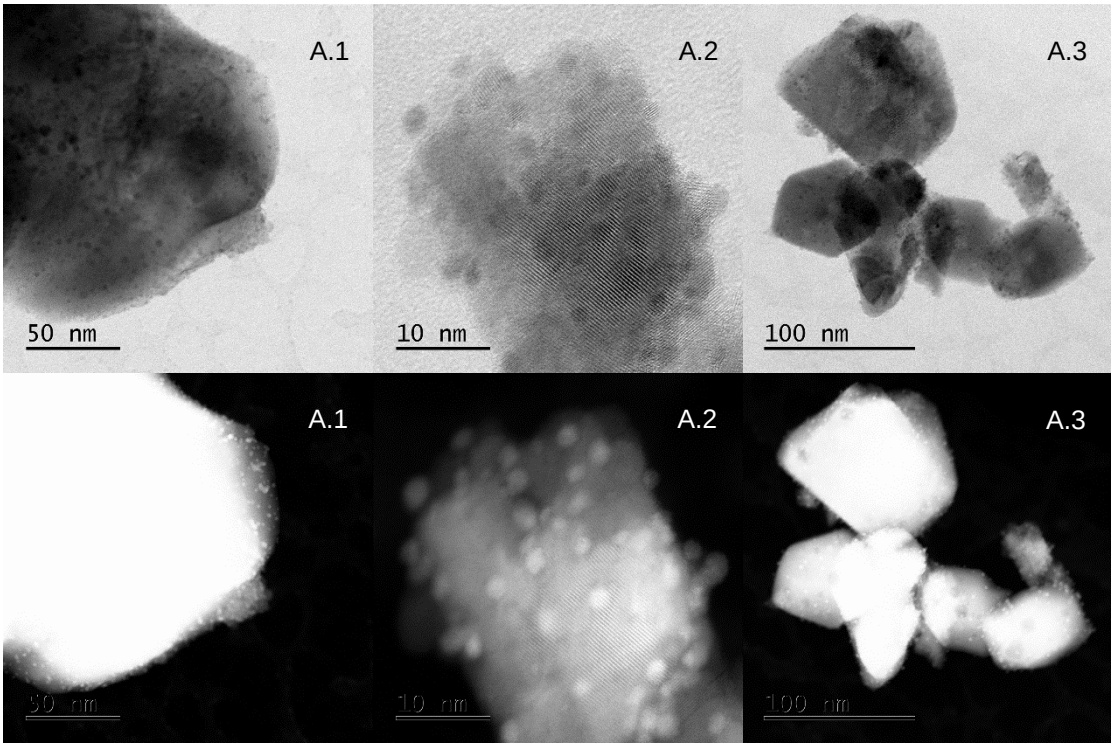

Figure F.1: (A) TEM and (B) corresponding HAADF images of the used 0.5 wt% Pt/CeO_2 catalyst from reactor 15 of the first set of kinetic experiments

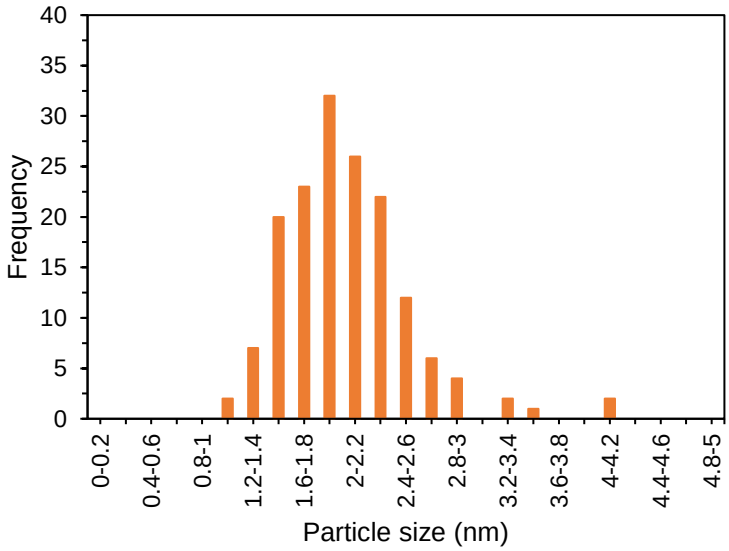

Figure F.2: Pt particle size distribution of the used 0.5 wt% Pt/CeO_2 catalyst from reactor 15 of the first set of kinetic experiments

F.2. Second Set of Kinetic Experiments, Reactor 4

The TEM and HAADF images of the used catalyst from reactor 4 (second set of kinetic experiments) are shown in Figure F.3. Figure F.4 shows the number-based TEM Pt nanoparticle size distribution.

Again, a reasonably narrow Pt particle size distribution is presented in Figure F.4, with an average Pt particle size of 2.0 ± 0.4 nm being determined from the TEM and HAADF images.

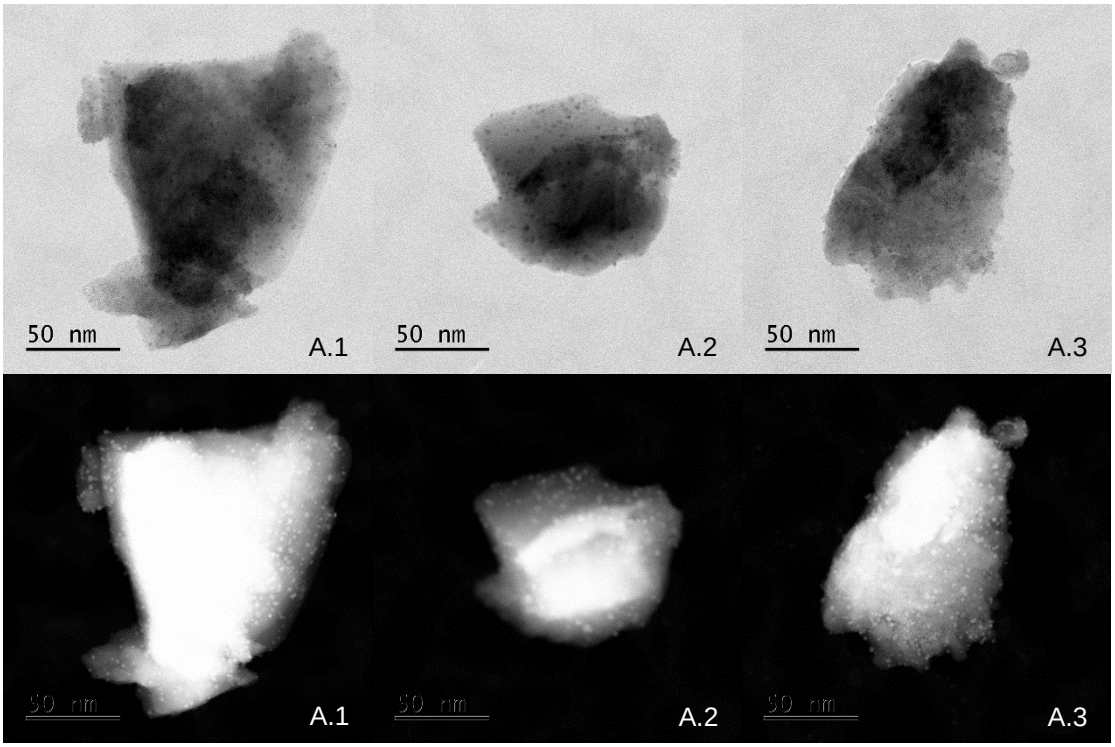

Figure F.3: (A) TEM and (B) corresponding HAADF images of the used 0.5 wt% Pt/CeO_2 catalyst from reactor 4 of the second set of kinetic experiments

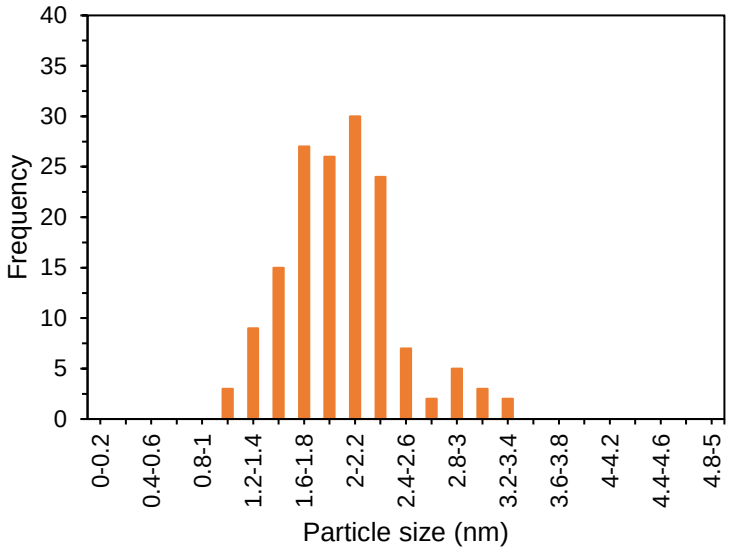

Figure F.4: Pt particle size distribution of the used 0.5 wt% Pt/CeO_2 catalyst from reactor 4 of the second set of kinetic experiments

F.3. Second Set of Kinetic Experiments, Reactor 7

The TEM and HAADF images of the used catalyst from reactor 7 (second set of kinetic experiments) are shown in Figure F.5. Figure F.6 shows the number-based TEM Pt nanoparticle size distribution.

The Pt particle size distribution presented in Figure F.6 corresponds to an average Pt particle size of 2.2 ± 0.5 nm. A narrow Pt particle size distribution is observed.

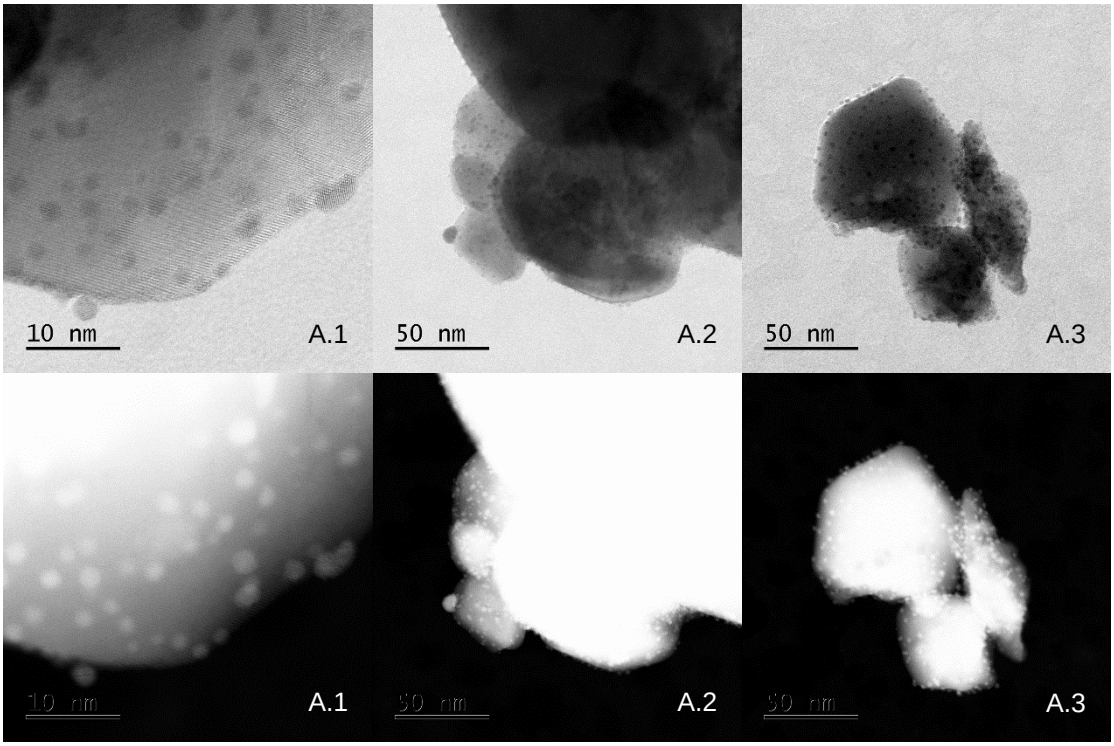

Figure F.5: (A) TEM and (B) corresponding HAADF images of the used 0.5 wt% Pt/CeO_2 catalyst from reactor 7 of the second set of kinetic experiments

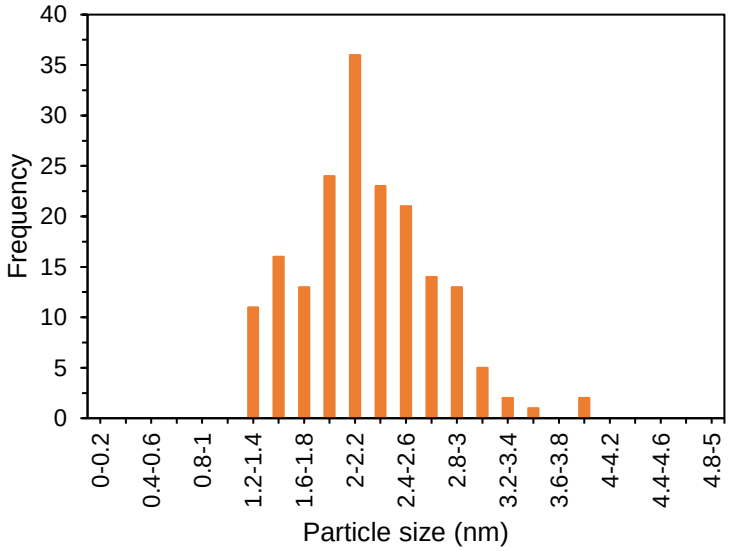

Figure F.6: Pt particle size distribution of the used 0.5 wt% Pt/CeO_2 catalyst from reactor 7 of the second set of kinetic experiments

F.4. Second Set of Kinetic Experiments, Reactor 15

The TEM and HAADF images of the used catalyst from reactor 15 (second set of kinetic experiments) are shown in Figure F.7. Figure F.8 shows the number-based TEM Pt nanoparticle size distribution.

A narrow Pt particle size distribution is presented in Figure F.8, with an average Pt particle size of 2.0 ± 0.5 nm being determined from the TEM and HAADF images.

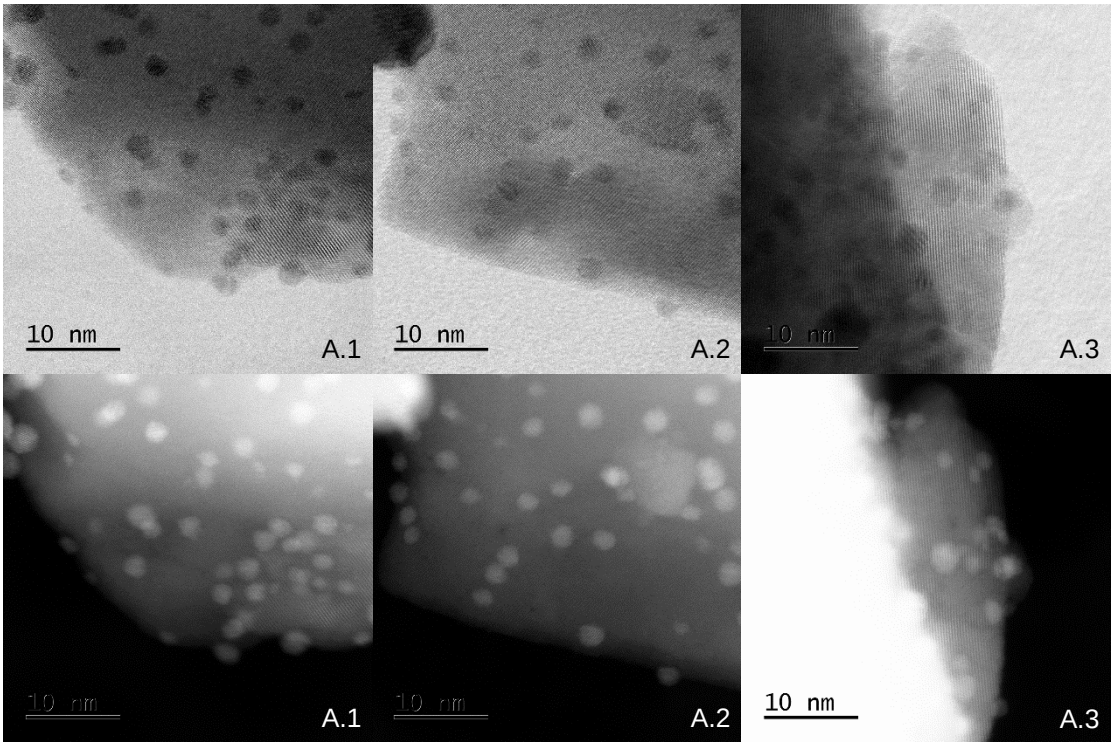

Figure F.7: (A) TEM and (B) corresponding HAADF images of the used 0.5 wt% Pt/CeO_2 catalyst from reactor 15 of the second set of kinetic experiments

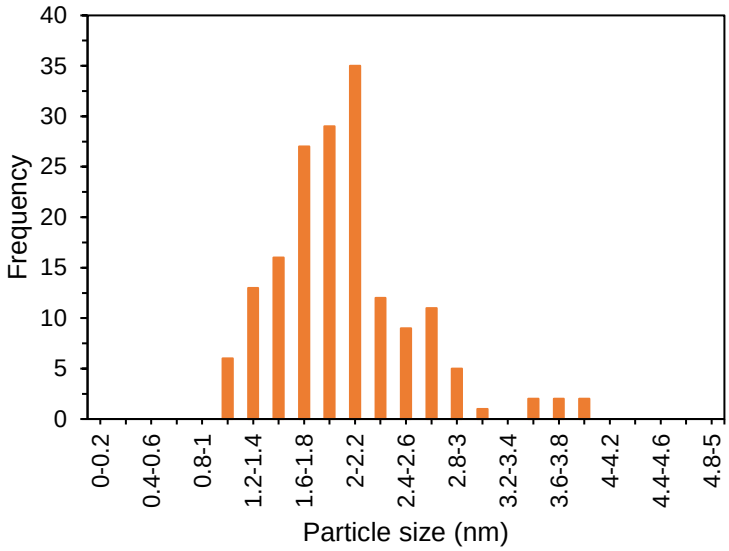

Figure F.8: Pt particle size distribution of the used 0.5 wt% Pt/CeO_2 catalyst from reactor 15 of the second set of kinetic experiments

Appendix G: Derivation of Langmuir-Hinshelwood type rate expressions

An example derivation of a Langmuir-Hinshelwood type rate expression is presented below. The example presented follows the mechanistic steps represented in case 1 (Chapter 7, section 7.2.1), with step 2 assumed to be the rate limiting step.

Firstly, for each mechanistic step presented, the following rate equations exist (Table G.1). In the rate equations presented below, r_i is the reaction rate equation for step i, k_i is the reaction rate constant for step i, P_i is the partial pressure of component i, C_{Si} is the concentration of vacant active site i's, C_{i-Si} is the concentration of component i on active site j and K_i is the ratio of the reverse rate constant to the forward rate constant for step i.

Table G.1: Rate equations corresponding to each mechanistic step presented in case 1

Step number	Rate equation
1	$r_1 = k_1 \cdot \left(P_{CO} \cdot C_{S1} - \frac{C_{CO-S1}}{K_1}\right)$
2	$r_2 = k_2 \cdot \left(C_{CO-S1} \cdot C_{O-S2} - \frac{C_{CO_2-S1} \cdot C_{S2}}{K_2}\right)$
3	$r_3 = k_3 \cdot \left(P_{CO_2} \cdot C_{S1} - \frac{C_{CO_2-S1}}{K_3}\right)$
4	$r_4 = k_4 \cdot \left(P_{H_2O} \cdot C_{S2} - \frac{C_{H_2O-S2}}{K_4}\right)$
5	$r_5 = k_5 \cdot \left(C_{H_2O-S2} \cdot C_{S1}^2 - \frac{C_{O-S2} \cdot C_{H-S1}^2}{K_5}\right)$
6	$r_6 = k_6 \cdot \left(P_{H_2} \cdot C_{S1}^2 - \frac{C_{H-S1}^2}{K_6}\right)$

If we assume step 2 to be the rate determining (limiting) step, we are assuming all other steps are significantly faster than this step. That is, we assume the rate constants of all other steps are very large when compared to the rate constant for step 2. This assumption can be represented the constraint shown in Equation G.1. In Equation G.1, i takes on the values 1, 3, 4, 5 and 6.

$$\frac{r_i}{k_i} \approx 0 \qquad \text{Equation G.1}$$

Since the concentration of components on the active sites (C_{i-Si}) cannot be measured, these concentrations need to be determined in terms of the partial pressures of the gaseous

components, which can be measured. This is done by applying the constraint in Equation G.1 to the rate equations for steps 1, 3, 4, 5 and 6. Applying the constraint to step 1, we get:

$$C_{CO-S1} = K_1 \cdot P_{CO} \cdot C_{S1}$$ Equation G.2

Applying the constraint to step 3, we get:

$$C_{CO_2-S1} = K_3 \cdot P_{CO_2} \cdot C_{S1}$$ Equation G.3

Applying the constraint to step 4, we get:

$$C_{H_2O-S2} = K_4 \cdot P_{H_2O} \cdot C_{S2}$$ Equation G.4

Applying the constraint to step 5, we get:

$$C_{H-S1}^2 = K_6 \cdot P_{H_2} \cdot C_{S1}^2$$ Equation G.5

Applying the constraint to step 6, we get:

$$C_{O-S2} = \frac{K_5 \cdot C_{H_2O-S2} \cdot C_{S1}^2}{C_{H-S1}^2}$$ Equation G.6

Further substitutions of Equation G.4 and Equation G.5 into Equation G.6 will eliminate the unknown concentrations in Equation G.6. Then, substituting Equation G.2 through Equation G.6 into the rate equation from step 2 (the rate determining step) results in the following rate equation being obtained:

$$r_2 = k \cdot C_{S1} \cdot C_{S2} \cdot \left(\frac{K_1 \cdot K_4 \cdot K_5}{K_6}\right) \cdot \left(\frac{P_{CO} \cdot P_{H_2O}}{P_{H_2}} - \frac{P_{CO_2}}{K_{Eq}}\right)$$ Equation G.7

In Equation G.7, C_{S1} and C_{S2} cannot be measured and change constantly during the reaction. The total number of active sites, however, is constant. Therefore, a site balance can be used to eliminate C_{S1} and C_{S2}. A site balance for S1 is represented in Equation G.8 and a site balance for S2 is represented in Equation G.9. In these equations, C_{Ti} is the total number of active sites for site i.

$$C_{T1} = C_{S1} + C_{CO-S1} + C_{CO_2-S1} + C_{H-S1}$$ Equation G.8

$$C_{T2} = C_{S2} + C_{O-S2} + C_{H_2O-S2}$$ Equation G.9

Substituting Equation G.2 through Equation G.6 into both Equation G.8 and Equation G.9 and rearranging to solve for the unknown C_{S1} and C_{S2} results in Equation G.10 and Equation G.11 being obtained.

$$C_{S1} = \frac{C_{T1}}{1 + K_1 \cdot P_{CO} + K_3 \cdot P_{CO_2} + \sqrt{K_6 \cdot P_{H_2}}}$$ Equation G.10

$$C_{S2} = \frac{C_{T2}}{1 + \frac{K_4 \cdot K_5}{K_6} \cdot \frac{P_{H_2O}}{P_{H_2}} + K_4 \cdot P_{H_2O}}$$ Equation G.11

Lastly, substituting Equation G.10 and Equation G.11 into Equation G.7 gives the rate equation described by assuming step 2 to be the rate determining step. The final rate equation is given in Equation G.12.

$$r_2 = \frac{k \cdot \left(\frac{K_1 \cdot K_4 \cdot K_5}{K_6}\right) \cdot \left(\frac{P_{CO} \cdot P_{H_2O}}{P_{H_2}} - \frac{P_{CO_2}}{K_{Eq}}\right)}{\left(1 + K_1 \cdot P_{CO} + K_3 \cdot P_{CO_2} + \sqrt{K_6 \cdot P_{H_2}}\right) \cdot \left(1 + \frac{K_4 \cdot K_5}{K_6} \cdot \frac{P_{H_2O}}{P_{H_2}} + K_4 \cdot P_{H_2O}\right)}$$ Equation G.12

Appendix H: EBE Faculty 'Assessment of Ethics in Research Projects Form'

EBE Faculty: Assessment of Ethics in Research Projects

Any person planning to undertake research in the Faculty of Engineering and the Built Environment at the University of Cape Town is required to complete this form before collecting or analysing data. When completed it should be submitted to the supervisor (where applicable) and from there to the Head of Department. If any of the questions below have been answered YES, and the applicant is NOT a fourth year student, the Head should forward this form for approval by the Faculty EIR committee: submit to Ms Zakiya Chikte (Zakiya.chikte@uct.ac.za); New EBE Building, Ph 021 650 5739). Students must include a copy of the completed form with the dissertation/thesis when it is submitted for examination.

Name of Principal Researcher/Student: Darryl Brown **Department:** Chemical Engineering

If a Student: **Degree:** MSc (Eng) Chemical Engineering **Supervisor:** Prof. J.C.Q. Fletcher

If a Research Contract indicate source of funding/sponsorship:

Research Project Title: Water Gas Shift Reaction Kinetics for Carbon Monoxide Reduction in Hydrogen Rich Reformate Streams

Overview of ethics issues in your research project:

Question 1: Is there a possibility that your research could cause harm to a third party (i.e. a person not involved in your project)?	YES	NO ✓
Question 2: Is your research making use of human subjects as sources of data? If your answer is YES, please complete Addendum 2.	YES	NO ✓
Question 3: Does your research involve the participation of or provision of services to communities? If your answer is YES, please complete Addendum 3.	YES	NO ✓
Question 4: If your research is sponsored, is there any potential for conflicts of interest? If your answer is YES, please complete Addendum 4.	YES	NO ✓

If you have answered YES to any of the above questions, please append a copy of your research proposal, as well as any interview schedules or questionnaires (Addendum 1) and please complete further addenda as appropriate.

I hereby undertake to carry out my research in such a way that

- there is no apparent legal objection to the nature or the method of research; and
- the research will not compromise staff or students or the other responsibilities of the University;
- the stated objective will be achieved, and the findings will have a high degree of validity;
- limitations and alternative interpretations will be considered;
- the findings could be subject to peer review and publicly available; and
- I will comply with the conventions of copyright and avoid any practice that would constitute plagiarism.

Signed by:

	Full name and signature	Date
Principal Researcher/Student:	Darryl Brown	29/02/2016

Signed

This application is approved by:

Supervisor (if applicable):		29/02/2016
HOD (or delegated nominee): Final authority for all assessments with NO to all questions and for all undergraduate research.	HARRO VON BLOTTNITZ	15·3·16
Chair : Faculty EIR Committee For applicants other than undergraduate students who have answered YES to any of the above questions.		